

Constraints on the Polarized Dust and the Cosmic  
Microwave Background Using BICEP / Keck Array  
Series of Telescopes

Thesis by  
Sinan Kefeli

In Partial Fulfillment of the Requirements for the  
Degree of  
Doctor of Philosophy

The logo for the California Institute of Technology (Caltech), featuring the word "Caltech" in a bold, orange, sans-serif font.

CALIFORNIA INSTITUTE OF TECHNOLOGY  
Pasadena, California

2023  
Defended (23 August 2022)

© 2023

Sinan Kefeli

ORCID: 0000-0002-8604-3516

All rights reserved

## ABSTRACT

BK18 data consists of all the data taken by the BICEP2, KECK ARRAY, and BICEP3 CMB polarization experiments, as well as publicly available WMAP and PLANCK maps. The Q/U maps reach depths of 2.8, 2.8 and 8.8  $\mu\text{K}_{\text{CMB}}$  arcmin at 95, 150, and 220 GHz respectively over an effective area of  $\sim 600$  square degrees at 95 GHz and  $\sim 400$  square degrees at 150 and 220 GHz. The likelihood analysis yields  $r < 0.036$  at 95% confidence, with unbiased simulations yielding  $\sigma(r) = 0.009$ . The multi-component model that is used in the likelihood analysis consists of lensed- $\Lambda\text{CDM}$ , tensor modes, and polarize dust and synchrotron components. Foreground model consists of thirteen parameters, some of which are estimated in the likelihood analysis with priors derived from larger regions of sky from WMAP and PLANCK: amplitude, spectral index, and spatial index for dust and sync, as well as their spatial correlation; dust frequency decorrelation and tensor-to-scalar-ratio. Spectral index for dust emission no longer requires a prior taken from measurements on other regions of the sky.

In the BK papers, EE spectra are not used to derive the model, however the spectra agree well with the assumption that  $\text{EE}/\text{BB} = 2$  for dust. In this thesis we expand on this assumption, sharing the results for the EE/BB estimate for dust when this is a free parameter in the likelihood calculation. We use the map-based and spectral-based band difference approaches to include E-modes in the likelihood analysis. In the BK papers, dust parameters are assumed to be constant over the sky. We will go over the likelihood work on the spatial constraints for the dust spectral index to examine the validity of this assumption.

# TABLE OF CONTENTS

Abstract . . . . .	iii
Table of Contents . . . . .	iv
List of Illustrations . . . . .	vi
List of Tables . . . . .	xxi
<b>Chapter I: Introduction . . . . .</b>	<b>1</b>
1.1 Standard Model of Cosmology . . . . .	2
1.2 Cosmic Microwave Background . . . . .	5
1.3 Inflation . . . . .	12
1.4 Perturbations . . . . .	24
1.5 Foregrounds . . . . .	27
<b>Chapter II: BICEP/Keck Array Array Experiment . . . . .</b>	<b>36</b>
2.1 BICEP/Keck Array Instrument . . . . .	37
2.2 Observation Site . . . . .	42
2.3 Observation Strategy . . . . .	44
2.4 Detectors . . . . .	46
2.5 Readout . . . . .	51
<b>Chapter III: Keck Array High Frequency and BICEP3 Instrument Character-</b>	
<b>ization . . . . .</b>	<b>54</b>
3.1 Optical Efficiency . . . . .	55
3.2 Spectral Response . . . . .	58
3.3 G Measurement . . . . .	62
3.4 Beam Measurements . . . . .	65
3.5 Polarization Efficiency . . . . .	67
3.6 Partial Load Curves . . . . .	68
3.7 Bias Selection . . . . .	70
3.8 Correlated Row Noise . . . . .	74
<b>Chapter IV: Analysis Pipeline . . . . .</b>	<b>80</b>
4.1 Data Pipeline . . . . .	81
4.2 Simulations . . . . .	93
4.3 Filtering for PSD Estimators . . . . .	95
4.4 Power Spectra . . . . .	96
<b>Chapter V: Multi-Component Analysis . . . . .</b>	<b>105</b>
5.1 Historical Overview and Motivation . . . . .	106
5.2 Multi-Component Model . . . . .	106
5.3 Data Selection . . . . .	110
5.4 Likelihood Analysis . . . . .	112
5.5 BK18 Likelihood . . . . .	113
5.6 Fisher Forecasting . . . . .	115
5.7 Forecasting with Maximum Likelihood . . . . .	117

5.8 Priors in Fisher and ML Search . . . . .	118
Chapter VI: Dust Polarization Analysis . . . . .	121
6.1 Dust Decorrelation . . . . .	122
6.2 High Frequency Band Forecasting . . . . .	122
6.3 Spatial Variations in $\beta_d$ . . . . .	126
6.4 EE to BB Ratio For Dust . . . . .	131
Chapter VII: Conclusion . . . . .	149
Bibliography . . . . .	151

## LIST OF ILLUSTRATIONS

<i>Number</i>	<i>Page</i>
1.1 CMB Temperature Fluctuations measured by Planck satellite. Colorbar corresponds to $\pm 500\mu\text{K}$ (Credit: Planck Team). . . . .	6
1.2 CMB spectrum waves per centimeter vs. intensity. The data matches the curve so well that the error uncertainties are only a fraction of the width of theory blackbody curve. . . . .	7
1.3 Angular power spectrum of CMB temperature fluctuations measured by Planck Collaboration. Upper Panel: Red line corresponds to best fit $\Lambda\text{CDM}$ model and the blue points are the measured APS values. Low multipole values are limited by cosmic variance. Lower Panel: Residual difference between the best fit $\Lambda\text{CDM}$ model and the measured APS values. Figure from [16]. . . . .	9
1.4 Thomson scattering of CMB photons. Blue lines on the photons coming from the left represent hot and red lines on the photons coming from up. Figure from [56]. . . . .	10
1.5 The CMB angular power spectrum measurements play an important role in modern cosmology. In this figure, we present a set of measurements from 2018, showing the temperature and polarization power spectra, lensing deflection power spectrum, cross-correlation between $T$ and $B$ is shown. Each experiment is represented by a different color, keeping the original binning. EE spectra with large error bars are omitted for multiple experiments. The dashed line in the figure represents the best-fit $\Lambda\text{CDM}$ model to the <i>Planck</i> temperature, polarization, and lensing data. Figure taken from [24]. . . . .	13

- 1.6 A schematic illustration of the polarization patterns in the CMB resulting from density and gravitational waves. On the upper panel, when a single density wave propagates in the direction indicated by the arrow, an electron will perceive hotter and colder photons parallel or perpendicular to the plane of the wave. This can only generate E-mode polarization pattern, as shown on the upper right part of the figure. In contrast, a single gravitational wave propagating in the same direction as the density wave stretches and compresses space in directions perpendicular to the propagation. Depending on the orientation of the stretch/squeeze motion, the resulting polarization pattern can either be E-mode or B-mode. This is shown on the lower right part of the figure. Image taken from BICEP/Keck Array collaboration. . . . . 14
- 1.7 Regions that were in causal contact in the early universe should have similar properties today. Observations of the cosmic microwave background radiation indicate that the universe is highly uniform on large scales, even in regions that were not in causal contact. The horizon problem arises from the fact that at the time of recombination, only angular scales up to about 1.7 degrees across the sky had been in causal contact. Figure from [32]. . . . . 18
- 1.8 Inflation offers to solve the horizon problem by postulating that the universe underwent a period of exponential expansion shortly after the Big Bang. During this period, regions that were previously in causal contact could have been stretched far enough apart so that they appear to be outside of each other's observable horizon today. Figure from [32]. . . . . 19
- 1.9 Slow roll inflation is the period of inflation where the scalar field that drives inflation rolls slowly down its potential. During this period the universe undergoes an exponential expansion. Figure from [32] . . . . 21

- 1.10 The Planck 2018 baseline analysis provides constraints on the tensor-to-scalar ratio  $r$  and the scalar spectral index  $n_s$  (Green). These constraints are further improved by including BICEP/Keck data up to the end of the 2018 season and baryon acoustic oscillation data to enhance the constraint on  $n_s$ . As a result, the upper limit on  $r_{0.05}$  tightens from  $r_{0.05} < 0.11$  to  $r_{0.05} < 0.035$ . Additional inflationary models are shown, the purple region representing natural inflation, and the red curves representing  $\phi^p$  models. Figure taken from [18]. . . . . 23
- 1.11 BK18 published analysis places constraints on the inflationary parameters  $r$  and  $n_s$ . On the left is the case with  $r = 0.01$  and on the right  $r = 0$ . Planck 2018 provides hilltop quartic model [35] band, as well as the vertical  $\phi^2$ -derived  $\alpha$  attractor T-model band that extends down to  $r = 0$ . On the left, if  $r$  is non-zero, it would provide significant evidence for models such as the  $3\alpha = 7$  model [62]. On the right, evidence against the hilltop quartic class and the first couple of Poincare disk models, as well as some evidence against the  $R^2$  [86] and fibre models [38] are visible, while the Higgs [33] and the lower Poincare models would still be viable. . . . . 25
- 1.12 Examples of polarization vectors located within filaments. The image has two circles that identify points that hold equal weight to E and B at the center of the circles. When moving along the smaller circle, the contribution from points cancels out, whereas the contribution from the second circle is not zero. In this specific example, the contribution is mostly E. The first pair of filaments, shown as a, generates E-mode polarization inside the filaments, whereas the second pair, shown as b, produces B-mode polarization. Figure taken from [98]. . . . . 30
- 1.13 Linearly polarized structure in Galactic neutral hydrogen HI (upper) correlates well with the orientation of the magnetic field inferred by Planck 353 GHz polarized dust emission. Figure taken from [40]. . . . . 31

- 1.14 Polarized dust emission, are much brighter compared to the primordial B-mode signal that we target to detect. The polarized foregrounds have distinctive spectral shapes that differ from the primordial B-mode signal. These spectral differences allow us to distinguish between the foregrounds and the B-mode signal. Figure taken from [24]. . . . . 33
- 1.15 Commander polarized foreground maps from Planck 2018. Upper: Polarized thermal dust amplitude map at 5 arcmin FWHM resolution, scaled to 353 GHz. Bottom: Polarized synchrotron amplitude map at 40 arcmin FWHM resolution, scaled to 30 GHz. Figures taken from [27]. . . . . 34
- 1.16 The lensing B-mode polarization is caused by the deflection of E-modes into B-modes as CMB photons pass through the gravitational potential wells. Figure taken from [55]. . . . . 35
- 2.1 BICEP2 and the mount are located at the Dark Sector Laboratory (DSL). The telescope is mounted on a three-axes mount that allows for precise control of its orientation in azimuth, elevation, and boresight (deck rotation). To minimize interference from ground radiation, the telescope is enclosed by a reflecting ground shield that blocks the line of sight from the ground. Additionally, an absorbing forebaffle is mounted on the receiver and prevents light outside of field-of-view. The telescope is located within a liquid helium cryostat, where the detectors are cooled down to 270 mK using a  $^4\text{He}/^3\text{He}/^3\text{He}$  sorption fridge system. Readout cards contain multi-channel electronics and housekeeping electronics and are attached to the bottom of the cryostat to control and monitor the operation of the telescope. Figure from [10]. . . . . 39

2.2	Cross-sectional view of a <i>Keck</i> Array telescope. The entire assembly is cooled down to 4 K using liquid helium. The optics tube provides support for various components such as lenses, filters, and aperture stop. The camera tube assembly houses the sub-kelvin sorption refrigerator and the cryogenic readout electronics, both of which are thermally and radiatively protected. The sub-kelvin focal plane assembly sits inside a superconducting Nb magnetic shield and is thermally connected to the fridge through a passive thermal filter. This setup is designed to reduce thermal noise. Figure from [10]. . . . .	41
2.3	Cross-sectional view of a BICEP3 telescope. The pulse tube has two stages at 50K and 4K, while the helium sorption fridge has three stages at 2K, 350mK, and 250mK. The thermal stages are mechanically supported by sets of carbon fiber and G-10 fiberglass support. The focal plane has 20 detector modules and 2400 detectors, and is located at the 250mK stage, surrounded by multiple layers of RF and magnetic shielding. Figure from [6]. . . . .	42
2.4	BICEP/ <i>Keck</i> Array series of instruments use antenna-coupled TES bolometers in all of its generations. BICEP2 has 500 detectors at 150 GHz, while BICEP3 has 2400 detectors at 95 GHz. In the future, the BICEP ARRAY is expected to have over 10,000 detectors ranging from 30 to 270 GHz. . . . .	44
2.5	CMB observing field of the BICEP3 telescope (solid white) on the southern celestial sphere. The BICEP2/ <i>Keck</i> field is also shown as a dashed white area, while the SPT-3G 1500 deg <sup>2</sup> survey is represented by a dotted green area. The background image displays the polarized intensity of the Planck component-separated dust map (SMICA), which has been rescaled assuming a gray-body spectrum. Figure from [6]. . . . .	47
2.6	he observation pattern of a typical three-day schedule. The scansets of Phase G are numbered, with the first scanset at the lowest elevation. The Galactic D phase is shown at the lowest of four elevation steps, while the CMB G phase is shown at the lowest of three elevation steps. Figure from [10]. . . . .	48

2.7	The assembled focal plane on the carbon fiber truss structure and 350 mK Nb plate. The focal plane is made of four anti-reflection tiles. The assembly is shielded by an aluminized Mylar radio frequency shield, with a square opening above the detector tiles. Figure from [10]. . . . .	49
2.8	Resistance vs. Temperature characteristic for a TES detector. Within 5 mK, the resistance reaches 90% of the normal state resistance. Figure from [10]. . . . .	50
2.9	The 150 GHz band-defining filter, which is made of three inductors arranged in series, and interconnected through a T-network of capacitors via coupling. Figure from [10]. . . . .	51
2.10	UBC readout used in the BICEP/Keck Array series of instruments. Figure from UBC. . . . .	53
3.1	Load curves were taken to measure the optical efficiency of Al, with blue curves taken using a 300 K source and green curves taken using liquid nitrogen at 77 K. . . . .	56
3.2	Optical Efficiency for the BICEP3 2016 and 2017 seasons. Figure from [6]. . . . .	57
3.3	Atmospheric Transmission at the South Pole as a function of observation frequency. The BICEP/Keck Array bands are designed to avoid the oxygen absorption band around 60 GHz, and the spectral lines of oxygen at 118.8 GHz. . . . .	59
3.4	A high signal-to-noise raw detector interferogram response at 150 GHz to a beam filling source. The raw data has been filtered of thermal drifts in the ambient temperature by a polynomial filter of third order. The position is tracked by an encoder and shown in the x-axis. Figure from [89]. . . . .	61
3.5	Band-pass response of BICEP/Keck Array series of instruments. The median atmospheric transmission during the observing season is shown as black. Figure from [76]. . . . .	62

3.6	Coadded and peak-normalized BICEP3 Spectral Response (blue) plotted against South Pole atmospheric transmission (black). The band center is measured at $96.1 \pm 1.5$ GHz and the bandwidth is $26.8 \pm 1.3$ GHz. This corresponds to 27% fractional spectral bandwidth. Abnormal features observed in the 2016 season spectrum due to delaminated filters are also shown: a spectrum with a spike feature (dashed blue corresponding to $e = -0.51$ ) and a spectrum with a dip feature (dotted blue corresponding to $e = -0.20$ ). Figure taken from [6]. . . . .	63
3.7	Spike-dip estimator $e$ for the BICEP3 obtained from FTS measurements in the 2016 and 2017 seasons. In the 2016 season, delaminated mesh filters result in peaks of the spike/dip value at around $-0.4$ and $0.4$ reflecting the observed abnormal features. In the 2017 season, delaminated mesh filters were replaced and no signs of abnormal features persisted in the spectral measurements. Figure taken from [6].	64
3.8	Sample G measurement taken at Pole. On the left are the I bias vs I tes figures. Each focal plane temperature is plotted in a different color. In the middle panel is the P-R curve. The right panel shows the best-fit model to estimate $G$ . . . . .	66
3.9	BICEP3 Near Field Beam Mapping results. Figure taken by [6]. . . . .	67
3.10	Polarization grid used to take the polarization efficiency measurement.	68
3.11	Polarization Efficiency measurements and the best fit models shown in blue and red. . . . .	69
3.12	Partial load curve measurement taken at the South Pole station with the BICEP3 instrument. On the left is the TES response as a function of current bias. The region between the green vertical lines are used to determine the titanium normal resistance. On the right is the PR curve corresponding to this measurement. . . . .	70
3.13	$P_{\text{load}}$ measurements from BICEP3 . The mean value is at 0.179 pW. . . . .	71
3.14	$P_{\text{dark}}$ measurements from BICEP3 . The mean value is at 3.958 pW. . . . .	72
3.15	Procedure used to find the optimal bias to minimize NET. . . . .	73
3.16	Pair difference in correlation figures. Top figure: detectors are in MCE column order. Bottom figure: detectors are in MCE row order. . . . .	75

3.17	Raw data taken at 50 MHz, consisting of 65536 samples by "freezing with the PID servo inactive" on a given row and column. MCE does not downsample and row order is changed to stay in a given row. A large spike is present at 4 MHz. . . . .	77
3.18	Same as previous figure except K5 power off and power cable ground connected to backpack. Spike at 4 MHz comes down significantly, indicating an issue of ground. . . . .	78
4.1	Reduc plots show the scanning motion of telescopes and timestream response for detectors. Left and right columns are the leading and trailing elnods, while the center column shows constant-elevation scans. The pair-sum timestream has scan-synchronous response, while the pair-diff shows very little due to common-mode rejection. . . . .	84
4.2	Differences of elliptical Gaussian beams, where the total difference beam is the linear combination of these modes. These difference beams couple to different derivatives of the CMB temperature field in the deprojection pipeline. Figure from [34]. . . . .	90
4.3	Temperature maps from Planck are used for converting ADU to $\mu\text{K}_{\text{CMB}}$ in the absolute calibration procedure. . . . .	92
4.4	E-mode spectrum on two-dimensional Fourier Plane for BICEP3 lensed- $\Lambda\text{CDM}$ simulation. These two concentric rings of brighter modes are the first and second acoustic peaks, respectively. At higher values of $\ell$ response is suppressed with the beam rolling. Modes along $ l_x  \lesssim 40$ are suppressed as a result of polynomial and scan-synchronous timestream filters due to constant declination scanning strategy. The left side shows the imaginary part of complex Fourier modes, and the right side shows the real part of complex Fourier modes. The faint red circles indicate the bandpower bins, where bins 2 through 10 are used for cosmological results. . . . .	98
4.5	Bandpower window functions (BPWFs) $M_{\ell\ell'}^{XX}$ with coupling of input $TT, EE, BB$ to measured spectra. E to B and B to E leakage are labeled as $EE \rightarrow BB$ and $BB \rightarrow EE$ respectively. The beam function dominates the suppression factor at high $\ell$ , filtering dominates at low $\ell$ . Purification of the $B$ -modes suppress the BPWFs for $EE \rightarrow BB$ compared to the symmetric case of $BB \rightarrow EE$ . Figure from [7]. . . . .	100

- 4.6 *BB* suppression factor. The beam function dominates the suppression factor at high  $\ell$ , filtering dominates at low  $\ell$ . The map window function for  $0^\circ.25$  pixels and finite size of the map is shown as dashed lines. Figure from [7]. . . . . 101
- 4.7 The magnitude-ordered generalized eigenvalues for the BICEP2 observed covariance matrix. The largest and the smallest 1/4 of the eigenvalues are used to construct the *B* and *E* modes that can be observed with BICEP/Keck Array scanning strategy and analysis. Eigenvalues close to 1 correspond to ambiguous modes, the modes that are simultaneously E and B in the observed space and are thrown out. Figure from [7]. . . . . 104
- 5.1 *BB* bandpower expectation values and noise uncertainties in BICEP/Keck Array field. The expected signal power of lensed- $\Lambda$ CDM and tensor-only cosmological models are shown as solid and dashed black lines. The signal levels are flat with frequency since CMB units are used. The blue bands represent the range of dust, while the red shaded region shows the 95% upper limit on synchrotron emissions in the baseline analysis, including the uncertainties in the amplitude and frequency spectral index parameters. The noise uncertainties of the BICEP/Keck Array auto-spectrum are shown as large blue circles, and WMAP/Planck evaluated in the BICEP/Keck Array field are shown in black. The noise uncertainty of selected cross-spectra is represented by blue crosses. Figure taken from [9]. . . . . 107
- 5.2 A summary of B-mode polarization measurements. The lensing B-modes, which are expected to peak at arcminute scales, are represented by solid red lines, while the tensor modes are shown by dashed red lines. Upper bounds on the tensor-to-scalar ratio are denoted by triangles, while detections are represented by circles. Galactic foregrounds have been removed from the BK18 data shown in this figure. Figure taken from [9]. . . . . 108

- 5.3 Multicomponent multi-spectral likelihood analysis of BICEP/Keck Array data. The red curves correspond to the results obtained in the BK15 results, whereas the black curves represent the baseline BK18 results. These results include a significant amount of additional data at 95 and 220 GHz, observed by Keck Array and BICEP3 during the 2016-2018 observing seasons. The upper limit on the tensor-to-scalar ratio is further constrained to  $r < 0.036$  at a 95% confidence level. The parameters  $A_d$  and  $A_s$  denote the amplitudes of the dust and synchrotron B-mode power spectra, respectively, and  $\beta$  and  $\alpha$  represent their corresponding frequency and spatial spectral indices. We also include a spatial correlation coefficient  $\epsilon$  between dust and synchrotron. The dashed lines here correspond to priors that were placed on these parameters. Gaussian prior on  $\beta_d$  has been removed going from BK15 to BK18 as the additional data 220 GHz has enough constraining power. Figure from [18]. . . . . 114
- 5.4 Maximum likelihood results from 499 realizations of  $\Lambda$ CDM +  $r$  + dust + synchrotron + noise simulations ( $r = 0$ ,  $A_d = 3.75 \mu\text{K}^2$ ,  $A_s = 0 \mu\text{K}^2$ ,  $\beta_d = 1.6$ ,  $\alpha_d = -0.42$ ). The input values are show in vertical black lines. The recovered likelihoods of the 499 realizations are shown in blue histogram and the red vertical lines are their mean values. The vertical dashed green lines are the likelihood results from real BK18 data. Figure from [18]. . . . . 115
- 5.5 BB spectral decomposition into synchrotron (red), CMB (black), and dust (blue) components at 95 GHz (filled) or 150 GHz (open). The decomposition is calculated independently in each bandpower, and marginalized over  $\beta_d$ ,  $\beta_s$ , and  $\epsilon$ . Error bars correspond to 68% intervals, with the point marking the most probable value. For synchrotron, which is not detected, the downward triangles correspond to 95% upper limits. Figure from [18]. . . . . 116

5.6	Projection of the sensitivity of the ongoing and future <i>BICEP/Keck</i> Array program. The projections involve direct scaling from published end-to-end analyses and include real-world inefficiencies and removal of dust and synchrotron foregrounds. The top panel provides a representation of the program, showing the frequency bands covered by the various receivers through each observing season. The middle panel shows the map depth for each frequency, and the bottom panel displays the sensitivity to the tensor-to-scalar ratio, after marginalizing over all foreground parameters, as well as the raw sensitivity, which is the sensitivity achieved if there were no no-foregrounds. The solid line shows the gain in sensitivity with delensing effort that we can achieve by working with SPT-3G. Figure from [76]. . . . .	118
6.1	Likelihood results when dust decorrelation is added as a free parameter. The results are consistent with no loss of correlation in dust in the <i>BICEP/Keck</i> Array field. . . . .	123
6.2	Fisher forecasting for BK15 and BK18 data when adding an experiment at 1.2 THz at various levels of signal-to-noise. . . . .	124
6.3	Commander dust spectral index plotted in the <i>BICEP3</i> field. Planck Commander Maps use Bayesian parametric component separation, where each component is modelled with an amplitude and spectral index for each pixel. MCMC Gibbs sampling is used to fit these parameters to data. . . . .	127
6.4	GNILC dust spectral index plotted in the <i>BICEP3</i> field. These maps are CIB-removed dust spectral index map produced by the GNILC method, using Planck data release 2 (PR2) frequency maps from 30 to 857 GHz, and a 100 micron hybrid map combined from the SFD map at large angular scales ( $> 30'$ ) and the IRIS map at small angular scales ( $< 30'$ ). Spectral index for dust was found by fitting MBB to the dust component maps of GNILC at 353, 545, 857 HFI bands, and 100 $\mu\text{m}$ . . . . .	128

- 6.5 EE (shown in green background) and BB (shown in blue background) auto (dark colors) and cross spectra (light colors) using BICEP3 95 GHz, Bicep2 / Keck 150 GHz, 220 GHz, and Planck 353 GHz bands. BK bands use data taken up to and including 2018 season (BK18).  $\Lambda$ CDM model expectations are plotted in black.  $\Lambda$ CDM + dust model expectations are plotted in red. The model shown has  $r = 0$ ,  $A_d = 4.75 \mu K$ ,  $\beta_d = 1.6$ ,  $\alpha_d = -0.4$ . The model in this Figure is fit using only BB and excluding the newly added BICEP 95 GHz. However the agreement with EE and the newly added 95 GHz is a good validation. Figure taken from [18]. . . . . 132
- 6.6 The figure shows the results of the maximum likelihood search for BB only (top two), EE only (middle two), and BB+EE (bottom two). Real data is presented as green, black is model input, and red is the mean of the realizations. When fitting for EE+BB, the ratio of dust EE to BB is set as a free parameter. We observe that real values of data have  $r$  and  $\beta d$  showing a significant increase. However when switching from BB to EE,  $\sigma(A_d)$ ,  $\sigma(A_s)$ , and  $\sigma(\beta_s)$  all decrease, while  $\sigma(\beta_d)$  slightly increases. The EE-only case lacks constraining power on  $r$ , as expected. . . . . 133
- 6.7 The spectral-based approach, where the final spectra that have already been corrected for all the suppression factors due to filtering and beam effects, have been subtracted from each other for all *Keck* Array and BICEP3 spectra in the smaller field of observation. This spectral-based approach is expected to cancel common signals, leaving spectra that are free of lensed E-modes and  $\Lambda$ CDM in our region. However EE spectrum of  $150 \times 150 - B95sf \times B95sf$  does not match the expected difference based on simulations that include lensed  $\Lambda$ CDM, noise, and dust. Furthermore, the subtracted spectra obtained from the maps are not consistent with zero for lensed  $\Lambda$ CDM only simulations, especially at high  $\ell$ . This is because at high  $\ell$ , the bandpower window functions become more non-ideal, leading to leakage of the lensed- $\Lambda$ CDM E-modes and B-modes into the subtracted spectra. . . . . 134

6.8	Bandpower window functions (BPWFs) $M_{\ell\ell'}^{XX}$ obtained from BK18 data with E to E leakage are labeled as $EE \rightarrow EE$ . At high $\ell$ the BPWF shapes become increasingly non-ideal. Points that sit on the theory line are plotted estimated by the at the center-of-gravity of the BPWF, shown as the black crosses in the figure, and are not at the peak locations for higher $\ell$ values. . . . .	135
6.9	Our proposed approach to correct for abscal is to combine all years of observation for each band. In addition, since the BICEP3 map was calculated for a large field, we also repeated the analysis by restricting the map to the smaller field. This resulted in a correction factor of 0.9923 for BICEP3 . We also obtained a coadded correction factor for all 150 GHz receivers over the observing seasons of 2013-2018, which is 1.0124 at $\ell = 80$ . Plotted in this figure are the corrections obtained for <i>Keck</i> Array receivers. . . . .	137
6.10	Spectral Difference of Bands after abscal corrections. Abscal is a plausible contributing factor for the observed discrepancy between the real data and simulations. The corrected spectra (shown in red) are in better agreement with the realizations. . . . .	138
6.11	The left panel displays the EE power spectra for various experiments, while the right panel shows the BB power spectra. Figure taken from <a href="https://ned.ipac.caltech.edu">https://ned.ipac.caltech.edu</a> . . . . .	139
6.12	Expected normalized EE leakage for $D_\ell = \delta(\ell - 107)$ , drops down very quickly. The red points are the expected leakage due to difference in the bandpower window functions. . . . .	140
6.13	Beam window functions $B_\ell$ for the BICEP/ <i>Keck</i> Array bands obtained by a Fourier transform of the beams after they are averaged in azimuth. . . . .	141
6.14	Convolution / deconvolution procedure, where the 150 GHz maps band is deconvolved with the 150 GHz beam and convolved with the 220 GHz beam. This plot shows the beams that have been deconvolved and convolved, along with the total filter. The beam that is being deconvolved is plotted on the left, while the beam that is being convolved is plotted on the right. The total filter is shown in magenta. . . . .	142

- 6.15 We used a Keck 220 GHz map, which we first applied the deconvolution using the K220 beam profile. Next, we convolved the resulting map with the K150 beam profile. As a result, the finer details in the original map got smoothed out. To visualize this, we show the original Keck 220 Q polarization map in the lower panel, and the processed map in the upper panel. . . . . 143
- 6.16 The B-mode maps from map based difference (left column) and expected noise from signflip realizations (right column) maps for the difference maps of 150-B95, 220-150, and 220-B95 GHz in CMB units. These maps have been filtered to degree angular scales. This approach is expected to eliminate common signals in the difference maps, leading to maps that are free of lensed E-modes in our region of interest. . . . . 144
- 6.17 The E-mode maps from map based difference (left column) and expected noise from signflip realizations (right column) maps for the difference maps of 150-B95, 220-150, and 220-B95 GHz in CMB units. These maps have been filtered to degree angular scales. This approach is expected to eliminate common signals in the difference maps, leading to maps that are free of  $\Lambda$ CDM in our region of interest. 145
- 6.18 the noise spectra of the BK18 maps, represented by solid lines, alongside the anticipated noise levels of the difference spectra denoted by dashed lines. The noise levels for the BICEP3 95 GHz map are depicted in red, the BICEP2/Keck 150 GHz map in green, and the Keck 220 GHz map in blue. Additionally, the difference spectra are indicated by dashed lines: the 150-B95 difference in black, the 220-150 difference in cyan, and the 220-B95 difference in magenta. The filtering effects due to beam roll-off, timestream filtering, and B-mode purification have been corrected in the spectra. We did not apply any  $\ell^2$  scaling. 220-B95 and 220-150 maps are dominated by the dust and noise levels of 220 maps. Due to the comparable levels of B95 and 150 GHz noise, we expect an increase in the overall noise levels of approximately 40% for 150-95. . . . . 146

- 6.19 Dust model (cyan) agrees well with the mean of simulations (gray). The dust model is obtained by the difference of dust and temperature scaling, but does not use the bandpass information. We can estimate the EE/BB from the spectra directly, or feed it into the likelihood analysis to obtain all the parameters. . . . . 147
- 6.20 This figure is similar to Figure 6.19, but with the addition of noise debiasing to remove the leakage resulting from mismatch in the band-power window function. The bias is estimated as the mean value of the  $\Lambda$ CDM-only realizations. . . . . 148

## LIST OF TABLES

<i>Number</i>	<i>Page</i>
2.1 Deployment history of BICEP/Keck Array . . . . .	43
2.2 BICEP3 Phases in a Typical Schedule . . . . .	48
4.1 Round 1 Cut Parameters. . . . .	86
4.2 Round 2 Cut Parameters. . . . .	87
5.1 A summary of Multicomponent Model Parameters . . . . .	111
6.1 Maximum Likelihood Results for Forecasting an Experiment at 1.2 THz . . . . .	125
6.2 As the smoothing is increased, we observe smaller gradient in mean subtracted maps, however errors average out and lead to greater values of $\chi$ . . . . .	130
6.3 We present maximum likelihood (ML) search results for the tensor-to-scalar ratio ( $r$ ) using the Commander spectral index for the BK field and the GNILC spectral index for the same field. The values of $r$ obtained from these two methods are denoted as $r_{COMM}$ and $r_{GNILC}$ respectively. The difference between these values is represented by $\Delta r$ , and the sensitivity of the results is quantified by $\sigma(r_{COMM})$ . To estimate the statistical significance of our results, we calculate the ratio $\sigma_r \equiv \sqrt{499}\Delta r/\sigma(r)$ . . . . .	130
6.4 We report the parameter sensitivities obtained from our maximum likelihood (ML) search. Our results indicate that there is no statistically significant difference between the constant and spatially varying $\beta_d$ realizations. . . . .	131

*Chapter 1*

## INTRODUCTION

Cosmology is the study of the universe as a whole, focusing on its origin, evolution, structure, and dynamics. The field has captured the human imagination for thousands of years, and inspired philosophical, and scientific inquiries.

Over the past century, cosmology had a dramatic transformation, due to the development of new observational and theoretical discoveries. Advances in technology, such as telescopes, balloon-borne experiments, and space missions, have allowed scientists to observe the universe in greater detail and at larger scales. Theoretical breakthroughs, such as the Big Bang model and the inflationary universe hypothesis, have provided a conceptual framework for a better understanding of the universe.

The standard model of cosmology, also known as the  $\Lambda$ CDM model, currently characterizes our observations of the universe. According to this model, there is a background radiation from the early plasma, observed primordial abundances of light elements, a large scale structure and an accelerated expansion of the universe.

The cosmic microwave background (CMB) is one of the most important discoveries for the Big Bang model. It is the oldest light in the universe and appears as a nearly uniform glow of microwave radiation that fills the entire universe. CMB also contains small temperature fluctuations that contains information about the early universe.

Many techniques have been developed to measure the temperature fluctuations in the CMB with increasing precision. In recent years, the polarization of the CMB has been the primary observational focus for studying the early history of the universe. This polarization results from the interaction of the CMB photons with matter and radiation in the early universe. CMB polarization can be used to probe the existence of primordial gravitational waves, which could have been produced by inflation in the first moments of the universe's existence.

## 1.1 Standard Model of Cosmology

On large scales, the dynamics and evolution of the universe are governed by Einstein's field equations, which relate the curvature of spacetime to the distribution of matter and energy in the universe:

$$R_{\mu\nu} - \frac{1}{2}g_{\mu\nu}R + g_{\mu\nu}\Lambda = \frac{8\pi G}{c^4}T_{\mu\nu}, \quad (1.1)$$

where  $R_{\mu\nu}$  is the Ricci tensor,  $R$  is the Ricci scalar,  $g_{\mu\nu}$  is the metric tensor,  $\Lambda$  is the cosmological constant  $G$  is the gravitational constant,  $c$  is the speed of light, and  $T_{\mu\nu}$  is the stress energy tensor.

The symmetric, divergence-free Einstein tensor  $G_{\mu\nu}$ , defined as  $G_{\mu\nu} \equiv R_{\mu\nu} - \frac{1}{2}g_{\mu\nu}R$  describes the spacetime curvature. The stress-energy tensor  $T_{\mu\nu}$  captures the density and flux of energy and momentum information, sourcing the curvature of geometry due to gravitational fields in the equation. The cosmological constant, denoted as  $\Lambda$ , can be interpreted as intrinsic energy density of the vacuum  $\Lambda = 8\pi\rho_{\text{vac}}G/c^4$ . The interested reader is referred to the following references for a full review on general relativity: [51, 75, 92].

Einstein's field equation implies that the curvature of spacetime is determined by the distribution of matter and energy, which means that the presence of matter and energy causes spacetime to curve, and this curvature determines the motion of other particles nearby.

Cosmological principle states that the universe is homogeneous and isotropic on large scales. In other words, on large enough scales, the universe looks the same in all directions from all locations. Cosmological models are based on the assumption of cosmological principle. The Friedmann-Robertson-Walker (FRW) metric uniquely describes a homogeneous, isotropic, expanding universe, that is in agreement with the cosmological principle. The invariant metric element  $ds^2$  can be written in terms of the metric tensor  $g_{\mu\nu}$ :

$$ds^2 \equiv g_{\mu\nu}dx^\mu dx^\nu \quad (1.2)$$

$$= -c^2 dt^2 + a^2(t) \left[ \frac{dr^2}{1 - kr^2} + r^2 (d\theta^2 + \sin^2 \theta d\phi^2) \right], \quad (1.3)$$

where  $k$  is a parameter describing the geometry of the universe:

$$k = \begin{cases} +1 & \text{spherical} \\ -1 & \text{hyper-spherical,} \\ 0 & \text{Euclidean,} \end{cases} \quad (1.4)$$

and  $a(t)$  is the scale factor of the universe used to describe the relative size of the universe.

The stress-energy tensor  $T_{\mu\nu}$  is used to model the distribution of energy and momentum and consists of energy density  $\rho$  and pressure  $p$ . The Friedmann equations are a set of equations that describe the evolution of the universe using general relativity. FRW metric and Einstein equations are used to derive the two independent Friedmann equations for an isotropic and homogeneous universe. The two Friedmann equations are:

$$H^2 \equiv \left(\frac{\dot{a}}{a}\right)^2 = \frac{8\pi G}{3}\rho - \frac{kc^2}{a^2} + \frac{\Lambda}{3}, \quad (1.5)$$

and:

$$\frac{\ddot{a}}{a} = -\frac{4\pi G}{3}\left(\rho + \frac{3p}{c^2}\right) + \frac{\Lambda c^2}{3}, \quad (1.6)$$

where the  $H(t) \equiv \dot{a}/a$  is the Hubble parameter and describes the rate of expansion.

The divergence of the stress-energy tensor is equal to zero:

$$\nabla_\nu T^{\mu\nu} = 0, \quad (1.7)$$

and indicates that the total amount of energy and momentum in the system is conserved. The conservation of stress-energy tensor results in conservation the equation:

$$\frac{\partial\rho}{\partial t} + 3\left(\frac{\dot{a}}{a}\right)(\rho + P) = 0. \quad (1.8)$$

The equation of state, denoted by the parameter  $w$ , is a dimensionless quantity that describes the relationship between the pressure  $P$  and the density  $\rho$  of a fluid in the universe:

$$w \equiv \frac{P}{\rho}. \quad (1.9)$$

Non-relativistic matter in the universe, such as stars, galaxies, and gas clouds, has an equation of state parameter of zero, indicating that the pressure is zero. Ultra-relativistic particles and radiation have an equation of state parameter of 1/3. Dark

energy, which is thought to be responsible for the accelerating expansion of the universe, has an equation of state parameter parameter of  $-1$ , meaning that it exerts negative pressure and corresponds to a cosmological constant.

Energy density can be expressed in terms of the scale factor  $a$ , using the equation of state  $w$ , with the conservation laws:

$$\rho = \rho_0 a^{-3(w+1)}. \quad (1.10)$$

Friedmann equations are used to obtain the scale factor  $a$  as a function of time  $t$  and equation of state parameter  $w$ :

$$a(t) \propto \begin{cases} t^{2/3(1+w)} & w \neq -1 \\ e^{Ht} & w = -1, \end{cases} \quad (1.11)$$

where  $w = -1$  corresponds to exponential expansion for cosmological constant equation of state parameter.

The total energy in a comoving volume stays constant while the energy density decreases as the volume increases, therefore in an expanding universe, the energy density for non-relativistic matter scales with  $a^{-3}$ . There is an additional factor of  $a^{-1}$  for radiation as a result of redshift from the expansion of the universe. The total energy contribution of radiation scales with  $a^{-4}$ . Dark energy does not depend on the volume, and has constant contribution.

Substituting the equation of state parameters  $w$ , we find:

$$a(t) \propto \begin{cases} t^{1/2} & \text{radiation dominated} \\ t^{2/3} & \text{non-relativistic matter dominated} \\ \exp\left(\sqrt{\frac{\Lambda}{3}}t\right) & \text{dark energy dominated} \end{cases}. \quad (1.12)$$

Currently, the energy that makes up the majority of the energy density of the universe is believed to be dark energy, make up about 68% of the total energy density of the universe. The main contribution to the energy density was radiation and governed the dynamics of expansion until matter-dominated era about 50,000 years after the big bang.

Shortly after inflation, the universe is radiation-dominated, where the main contribution of energy was coming from photons, neutrinos, and other particles. This

era lasted about 50,000 years after the Big Bang. The universe entered a matter-dominated era afterwards, during which the dominant energy was matter. The current epoch began about 5 billion years ago, in which the dominant energy is believed to be dark energy.

The Friedman equation can be expressed in terms of density parameters  $\Omega_\Lambda$ ,  $\Omega_m$ ,  $\Omega_r$ ,  $\Omega_k$ :

$$\rho = \frac{3H_0^2}{8\pi G} \left[ \Omega_\Lambda + \Omega_m \left( \frac{a_0}{a} \right)^3 + \Omega_r \left( \frac{a_0}{a} \right)^4 \right], \quad (1.13)$$

such that:

$$\Omega_\Lambda + \Omega_m + \Omega_r + \Omega_k = 1. \quad (1.14)$$

Critical density given by:

$$\rho_{\text{cr}} \equiv \frac{3H_0^2}{8\pi G}, \quad (1.15)$$

which is the density of matter and energy in the universe that is required for it to be spatially flat, meaning that the curvature is zero. The overall geometry of the universe is determined by the comparison between the actual density and the critical density, with a flat (Euclidean) geometry occurring when they are equal. In earlier models that did not incorporate a cosmological constant term, the critical density was originally defined as the threshold point between an expanding and a contracting universe.

## 1.2 Cosmic Microwave Background

The Cosmic Microwave Background (CMB) is the leftover electromagnetic radiation dating to the epoch of recombination at about 380,000 years after the big bang. At earlier times, the density and energy of matter and radiation were high enough to be in thermal equilibrium through Thomson scattering, resulting in a blackbody spectrum. As the the universe expanded, the photons lost enough energy for electrons and protons to combine during the recombination era. After this time, at the surface of last scattering, the photons decoupled from the plasma and streamed freely at a redshift value of about 1100. As the universe continued to cool afterwards, atoms that are heavier than Hydrogen were able to form.

The CMB is first observed by Arno Penzias and Robert Wilson in 1965, who detected a faint, isotropic signal coming from all directions in the sky. Measurements

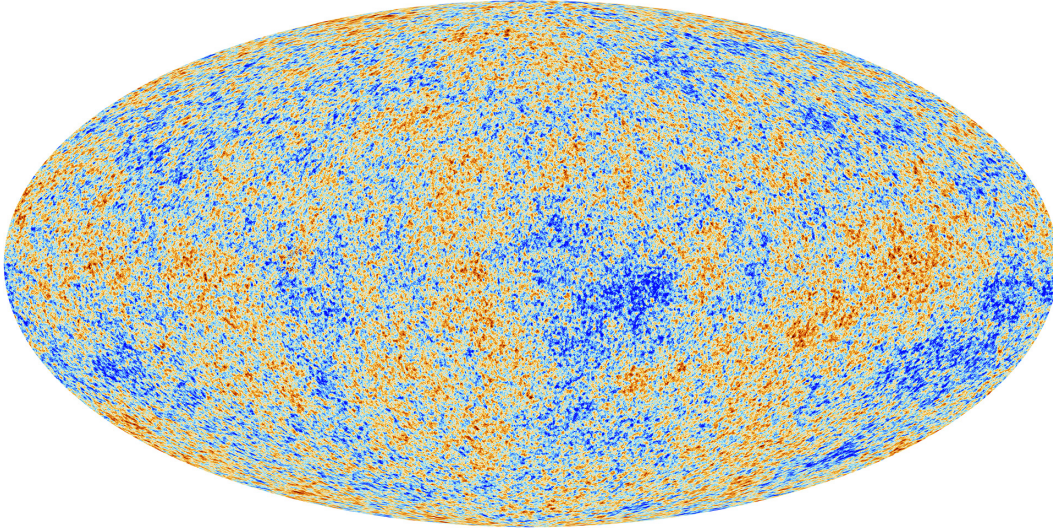


Figure 1.1: CMB Temperature Fluctuations measured by Planck satellite. Colorbar corresponds to  $\pm 500 \mu\text{K}$  (Credit: Planck Team).

indicate that the spectrum fits a blackbody radiation described by Planck's law at a temperature of about 2.7 Kelvin quite remarkably and the isotropic to 1 in 100,000. A blackbody emits radiation according to the spectrum:

$$B_\nu(\nu, T) = \frac{2h\nu^3}{c^2} \frac{1}{\exp(h\nu/k_B T) - 1}. \quad (1.16)$$

The temperature of CMB photons observed today are cooled down to  $2.7260 \pm 0.0013\text{K}$  due to the redshift of the photons, which is a result of the expansion of the universe.

### CMB Anisotropies

The temperature anisotropies of the CMB can be decomposed in terms of spherical harmonics  $Y_{\ell m}(\theta, \phi)$ :

$$\frac{\Delta T}{\bar{T}}(\theta, \phi) = \sum_{\ell=0}^{\infty} \sum_{m=-\ell}^{\ell} a_{\ell m} Y_{\ell m}(\theta, \phi), \quad (1.17)$$

where  $\theta$  and  $\phi$  are spherical coordinates and  $a_{\ell m}$  are spherical harmonic coefficients. A temperature fluctuation realization over the full sky can be represented by a set of spherical harmonic coefficients  $a_{\ell m}$ , and can be expressed as:

$$a_{\ell m} \equiv \int_{\Omega} \frac{\Delta T}{\bar{T}}(\theta, \phi) Y_{\ell m}^*(\theta, \phi) d\Omega. \quad (1.18)$$

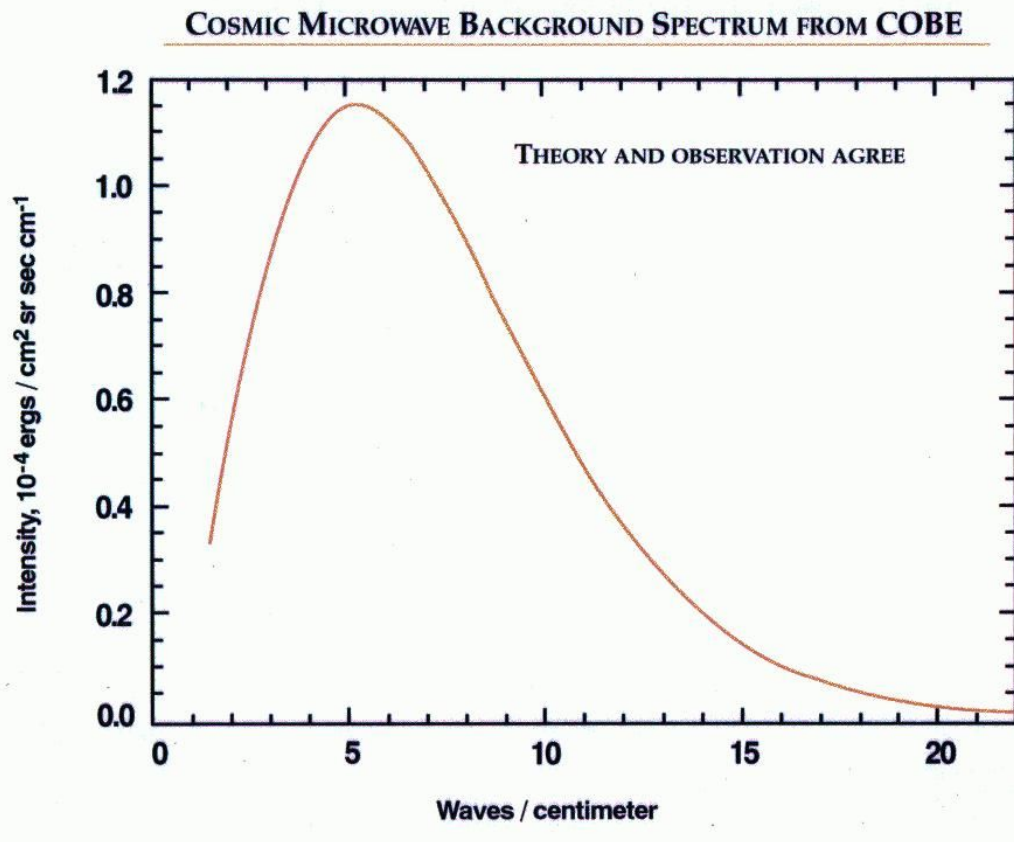


Figure 1.2: CMB spectrum waves per centimeter vs. intensity. The data matches the curve so well that the error uncertainties are only a fraction of the width of theory blackbody curve.

Because the fluctuations  $\Delta T$  are defined with respect to the mean, the  $a_{\ell m}$  have also zero mean. This implies that the density fluctuations are driven by a Gaussian random process and making it possible to represent the information using a power spectrum:

$$C_{\ell} \delta_{\ell\ell'} \delta_{mm'} = \langle a_{\ell m} a_{\ell' m'}^* \rangle, \quad (1.19)$$

where the brackets  $\langle \dots \rangle$  denote an ensemble average of the quantity inside. However since there is only one sky realization to observe, the estimate on the power spectrum is a finite sum average for any given multipole value  $\ell$ :

$$C_{\ell} = \frac{1}{2\ell + 1} \sum_{m=-\ell}^{\ell} a_{\ell m}^* a_{\ell m}, \quad (1.20)$$

where  $C_\ell$  only depend on the the multipole  $\ell$  and average over  $m$  values. Note that typically the scaled angular power spectrum  $D_\ell \equiv \ell(\ell+1)C_\ell/2\pi$  is preferred instead of  $C_\ell$ .

For a given multipole  $\ell$ , the power spectrum estimate is done over a limited number of modes  $m$ . Quantitatively this implies an uncertainty since we can only observe one realization of the cosmic microwave background. This results in a cosmic variance quantified by:

$$\Delta C_\ell^2 = \frac{2}{2\ell+1} C_\ell^2. \quad (1.21)$$

The cosmic variance places stronger limits on larger scales, corresponding to smaller multipole values.

Angular power spectrum of CMB temperature fluctuations as measured by Planck are shown in Figure 1.3. The spectrum provides information on the physics at the time of the recombination and constraints on cosmological parameters. The first peak has the highest amplitude, and can be used to constrain the spatial curvature of the universe, which is observed to be very close to being spatially flat. The second peak is suppressed compared to the first and third peak, indicating substantial amounts of dark baryons, which is consistent with the predictions of nucleosynthesis. The third peak is sensitive to the density of dark matter. At higher peaks, the dampening tail is a consistency check and the scale depends on the mean free path of photons during recombination [57]. Low multiple values are limited by cosmic variance.

### CMB Polarization

CMB is partially polarized due to the Thomson Scattering of photons off of electrons at the surface of last scattering. Similar to temperature, polarization signal also has anisotropies. The cross-section of Thomson scattering depends on the polarization:

$$\frac{d\sigma_T}{d\Omega} \propto |\hat{\epsilon} \cdot \hat{\epsilon}'|^2, \quad (1.22)$$

where  $\hat{\epsilon}$  and  $\hat{\epsilon}'$  are the polarization directions of incident and scattered photons. If the incoming photons have the same temperature (isotropic), the resulting photon is unpolarized. A net quadrupolar temperature anisotropy is required for a net polarization [56].

Stokes parameters are defined to characterize the polarization state of electromagnetic waves. Consider a photon propagating in the  $\hat{z}$  direction. The electric field

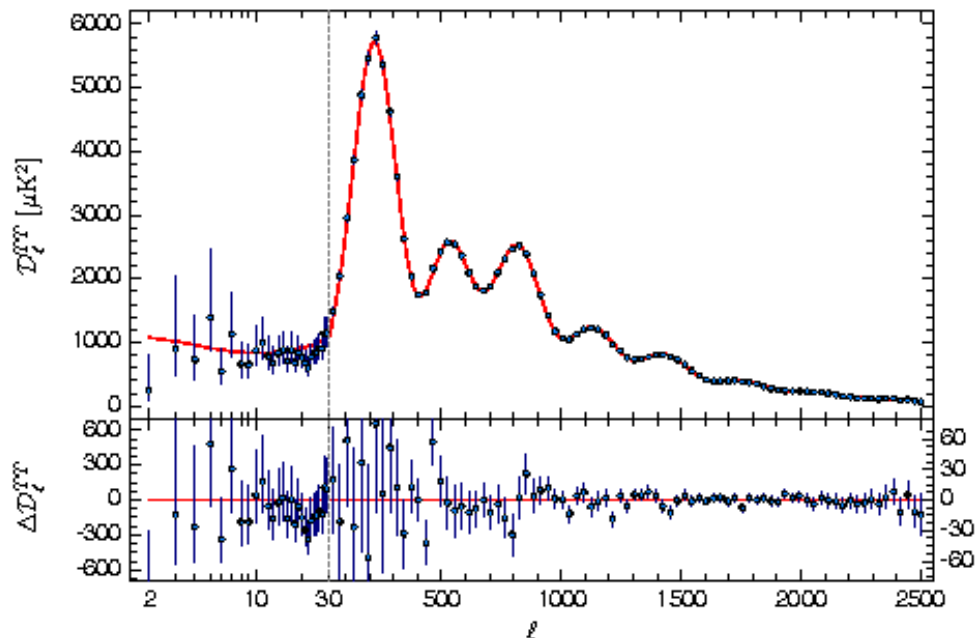


Figure 1.3: Angular power spectrum of CMB temperature fluctuations measured by Planck Collaboration. Upper Panel: Red line corresponds to best fit  $\Lambda$ CDM model and the blue points are the measured APS values. Low multipole values are limited by cosmic variance. Lower Panel: Residual difference between the best fit  $\Lambda$ CDM model and the measured APS values. Figure from [16].

vector  $\vec{E}(t)$ , as a function of time  $t$ , is expressed in terms of complex electric field amplitudes  $E_x$  and  $E_y$  in the  $\hat{x}$  and  $\hat{y}$  directions respectively:

$$\vec{E}(t) = E_x \cos(\omega t - \phi_x) \hat{x} + E_y \cos(\omega t - \phi_y) \hat{y}. \quad (1.23)$$

The four Stokes parameters  $T$ ,  $Q$ ,  $U$ , and  $V$  fully describe the polarization state of the incoming light. These parameters are defined as:

$$\begin{aligned} I &\equiv \langle E_x^2 \rangle + \langle E_y^2 \rangle \\ Q &\equiv \langle E_x^2 \rangle - \langle E_y^2 \rangle \\ U &\equiv 2 \langle E_x E_y \rangle \cos(\phi_x - \phi_y) \\ V &\equiv 2 \langle E_x E_y \rangle \sin(\phi_x - \phi_y) \end{aligned} \quad (1.24)$$

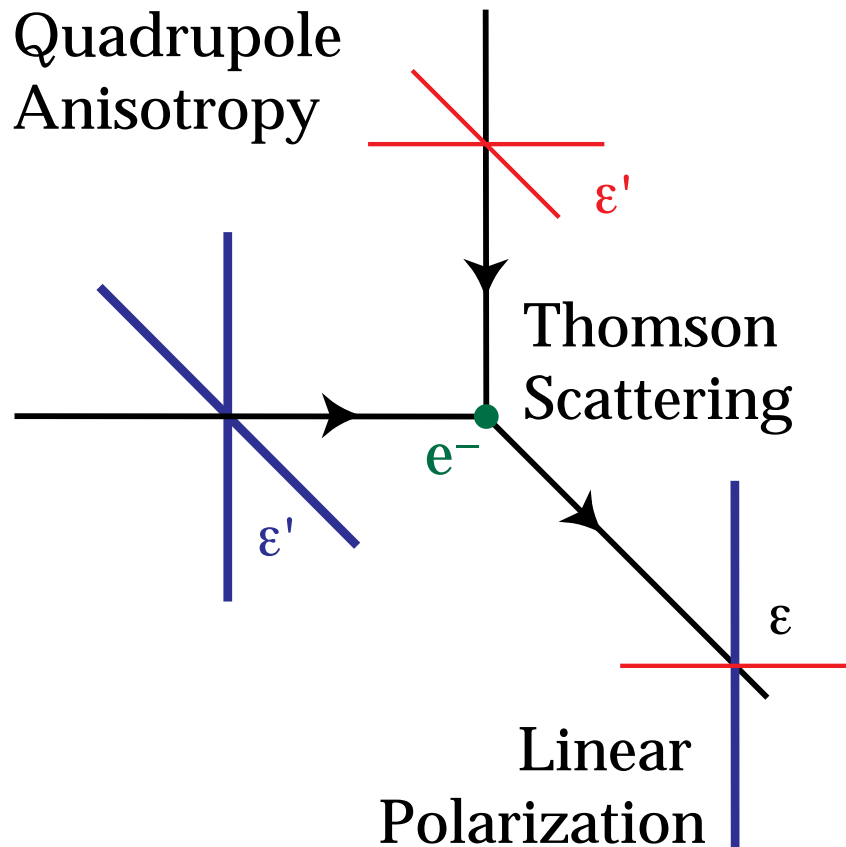


Figure 1.4: Thomson scattering of CMB photons. Blue lines on the photons coming from the left represent hot and red lines on the photons coming from up. Figure from [56].

where the brackets  $\langle \dots \rangle$  denote average over time  $t$ .  $I$  is the intensity,  $Q$  and  $U$  are the linear polarizations in plus + and cross x direction, and  $V$  is the circular polarization. Thomson scattering cannot generate circular polarization and hence it is expected to be zero for the CMB.

$Q$  and  $U$  depend on the choice of coordinates. When the coordinate system is rotated by an angle of  $\phi$ , the quantity  $(Q \pm iU)$  follows a spin-2 field transformation:

$$(Q \pm iU)' = e^{\mp 2i\phi} (Q \pm iU). \quad (1.25)$$

Polarization field can be decomposed using spin-2 spherical harmonics  ${}_{\pm 2}Y_{\ell m}(\hat{n})$

and coefficients  ${}_{\pm 2}a_{\ell m}$ :

$$(Q + iU)'(\hat{n}) = \sum_{\ell=2}^{\infty} \sum_{m=-\ell}^{\ell} {}_{\pm 2}a_{\ell m} {}_{\pm 2}Y_{\ell m}(\hat{n}). \quad (1.26)$$

Even and odd parity basis can be reconstructed in terms of linear combinations of the harmonic coefficients that are also rationally invariant [99] [80]. E and B modes are a coordinate independent measure of polarization [63]:

$$\begin{aligned} a_{\ell m}^E &\equiv -\frac{1}{2} ({}_{+2}a_{\ell m} + {}_{-2}a_{\ell m}) \\ a_{\ell m}^B &\equiv -\frac{i}{2} ({}_{+2}a_{\ell m} - {}_{-2}a_{\ell m}) \\ X_{1,\ell m} &\equiv +\frac{1}{2} ({}_{+2}Y_{\ell m} + {}_{-2}Y_{\ell m}) \\ X_{2,\ell m} &\equiv +\frac{1}{2} ({}_{+2}Y_{\ell m} - {}_{-2}Y_{\ell m}). \end{aligned} \quad (1.27)$$

The linear polarization  $Q$  and  $U$  can be expressed in terms of the above quantities:

$$\begin{aligned} \begin{bmatrix} Q(\hat{n}) \\ U(\hat{n}) \end{bmatrix} &= -\sum_{\ell=2}^{\infty} \sum_{m=-\ell}^{\ell} a_{\ell m}^E \begin{bmatrix} X_{1,\ell m}(\hat{n}) \\ -iX_{2,\ell m}(\hat{n}) \end{bmatrix} + a_{\ell m}^B \begin{bmatrix} iX_{2,\ell m}(\hat{n}) \\ X_{1,\ell m}(\hat{n}) \end{bmatrix} \\ &= -\sum_{\ell=2}^{\infty} \sum_{m=-\ell}^{\ell} a_{\ell m}^E Y_{\ell m}^E(\hat{n}) + a_{\ell m}^B Y_{\ell m}^B(\hat{n}). \end{aligned} \quad (1.28)$$

with orthonormal basis  $Y_{\ell m}^E(\hat{n})$  and  $Y_{\ell m}^B(\hat{n})$  for E and B modes, implicitly defined in the second line. Intuitively, E-mode orthonormal basis  $Y_{\ell m}^E(\hat{n})$  produces a curl-free polarization pattern similar to a gradient of a vector field and B-mode orthonormal basis  $Y_{\ell m}^B(\hat{n})$  produces a divergence-free polarization field similar to a curl of a vector field.

The power spectrum of polarization shares similarities with temperature. Specifically, the power spectrum for polarization auto and cross spectra can be expressed as:

$$C_{\ell}^{XY} \delta_{\ell\ell'} \delta_{mm'} = \left\langle a_{\ell m}^X a_{\ell' m'}^{Y*} \right\rangle. \quad (1.29)$$

The  $X$  and  $Y$  can represent temperature and E and B modes of polarization fields of the CMB, i.e,  $X, Y \in \{T, E, B\}$ . We consider the auto-spectra  $TT, EE, BB$ , along with the cross spectra  $TE$ .

Density waves generated by the quadrupolar temperature anisotropy at the time of recombination will always see hotter and colder photons in a direction parallel or perpendicular to the plane of the density wave. This can only produce E-mode polarization regardless of the direction of the density wave.

Gravitational waves propagate in the same direction with density waves. The gravitational waves stretch and squeeze space in a direction perpendicular from it, sourcing both E-mode and B-mode polarization depending on the orientation. B-modes cannot be sourced by density waves, therefore an observation of primordial B-modes is a probe of inflationary gravitational waves.

Due to symmetry,  $TB$  and  $EB$  are expected to be zero. Since we only have one sky realization to observe, the estimate on the power spectrum is a finite sum average for any given multipole value  $\ell$ . Sharing similarities to the temperature power spectrum, all fields  $X, Y \in \{T, E, B\}$  can be represented by the finite sum:

$$C_\ell^{XY} = \frac{1}{2\ell + 1} \sum_{m=-\ell}^{\ell} a_{\ell m}^{X*} a_{\ell m}^Y. \quad (1.30)$$

### 1.3 Inflation

Inflation is a period of extreme rapid expansion of the universe that is believed to have occurred after the Big Bang, during which the universe is thought to have undergone an exponential expansion. It is an extension of the  $\Lambda$ CDM model, proposed in the early 1980s to explain several problems of the the  $\Lambda$ CDM model [48, 69, 30]. Horizon problem, one of the problems of the  $\Lambda$ CDM model, arises from the observation that causally disconnected regions are in thermal equilibrium. Inflation proposes to solve this problem by allowing these regions to have been in causal contact during the exponential expansion stage, and then stretched out of causal contact during inflation. Another problem is the flatness problem, which arises from the observation that the curvature of the universe appears to be very close to zero. Inflation proposes to solve this problem by diluting the curvature of the universe to zero during the exponential expansion.

Alan Guth first proposed the idea of inflation during his study of the absence of magnetic monopoles in the universe. He discovered that a false vacuum possessing positive energy has the ability to cause a rapid and exponential expansion of space.

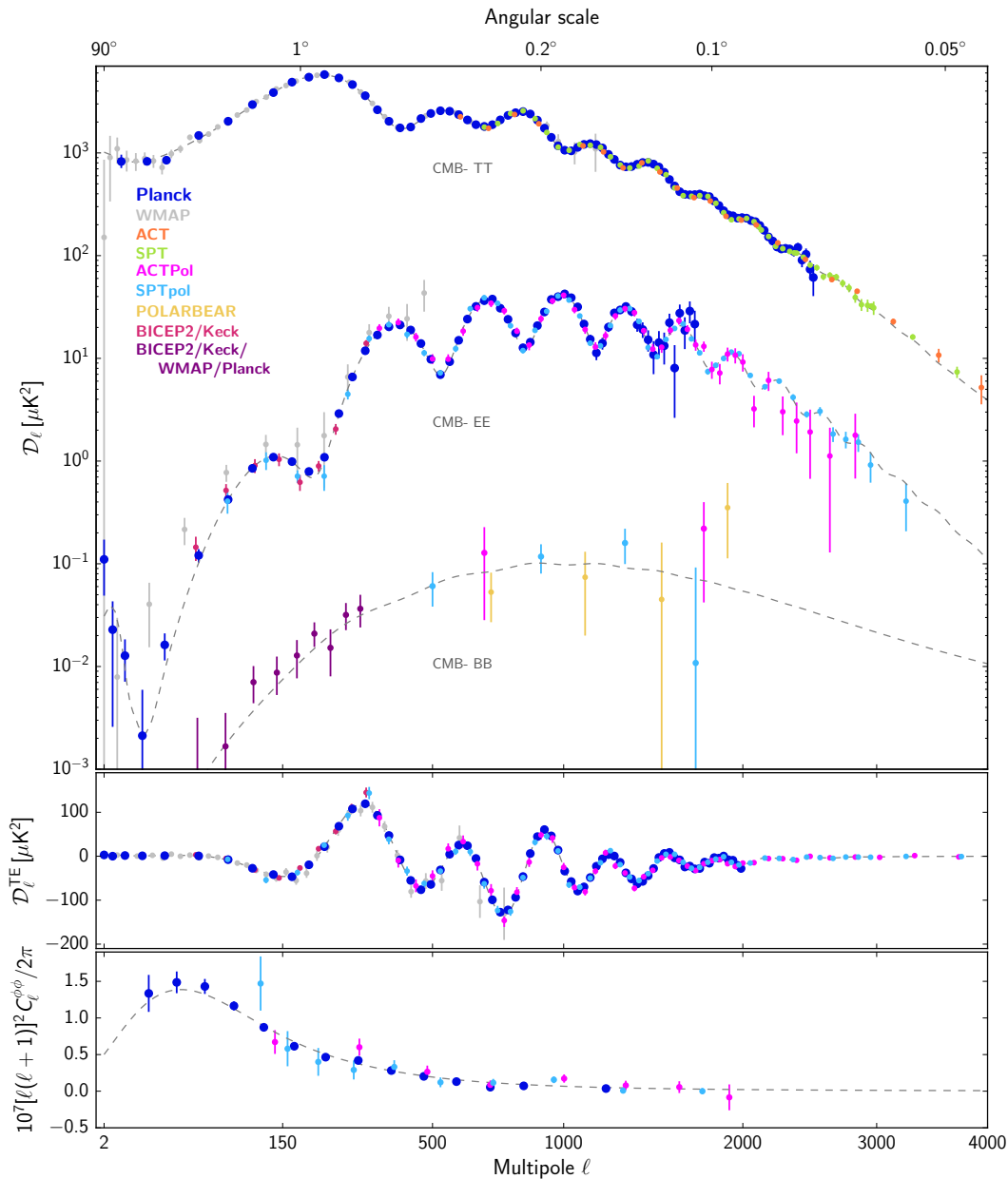


Figure 1.5: The CMB angular power spectrum measurements play an important role in modern cosmology. In this figure, we present a set of measurements from 2018, showing the temperature and polarization power spectra, lensing deflection power spectrum, cross-correlation between  $T$  and  $B$  is shown. Each experiment is represented by a different color, keeping the original binning. EE spectra with large error bars are omitted for multiple experiments. The dashed line in the figure represents the best-fit  $\Lambda$ CDM model to the *Planck* temperature, polarization, and lensing data. Figure taken from [24].

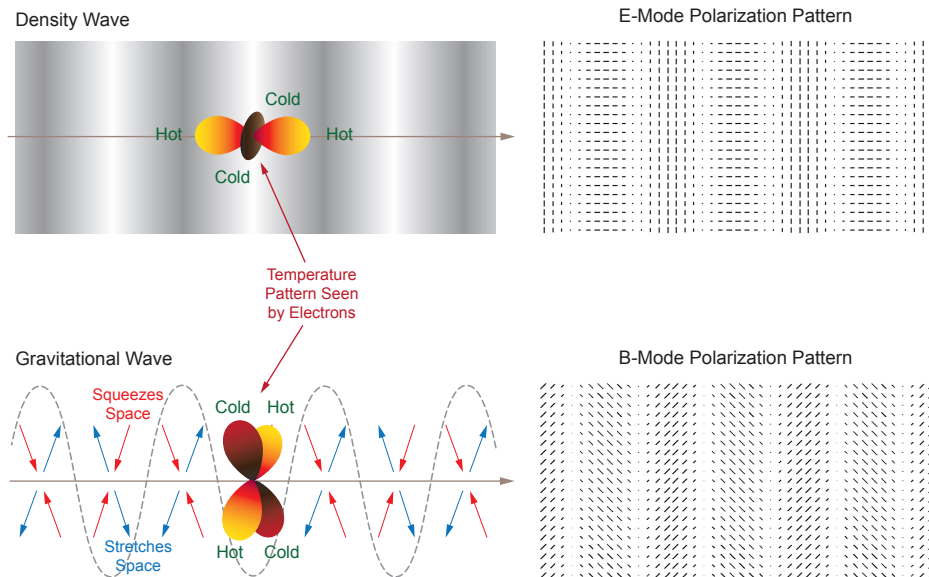


Figure 1.6: A schematic illustration of the polarization patterns in the CMB resulting from density and gravitational waves. On the upper panel, when a single density wave propagates in the direction indicated by the arrow, an electron will perceive hotter and colder photons parallel or perpendicular to the plane of the wave. This can only generate E-mode polarization pattern, as shown on the upper right part of the figure. In contrast, a single gravitational wave propagating in the same direction as the density wave stretches and compresses space in directions perpendicular to the propagation. Depending on the orientation of the stretch/squeeze motion, the resulting polarization pattern can either be E-mode or B-mode. This is shown on the lower right part of the figure. Image taken from BICEP/Keck Array collaboration.

This type of expansion can potentially offer explanations to some of longstanding cosmic problems.

Gravitational waves are predicted by some models of inflation. During inflation, the universe underwent an extremely rapid expansion which would have left an imprint on the cosmic microwave background radiation, as B-mode polarization.

### **Magnetic Monopole Problem**

Grand Unified Theories (GUTs) are proposed extensions of the Standard Model of particle physics that attempt to unify the strong, weak, and electromagnetic forces into a single, unified force.

Magnetic monopoles are hypothetical particles that have a single magnetic pole and carries a net magnetic charge. At high temperatures the Grand United Theories that are proposed to unify strong, weak, and electromagnetic forces into a single force, predict the generation of magnetic monopoles. However no magnetic monopoles have been observed in experiments to date. These particles are both weighty and stable and would have remained a principal component of the universe to date. However, this idea is in conflict with the findings of all previous experimental attempts to find them. Inflation may have significantly reduced their density, making them extremely difficult for detection.

### **Horizon Problem**

The CMB is remarkably isotropic across the sky, having the same temperature in all directions with variations of a few parts in 100,000. To attain such a high degree of thermal equilibrium, the entire observable universe must have been in thermal contact at some point to avoid cosmological fine tuning problem. According to  $\Lambda$ CDM, calculations predict that the universe was not in causal contact before recombination.

To estimate the region of thermal contact, start by evaluating the comoving distance at a redshift value of  $z$ , which is given by:

$$r(z) = \int_0^z \frac{dz}{H(z)}. \quad (1.31)$$

During the epoch of recombination, the universe was matter dominated, and can be approximated by:

$$H^2(z) \approx \Omega_m H_0^2 (1+z)^3. \quad (1.32)$$

We use this approximation to estimate the comoving distance:

$$r(z) = \frac{1}{H_0\sqrt{\Omega_m}} \int_0^z \frac{dz}{(1+z)^{3/2}} = \frac{2}{H_0\sqrt{\Omega_m}} \left(1 - \frac{1}{\sqrt{1+z}}\right). \quad (1.33)$$

Recombination occurs around  $z \approx 1100$ , hence:

$$r(z) \approx \frac{2}{H_0\sqrt{\Omega_m}}. \quad (1.34)$$

The angular scale diameter distance as a function of redshift  $z$  is given by:

$$d_A(z) = \frac{r(z)}{(1+z)} \approx \frac{2}{H_0\sqrt{\Omega_m}} \frac{1}{(1+z)}. \quad (1.35)$$

The particle horizon is the maximum distance that light could have traveled, and is given by:

$$d_{\text{hor}}(z) = \frac{1}{1+z} \int_z^\infty \frac{dz}{H(z)} \approx \frac{2}{H_0\sqrt{\Omega_m}} \frac{1}{(1+z)^{3/2}}. \quad (1.36)$$

The horizon at a redshift of  $z$  is causally connected with an angle of:

$$\theta_{\text{hor}} = \frac{d_{\text{hor}}(z)}{d_A(z)} \approx \frac{1}{\sqrt{1+z}}. \quad (1.37)$$

The horizon problem arises from the fact that at the time of recombination, only angular scales up to about 1.7 degrees across the sky had been in causal contact. This is because at time of last scattering, which is a redshift of around 1100, the angular size of causal region was about 1.7 degrees. Any regions outside of this angular scale would be disconnected patches, which contradicts the observed thermal equilibrium of the universe. The horizon problem refers to the challenge of explaining how such regions could have reached thermal equilibrium in the absence of a causal contact.

In order to ensure that the universe was in causal contact by the time of recombination  $t_{\text{rec}}$ , the condition  $d_{\text{hor}}(t_{\text{rec}}) > d_A(t_{\text{rec}})$  needs to be satisfied to make sure universe was in causal contact. If we assume exponential expansion during inflation, with the inflationary epoch starting at  $t_*$  and ending at  $t_I$ , the scale factor can be written as:

$$a(t) = a(t_I) \exp(-H_I(t_I - t)) \quad (1.38)$$

$$= a(t) \exp(H_I(t - t_I)). \quad (1.39)$$

Let  $N \equiv H_I(t_I - t_*)$  be the number of  $e$ -foldings during inflation. In the limit  $e^N \gg 1$ , the horizon size at the time of recombination is given by:

$$d_{\text{hor}}(t_{\text{rec}}) = a(t_{\text{rec}}) \int_{t_*}^{t_{\text{rec}}} \frac{dt'}{a(t')} \quad (1.40)$$

$$\approx \frac{a(t_{\text{rec}})}{a(t_I)H_I} [e^N], \quad (1.41)$$

and the angular-diameter distance  $d_A$  of the surface of last scattering is of the order:

$$d_A(t_{\text{rec}}) \approx \frac{a(t_{\text{rec}})}{a(t_0)H_0}. \quad (1.42)$$

The condition for the causality can be simplified to:

$$e^N > \frac{a(t_I)H_I}{a(t_0)H_0}. \quad (1.43)$$

For the interested readers, further information on this topic can be found in [92].

### Flatness Problem

The flatness problem is the observation that the curvature of the universe appears to be very close to 0 meaning that the geometry is very close to being flat. Current measurements of the first peak of baryon acoustic oscillations indicate  $|\Omega_k| < 0.01$ . The evolution of this quantity goes with the inverse square of  $(aH)$ . However this suggests that the density of matter and energy in the early universe must have been extremely finely tuned to a very specific value to have a value close to 0 today.

The evolution of the density parameter  $\Omega$  varies with inverse square of the quantity  $(aH)$ :

$$\Omega - 1 = \frac{k}{(aH)^2}. \quad (1.44)$$

This equation implies that in a radiation-dominated universe, the deviation of  $1 - \Omega$  scales with  $t$ , while in a matter-dominated universe, it scales with  $t^{2/3}$ . Any deviation from the value of  $\Omega = 1$  today would require a much smaller deviation in the past, requiring a high degree of fine-tuning. By the time of big bang nucleosynthesis the deviation must have been less than approximately  $\sim 10^{-16}$ , while by the GUT era it had to be approximately  $\sim 10^{-55}$  and at the Planck scale  $\sim 10^{-61}$  [32].

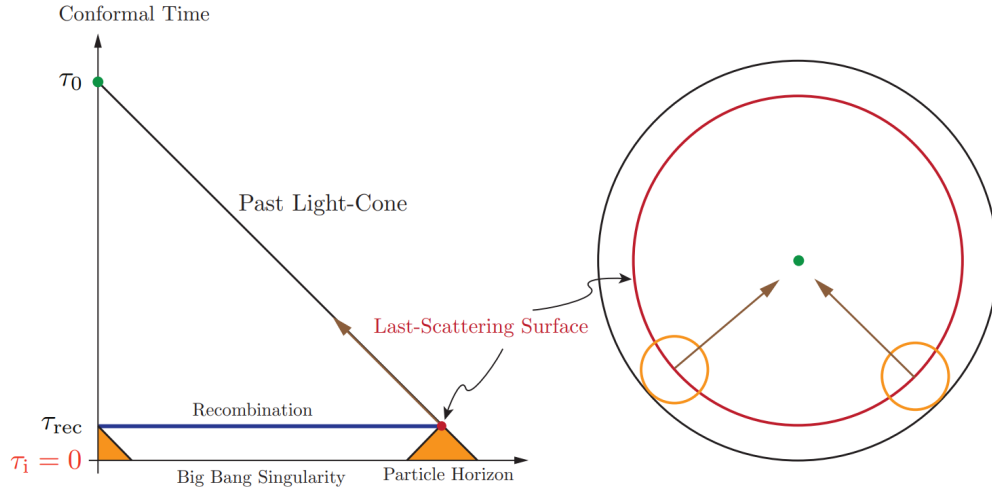


Figure 1.7: Regions that were in causal contact in the early universe should have similar properties today. Observations of the cosmic microwave background radiation indicate that the universe is highly uniform on large scales, even in regions that were not in causal contact. The horizon problem arises from the fact that at the time of recombination, only angular scales up to about 1.7 degrees across the sky had been in causal contact. Figure from [32].

Differentiating with respect to  $a$  we obtain:

$$\frac{d\Omega}{da}(1+3w)\frac{\Omega(\Omega-1)}{a}. \quad (1.45)$$

The value  $\Omega = 1$  is a fixed point of this differential equation, and is a repeller if  $(1+3w) > 0$  and attractor if  $(1+3w) < 0$ . During a period of exponential expansion with  $N$  number of  $e$ -foldings, where  $N \equiv H_I(t_I - t_*)$ , the evolution of this parameter goes with:

$$\Omega - 1 = \frac{k}{(aH)^2} \sim e^{-2N}, \quad (1.46)$$

driving the curvature close to 0.

### Scalar Field Einstein-Hilbert Action

The Einstein-Hilbert action for a scalar field  $\phi$  is given by:

$$S = \int d^4x \sqrt{-g} \left[ \frac{1}{2} M_{\text{Pl}}^2 R + \frac{1}{2} g^{\mu\nu} \partial_\mu \phi \partial_\nu \phi - V(\phi) \right], \quad (1.47)$$

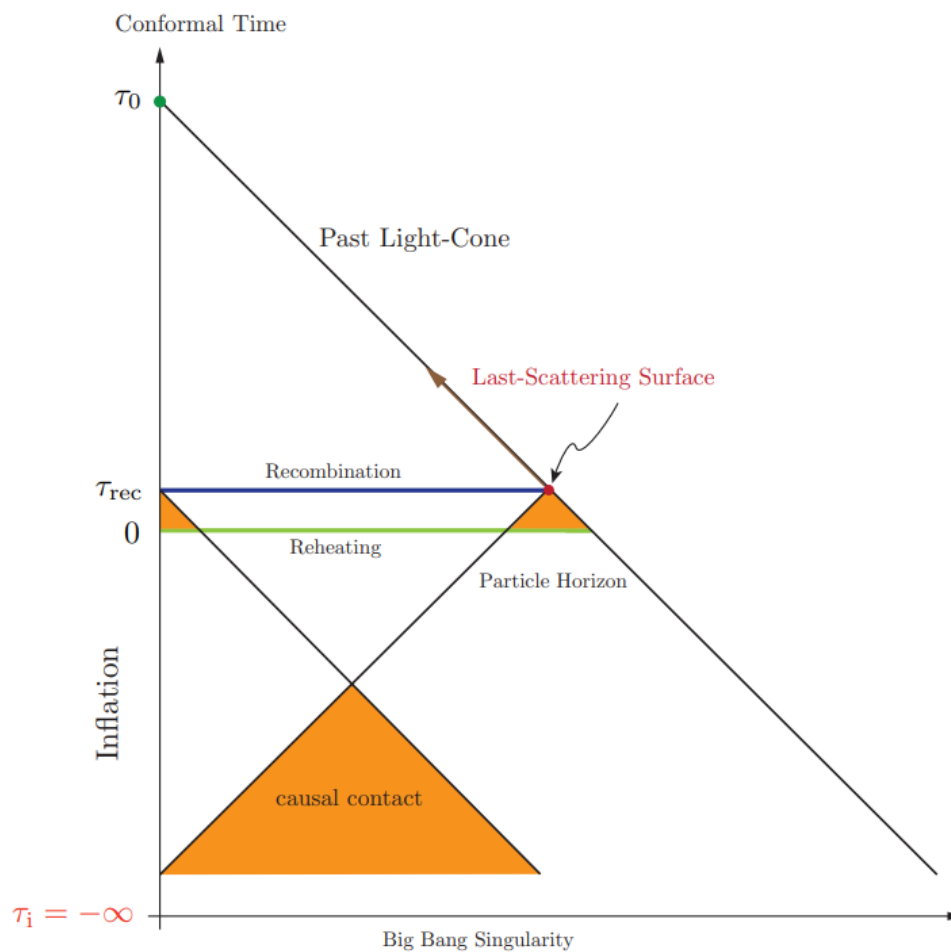


Figure 1.8: Inflation offers to solve the horizon problem by postulating that the universe underwent a period of exponential expansion shortly after the Big Bang. During this period, regions that were previously in causal contact could have been stretched far enough apart so that they appear to be outside of each other's observable horizon today. Figure from [32].

where  $\phi$  is the scalar field,  $R$  is the scalar curvature of the spacetime,  $g$  is the determinant of the metric tensor  $g_{\mu\nu}$ ,  $M_{\text{Pl}}$  is the Planck Mass, and  $V(\phi)$  is the potential of the scalar field.

The variation in this action reduces to a Friedmann constraint equation:

$$H^2 \equiv \left(\frac{\dot{a}}{a}\right)^2 \quad (1.48)$$

$$= \frac{1}{3M_{\text{Pl}}^2} \left(\frac{1}{2}\dot{\phi}^2 + V(\phi)\right) - \frac{kc^2}{a^2}. \quad (1.49)$$

The equation of motion for the scalar field in a FRW Universe is derived from energy conservation and is the equation of a simple damped harmonic oscillator:

$$\ddot{\phi} + 3H\dot{\phi} + V'(\phi) = 0. \quad (1.50)$$

The second term acts as a friction term in the harmonic oscillator, therefore it is called the Hubble friction term.

The energy density  $\rho$  and pressure  $p$  of the scalar field is can be expressed as the kinetic  $1/2\dot{\phi}^2$  and the potential  $V(\phi)$  terms of the scalar field  $\phi$ :

$$\rho = \frac{1}{2}\dot{\phi}^2 + V(\phi), \quad (1.51)$$

$$p = \frac{1}{2}\dot{\phi}^2 - V(\phi). \quad (1.52)$$

### Slow-Roll Approximation

For the inflation field to result in accelerated expansion, it must satisfy two conditions, which are called the slow roll conditions. The first condition is that the kinetic energy from the scalar field needs to be much smaller than the potential  $V(\phi) \gg \frac{1}{2}\dot{\phi}^2$ , hence the slow rolling. The second condition states that the kinetic term does not grow too rapidly.

The slow-roll parameters are defined as the parameters  $\epsilon$  and  $\eta$ :

$$\epsilon = \frac{\dot{H}}{H^2} \ll 1, \quad (1.53)$$

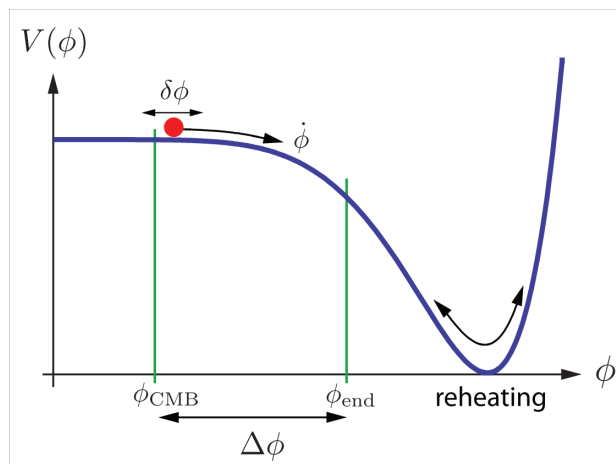


Figure 1.9: Slow roll inflation is the period of inflation where the scalar field that drives inflation rolls slowly down its potential. During this period the universe undergoes an exponential expansion. Figure from [32]

$$\eta = -\frac{\ddot{\epsilon}}{H\dot{\epsilon}} \ll 1. \quad (1.54)$$

Inflation ends when these slow-roll condition is no longer satisfied.

### Perturbations

Inflation states that the anisotropies of the Cosmic Microwave Background were seeded by quantum mechanical zero-point vacuum fluctuations of the inflation field during inflation, creating a nearly scale invariant spectrum of perturbations.

The perturbations can be decomposed into three components: Scalar perturbations, Vector perturbations, and Tensor perturbations.

Scalar perturbations result in non-uniformities in the plasma, and lead to temperature fluctuations of the CMB. The perturbations are expressed as:

$$\phi(t, \vec{x}) = \bar{\phi}(t, \vec{x}) + \delta\phi(t, \vec{x}). \quad (1.55)$$

Vector perturbations decay as  $1/a^2$  with expansion, and are not observable.

Tensor perturbations are transverse and traceless perturbations to the metric, and can be regarded as gravitational waves:

$$g_{\mu\nu}(t, \vec{x}) = \bar{g}_{\mu\nu}(t, \vec{x}) + \delta h_{\mu\nu}(t, \vec{x}). \quad (1.56)$$

Tensor perturbations result in quadrupole anisotropies that are not rotationally invariant and are oriented perpendicular to the direction of their propagation. If the gravitational waves have a plus (+) polarization, it results in E-mode polarization and if the gravitational waves have a cross ( $\times$ ) polarization, the polarization results in a B-mode pattern. However unlike E-mode polarization, B-mode polarization cannot be created by scalar perturbations, and thus it is not limited by sample variance.

It was discovered that the mechanism responsible for inflation in the early universe can also explain the origin of perturbations that initiate the formation of structures in the universe. Inflationary theories predict certain characteristics of these initial perturbations, which have been confirmed through experimental observations.

In the absence of fine-tuning of the inflationary potential or initial conditions, the primordial perturbations are Gaussian. These perturbations can take the form of density fluctuations that arise from adiabatic modes. Inflation predicts adiabatic perturbations.

The power spectrum is scale-invariant if the scalar power spectrum  $P_R(k)$  scales with  $k^{-3}$ . Inflation predicts a nearly scale-invariant scalar perturbation with a slight red tilt, which has been confirmed by observations of the cosmic microwave background. The red tilt indicates that the scalar spectral index  $n_s$  is slightly less than 1.

Planck measured an 95% upper limit on the tensor-to-scalar ratio  $r < 0.10$  using TT, low E, and lensing [19]. However using temperature only will not improve this limit significantly due to cosmic variance [1]. In order to make a sensitive measurement on the tensor-to-scalar ratio, polarization data is needed.

The BICEP/Keck results have yielded the discovery that the inflation model  $m^2\phi^2$ , which was previously considered convincing, is currently strongly disfavored. Furthermore, the BK18 results have invalidated two entire classes of previously popular single-field slow-roll models. The first category includes monomial potentials  $\phi^p$  with canonical kinetic terms, where models with  $p \leq 1$  have received significant attention in the last ten years as they can be naturally realized by axions in the

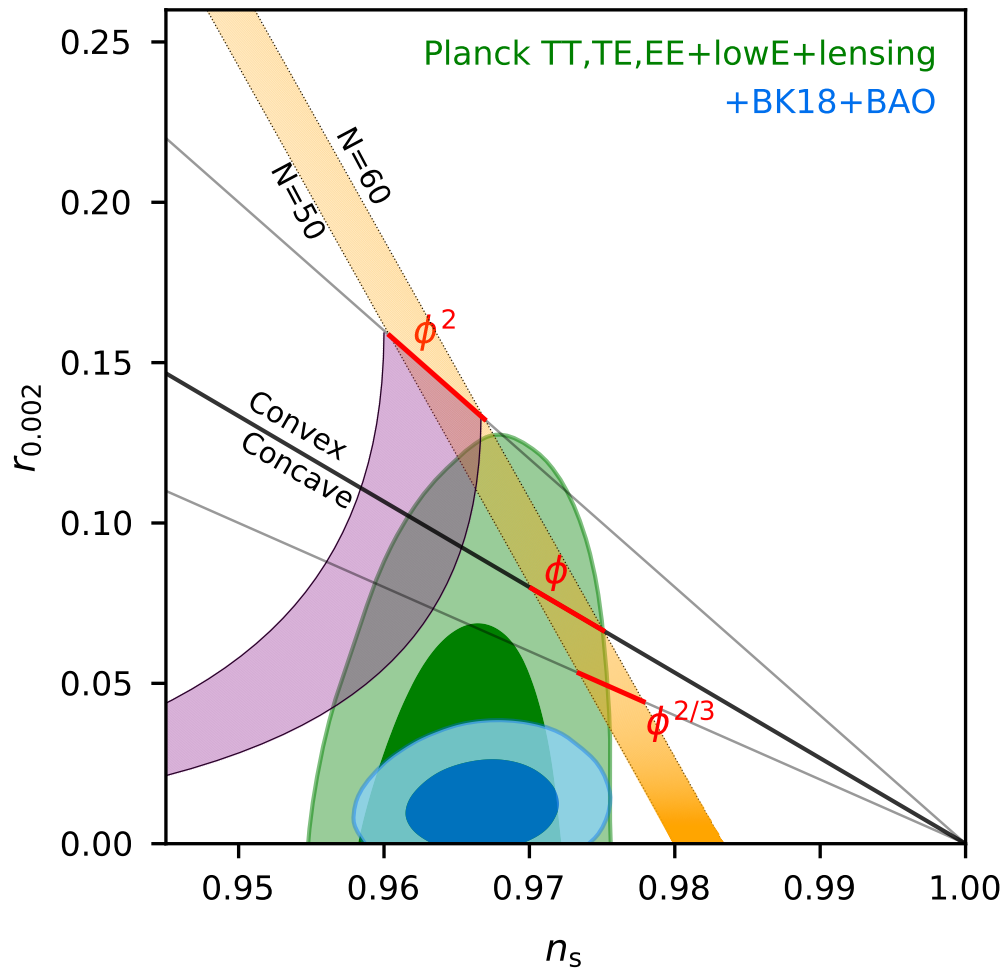


Figure 1.10: The Planck 2018 baseline analysis provides constraints on the tensor-to-scalar ratio  $r$  and the scalar spectral index  $n_s$  (Green). These constraints are further improved by including BICEP/Keck data up to the end of the 2018 season and baryon acoustic oscillation data to enhance the constraint on  $n_s$ . As a result, the upper limit on  $r_{0.05}$  tightens from  $r_{0.05} < 0.11$  to  $r_{0.05} < 0.035$ . Additional inflationary models are shown, the purple region representing natural inflation, and the red curves representing  $\phi^p$  models. Figure taken from [18].

context of string theory [83, 72] and possess super-Planckian field ranges. The specific examples of such models include the axion monodromy models with  $p = 1$  and  $p = 2/3$ . However, all these single-field models have been disfavored by the BK18 findings. The second category is natural inflation [45, 4], a classic model that employs a pseudo Nambu-Goldstone boson, which is commonly found in particle physics, to generate a flat potential. While this model had survived previous experimental tests, it is now well beyond the 95% confidence region.

Cosmological attractors are a class of cosmological solutions that possess a degree of universality, in the sense that they can be realized in a wide range of cosmological models. They are characterized by the fact that the evolution of the universe tends to converge to them, regardless of the initial conditions.

Cosmological attractors offer an explanation for the observed universality of inflationary predictions. Inflationary models typically predict a wide range of possible outcomes, depending on the initial conditions and the details of the inflation potential. However, it has been observed that many of these models tend to converge to a set of attractor solutions, which are characterized by specific features such as a fixed ratio between the tensor-to-scalar perturbation amplitudes, a specific spectral tilt, and a specific shape for the non-Gaussianity of the perturbations [62].

#### 1.4 Perturbations

Deviations from homogeneity are expected to be included in the model describing our universe. Evolution of perturbations are important for constraining cosmological parameters.

Inflation is a period of rapid expansion that could act as a mechanism to generate perturbations by amplifying quantum fluctuations to cosmic scales. Simple models of inflation are expected to generate scalar metric perturbations due to fluctuations in the scalar field, and tensor perturbations originating from inflationary gravitational waves due to rapid expansion. The slow roll parameters,  $\epsilon$  and  $\eta$  are assumed to be much smaller than 1 in the slow-roll approximation:

$$\begin{aligned}\epsilon &= \frac{M_{\text{Pl}}^2}{16\pi} \left( \frac{V'}{V} \right)^2, \\ \eta &= \frac{M_{\text{Pl}}^2}{8\pi} \left( \frac{V''}{V} \right).\end{aligned}\tag{1.57}$$

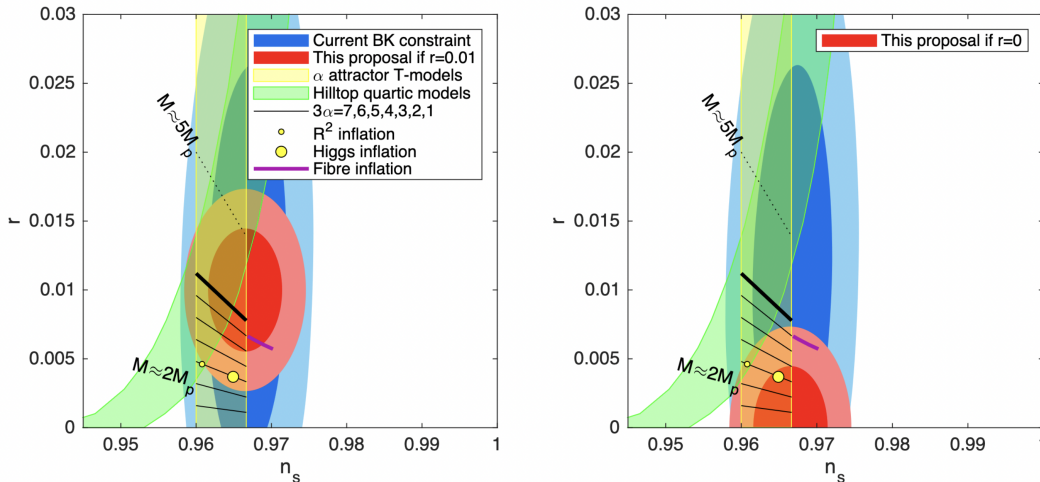


Figure 1.11: BK18 published analysis places constraints on the inflationary parameters  $r$  and  $n_s$ . On the left is the case with  $r = 0.01$  and on the right  $r = 0$ . Planck 2018 provides hilltop quartic model [35] band, as well as the vertical  $\phi^2$ -derived  $\alpha$  attractor T-model band that extends down to  $r = 0$ . On the left, if  $r$  is non-zero, it would provide significant evidence for models such as the  $3\alpha = 7$  model [62]. On the right, evidence against the hilltop quartic class and the first couple of Poincare disk models, as well as some evidence against the  $R^2$  [86] and fibre models [38] are visible, while the Higgs [33] and the lower Poincare models would still be viable.

Let  $\mathcal{P}$  denote the dimensionless power spectrum. The power spectrum for curvature perturbation  $\mathcal{R}$  and tensor perturbations, evaluated at the horizon crossing  $k = aH$ , for a single field slow-roll model are given by:

$$\begin{aligned} \mathcal{P}_{\mathcal{R}}(k) &= \frac{8}{3M_{\text{Pl}}^4} \left. \frac{V}{\epsilon} \right|_{k=aH}, \\ \mathcal{P}_t(k) &= \frac{128}{3M_{\text{Pl}}^4} V|_{k=aH}. \end{aligned} \quad (1.58)$$

The spectrum for curvature perturbation  $\mathcal{R}$  can be approximated by a power law, with spectral index  $n_s$  and a pivot scale  $k_*$ :

$$\mathcal{P}_{\mathcal{R}}(k) = A_s \left( \frac{k}{k_*} \right)^{n_s-1}. \quad (1.59)$$

The scalar spectral index can be expressed in terms of the slow-roll parameters  $\epsilon$

and  $\eta$ :

$$n_s = 1 - 6\epsilon + 2\eta. \quad (1.60)$$

Observations indicate an almost scale-invariant curvature perturbations. Planck measured the spectral index to be  $n_s = 0.965 \pm 0.004$  [22], which are the current most constraining observational limits. For reference a scale invariant spectrum corresponds to  $n_s = 1$ . The slight deviation from scale invariance is in agreement with the slow-roll prediction of inflation given in Equation (1.60).

Deviations from a power law for the initial spectra can be more accurately described by a Taylor expansion of  $\mathcal{P}_{\mathcal{R}}(k)$  evaluated at the pivot scale  $k_*$ , which allows a weak scale dependence on the spectral index:

$$\begin{aligned} \ln \mathcal{P}_{\mathcal{R}}(k) &= \ln \mathcal{P}_{\mathcal{R}}(k_*) \\ &+ (n_s(k_*) - 1) \ln \left( \frac{k}{k_*} \right) \\ &+ \frac{1}{2} \left. \frac{dn_s(k)}{d \ln k} \right|_{k=k_*} \ln^2 \left( \frac{k}{k_*} \right) \\ &+ \frac{1}{6} \left. \frac{d^2 n_s(k)}{d \ln k^2} \right|_{k=k_*} \ln^3 \left( \frac{k}{k_*} \right) \\ &+ \dots \end{aligned} \quad (1.61)$$

The term  $dn_s(k)/d \ln k|_{k=k_*}$  is called the running of the spectral index, and the term  $d^2 n_s(k)/d \ln k^2|_{k=k_*}$  is called the running of the running spectral index. Planck measured these values to be consistent with zero:  $dn_s(k)/d \ln k = 0.013 \pm 0.012$ , and  $d^2 n_s(k)/d \ln k^2 = 0.022 \pm 0.012$  [22].

Similarly the spectra for tensor perturbations can be approximated by a power law with spectral index  $n_t$  and a pivot scale  $k_*$ :

$$\mathcal{P}_t(k) = A_t \left( \frac{k}{k_*} \right)^{n_t}. \quad (1.62)$$

The spectral index for tensor modes  $n_t(k)$  can be expressed in terms of the slow-roll parameters  $\epsilon$  and  $\eta$ :

$$n_t = -2\epsilon. \quad (1.63)$$

In the literature, a scale-invariant tensor perturbation spectrum corresponds to  $n_t = 0$  as opposed to  $n_s = 1$  for scalar perturbations. The spectral tilt has not been measured since tensor modes have not been detected yet.

The spectral index for tensor perturbations  $n_t(k)$  can also be generalized to include scale dependence and running terms, similar to the spectral index for scalar perturbations  $n_s(k)$ :

$$\begin{aligned} \ln \mathcal{P}_t(k) &= \ln \mathcal{P}_t(k_*) \\ &+ n_t(k_*) \ln \left( \frac{k}{k_*} \right) \\ &+ \dots \end{aligned} \tag{1.64}$$

The quantity of interest for our experiment is the ratio of tensor perturbation spectra to the scalar perturbation spectra. This quantity is known as tensor-to-scalar ratio denoted by  $r$ :

$$r \equiv \frac{\mathcal{P}_t(k_*)}{\mathcal{P}_R(k_*)}. \tag{1.65}$$

The pivot scale  $k_*$  referenced in this work is chosen to be  $0.05 \text{ Mpc}^{-1}$ . The pivot scale is typically written as a subscript for the tensor to scalar ratio, which for this work corresponds to  $r_{0.05}$ .

## 1.5 Foregrounds

The anisotropies of the Cosmic Microwave Background (CMB) provide information on the early universe. Many ground-, balloon-, and space-based experiments have already placed strong constraints on cosmological parameters through measurements of the CMB.

The signal from the CMB is contaminated with foregrounds. Cosmological information can be extracted only after the foregrounds are removed.

The main sources of foreground emission consist of synchrotron emission from the galaxy at lower frequencies and thermal dust emission at higher frequencies. Spinning dust grains, thermal free-free emission, and rotational transitions of carbon monoxide also contribute to the total foregrounds. On large angular scales, the foreground emission is relatively smooth.

At high galactic latitudes CMB photons are dominated by the foregrounds. Astrophysical foregrounds and the E-modes from the CMB are both about 10% polarized. Primordial B-mode signal is expected to be smaller than 1% of the foreground emission, therefore it becomes more important to account for foregrounds.

### Synchrotron Emission

Synchrotron emission is generated by relativistic cosmic ray electrons accelerating in spirals due to galactic magnetic fields. Cosmic ray energy and magnetic field strength determine the intensity and the spectrum of the emission. The emission is partially linearly polarized perpendicular to the magnetic field lines [41].

The number density of these electrons is expressed as a power law  $N(E) \propto E^{-p}$ . The fraction of linear polarization, when normalized over all electron energies and frequencies, is given by  $f_s = (p + 1)/(p + 7/3)$  [79], could be as high as  $f_s \approx 0.75$  [65]. The intensity of synchrotron radiation is related to the electron energy distribution:

$$I_s(\nu) \propto \nu^{\beta_s}, \quad (1.66)$$

with  $\beta_s = -(p + 3)/2$ . For frequencies above 20 GHz, the intensity of synchrotron radiation is well approximated by the power law with spectral index  $\beta_s \approx -3$  [2].

Low-frequency full sky maps provided by WMAP and Planck below 40 GHz have significant synchrotron contribution. S-PASS made measurements of the southern sky in linear polarization at 2.3 GHz.

### Thermal Dust Emission

Dust grains, mostly consisting of graphites, silicates, and Polycyclic Aromatic Hydrocarbons (PAHs) emit polarized thermal emission. These grains align their major axis with the galactic magnetic field, and emit strongly along their shorter axis resulting in a net polarization. The polarization depends on the angle between the magnetic field and the line of sight, as well as material properties of the dust grains [53]. The emission from dust grains at temperature  $T_d$  can be approximated by a modified blackbody model (also referred as a gray-body model):

$$P_d(\nu) = A_d^P \left( \frac{\nu}{\nu_0} \right)^{\beta_d} B(\nu, T_d), \quad (1.67)$$

where  $B(\nu, T_d)$  is the Planck function [59]. High-frequency full sky maps provided by Planck HFI has a significant contribution from dust emission, which is very important for an accurate representation of dust in our field of observation. Dust contribution depends on the patch of sky observed. Galactic plane has the highest amount of dust contribution.

The residual foreground power needs be of order  $D_\ell^{BB} \sim 10^{-5} \mu\text{K}^2$  or less to achieve experimental sensitivities of  $\sigma(r) \sim 10^{-3}$  at  $\ell \lesssim 100$ .

### Dust Filaments

Elliptical dust grains rotate around their shorter axis. Their rotation axis align with galactic magnetic field and their polarization direction is perpendicular to B.

An asymmetry in power between the dust E- mode and B-modes has been reported by Planck in the 353 GHz band. Across a range of multipole values  $40 < \ell < 600$  the ratio of the amplitude of the dust E-mode to B-mode power is approximately two [3]. E-modes are not published in the BK18 paper, however it has been shown that the dust polarization foreground model used is in agreement with the E-mode to B-mode ratio obtained from Planck.

According to an analysis of dust polarization data from Planck in the diffuse interstellar medium at low and intermediate Galactic latitudes, it appears that the structure of interstellar matter tend to be aligned with the plane of the sky (POS) projection of the magnetic field. The occurrence of E-modes and B-modes are dependent on the polarization pattern's parity invariance [98]. There is E-only power if the plane of the sky magnetic field is either parallel or perpendicular to the filaments. If the plane of the sky magnetic field is oriented at  $+45^\circ$  or  $-45^\circ$  with respect to the filaments, there is B-only power. Magnetic fields are aligned with filaments, and expect to result in stronger E-modes. This asymmetry can be measured by the dust EE to BB ratio. Furthermore, alignment of filaments with magnetic fields explain observed TE correlation [40].

HI observations indicate a filamentary structure of the diffuse interstellar matter [39, 73]. Simulations of magneto-hydrodynamic (MHD) turbulence of the diffuse interstellar matter also show the presence of a preferential relative orientation [52, 85]. Amount of gas is a predictor of dust, dust reddening and NHI correlated. MHD stretches gas filaments along magnetic fields.

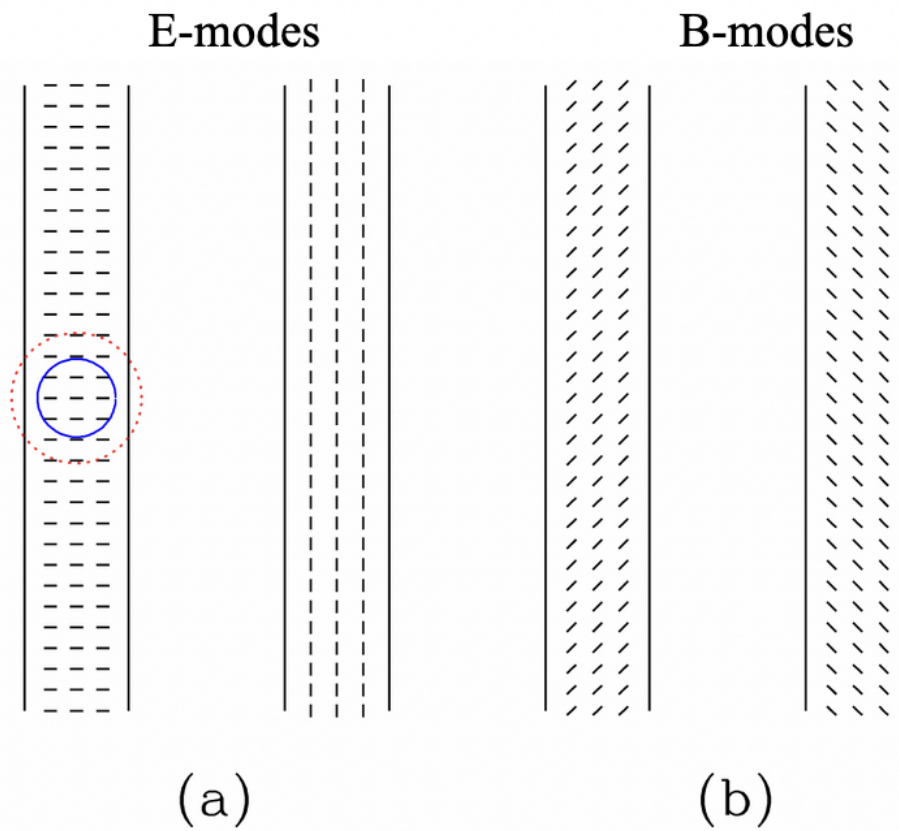


Figure 1.12: Examples of polarization vectors located within filaments. The image has two circles that identify points that hold equal weight to E and B at the center of the circles. When moving along the smaller circle, the contribution from points cancels out, whereas the contribution from the second circle is not zero. In this specific example, the contribution is mostly E. The first pair of filaments, shown as a, generates E-mode polarization inside the filaments, whereas the second pair, shown as b, produces B-mode polarization. Figure taken from [98].

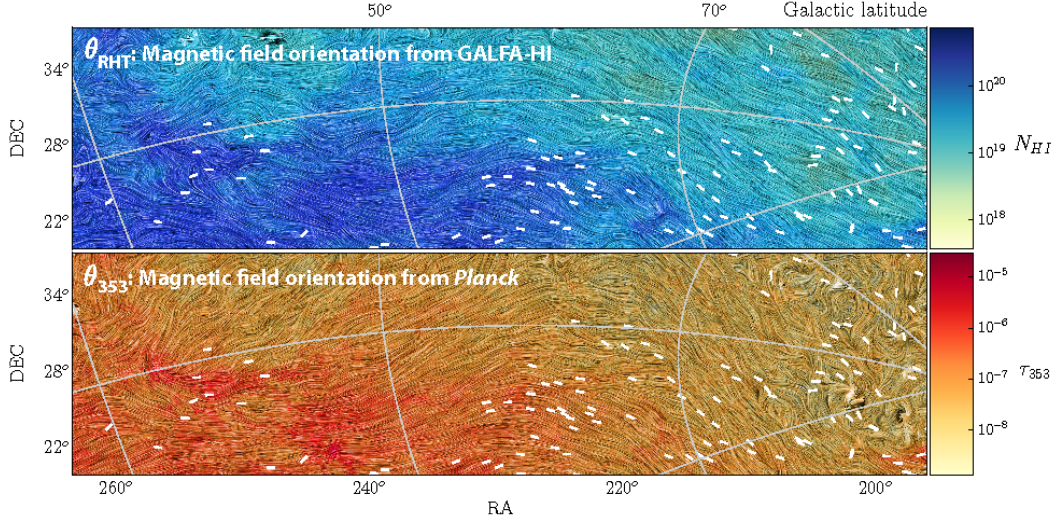


Figure 1.13: Linearly polarized structure in Galactic neutral hydrogen HI (upper) correlates well with the orientation of the magnetic field inferred by Planck 353 GHz polarized dust emission. Figure taken from [40].

### Dust Decorrelation

Even if we assume a perfect instrument, the experimental situation poses a challenge due to contamination of the signal of interest with foregrounds at any given frequency. The primary foregrounds are synchrotron radiation at low frequencies and thermal dust emission at high frequencies, which have distinct spectral indices in comparison to the cosmic microwave background (CMB). Consequently, it becomes possible to separate the foregrounds from the signal of interest. Typically, high frequency maps are employed to create a template of the dust contamination at lower frequencies, providing a high signal-to-noise ratio.

According to PIPL released by the Planck collaboration, there is evidence of considerable decorrelation in the B-mode signal at  $50 < \ell < 160$  between their 217 GHz and 353 GHz maps [23]. This indicates that the cross-correlation coefficient  $R_\ell^{BB}$  between the B-mode polarization in the two maps, is below unity on degree scales, where

$$R_\ell^{BB} \equiv \frac{D_{\ell, BB}^{353 \times 217}}{\sqrt{D_{\ell, BB}^{217 \times 217} D_{\ell, BB}^{353 \times 353}}}. \quad (1.68)$$

This implies that the two maps are not mere scaled versions of each other. Therefore, the 353 GHz map cannot serve as a dust contribution template for lower frequencies

without accounting for uncertainty in the assumed degree of correlation. PIPL also notes a noteworthy trend towards increased decorrelation at high galactic latitudes.

It is anticipated that there will be a certain degree of decorrelation due to variations in the polarization angle and temperature of dust clouds along the line of sight. This observation is in agreement with a physical model that explains the generation of dust polarization via the interaction of dust grains with the magnetic field of the galaxy. The amount of decorrelation reported in PIPL was surprisingly high.

The presence of dust decorrelation would lead to a reduction in power in the cross-spectrum between high-frequency maps, which are strong in dust, and lower-frequency maps, which exhibit greater sensitivity to cosmological B-modes. It would cause residuals to remain in lower-frequency maps that are cleaned using a template obtained from higher-frequency maps. Failure to account for either of these scenarios would result in an underestimation of the contribution of dust and an upward bias in the measurement of the tensor-to-scalar ratio  $r$  [82].

PIPL states that their measured level of decorrelation at  $50 < \ell < 160$ , a flat  $R_\ell^{BB} = 0.95$  would result in a bias of  $r = 0.046$  in the BICEP/Planck joint analysis [23]. If this trend of higher decorrelation in smaller sky fractions is accurate, the bias could be even greater. Such a finding could significantly impact future B-mode surveys as it would necessitate optimizing surveys towards a larger number of more closely spaced frequency bands. Decorrelation has been an important consideration for our multi-frequency coverage approach.

Subsequent analysis of this measurement, have shown that the hypothesis of no-decorrelation cannot be ruled out using the Planck data. There are three primary reasons for this: Firstly, cross-spectra between Planck data splits exhibit a considerable noise bias, which necessitates correction. Secondly, there is compelling evidence of unknown instrumental systematics. Thirdly, there are noteworthy correlations between measurements obtained from distinct areas of the sky, and these must be considered when evaluating the statistical significance of the results [82]. A subsequent analysis by Planck XI in 2018 have confirmed these systematic errors and noise question and found no evidence for a loss of correlation, indicating that these issues do not post a problem for CMB experiments aiming at a primordial B-mode detection on the tensor-to-scalar ratio of order  $r \approx 0.01$  [28].

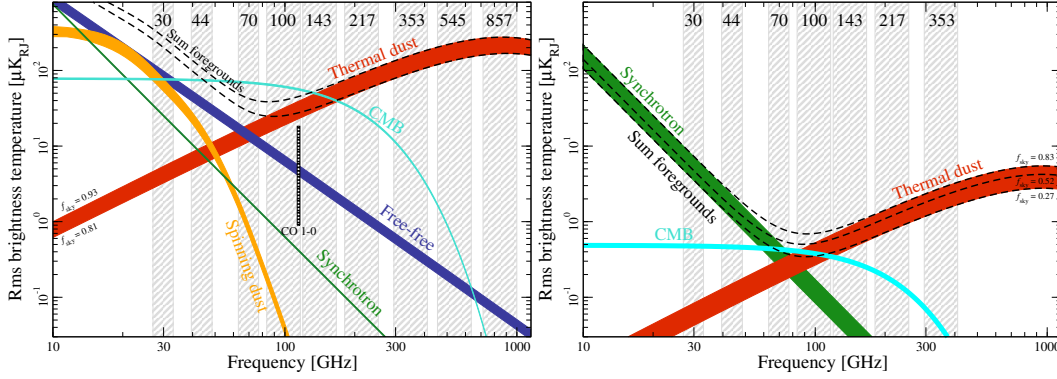


Figure 1.14: Polarized dust emission, are much brighter compared to the primordial B-mode signal that we target to detect. The polarized foregrounds have distinctive spectral shapes that differ from the primordial B-mode signal. These spectral differences allow us to distinguish between the foregrounds and the B-mode signal. Figure taken from [24].

### Gravitational Lensing

Primordial B-mode signals by the time of recombination would be sourced by inflationary gravitational waves. CMB photons are lensed by the gravitational potential field from intervening matter as they travel from the surface of last scattering to the observer. This lensing effect is capable of transforming lensed E-modes into B-modes [100, 68].

Since lensing B-modes are sourced by the CMB, they have the same frequency scaling. Lensing B-modes are stronger at higher multipole values compared to the primordial B-modes expected from tensor modes.

The distorted temperature field  $T(\hat{n})$  and the polarization fields  $Q(\hat{n})$  and  $U(\hat{n})$  are remapped:

$$\begin{aligned} T(\hat{n}) &= \tilde{T}(\hat{n} + \vec{\nabla}\phi) \\ (Q + iU)(\hat{n}) &= (\tilde{Q} + i\tilde{U})(\hat{n} + \vec{\nabla}\phi), \end{aligned} \quad (1.69)$$

where  $\vec{\nabla}\phi$  is the gradient of the gravitational potential integrated along the line-of-sight. Polarization direction and intensity are preserved through lensing, but there is distortion on the anisotropies.

Gravitational lensing has an impact on the TT, TE, and EE spectra, causing the peaks and troughs of the power spectra to be spread across all values of  $\ell$ . However,

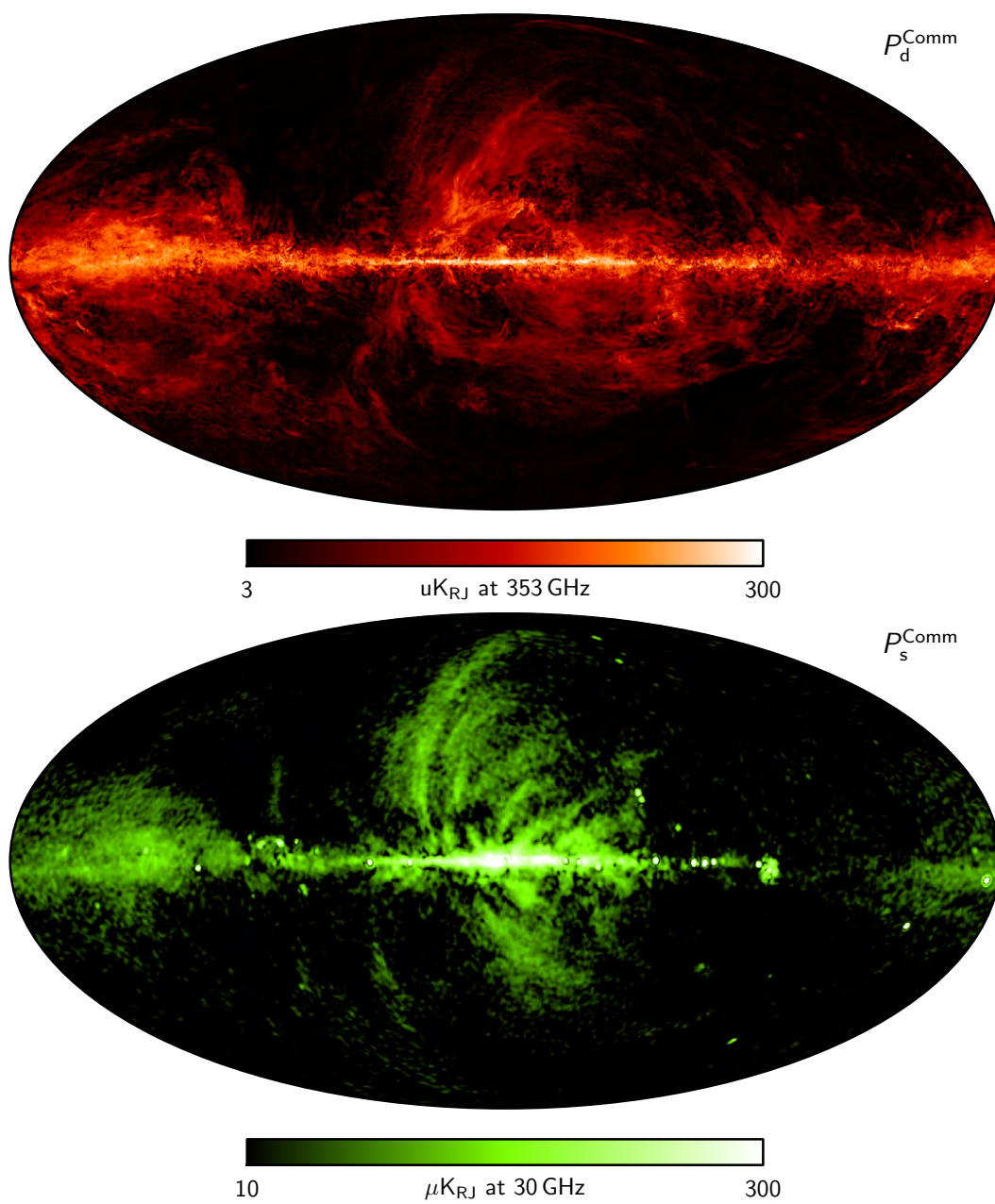


Figure 1.15: Commander polarized foreground maps from Planck 2018. Upper: Polarized thermal dust amplitude map at 5 arcmin FWHM resolution, scaled to 353 GHz. Bottom: Polarized synchrotron amplitude map at 40 arcmin FWHM resolution, scaled to 30 GHz. Figures taken from [27].

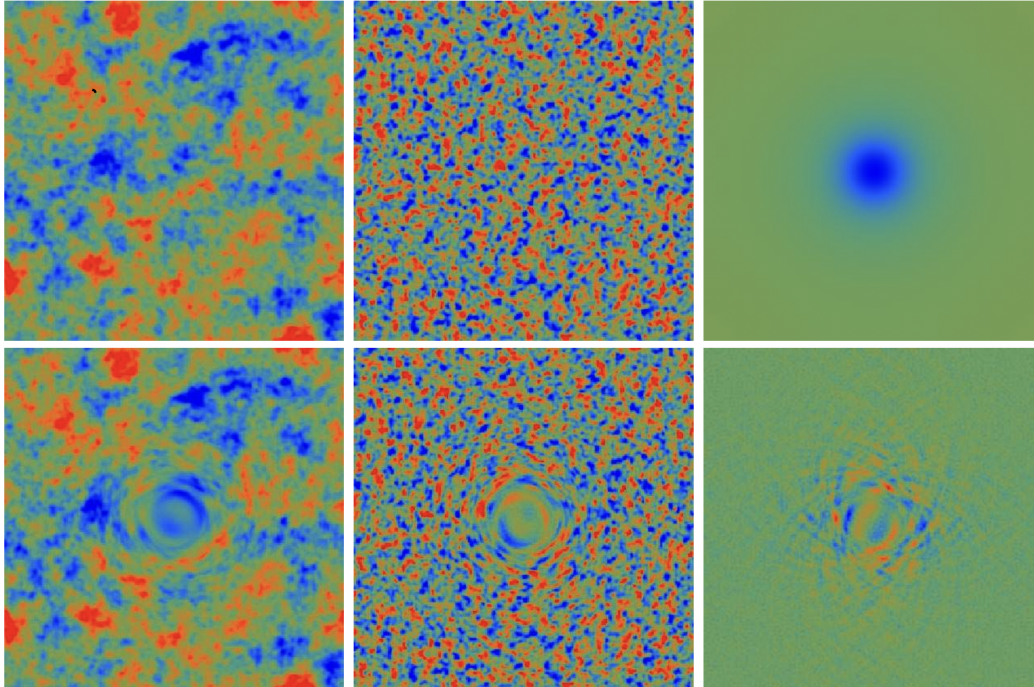


Figure 1.16: The lensing B-mode polarization is caused by the deflection of E-modes into B-modes as CMB photons pass through the gravitational potential wells. Figure taken from [55].

gravitational lensing generates a significant amount of BB power, which peaks around  $\ell \approx 1000$ . This results in non-Gaussian fluctuations, which are distinct from the Gaussian primordial fluctuations of the CMB. The non-Gaussianity of gravitational lensing allows for delensing a technique that involves using CMB polarization maps to estimate and removes lensing potential  $\phi$ . The lensing templates are typically based on cosmic infrared background and  $\Lambda$ CDM E-modes.

Multiple experiments, including SPT, Polarbear, and BICEP/Keck Array have detected B modes produced by gravitational lensing [50, 26, 8].

*Chapter 2***BICEP/KECK ARRAY ARRAY EXPERIMENT**

The BICEP/Keck Array series of telescopes are designed to search for evidence of cosmic inflation by aiming to detect primordial B-mode polarization signal from the Cosmic Microwave Background. The telescopes use a compact, on-axis refractive design that is optimized for sensitive measurements at degree-angular scales ( $\ell \approx 80$ ) while minimizing systematics. The telescopes observe a small, low-foreground patch of the sky from the Amundsen–Scott South Pole Station, where the exceptionally high altitude and dry weather conditions are ideal to produce sensitive and low-noise maps.

The experiments deploy modular structure that allow for quick upgrades to improve detector performance and diversify frequency coverage. With each successive generation, more detectors are deployed for increasing mapping speed. The primary scientific objective of the BICEP/Keck Array Collaboration is to measure the tensor-to-scalar ratio  $r$  defined in section 1.4, a quantity of interest for detecting primordial gravitational waves produced during inflation.

This chapter provides an overview of the telescopes deployed to date. The subsequent sections of the chapter provide further details about each component of the telescopes. The design objectives and operational strategies have been consistent across the telescopes deployed for a successful CMB experiment.

## 2.1 BICEP/Keck Array Instrument

The Bicep/Keck Array (BICEP/Keck Array) is a series of microwave polarimeters designed to detect the degree-scale polarization of the Cosmic Microwave Background (CMB) and search for signs of inflationary gravitational waves. The experiment consisting of the following instruments: BICEP1 [87], BICEP2 [77], Keck Array [81], BICEP3 [6], and the BICEP Array [58]

The results reported in this thesis are based on data collected from several sources. These include BICEP2 (deployed from 2010 through 2012), Keck Array (deployed 2011 through 2019), BICEP3 (deployed in 2015, currently active). BICEP Array has been deployed in 2020 and is currently active, however science data from BICEP3 has not been used in this thesis.

The telescopes are designed to observe angular degree scales B-mode polarization signal. Based on this goal, the instruments share similar features and design strategies:

- Compact design, featuring a small aperture, but still capable of achieving high sensitivity at a degree of angular resolution for the B-mode polarization signal.
- The telescope utilizes on-axis refractive optics to enable polarization modulation of Stokes  $Q$  and  $U$ , as well as measurement of instrumental systematics. Furthermore, the telescope can rotate around its boresight.
- The telescopes continuously observe a small section of the sky referred to as the "Southern Hole," where Galactic foreground emissions are anticipated to be small.
- The design of the telescope is modular, allowing for quick turnout and easy upgrades. With each successive instrument, more detectors are deployed, increasing the mapping speed.

### BICEP1

BICEP1 is a compact refractive telescope, with 25-cm aperture, consisting of 49 pairs of polarization-sensitive bolometers (PSBs). The bolometers are based on neutron transmutation doped (NTD) Germanium thermistors, and contained orthogonally placed polarization-sensitive grids behind a feed-horn and band-defining filter. [87]

In the 2006 observing season, 25 detector pairs were observing at 100 GHz, and 24 observing at 150 GHz. In the 2007/2008 season, two detector pairs at 150 GHz were replaced by detectors operating at 220 GHz. The detectors are operated at superconducting temperatures and cooled down to 250 mK using  $^4\text{He}/^3\text{He}/^3\text{He}$  sorption fridge system [97].

BICEP1 collected three years of B-mode measurements and placed an upper bound of  $r_{0.05} < 0.70$  on the tensor-to-scalar ratio [31]. Data from BICEP1 is not used in the results presented in this thesis.

## **BICEP2**

BICEP2 succeeded BICEP1 and reused the same mount at the South Pole. The neutron transmutation doped (NTDs) Germanium thermistors were replaced by Transition Edge Sensor (TES) bolometers, a new detector architecture in which beam-defining slot antennas are coupled to detectors imprinted in the same silicon wafer. The advantage of this design is a higher focal-plane packing density that can be fabricated quickly and with high uniformity. The detector readout in BICEP2 is multiplexed through SQUID amplifiers to reduce the number of wires on the focal plane, which in turn reduces the heat load [77, 10]. A BICEP2 focal plane hosted 500 optically coupled detectors at 150 GHz and 12 dark TES detectors. The cryostat required only liquid helium for cooling due to the inclusion of nested, vapor-cooled shields that replaced the need for liquid nitrogen stage [10].

BICEP2 observed three seasons from 2010 to 2012 and was operated from the Dark Sector Laboratory (DSL) located at the South Pole station. Using 150 GHz data from 2010 through 2012, BICEP2 reported the detection of B-modes at angular scales [11]. However, a subsequent analysis in collaboration with *Planck* found strong evidence for contribution of B-modes from galactic dust emission.

The results indicate no statistically significant evidence for tensor modes in the cosmic microwave background radiation, as observed by BICEP2 at a single frequency. The upper limit for the tensor-to-scalar ratio  $r_{0.05} < 0.12$  [13] is consistent with the absence of primordial gravitational waves. The analysis was limited by the inability to distinguish the inflationary B-modes from the polarized galactic dust emission. Future observations at multiple frequencies were needed to overcome this limitation and provide more definitive evidence for the detection of primordial gravitational waves.

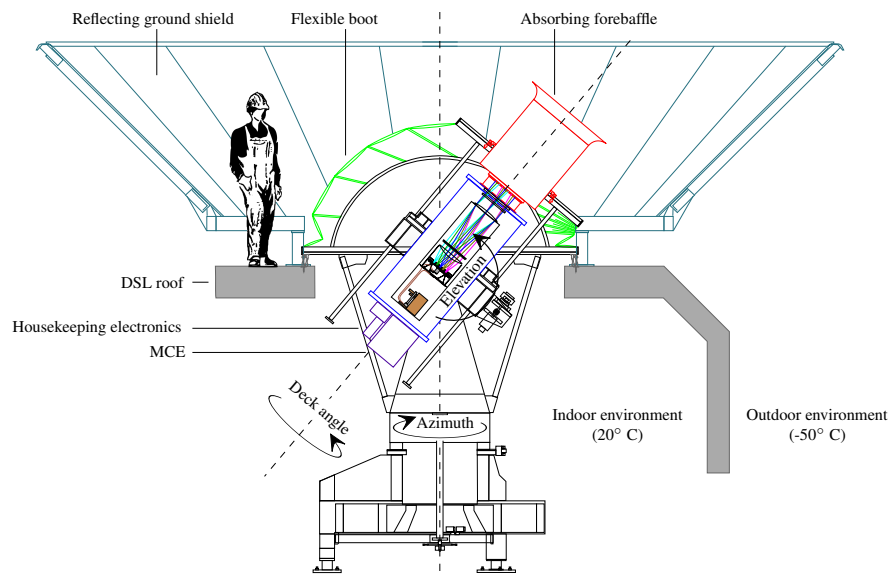


Figure 2.1: BICEP2 and the mount are located at the Dark Sector Laboratory (DSL). The telescope is mounted on a three-axes mount that allows for precise control of its orientation in azimuth, elevation, and boresight (deck rotation). To minimize interference from ground radiation, the telescope is enclosed by a reflecting ground shield that blocks the line of sight from the ground. Additionally, an absorbing forebaffle is mounted on the receiver and prevents light outside of field-of-view. The telescope is located within a liquid helium cryostat, where the detectors are cooled down to 270 mK using a  $^4\text{He}/^3\text{He}/^3\text{He}$  sorption fridge system. Readout cards contain multi-channel electronics and housekeeping electronics and are attached to the bottom of the cryostat to control and monitor the operation of the telescope. Figure from [10].

### ***Keck Array***

*Keck Array* consists of five microwave polarimeters that are designed to observe the cosmic microwave background radiation. Each *Keck Array* receiver is a compact on-axis refracting telescope that builds on the technology and techniques used in the BICEP2 experiment, but with some key improvements. One of the main upgrades is the use of a Cryomech PT-410 pulse-tube cooler that allows for smaller cryostats and more efficient cooling [81]. This change allows all receivers to fit into a single mount located at the telescope mount.

All five *Keck Array* receivers operated at 150 GHz during the 2012 and 2013 seasons. As the sensitivity on  $r$  became limited by foregrounds, the frequency coverage was changed to better characterize polarized galactic foreground. The modular design of the cryostats allowed for the optical elements and detectors to be swapped out

quickly for new frequencies.

To study the effects of galactic foregrounds on the BICEP2 results, two *Keck* Array receivers were swapped with new focal planes and optics to observe at 95 GHz for the 2014 season. Next season two more 150 GHz receivers were swapped with focal planes and optics that observed at 220 GHz [5]. Finally, the last 150 GHz focal plane was replaced with one at 270 GHz prior for the 2017 observing season.

Each *Keck* focal plane has contained 256 detector pairs (also known as pixels), at 150, 220, and 270 GHz, while 95 GHz focal plane contained 144 pairs due to bigger wavelengths. At higher frequencies, the detector readout is the limiting factor for the number of detectors that can be used for each focal plane.

*Keck* Array used a 26-cm aperture similar to BICEP2, which enables sensitive measurements at  $\ell \approx 100$ . The entire telescope, including lenses, filters, and detectors, is placed within a cryostat. The mount is designed to rotate freely along the boresight for polarization modulation of Stokes  $Q$  and  $U$  as well as measurements of instrumental systematics. Each of the five *Keck* Array cryostats, referred to as receivers, observes at a single frequency and is incrementally labeled as rx0, rx1, rx2, rx3, and rx4.

### **BICEP3**

BICEP3 began its science observation in 2016 and is the third generation upgrade to the BICEP/*Keck* Array series. BICEP3 has a larger optical aperture at 520 mm, and higher density of detectors allowing it to deploy 1280 bolometer pairs at 95 GHz. This is comparable to all five receivers of *Keck* Array packed into a single cryostat housing. BICEP3 uses Cryomech PT415 as the first stage of cooling system to accommodate for the larger size and increased cryogenic loading.

BICEP3 uses a modular focal plane structure. Detectors are located on a 3-inch monolithic tiles, each of which are packaged into a detector module containing the SQUIDs, Nyquist chips, magnetic shielding, and other components. Each module can easily be inserted or removed from the focal plane which allows for testing and replacing large numbers of detector modules before and during deployment. BICEP3 uses the same mount that was used for BICEP2 at the at the Dark Sector Laboratory (DSL) at the South Pole station.

Combined data from 2016 to 2018 reached  $2.8 \mu\text{K} - \text{arcmin}$  over an effective area

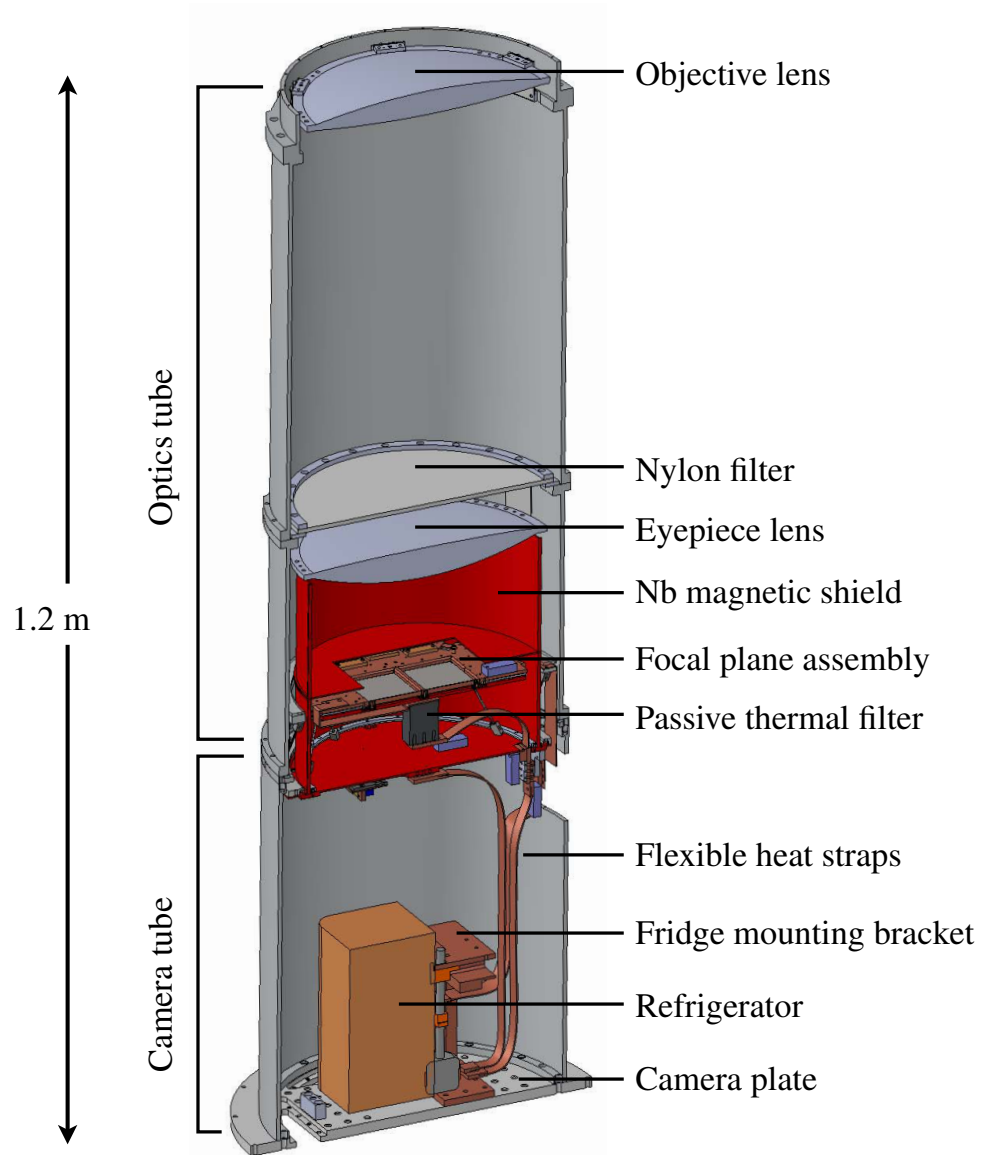


Figure 2.2: Cross-sectional view of a *Keck* Array telescope. The entire assembly is cooled down to 4 K using liquid helium. The optics tube provides support for various components such as lenses, filters, and aperture stop. The camera tube assembly houses the sub-kelvin sorption refrigerator and the cryogenic readout electronics, both of which are thermally and radiatively protected. The sub-kelvin focal plane assembly sits inside a superconducting Nb magnetic shield and is thermally connected to the fridge through a passive thermal filter. This setup is designed to reduce thermal noise. Figure from [10].

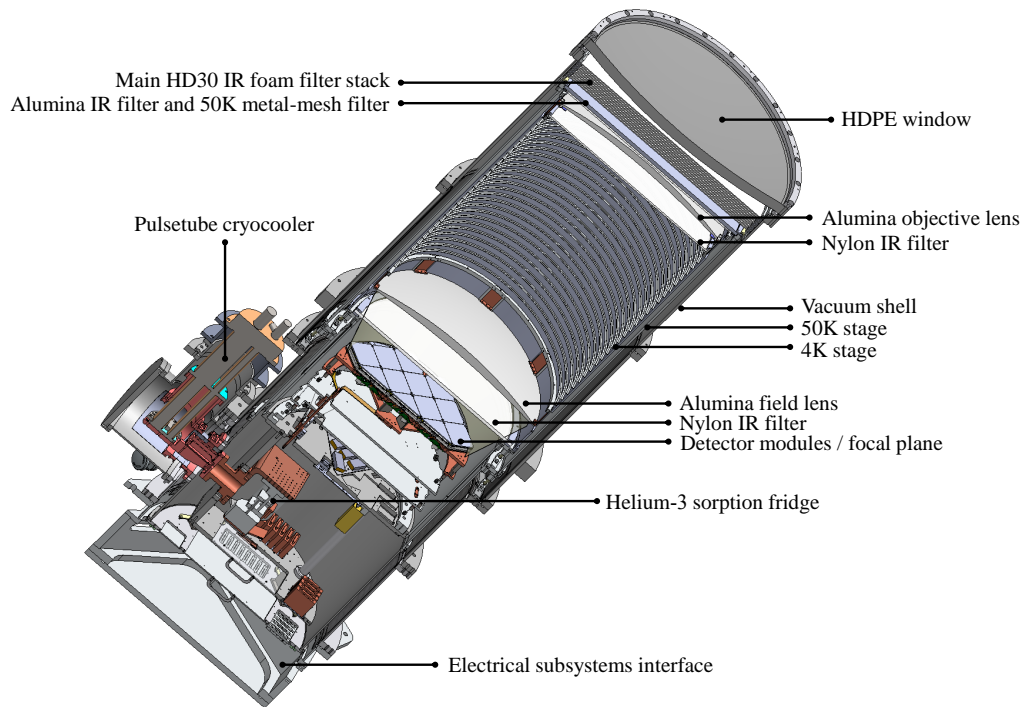


Figure 2.3: Cross-sectional view of a BICEP3 telescope. The pulse tube has two stages at 50K and 4K, while the helium sorption fridge has three stages at 2K, 350mK, and 250mK. The thermal stages are mechanically supported by sets of carbon fiber and G-10 fiberglass support. The focal plane has 20 detector modules and 2400 detectors, and is located at the 250mK stage, surrounded by multiple layers of RF and magnetic shielding. Figure from [6].

of 585 square degrees, and resulted in the tightest constraint on the tensor-to-scalar ratio  $r$  to date, with  $r < 0.036$  [6].

## 2.2 Observation Site

The BICEP/Keck Array series of telescopes are located at the Amundsen Scott South Pole Station. The location provides excellent observation conditions and a stable homogeneous view of the sky, since the celestial sphere does not change. This allows for higher sensitivities of the polarized CMB signal due to larger integration times.

South Pole is an ideal observing site for microwave experiments due to very low levels of water vapor in the atmosphere. The station is located at the Antarctic

Table 2.1: Deployment history of BICEP/Keck Array

Year	Receiver	Frequency (GHz)	Optically Coupled Detector Count
2010-12	BICEP2	150	500
2012	rx0	150	500
2012	rx1	150	500
2012	rx2	150	500
2012	rx3	150	500
2012	rx4	150	500
2013	rx0	150	500
2013	rx1	150	500
2013	rx2	150	500
2013	rx3	150	500
2013	rx4	150	500
2014	rx0	95	272
2014	rx1	150	500
2014	rx2	95	27
2014	rx3	150	500
2014	rx4	150	500
2015	rx0	95	272
2015	rx1	220	500
2015	rx2	95	272
2015	rx3	220	500
2015	rx4	150	500
2016	BICEP3	95	2400
2016	rx0	210	500
2016	rx1	220	500
2016	rx2	210	500
2016	rx3	220	500
2016	rx4	150	500
2017-18	BICEP3	95	2400
2017-18	rx0	210	500
2017-18	rx1	220	500
2017-18	rx2	210	500
2017-18	rx3	220	500
2017-18	rx4	270	500

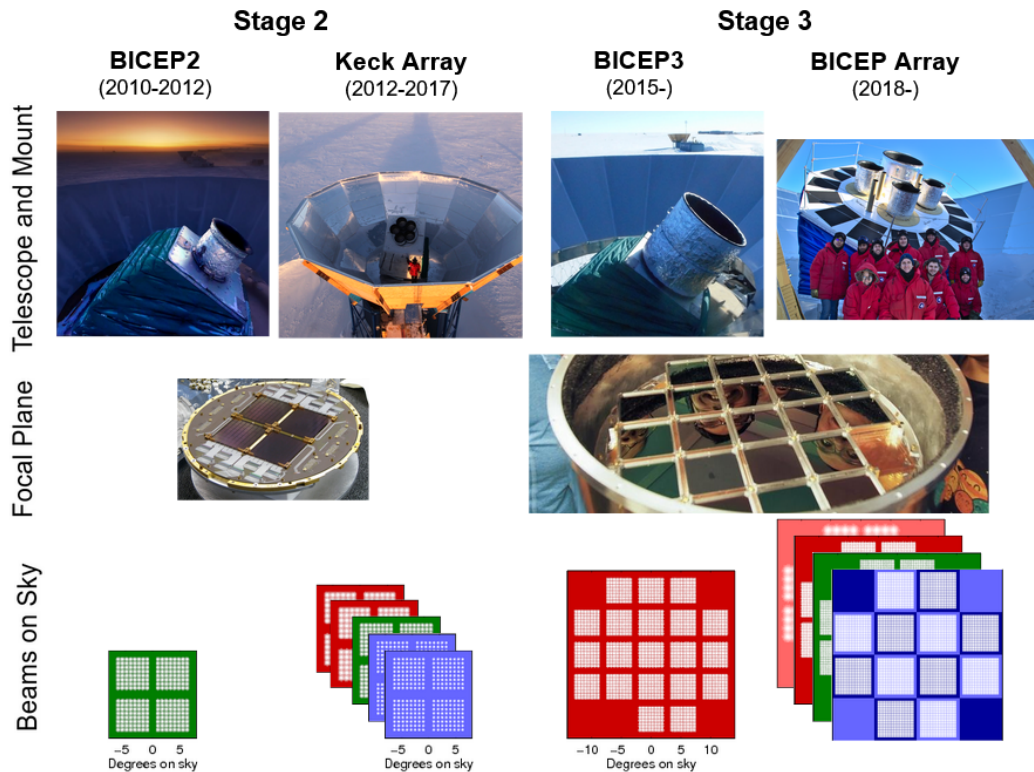


Figure 2.4: BICEP/Keck Array series of instruments use antenna-coupled TES bolometers in all of its generations. BICEP2 has 500 detectors at 150 GHz, while BICEP3 has 2400 detectors at 95 GHz. In the future, the BICEP ARRAY is expected to have over 10,000 detectors ranging from 30 to 270 GHz.

Plateau and at an elevation of about 2.8km from sea level.

BICEP/Keck Array series are hosted in two building in the Dark Sector of the South Pole station, which are kept free of wireless communication. Martin A. Pomerantz Observatory (MAPO) contains the DASI telescope mount which also hosted Keck Array . The DASI mount was replaced during the 2019-2020 season to hosts the new Bicep Array experiment and telescope mount. The Dark Sector Lab (DSL) hosted BICEP1 , BICEP2 , and BICEP3 experiments.

### 2.3 Observation Strategy

The BICEP/Keck Array experiments have all used similar observation strategies, observing the same small patch of sky, which covers an area covering about %1 of the sky. This region of sky was chosen for its low expected polarized foreground emission as shown in Figure 2.5, and is part of the region called the Southern Hole

[44].

The observations were centered at RA of  $0^{\text{hr}}$  and Dec of  $-57.5^{\circ}$  and measure an effective sky area of about  $400\text{deg}^2$  for BICEP2 and *Keck* Array . Because of its larger field of view BICEP3 and BICEP Array shifted the declination center of the patch to Dec  $-55^{\circ}$  and observe a sky area of about  $600\text{deg}^2$ .

The BICEP/*Keck* Array telescopes have a scanning strategy where each instrument observe the sky at a constant elevation in azimuth with a scan speed of  $2.8^{\circ}\text{s}^{-1}$ . The scan spans a total of  $64.4^{\circ}$  in azimuth, and after approximately fifty minutes of continuous observation, the telescope performs a quick nod in elevation, called an elnod, at a fixed azimuth. The nodding in elevation provides a calibration signal that is used to calibrate instrument response over time.

Overall, this scanning strategy has proven to be very effective for the BICEP/*Keck* Array instruments, allowing them to make high signal to noise measurements of the cosmic microwave background radiation.

- **Halfscan** Single full left or right sweep in one direction at a constant elevation covering  $64.6^{\circ}$  in azimuth. The scan maintains a constant speed of  $2.8^{\circ}\text{s}^{-1}$  with a smooth turnaround at the end of its scan.
- **Scanset**: A typical scanset consists of about 50 halfscans in both directions and lasts for approximately 50 minutes. A scanset is centered around a fixed azimuth and is receded and superseded by an elnod. During a scanset, the telescope scans back and forth over a specific ground-fixed region, allowing the sky to drift by 12.5 degrees over the course of the scanset. Each scanset is referred to as a tag.
- **Elnod**: Elnod refers to an "elevation nod", a  $1.28^{\circ}$  up and down scan around a nominal elevation angle at a fixed azimuth. This scanning pattern is performed before and after a scanset, with each repetition being a mirror image of the other (e.g. up-down-up followed by a down-up-down).
- **Partial Load Curve (PLC)** During a Partial Load Curve measurement, TES bias is ramped to move the detector along the normal-superconducting transition. Normal resistance and saturation power of TES can be extracted by measuring the current and voltage across the detector during this process.

- **Phase:** Individual scansets are grouped into phases consisting of 6-10 scansets each. During this process, adjustments are made to the elevation and azimuth to account for the rotation of the sky.
- **Schedule:** The largest observation unit of the BICEP/Keck Array scanning strategy is known as a schedule, which consists of a single cycle of phases sharing a common deck angle. A schedule begins with a sub-Kelvin fridge cycle and includes a telescope deck rotation, allowing the pixels to observe at various polarization angles. A collection of phases makes up a schedule, and the observations within that schedule share the same boresight angle, also known as the deck angle. For a better understanding, please refer to schematic description presented in Figure 2.6 or Table 2.2.

Observation schedules for *Keck* Array begin with a 6-hour cycle of the sub-Kelvin fridge, followed by two CMB observing phases consisting of 10 scansets each (Phase A and B). On the second day galactic plane (Phase D) is observed for 7 scansets. to characterize the instrument. This is followed by two more CMB observing phases of 10 scansets each (Phase E and F).

*Keck* Array is limited by the hold time of its sub-Kelvin fridge, but BICEP3 has a longer hold time allowing for an additional day of on the cycle. The third day is filled with a CMB observing phase consisting of 6 scansets (Phase G) followed by two observing phases of 10 scansets (Phase H and I).

Even though BICEP Array is capable of a three-day observing period, it is limited by *Keck* Array receivers on a two-day observation schedule since they share the same mount.

The phases in a typical three day BICEP3 CMB schedule are listed in Table 2.2. The projection for a typical three day schedule on the sky is shown in Figure 2.6.

*Keck* Array observes the sky using eight deck angles, ranging from  $23^\circ$  to  $338^\circ$ , evenly spaced at  $45^\circ$  increments.

## 2.4 Detectors

BICEP/Keck Array uses beam-defining slot antenna arrays coupled with Transition Edge Sensor (TES) bolometers, adapted from the design used in BICEP2 . These antennas are printed photo lithographically onto silicon wafers, fabricated in the

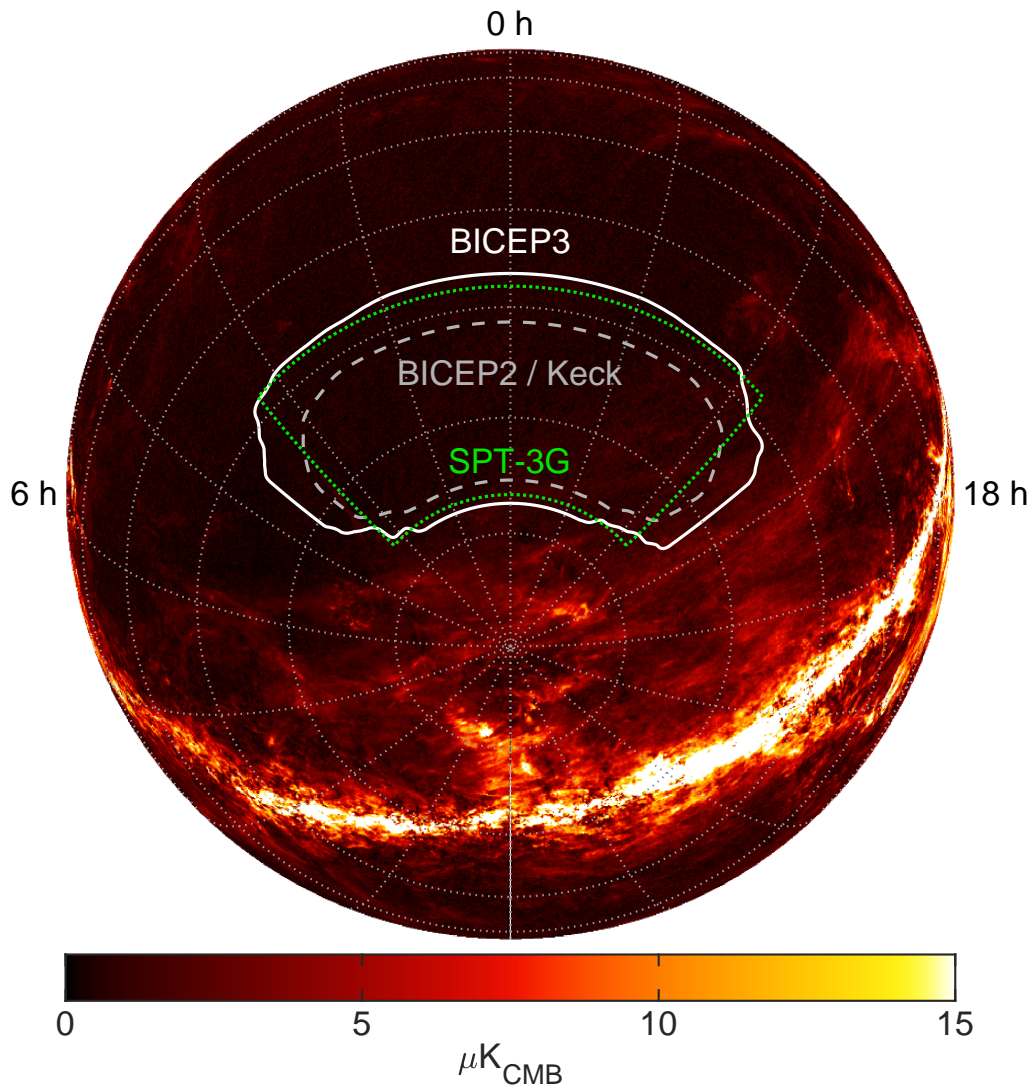


Figure 2.5: CMB observing field of the BICEP3 telescope (solid white) on the southern celestial sphere. The BICEP2/Keck field is also shown as a dashed white area, while the SPT-3G  $1500 \text{ deg}^2$  survey is represented by a dotted green area. The background image displays the polarized intensity of the Planck component-separated dust map (SMICA), which has been rescaled assuming a gray-body spectrum. Figure from [6].

Table 2.2: BICEP3 Phases in a Typical Schedule

Phase	LST	Field
A	Day 0 23:00	Cryo cycle
B	Day 1 05:30	CMB (high el)
C	Day 1 14:30	CMB (low el)
D	Day 1 23:00	Galactic
E	Day 2 05:30	CMB (low el)
F	Day 2 14:30	CMB (high el)
G	Day 2 23:00	CMB (variable el)
H	Day 3 05:30	CMB (high / low el)
I	Day 3 14:30	CMB (low / high el)

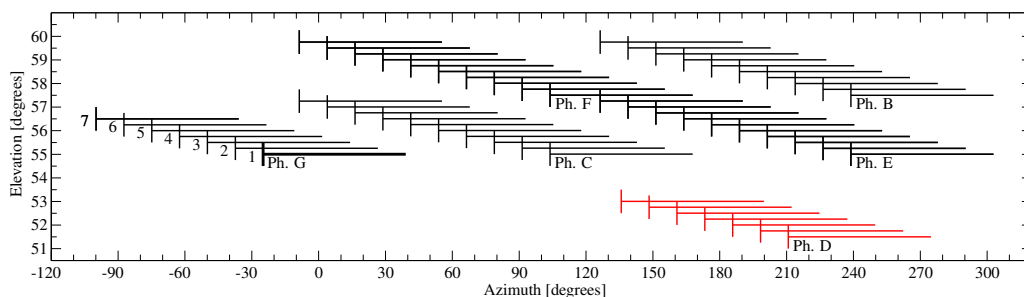


Figure 2.6: The observation pattern of a typical three-day schedule. The scansets of Phase G are numbered, with the first scanset at the lowest elevation. The Galactic D phase is shown at the lowest of four elevation steps, while the CMB G phase is shown at the lowest of three elevation steps. Figure from [10].

Micro devices Laboratory at JPL. Unlike the feedhorn design used in previous generation of CMB experiments such as BICEP1, the slot antenna array detectors could be mass produced and scaled to large numbers due to closer packing.

Each Keck receiver has 256 orthogonal pairs of detectors at 150 GHz and 220 GHz, and 144 pairs of detectors at 95 GHz. Each pair of detectors is called a pixel. These detectors are arranged into  $8 \times 8$  pixels in each tile at 150 GHz and 220 GHz, and  $6 \times 6$  pixels in each tile at 95 GHz.

The electrical signals from the antenna array pass through a integrated three-pole LC resonator band defining filter before reaching the TES islands with a fractional bandwidth of 25%. The band defining filters are integrated onto the detector tile and fabricated concurrently with the antennas. Each tile contain four TES that do not have a microstrip filter and are referred to as "dark TES" since they are not

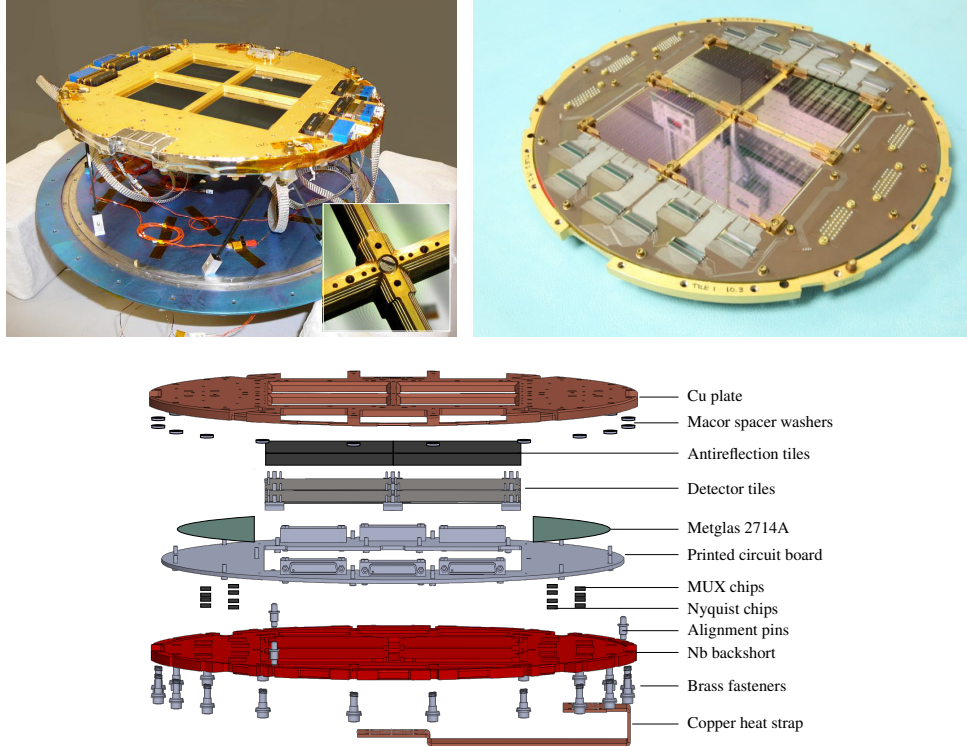


Figure 2.7: The assembled focal plane on the carbon fiber truss structure and 350 mK Nb plate. The focal plane is made of four anti-reflection tiles. The assembly is shielded by an aluminized Mylar radio frequency shield, with a square opening above the detector tiles. Figure from [10].

electrically connected to the antenna array.

When a photon hits a thermally isolated mass, it increases its temperature. The incoming power can be estimated by measuring the change in the temperature. This is the main principle of a bolometer. The mass has a weak thermal link to a thermal bath, described by the thermal conductance  $G$ . According to the conservation of energy:

$$C \frac{dT}{dt} = -P_{\text{bath}} + P_J + P, \quad (2.1)$$

for a mass of heat capacity of  $C$ , at temperature  $T$ , with  $P_{\text{bath}}$  power flowing to the heat bath, and  $P_J$  the Joule power dissipation. This is called the thermal differential equation [60].

The time constant of power dissipation, denoted by  $\tau$ , of a bolometer is given by  $\tau = C/G$ . The sensitivity of the detectors would be lower if  $\tau$  is too small, since

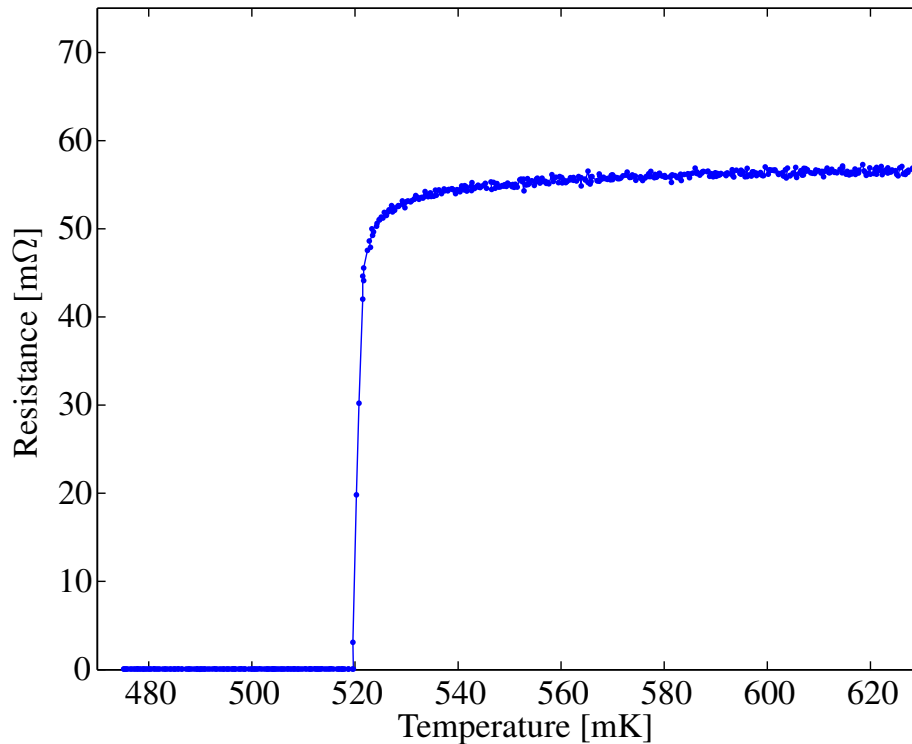


Figure 2.8: Resistance vs. Temperature characteristic for a TES detector. Within 5 mK, the resistance reaches 90% of the normal state resistance. Figure from [10].

optical power would be quickly dissipated with the thermal bath. The detectors will go off transition if  $\tau$  is too large since the heat load on the island will be too large due to optical loading.

A voltage bias is applied on the TES to keep the temperature around the superconducting transition for titanium. A feedback loop keeps the detectors on the transition.

Detectors have aluminium TES and titanium TES, connected in series. The critical temperature is  $T_c \approx 1.2$  K for aluminium and  $T_c \approx 0.5$  K for titanium. In higher optical loading settings, such as lab testing and calibration process, titanium TES saturates to normal conducting state and because of its higher critical temperature, the detectors use aluminium TES. In lower optical loading settings, such as CMB observation, titanium is used to provide sensitive measurements due to its lower noise.

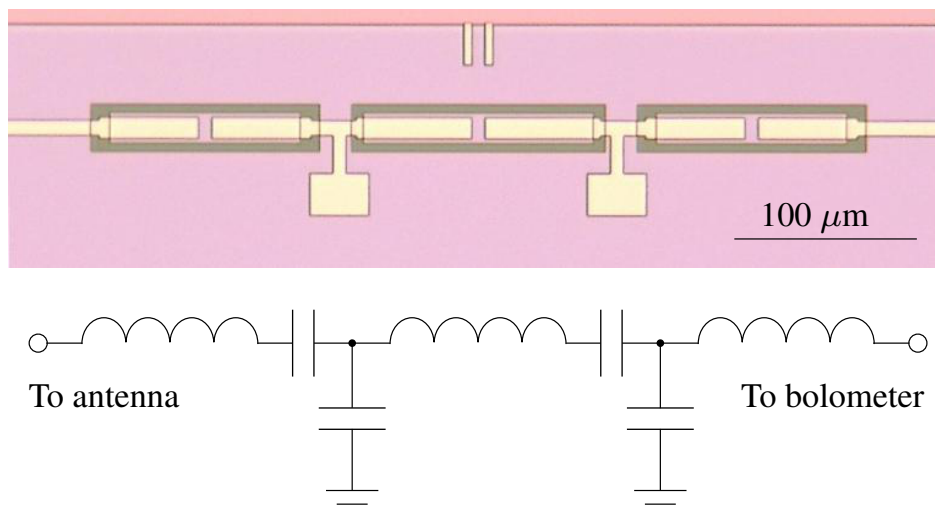


Figure 2.9: The 150 GHz band-defining filter, which is made of three inductors arranged in series, and interconnected through a T-network of capacitors via coupling. Figure from [10].

## 2.5 Readout

Superconducting quantum interface devices (SQUIDs) are used to amplify weak signals generated by the transition edge sensor (TES) bolometers and multiplex them in time domain. Each Keck focal plane hosts an order of few hundred detector pairs, therefore it is not feasible both from an engineering and a heat load perspective, to have a separate wiring for each detector. To achieve this goal SQUIDS are operated in time-domain multiplexing readout. This allows the data to be read by fewer cables, minimizing the head load on the focal plane. BICEP2, Keck, and BICEP3 use "MUX07a", "MUX09s", and "MUX11d" models of multiplexing system developed by NIST respectively.

There are three stages of SQUIDS used for BICEP2 / Keck. TES and feedback circuits are inductively coupled to a first-stage SQUID (SQ1). Each of these SQ1 has an assigned row and column for all detectors, consisting of 33 row and 16 columns. The 33 rows are arranged such that 32 rows are coupled inductively to detectors, and one dark row where the squids are not connected to any detectors. Dark row responds to the changes in magnetic field in the cryostat and reflects how the signal is affected. Each SQ1 in the same row share the same bias to have less cryogenic wiring. Each column, consisting of 33 rows are coupled to second-stage SQUID (SQ2) after being fed into a summing coil. Each SQ2 has an assigned

column. The final stage of SQUID is the SQUID series array (SSA). Each SSA has an assigned column. The multiplexing occurs in earlier stages of SQUIDS, therefore SSAs don't need to be in the focal plane. Instead they are located in the cryostat in the camera insert at 4K [64]. The BICEP3 does not require SQ2 before SSA and instead uses row-selects, which are a superconducting-to-normal flux activated switch.

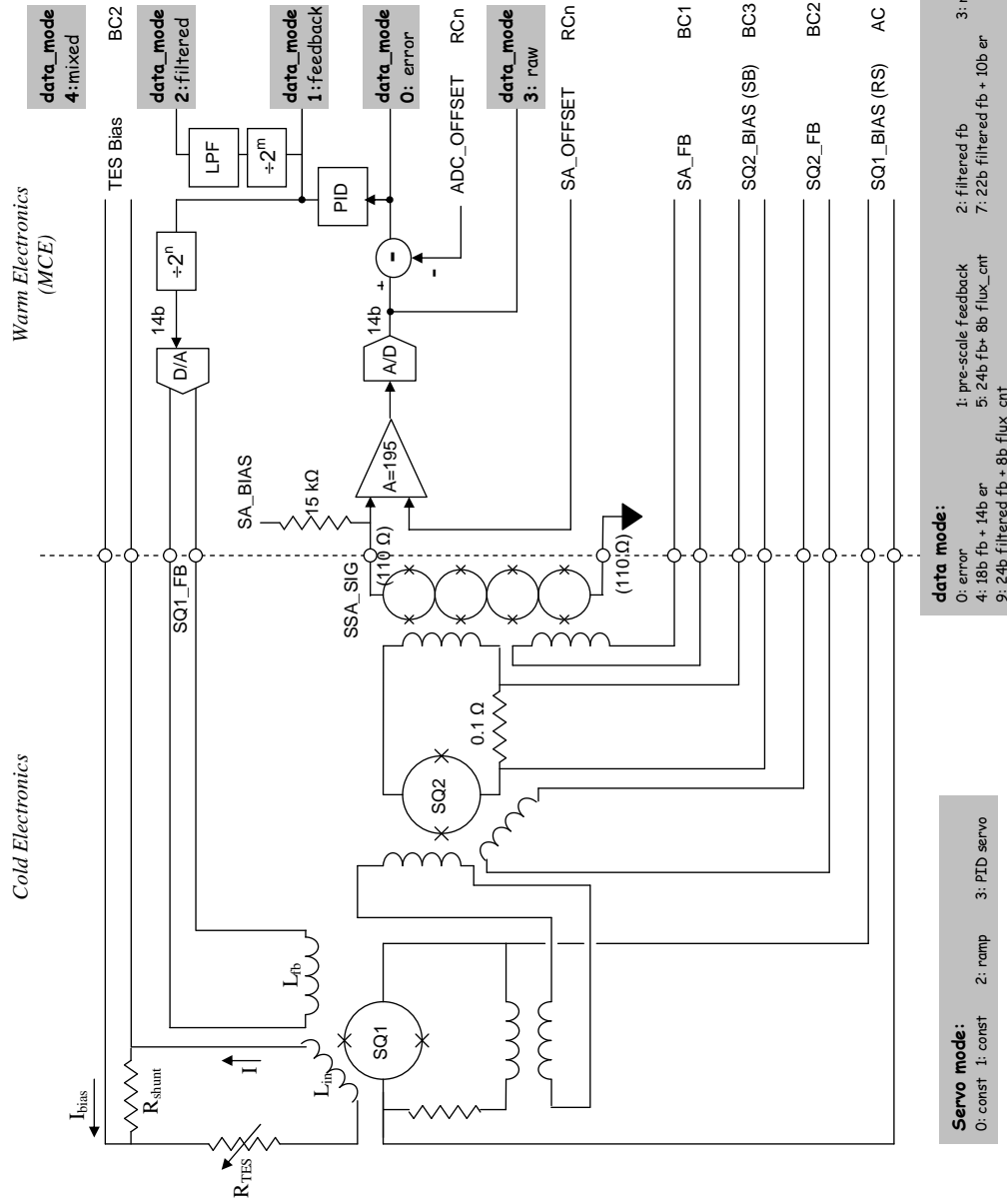


Figure 2.10: UBC readout used in the BICEP/Keck Array series of instruments. Figure from UBC.

*Chapter 3***KECK ARRAY HIGH FREQUENCY AND BICEP3  
INSTRUMENT CHARACTERIZATION**

A detection of primordial B-modes will improve our understanding of the early universe. In order to achieve precise and high signal to noise measurements of the polarization of the CMB, it is important to correctly characterize the instruments being used, including calibration measurements both in the laboratory and at the deployment site.

BICEP/Keck Array series of instruments have a number of such measurements that were carried out. The emphasis on assessing detector yield, efficiency, spectral response, and noise performance of the instruments, as well as identifying factors that could possibly introduce systematic errors. This chapter provides an overview of some of the key calibration measurements that were performed.

B-modes are faint and obscured by polarized foregrounds. CMB, polarized dust, and polarized synchrotron emission have distinct spectral profiles that allow us to separate the foregrounds from any primordial B-mode signal. To accurately account for this separation measurements are taken at multiple frequencies, each with a different spectral response, to help disentangle the different contributions to the polarization signal. This means that a precise spectral response of the instruments are needed to be measurement.

### 3.1 Optical Efficiency

To obtain the characteristics of a Transition Edge Sensor detector, load curves are typically taken after the SQUID tuning stage. This involves running the TES bias current  $I_{\text{Bias}}$  through each TES detector and its shunt resistor, while varying the TES bias current and measuring the feedback current  $I_{\text{TES}}$  in each TES.

An example load curve is show on Figure 3.1 where blue curves were taken using a 300 K source and green curves taken using liquid nitrogen at 77 K. The measurements are done in DAC units and calibrated to Voltage and Ampere units during the analysis.

The normal titanium resistance, also referred as  $R_N$  of a TES can be determined by measuring the slope of the normal portion of its I-V curve. Typical values for the normal resistance of a TES made of titanium are found to be between 50 and 150m $\Omega$ .

To avoid excessive heating of the focal plane due to the high TES bias, load curves are taken in chunks grouped in Multiplexed Readout Control Electronics (MCE). The load curve procedure is important for diagnosing whether the detectors can be biased on titanium and aluminum superconducting transitions.

The optical efficiency of a receiver is a measure of the fraction of incident light that is absorbed by the detectors after passing through the receiver window. For a beam filling black-body source, the power absorbed by a detector is given by:

$$P_{\text{opt}} = \frac{\eta}{2} \int d\Omega d\nu B(\nu, T) S(\nu), \quad (3.1)$$

where  $S(\nu)$  is the spectral response and  $B(\nu, T)$  is the Planck blackbody spectrum at temperature  $T$ . In the Rayleigh-Jeans limit on a blackbody source ( $h\nu \ll k_B T$ ) this expression simplifies to:

$$\begin{aligned} P_{\text{opt}} &= k_B T \int d\nu S(\nu) \\ &= k_B T \eta \Delta\nu. \end{aligned} \quad (3.2)$$

A blackened coned with microwave absorbing is placed on top of the window as a beam filling blackbody source. The measurements at South Pole are taken at liquid

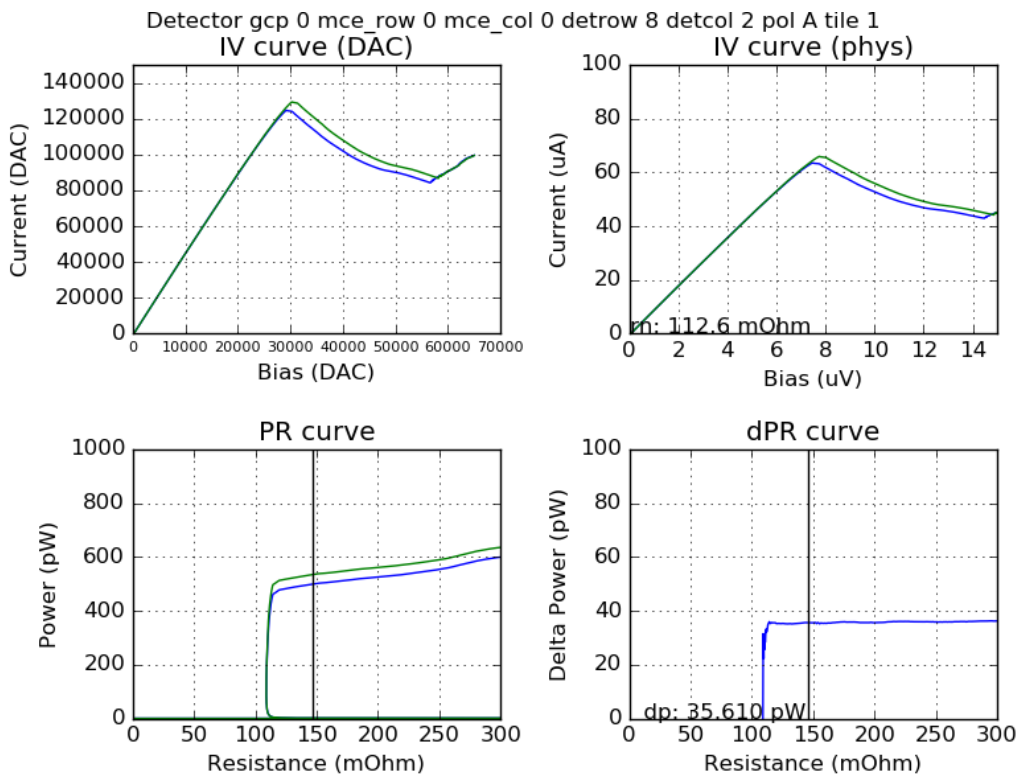


Figure 3.1: Load curves were taken to measure the optical efficiency of Al, with blue curves taken using a 300 K source and green curves taken using liquid nitrogen at 77 K.

nitrogen temperature 74 K, and ambient temperature 266 K. The optical efficiency of this measurement is estimated by:

$$\eta = -\frac{P_1 - P_2}{k_B(T_1 - T_2)\Delta\nu}, \quad (3.3)$$

where  $P_1$  and  $P_2$  are the Joule power at temperatures  $T_1$  and  $T_2$  for a detector of bandwidth  $\Delta\nu$ . The difference in power  $\Delta P \equiv P_2 - P_1$  is directly measured from PR curves as shown in Figure 3.1, whereas the difference in temperature is a controlled quantity  $\Delta T \equiv T_2 - T_1 = 266 \text{ K} - 74 \text{ K} = 192 \text{ K}$ .

Detector wafers typically include a few dark TESs that are not connected to the antenna as discussed in section 2.4. These TESs can be used to measure the dark response in the optical efficiency measurement, denoted as  $dP_{\text{dark}}/dT$ . By subtracting the dark response from the measured  $dP/dT$  of the light pixels, an

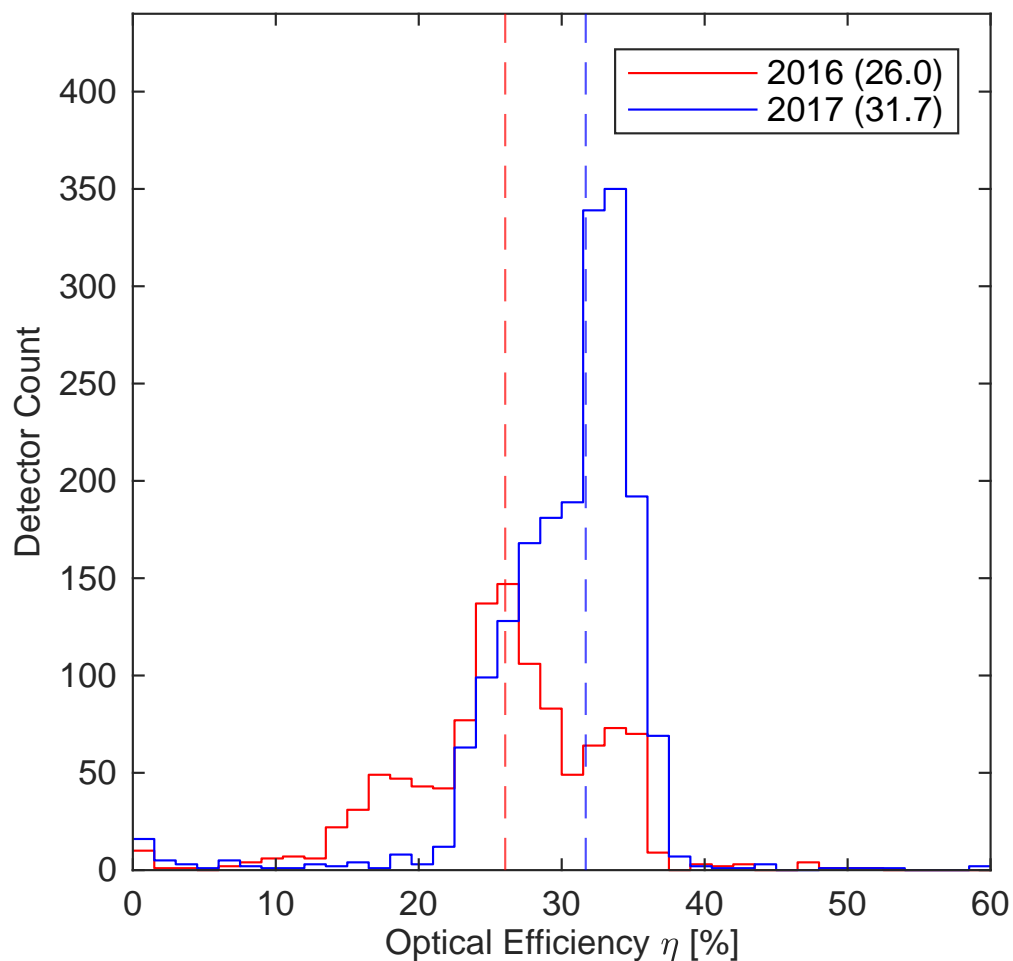


Figure 3.2: Optical Efficiency for the BICEP3 2016 and 2017 seasons. Figure from [6].

estimation of the in-band response can be obtained:

$$\frac{dP_{\text{light}}}{dT} = \frac{dP}{dT} - \frac{dP_{\text{dark}}}{dT}. \quad (3.4)$$

BICEP3 has optical efficiency 0.08 pW/K and 0.11 pW/K, corresponding to an efficiency of 23% and 29% in 2016 and 2017 seasons respectively. Between the two seasons 300 K thermal filters and four modules were replaced attributing to the higher optical efficiency between the two seasons.

### 3.2 Spectral Response

The sensitivity  $\sigma(r)$  on the tensor to scalar ratio  $r$  depends on how well foreground components are separated. In the absence of any foregrounds or lensed B-modes, BK18 has a raw sensitivity of  $\sigma(r) = 0.002$ . The sensitivity is  $\sigma(r) = 0.007$  when there are lensed B-modes but no foreground components. With foregrounds and lensed B-modes, the reported sensitivity is  $\sigma(r) = 0.009$  [18].

Fortunately CMB, dust and synchrotron have distinct spectral response, which allows the overall signal to be separated into its components. Observations at different frequencies are required to measure the foregrounds, therefore a precise characterization of the spectral response is critical to separate astrophysical foregrounds accurately.

Other probable systemic contamination in our polarization data is also revealed by bandpass measurements. A mismatch in relative gain will result in a temperature to polarization leakage.

Molecules emit when there is a transition of the quantized orbital energy levels. Carbon monoxide has its first three rotational molecular lines  $J = 1 \rightarrow 0$ ,  $J = 2 \rightarrow 1$ , and  $J = 3 \rightarrow 2$  at 115, 230, and 345 GHz respectively [21]. CO emission is at most a few percent polarized. Temperature leaks into polarization depending on the differential response and spectral mismatch of the orthogonal detectors. CO emission does not follow a black body spectrum whereas deprojection relies on an accurate temperature map. Leakage could happen since molecular emission is not deprojected. A good measurement of the spectra is key to estimate the bias on  $r$  due to this molecular line T->P leakage. The expected leakage is shown to be small,  $r < 10^{-4}$ , however it will be more relevant in more sensitive future CMB experiments.

The antennas, band-defining and low-pass edge filters determines the detector spectral response. The bands are chosen to allow observation at the South Pole, avoiding oxygen and water spectral lines at 60 GHz, 118 GHz and 183 GHz. Bands defining microstrip filters are designed to have a bandwidth of about 25 percent within these oxygen and water lines. BICEP / Keck bands are using the high transmission windows from 30 to 300 GHz. Above this frequency the transmission decays very rapidly at making it less feasible for a ground based observation at the South Pole.

The spectra is measured by a Martin-Puplett interferometer, custom built to be

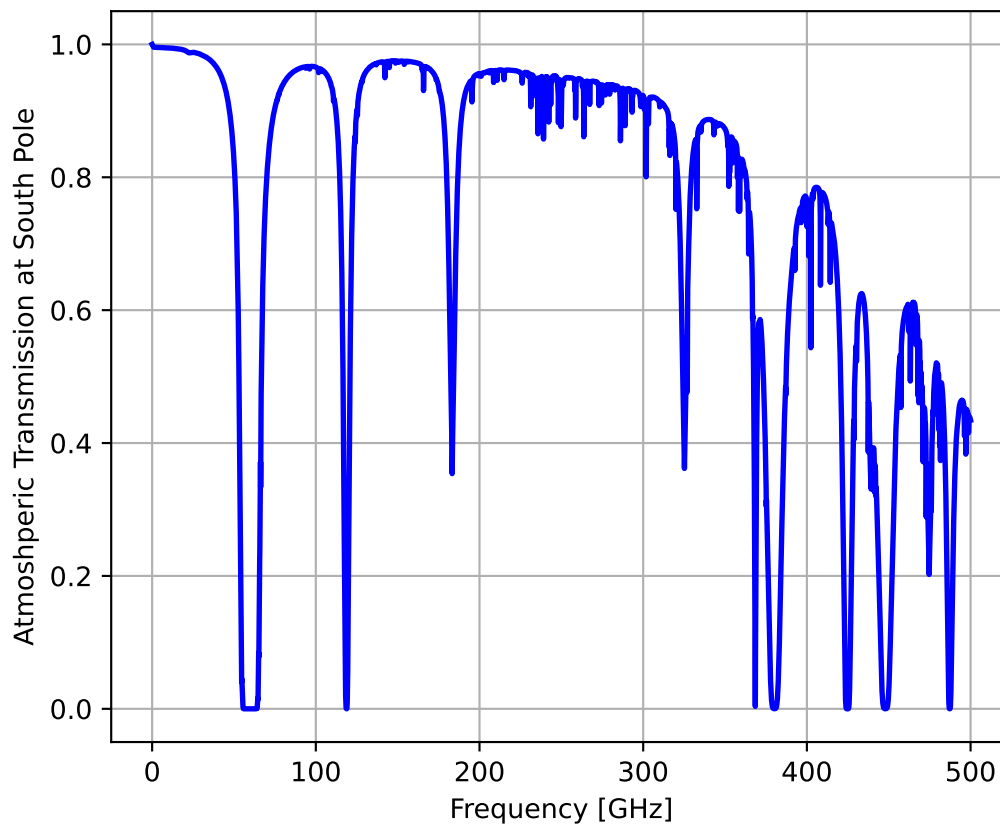


Figure 3.3: Atmospheric Transmission at the South Pole as a function of observation frequency. The BICEP/Keck Array bands are designed to avoid the oxygen absorption band around 60 GHz, and the spectral lines of oxygen at 118.8 GHz.

mounted on top of the BICEP / Keck cryostats [71]. Liquid nitrogen is contrasted with ambient temperatures as a source. One mirror is located on a translation stage, while the other one is kept at a fixed from the beam splitter. There is constructive interference for all wavelengths when the mirrors are at a same distance from the beam splitter. When the mirror on the translation stage moves a distance  $x$ , there is constructive interference for wavelengths of  $2nx$  and destructive interference for wavelengths of  $(2n - 1)x$  [89].

The interferometer is placed on an automated translation stage, scanning over multiple pointings on the window to cover all the detectors in the focal plane. The entire setup is taken at various orientations to cover all detector polarizations.

The raw detector response is used to record interferogram data with the moving mirror setup in the interferometer. The encoder keeps track of the mirror position. The first step of identifying white light fringes (WLF) is to choose a point close to the true value by inspection. In the second step the algorithm measures symmetry between the left and the right for each point around the chosen WLF in the initial step. The point with the greatest symmetry measure is chosen to be the WLF.

Changes in ambient temperature cause an issue with the WLF algorithm, therefore a polynomial filtering of third order is applied on the raw data. A Blackman-Harris window is used smooth the interferograms, and reduce spectral ringing. However the smoothing comes with a small penalty in spectral resolution.

Individual spectral detectors are coadded to form the spectral response shown for Keck bands in Figure 3.5 and BICEP3 in Figure 3.7.

For a spectral response  $S(\nu)$  the band center of the detector is given by:

$$\langle \nu \rangle = \int \nu S(\nu) d\nu, \quad (3.5)$$

and the bandwidth is given by:

$$\Delta\nu = \frac{\left( \int S(\nu) d\nu \right)^2}{\int S^2(\nu) d\nu}. \quad (3.6)$$

In the 2016 season the spectral response of BICEP3 at South Pole had two types of abnormal features that were common among detectors for each given module. The two observed features are a suppressed at the outer edge creating a "spike" profile or suppressed at the center creating a "dip" profile. The frequency of the spectral features were consistent among the detectors. As a result the empirically derived estimator that characterizes the spikes / dips yield the best discriminating power when it is defined as:

$$e = \text{mean}_{\nu \in I_1 \cup I_3} \left[ B'(\nu) \right] - \text{mean}_{\nu \in I_2} \left[ B'(\nu) \right], \quad (3.7)$$

where  $B'(\nu) = G(\nu; \sigma) * B(\nu)$  is the spectral response convolved with a Gaussian smoothing kernel  $G(\nu; \sigma)$  of  $\sigma = 1$  GHz for a peak normalized spectral response  $B(\nu)$ . Mean values are calculated in the frequency ranges:

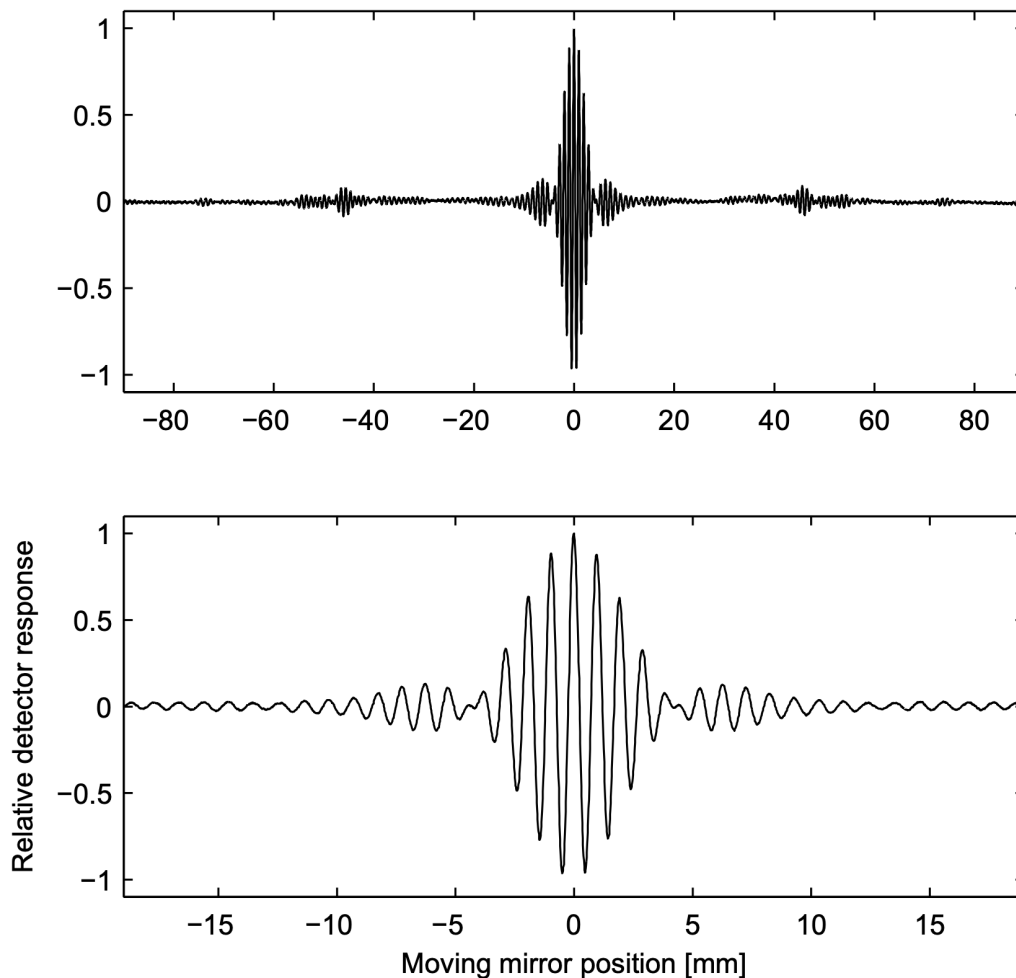


Figure 3.4: A high signal-to-noise raw detector interferogram response at 150 GHz to a beam filling source. The raw data has been filtered of thermal drifts in the ambient temperature by a polynomial filter of third order. The position is tracked by an encoder and shown in the x-axis. Figure from [89].

$$I_1 = \{\nu | 84 \text{ GHz} < \nu < 90 \text{ GHz}\} \quad (3.8)$$

$$I_2 = \{\nu | 90 \text{ GHz} < \nu < 98 \text{ GHz}\} \quad (3.9)$$

$$I_3 = \{\nu | 98 \text{ GHz} < \nu < 106 \text{ GHz}\}. \quad (3.10)$$

The spike/dip estimator  $e$  shows spike behavior when  $e < 0$  and dip behavior when  $e > 0$ . The estimator is bounded by  $-1$  and  $1$ , and reflects more ideal response when the estimator is closer to  $0$ .

Out of band spectral response is filtered with metal mesh low-pass edge filters made

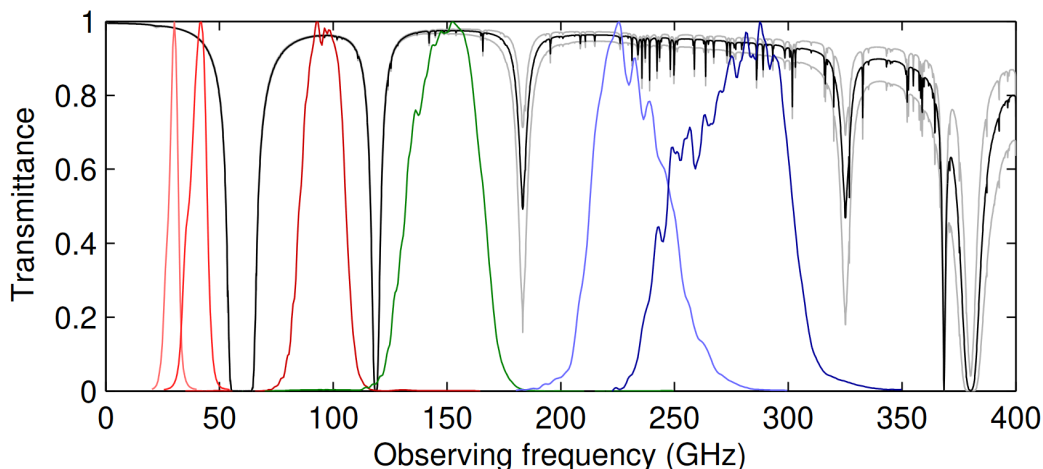


Figure 3.5: Band-pass response of BICEP/Keck Array series of instruments. The median atmospheric transmission during the observing season is shown as black. Figure from [76].

from multiple polypropylene substrate layers (Ade et al 2006). A resonant filter is formed by hot-pressed each copper grid layer together. The low-pass filter has cutoff at  $4 \text{ cm}^{-1}$ .

In the 2016 season each detector module were mounted with their independent  $76 \text{ mm} \times 76 \text{ mm}$  mesh filters. However after observing the spike/dip behavior in the spectra it was later discovered that the layers of the mesh filters were delaminated. The likely cause of the delamination is insufficient temperature during fabrication as well as the extra stress due to small modular structure on the detector modules.

In the 2017 seasons the mesh filters were replaced. The new filters were fabricated at a higher temperature. The new design is  $23 \text{ cm} \times 15 \text{ cm}$  such that each filter covers 5 modules to reduce the stress on the filters. After the mesh filters were replaced no sign of filter delamination was detected in subsequent FTS measurements in the following season. The spike/dip estimator  $e$  obtained from FTS measurement in the 2017 measurement has a narrow bandwidth centered at 0 indicating no evidence of delamination [6] as seen in Figure 3.7.

### 3.3 G Measurement

During the detector screening and characterization process, thermal conductance  $G_0$ , thermal conductance exponent  $\beta$  and critical temperature  $T_c$  are measured. In order to minimize optical loading, the measurements are taken on dark or covered

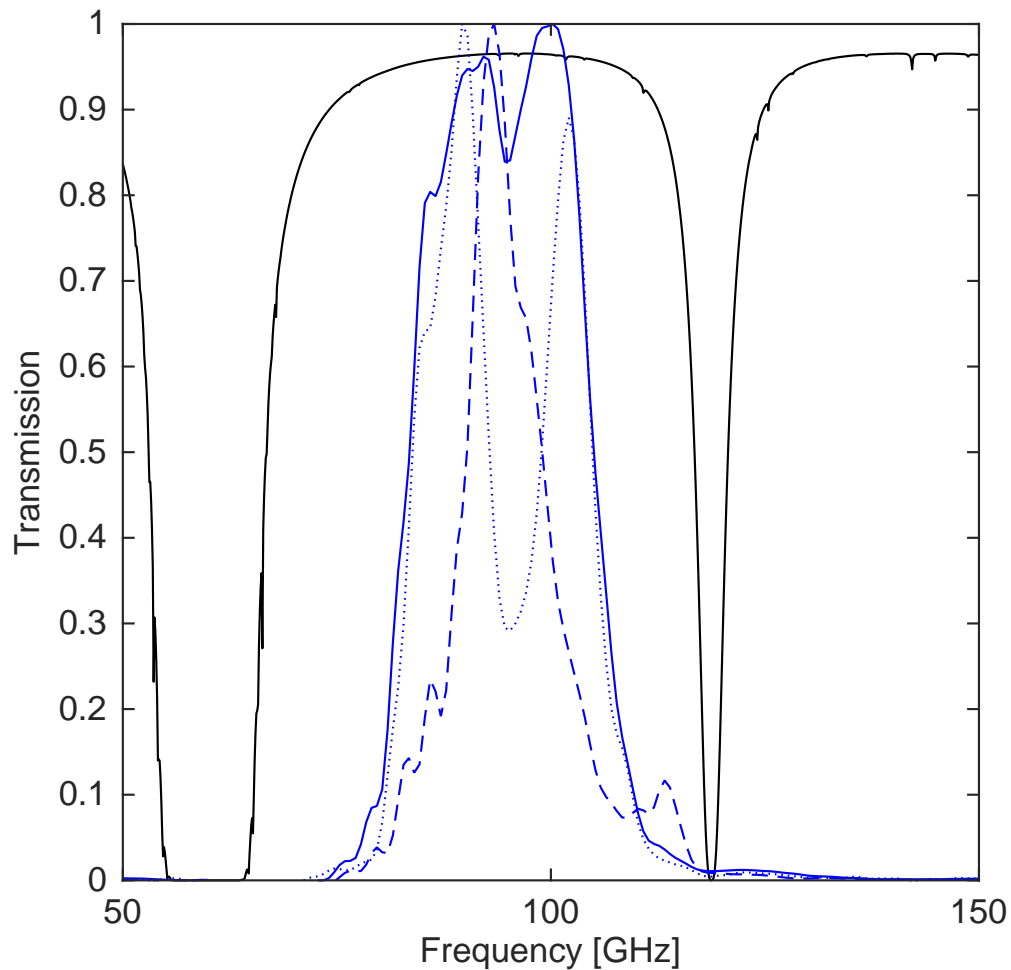


Figure 3.6: Coadded and peak-normalized BICEP3 Spectral Response (blue) plotted against South Pole atmospheric transmission (black). The band center is measured at  $96.1 \pm 1.5$  GHz and the bandwidth is  $26.8 \pm 1.3$  GHz. This corresponds to 27% fractional spectral bandwidth. Abnormal features observed in the 2016 season spectrum due to delaminated filters are also shown: a spectrum with a spike feature (dashed blue corresponding to  $e = -0.51$ ) and a spectrum with a dip feature (dotted blue corresponding to  $e = -0.20$ ). Figure taken from [6].

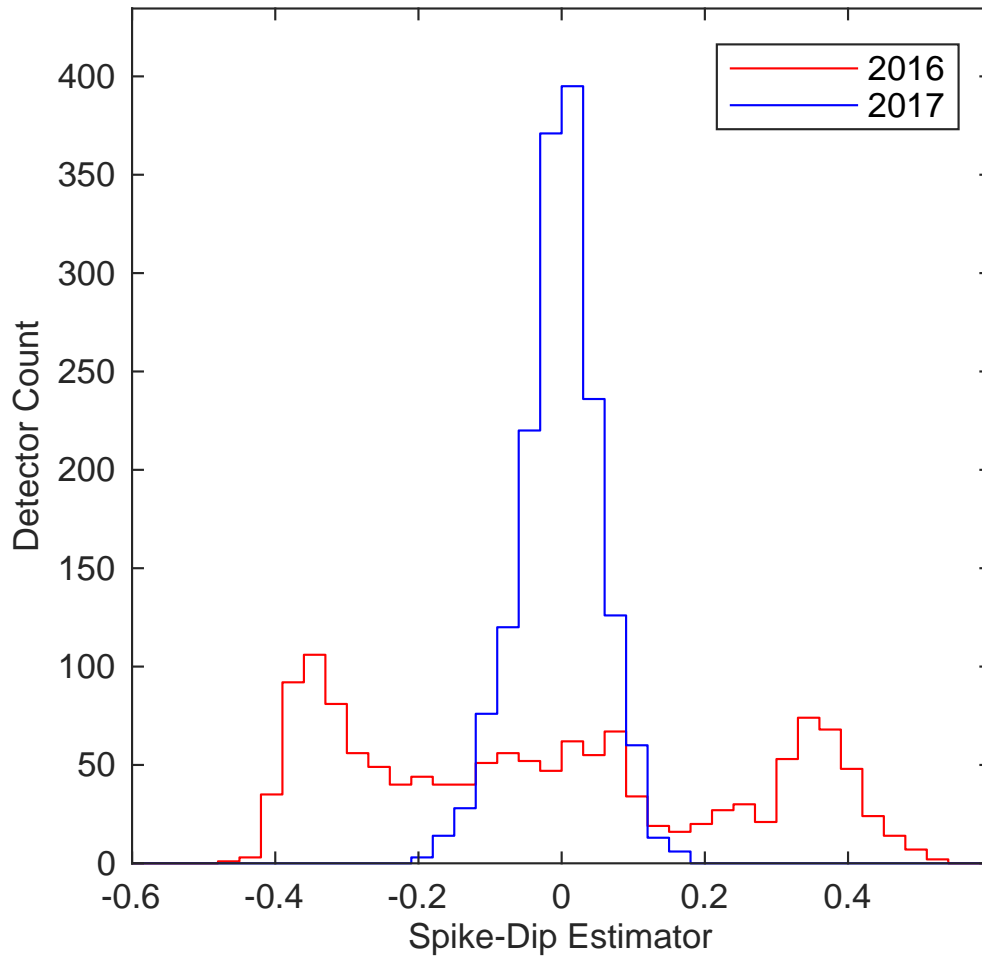


Figure 3.7: Spike-dip estimator  $e$  for the BICEP3 obtained from FTS measurements in the 2016 and 2017 seasons. In the 2016 season, delaminated mesh filters result in peaks of the spike/dip value at around  $-0.4$  and  $0.4$  reflecting the observed abnormal features. In the 2017 season, delaminated mesh filters were replaced and no signs of abnormal features persisted in the spectral measurements. Figure taken from [6].

cryostats, on dark detectors covered by microwave-blacken plate.

For Keck array, archival G measurement on all Keck receivers has been done in the 2016-17 deployment season at South Pole. The measurement is done by taking titanium load curves starting from a bias of 12000 ADU and going down incrementally in steps of 10 ADU until it reaches 1200 ADU, which is enough to observe titanium superconducting transition at Pole. This measurement is repeated for plane temperatures in the range of 270 mK to 425 mK. TCM heaters in a PID loop keep FPU temperature stable during the procedure.

The first step in the analysis is to measure Ti normal resistance by taking the ratio  $I_{tes}/I_{bias}$  in the normal region. This is usually done by fitting a linear line in the Ti normal region. To estimate saturated power correctly,  $I_{TES}$  is shifted so that Ti normal passes through the origin. Detector quality cuts are based on the measured value of Ti normal resistance. The TES resistance  $R$  and the power  $P$  values are estimated by:

$$R = R_{shunt} = \left( \frac{I_{bias}}{I_{TES}} - 1 \right), \quad (3.11)$$

and:

$$P = RI_{bias}^2. \quad (3.12)$$

The saturation power  $P_{sat}$  of the detectors are given by:

$$P_{sat} = \frac{G}{\beta + 1} \frac{T_c^{\beta+1} - T^{\beta+1}}{T_c^{\beta+1}}. \quad (3.13)$$

This is not a linear problem so a non-linear least square methods, with initial parameter guesses of  $G = 100$ ,  $T_c = 0.5$ , and  $\beta = 2$  are used. The results for a dark Keck pixel can be seen in Figure 3.8.

### 3.4 Beam Measurements

The angular response of each detector on the sky is called a beam measurement. Temperature to polarization leakage would result from a mismatch in beam characteristics between the orthogonal detector pairs.

The far-field distance criterion for beam mapping is  $2D^2/\lambda$  where  $D$  is the aperture size and  $\lambda$  is the wavelength. The aperture size is 26 cm for Keck, 52 cm for BICEP3.

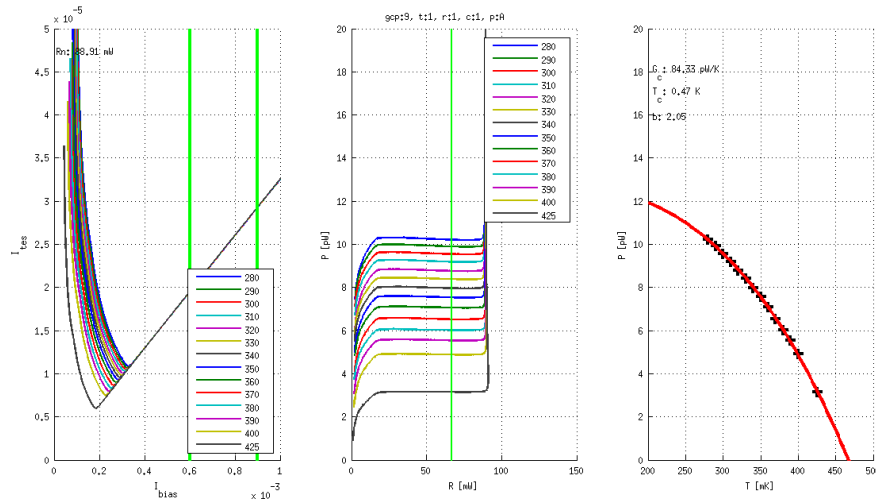


Figure 3.8: Sample G measurement taken at Pole. On the left are the  $I_{bias}$  vs  $I_{TES}$  figures. Each focal plane temperature is plotted in a different color. In the middle panel is the P-R curve. The right panel shows the best-fit model to estimate  $G$ .

The wavelengths are 3.3 mm at 90 GHz, 2.0 mm at 150 GHz, and 1.4 mm at 220 GHz. Therefore the far field distance are 46, 70, and 103 m for Keck Array at 95, 150, and 220 GHz, and 180 m for BICEP3 at 90 GHz.

### Near Field Beam Measurements

The near field beam map measurement is sensitive to the phase of the electric field in the focal plane [5]. Near field beam mapping is a standard procedure after a receiver is closed. This serves as a first check of the optical throughput of the system and used to identify any problems after the detectors are superconducting in a closeup procedure.

The near field beam mapper is a unpolarized chopped hot thermal source mounted on an XY translation stage. A hot porcelain block is used as the source, which is behind a 7mm aperture. Typically the source is chopped at 20 Hz by a Thorlabs Chopping wheel covered with HR-10 so that the chopping happens at two different temperatures. The entire setup is lifted above the cryostat on a mounting structure coated with Eccosorb HR10 to have less reflections and sits about 30 cm above the window.

Due to the high loading of this procedure the detectors are biased at aluminum transition. Chopping signal and the coordinates of the source are stored along with

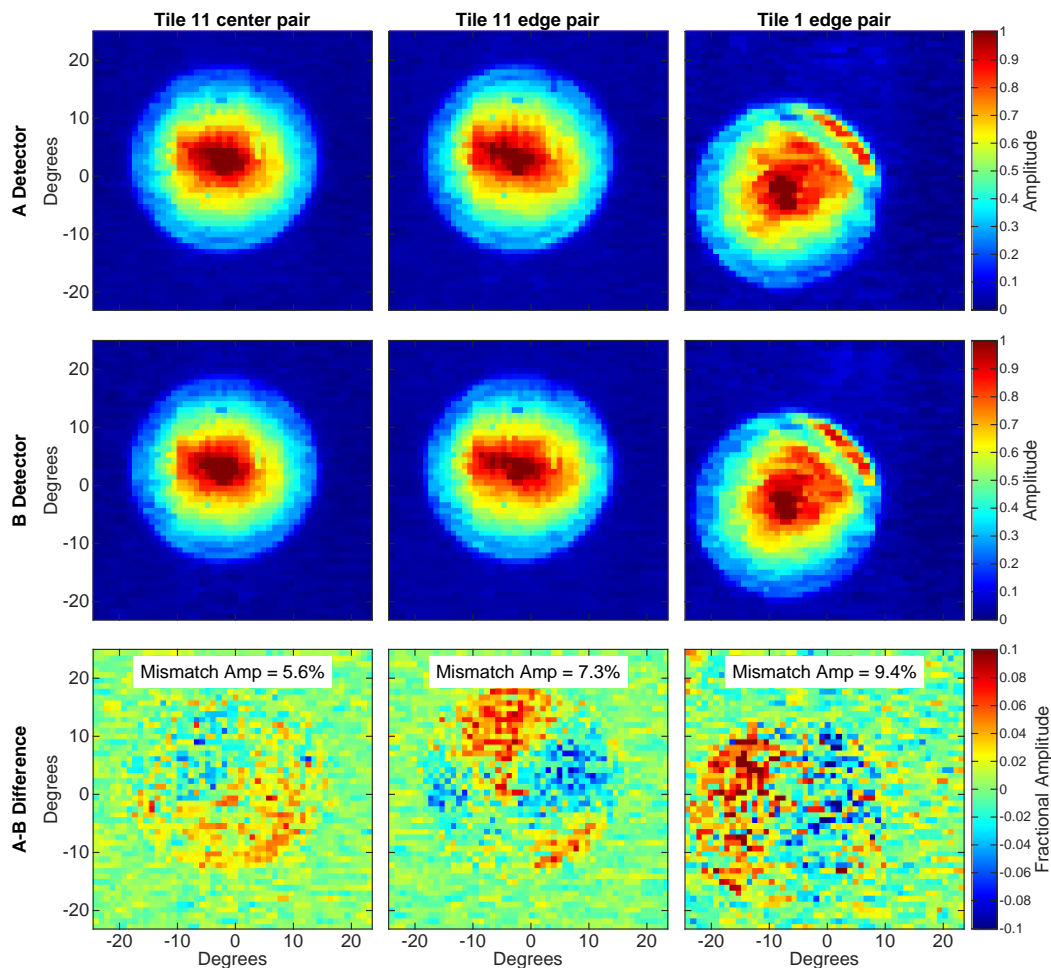


Figure 3.9: BICEP3 Near Field Beam Mapping results. Figure taken by [6].

the timestream data. In the analysis stage the timestream data is deconvolved with the chopper signal, and binned in two dimensions of the source encoding. The detectors closer to the edge of the focal plane exhibit a beam steer effect displacing the center of the beam to the sides.

### 3.5 Polarization Efficiency

NFBM is mounted on the aperture, source at 40% power and centered on the aperture, chopper at 25Hz. Found 11"-ID polarizing grid, mounted it on a 16"-OD, 10" ID annulus, which has been coated with eccosorb on the side facing the window. 36 marks (every 10 deg) have been made on the perimeter of the annulus, which we will rotate manually on the aperture, in correspondence with a tick on the base of the NFBM for reference. Position "zero" corresponds to the grid almost

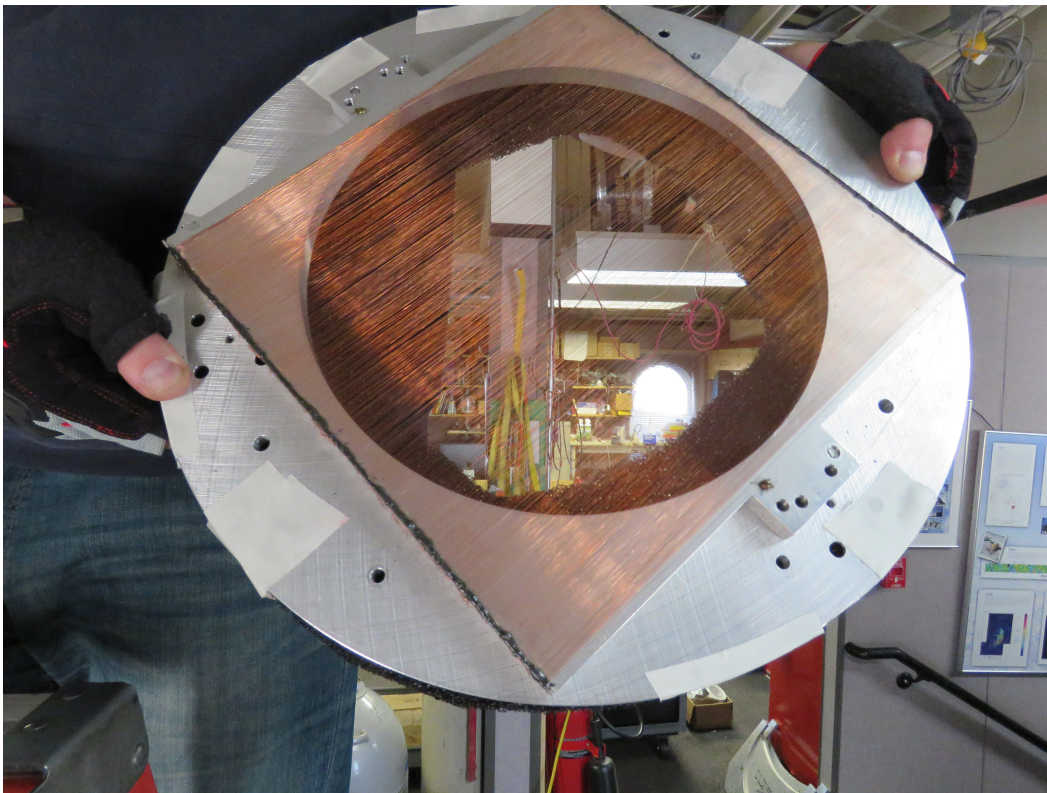


Figure 3.10: Polarization grid used to take the polarization efficiency measurement.

aligned perfectly with polarization A (almost no signal on polarization B). Will take 2 minutes of data per 10 degrees, hoping for at least 1 minute of good data within that Data are acquired using MAPODAQ.

Demodulated data points are shown for each detector pair (black, error bars estimated from the white-noise level at about 10Hz), as well as two models: 1)  $2-\theta + 4-\theta$  component (red) and 2)  $1-\theta + 2-\theta$  component (blue). The plots include the polarization angle with respect to the starting angle (close to aligned with polarization A), as well as the chi squares for the two models. These 3 numbers all to be taken with a grain of salt, given that the grid is probably causing lots of polarization leakage, which is evident from the modulation curves not going through actual zero. Additionally, we print out the modulation amplitudes "A", which correlate well with the  $dP/dT$  as measured by the optical efficiency analysis.

### 3.6 Partial Load Curves

A partial load curve at varying degrees of elevation can be taken to estimate the saturation power of each detector. Titanium normal resistance is determined by the

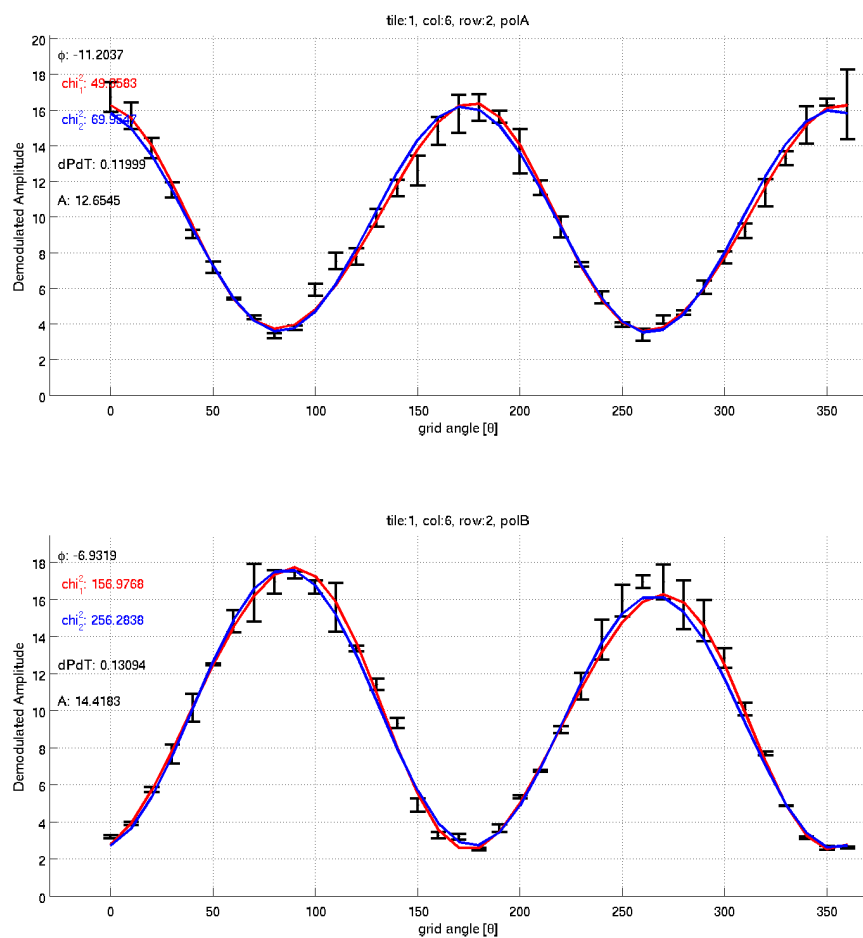


Figure 3.11: Polarization Efficiency measurements and the best fit models shown in blue and red.

slope of  $I_{\text{TES}}$  as a function of  $I_{\text{Bias}}$  in the titanium normal region. Resistance and Power curves are calculated by

$$R = R_{\text{shunt}} \left( \frac{I_{\text{Bias}}}{I_{\text{TES}}} - 1 \right), \quad (3.14)$$

and:

$$P = R I_{\text{TES}}^2. \quad (3.15)$$

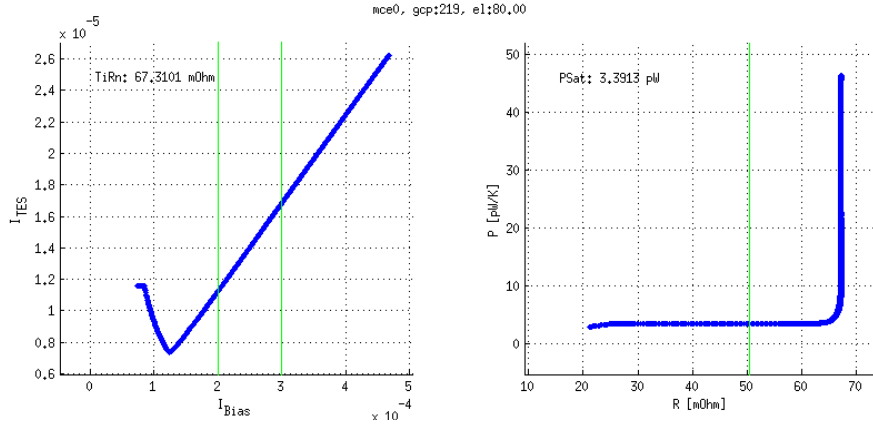


Figure 3.12: Partial load curve measurement taken at the South Pole station with the BICEP3 instrument. On the left is the TES response as a function of current bias. The region between the green vertical lines are used to determine the titanium normal resistance. On the right is the PR curve corresponding to this measurement.

The saturation power  $P_{\text{sat}}$  is related to the inverse sin of the elevation angle  $\phi$

$$P_{\text{sat}} = \frac{h}{\sin \phi} + P_0, \quad (3.16)$$

where  $P_0$  contains power from dark detectors  $P_{\text{dark}}$  and instrument loading  $P_{\text{load}}$

$$P_0 = P_{\text{dark}} + P_{\text{load}}, \quad (3.17)$$

where  $P_{\text{dark}}$  is estimated by the  $P_0$  values of dark pixels. Detectors in each tile share the same estimate for  $P_{\text{dark}}$ , the median of dark  $P_0$  values on that specific tile.

Measurements were made on run 9 of BICEP3 deployment. The histograms for  $P_{\text{load}}$  and  $P_{\text{dark}}$  are shown in Figure 3.13 and Figure 3.13 respectively.

### 3.7 Bias Selection

Transition edge sensor bolometers used in the receivers are voltage biased at the titanium normal superconducting transition. Detectors are in strong electrical feedback, and the responsivity of the detectors is given by:

$$\frac{dI}{dP} \approx \frac{dI}{dP_{\text{elec}}} = \frac{1}{V}. \quad (3.18)$$

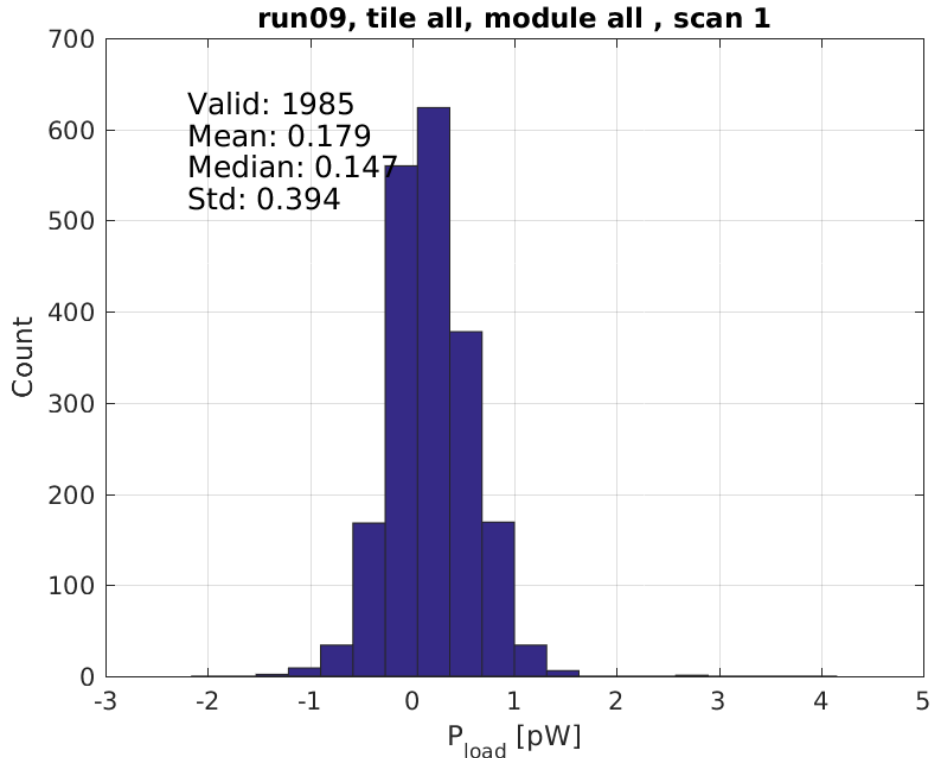


Figure 3.13:  $P_{\text{load}}$  measurements from BICEP3 . The mean value is at 0.179 pW.

Detectors have higher responsivity when the biasing voltage is lower. But when the the voltage is lower there is also more noise. Furthermore at lower voltages TES can oscillate due to thermal and the electrical time constants making the TES unstable. The optimal bias is a trade off, with good responsivity closer to the normal conducting state and not so high on the noise further away from the normal conducting state.

The first stage of bias selection is done in the lab by eye from load curve measurements during summer deployment. These values are finalized during the winter season with the responsivity schedule. For all detectors, noise levels and responsivity are measured as a function of detector bias during this schedule. For each bias point on the titanium transition region, an elevation nod is followed by five minutes of noise data taken while the telescope is pointing at the zenith.

The noise is typically measured as Noise Equivalent Temperature (NET), a quantity in units of  $\mu\text{K}_{\text{CMB}}\sqrt{s}$  which has the same units with the square root of power spectral density (PSD).

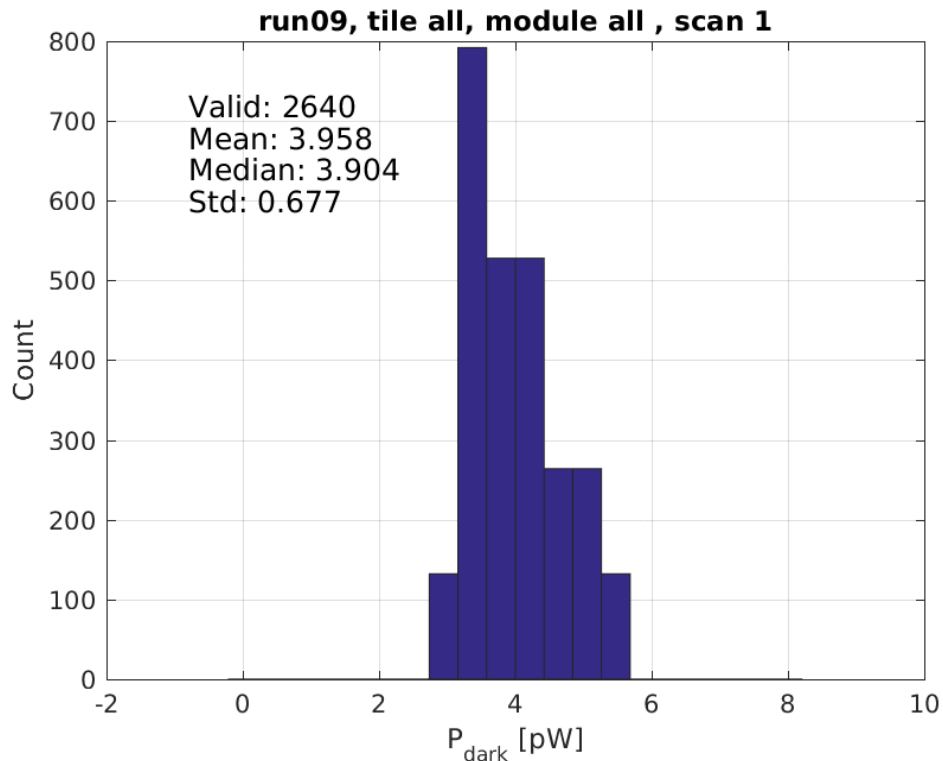


Figure 3.14:  $P_{\text{dark}}$  measurements from BICEP3 . The mean value is at 3.958 pW.

These measurements are used to calculate the noise at each bias value. In order to remove drifts from timestream data, the noise are median subtracted 3rd order polynomial filtered. Initially the absolute calibration of the sky is unknown, so the analog-to-digital units (ADU) are converted to  $\mu\text{K}$  using the relative gains from elnod calibrations to normalize, as discussed in Section (refer relgain) and an estimate of sky temperature of about at the frequencies observed. Similar to science data, pair difference PSD is used to minimize atmospheric fluctuations. The total noise is estimated in the white noise region of 1 - 3 Hz range, which is above the atmospheric knee for  $1/f$  contribution, after accounting for the inverse quadrature.

The sky temperature is around 9 - 13 K for the bands of observation therefore this measurement does not give the absolute sensitivity of the detectors, however optimal values for the bias can still be determined.

The optimal bias is determined on a column basis since MCE bias is shared among per detector column line. There could be crosstalk and data quality related issues if there are unstable detectors.

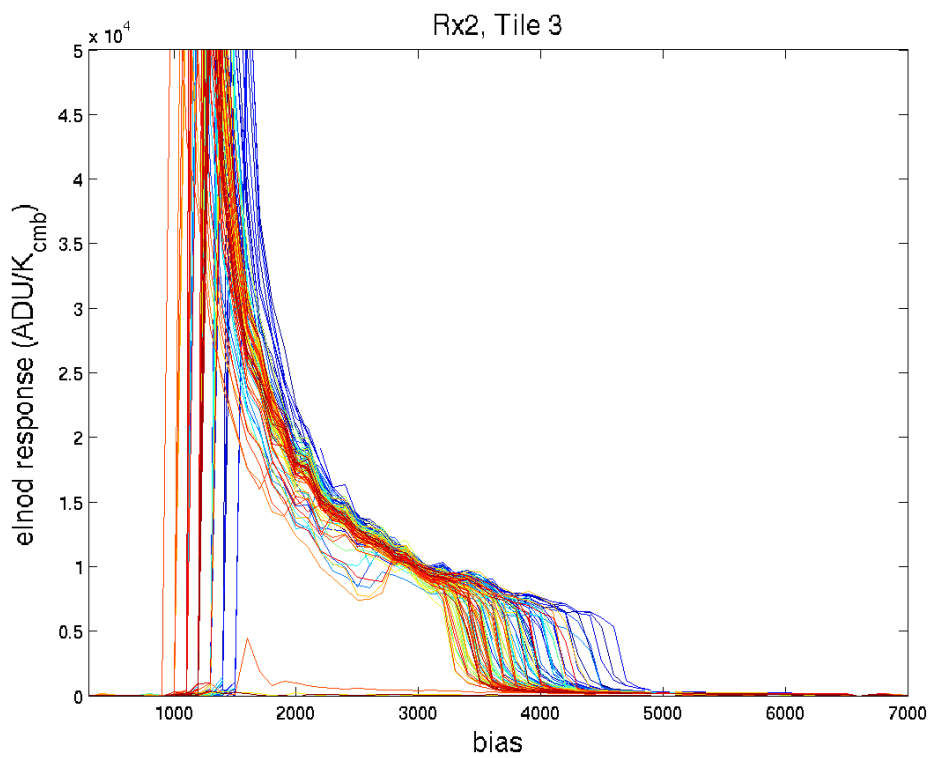
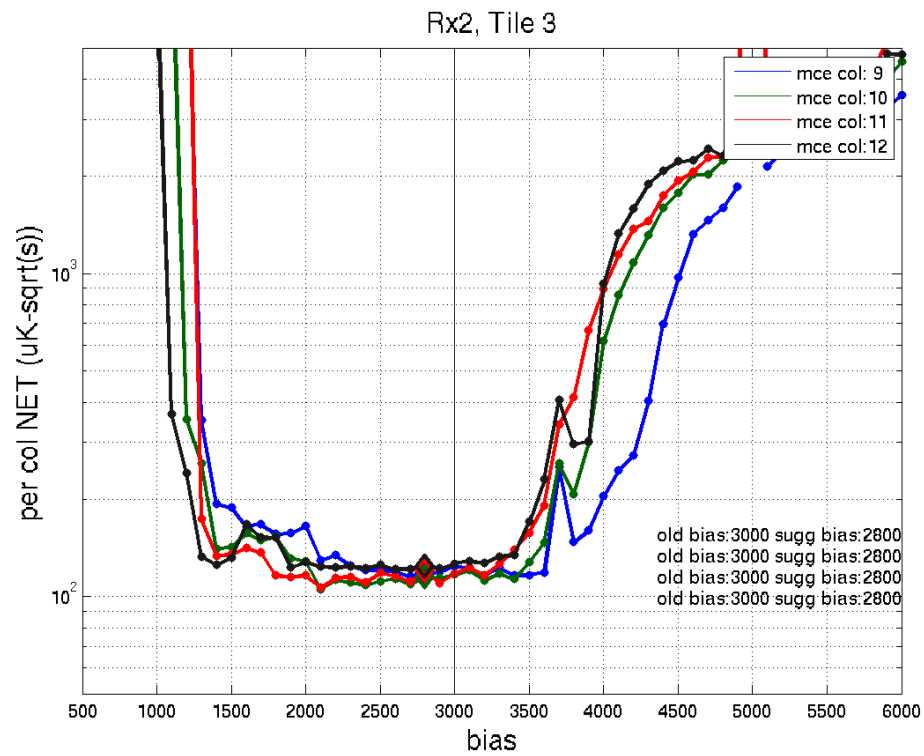


Figure 3.15: Procedure used to find the optimal bias to minimize NET.

### 3.8 Correlated Row Noise

In the 2017 observing season, row correlated noise was observed in the reduction covariance plots for the rx4/K5 receiver of Keck when the 270 GHz E12 focal plane was installed in the cryostat. This noise was initially detected by the appearance of diagonal stripes in the pair difference correlation figure. The detectors in the correlation plot are arranged according to their MCE column ordering, but a reordering to the MCE rows clearly showed that the detectors in the same MCE row were highly correlated, as shown in Figure 3.16.

Despite swapping out the E12 focal plane with E13 during deployment, the row-correlated noise persisted in the Keck rx4/K5 receiver during the 2018 observing season. This led to suspicion that the issue was not with the focal plane itself but rather within the cryostat.

One of the first tests we have done is to take data at higher frequencies. This can be achieved by "freezing with the PID servo inactive" on a given row and column. As a result, the row order parameter changed to maintain the same row, and MCE did not downsample the data. Using this method, we were able to acquire data at a sampling rate of 50 MHz, one detector at a time, with a maximum of 65536 samples per detector. Alongside the 50 MHz data, we also measured 180 Hz data to investigate whether correlated row noise leaked to our science data. During this procedure, the detectors were biased at the Titanium transition.

We wanted to test whether the correlated row noise is associated with the 4 MHz signal possibly through aliasing. To investigate this, we chose a specific number of samples per row at 50 MHz to be averaged. The transfer function is given by:

$$T = \frac{\sin(fn\pi/f_s)^2 n^2}{(f f_s \pi)^2}. \quad (3.19)$$

A digital notch filter was applied to test whether the correlated row noise was related to the 4 MHz signal aliased down digitally. The transfer function of the notch filter has nulls at  $n = \text{integer multiples of } f_s/f$ , where  $f_s$  is the sampling rate and  $f$  is the frequency of the signal. Different sample numbers were chosen to achieve the desired notch frequency. When using sample numbers of 10, 12, and 13, the expected reduction in power is estimated to be 13, 28, and 28 dB, respectively. A sample number of 6 is expected to increase the power. Despite applying the digital notch filter, there was no significant difference in the correlated row noise.

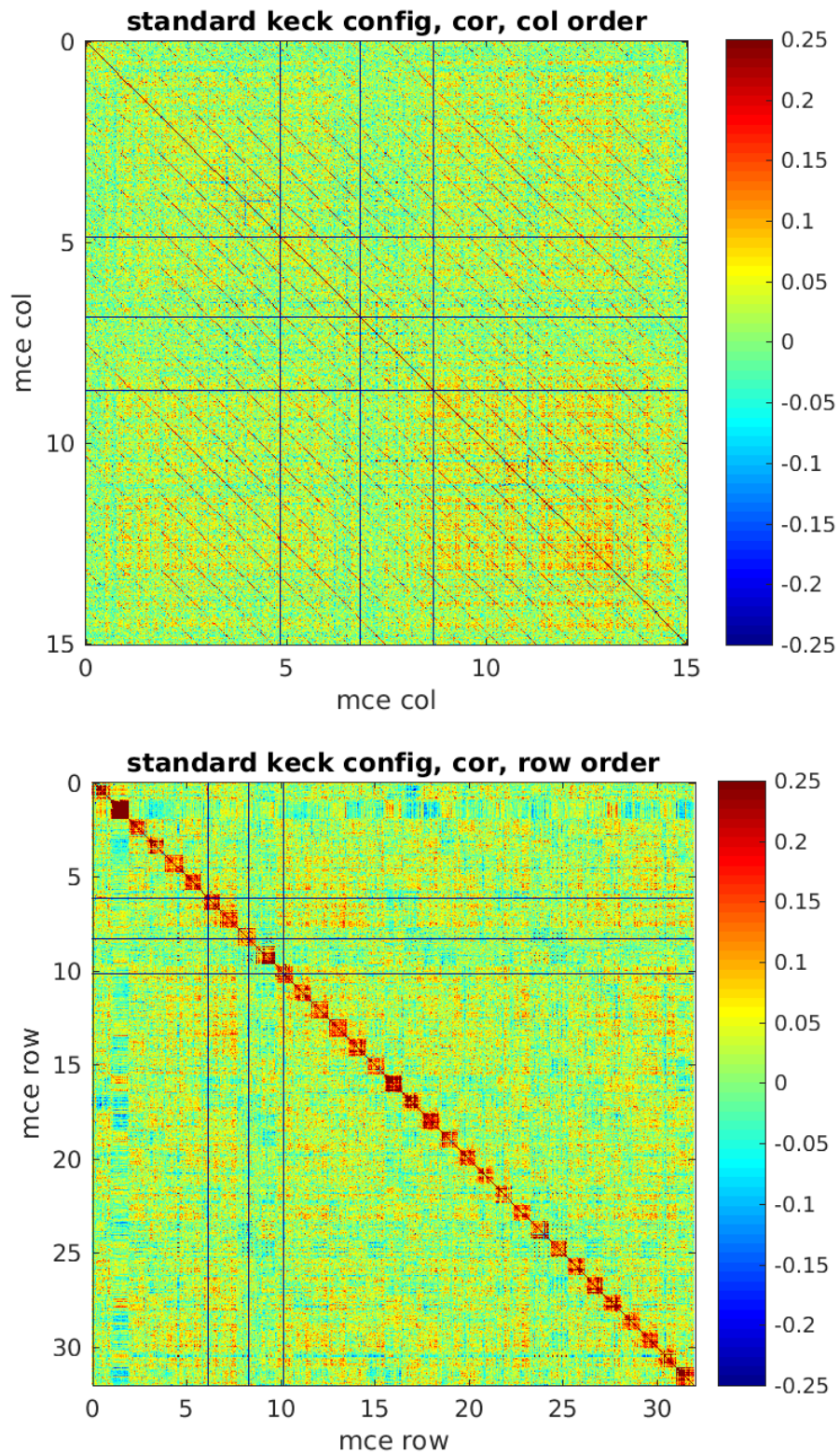


Figure 3.16: Pair difference in correlation figures. Top figure: detectors are in MCE column order. Bottom figure: detectors are in MCE row order.

As a next step, 220 nF surface mount capacitors were added to the housekeeping spare modules. However, the addition of these capacitors did not show any improvement in the correlated row noise, except for some minor improvements in  $1/f$ . The addition of these capacitors caused problems with the housekeeping readout, and they were eventually removed. Taking data at 180 Hz proved to be unreliable due to temperature issues.

When the housekeeping data is unplugged, the 4 MHz noise and the  $1/f$  bump came down significantly. Turning off the blastbus eliminated the 4 MHz noise. Removing the power cable from K5 was the next best solution. Removing the digital cable had little effect.

In 2020, the correlated row noise in the 270GHz receiver appears to have decreased significantly. Analysis shows that in 2018, Keck rx5 suffered about a 60% penalty due to correlated row noise, whereas in the 2020 season with the Bicep Array, this penalty has reduced down to 10%. Due to low levels of signal to noise, the 270 GHz data is not used for scientific data.

Here is a summary of the different measurements taken:

- Measurement with all housekeeping boxes mounted, all cables and power on. Capacitors added to K5 housekeeping backpack. Bead added to digital cable of rx4.
- Measurement with digital cable removed from rx4.
- Measurement with blastbus turned off.
- Switched housekeeping cards so that K5 backpack has no additional 220 pF capacitors.
- Baseline measurement.
- Measurement with only K5 power cable unplugged. All other cables plugged in (digital cable plugged back in).
- Measurement with K5 power cable unplugged and all digital cables unplugged.
- Measurement with all power and digital cables unplugged.
- Measurement with all power off and all digital cables connected.

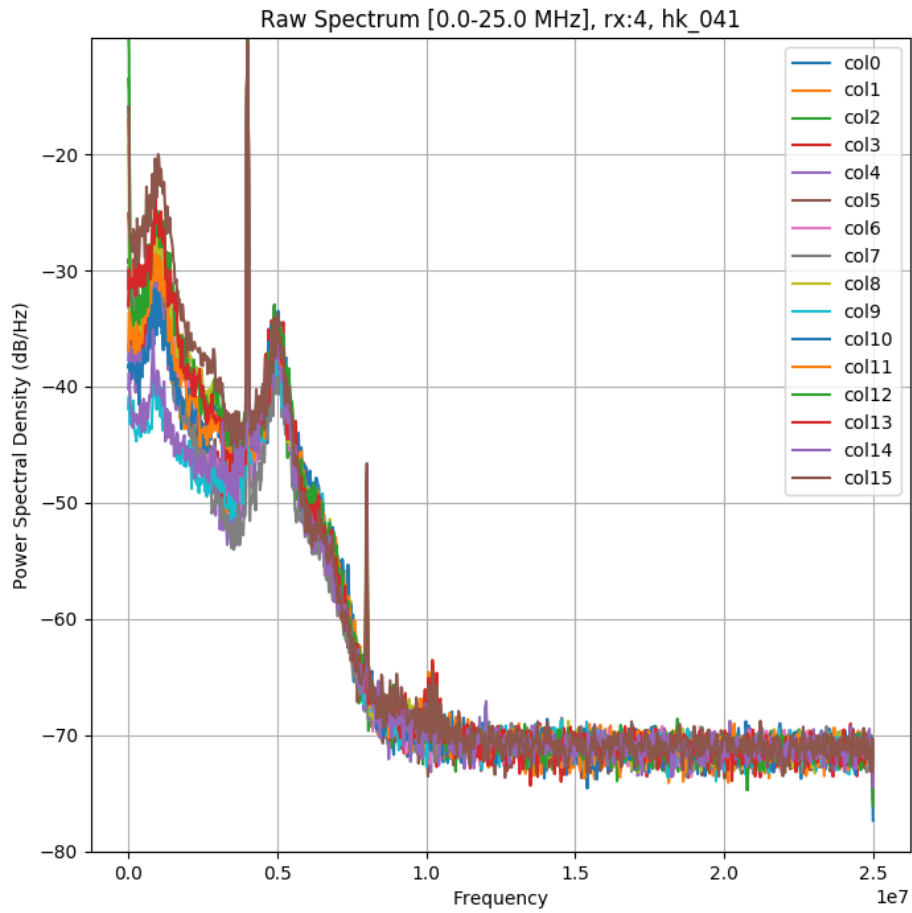


Figure 3.17: Raw data taken at 50 MHz, consisting of 65536 samples by "freezing with the PID servo inactive" on a given row and column. MCE does not downsample and row order is changed to stay in a given row. A large spike is present at 4 MHz.

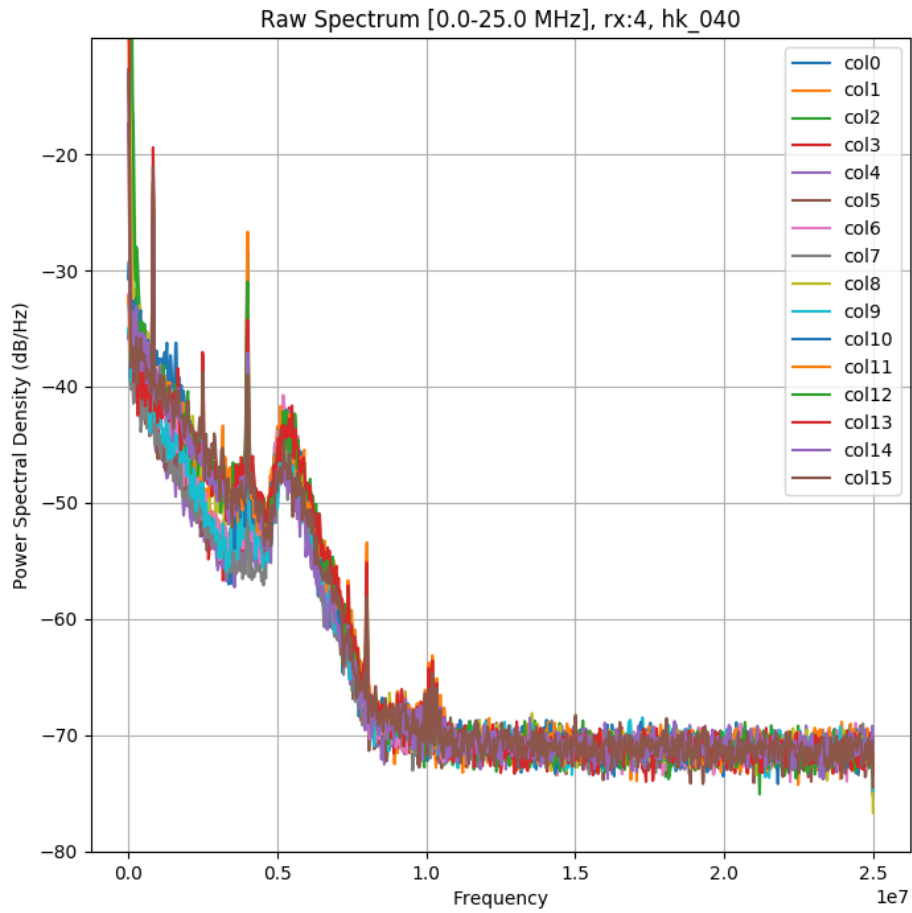


Figure 3.18: Same as previous figure except K5 power off and power cable ground connected to backpack. Spike at 4 MHz comes down significantly, indicating an issue of ground.

- Measurement with K5 power off and power cable ground connected to back-pack.

*Chapter 4*

## ANALYSIS PIPELINE

The goal of the BICEP / Keck series of telescopes is to measure the tensor to scalar ratio  $r$ . To achieve this, the analysis pipeline is designed as a compression algorithm [88] that takes terabytes of time-ordered data (TOD) as input and estimates  $r$  as output while minimizing information loss and avoiding systematic contamination. Time ordered data are transformed into polarized sky maps and then into angular power spectra followed by an estimation of  $r$ .

The analysis pipeline of BICEP/Keck Array is based on the pipeline used by QUAD and BICEP1 . The pipeline uses a MATLAB implementation of the MASTER (Monte Carlo Apodized Spherical Transform Estimator) algorithm [54]. This algorithm efficiently estimates the CMB anisotropy angular power spectrum through Monte Carlo simulations.

Limited sky coverage, and filtering introduces bias in the power spectrum estimate. To address this, the simulation pipeline applies the same filtering and processing steps as the real data. By using the inputs provided for the simulations, numerical correction factors are obtained that are applied to the real data to mitigate the bias introduced.

The sequence of timestream data collected by the Transition Edge Sensors (TESs) is recorded continuously, along with thermal measurements, telescope pointing, boresight angle, and timestamps. The data obtained at the South Pole is transmitted to the Odyssey cluster at Harvard via satellites, where further analysis is takes place.

## 4.1 Data Pipeline

### Low Level Data Reduction

The control system of the telescope continuously saves time-ordered data (TOD) to disk. The data recorded includes simultaneous samples from various components of the telescope system, such as bolometer readouts, mount pointing and trajectory information, and cryostat thermometry. The data is divided into 50-minute chunks from a scanset, which includes leading and trailing elnods and partial load curves (PLCs) as discussed in Section 2.3.

### Data Sampling

The Multi-Channel Electronics (MCE) readout acquires data at a rate of 50 MHz, which is distributed among the detectors in a readout column. During the readout process, timestream data is filtered using digital filters. These filters include a Butterworth low-pass filter from MCE and a Finite Impulse Response (FIR) low-pass filter from The Linux General Control Program (gcp). The combined transfer function is deconvolved from the timestream data, a process which is described in more detail by [93].

To estimate the smallest resolvable angular size in astronomical observations for a given data rate, we can use:

$$\ell \approx \frac{2\pi f}{r} \cos \theta, \quad (4.1)$$

where  $f$  is the data sample rate,  $r$  is the azimuth scanning rate at an elevation angle  $\theta$ .

The inflationary spectrum is expected to peak in the multipole range of  $20 < \ell < 200$ . To save bandwidth for data transfer, timestreams are further downsampled. A sample rate of  $f = 2.4$  Hz is sufficient to keep science signal up to  $\ell \approx 580$  for a scan speed of  $2.8^\circ \text{s}^{-1}$  centered around Dec of  $-57.5^\circ$ . Inflationary signal are expected to peak in the range of 0.1 to 2.5 Hz. To achieve this sampling rate, gcp down-samples the timestreams further resulting in a final data rate of approximately 20 – 30 Hz. To suppress high-frequency noise outside our science band, a final low-pass filter with a cut-off frequency of 5 Hz is applied.

### De-glitching

The first step in the data analysis pipeline is the de-glitching step, which deals with spikes and discontinuous steps that results from cosmic ray hits on the TES island or flux jumps in the SQUIDs. We improve data quality and accuracy by applying this de-glitching process, making sure that only relevant signals are used in the subsequent parts of analysis.

The high gain detectors and readout system can make the time-ordered data sensitive to external signals, which results in spikes and discontinuous steps in the data. To remove these features, we apply a de-glitching algorithm before processing the data further.

The glitches in the signal can occur when flux jumps cause the SQUIDs to jump from one lock point to another, which results in discontinuous steps in the signal. For their removal we adjust the DC level of the time-ordered data before and after the step to match the offset.

Cosmic rays can also produce spikes in the signal, and can lead to detector cross-talk. To address these spikes, we cut the time-ordered data these cut samples with NaNs. When glitches are detected in the TES islands, the affected segment and a small section of adjacent time series are masked in the data.

### **Relative Gain Calibration (relgain)**

The BICEP/Keck Array instruments observe and records timestream data in analog-to-digital units (ADU). This unit is not consistent for all detectors pairs, resulting in different gains for each detector. To address this issue, an elnod as discussed in Section 2.3 is used to calibrate the relative gain between the detectors.

The elnod causes the detectors to respond to a secant function that is caused by the elevation gradient in sky temperature. The relative gain, denoted by  $\eta$ , is then calculated and corrected for each detector based on elnod response.

The elevation gradient in temperature results from the airmass change as the telescope moves up and down. The airmass is a measure of the amount of atmosphere through the line of sight of the telescope. The airmass is 1 when the telescope looks directly overhead and increases as the telescope looks towards the horizon. The temperature of the sky decreases as the airmass increases which scales with  $1/\cos \theta$ , where  $\theta$  is the elevation angle from the zenith.

The relative gains are calculated by fitting the elnod response with a  $1/\cos \theta$  term

and compared to the median of detectors in the same instrument. Relative gains are calculated and accounted for each detector.

$$\text{DOT}_{\text{calibrated}}(t) = \text{DOT}_{\text{uncalibrated}}(t) \times \text{relgain}, \quad (4.2)$$

where:

$$\text{relgain} = \frac{\text{median}_{\text{band}}(\text{elnod gain})}{\text{elnod gain}} \Big/ 2. \quad (4.3)$$

where  $\text{DOT}_{\text{calibrated}}$  is the calibrated timestream, and  $\text{DOT}_{\text{uncalibrated}}$  is the uncalibrated timestream [96].

It's worth noting that while this calibration step corrects for the relative gain between detectors, it does not provide an absolute calibration of the instrument. The final calibration is done by correlating the *BICEP/Keck* Array maps with the Planck temperature map, which is performed later in the analysis pipeline during the absolute calibration stage. During that stage ADU units are converted to  $\mu\text{K}_{\text{CMB}}$  in the analysis pipeline.

### **Timestream Data**

After the relative calibration step, we create pair-sum and pair-difference timestreams. The pair-sum timestreams represent the total power detected by the pair of detectors, while the pair-difference timestreams corresponds to the polarization between the two detectors. An example of a 50-minute scanset is shown in Figure 4.1, which includes the mount motion, pair-sum, pair-difference timestreams, and the elnod response before and after the scanset.

The pair-sum contains significant scan-synchronous signals due to the back and forth motion of the mount. The pair-difference timestreams in the other hand show little to no scan-synchronous signal because the atmosphere is largely unpolarized. Both types of timestreams contain residual atmospheric  $1/f$  atmospheric noise, and is removed by fitting and subtracting a 3rd order polynomial on a per-halfscan basis.

This process removes the slow-varying atmospheric noise that can mask the CMB signal and help us improve signal to noise levels of the CMB polarization signal. The resulting timestreams are then used to produce maps of the CMB temperature and polarization.

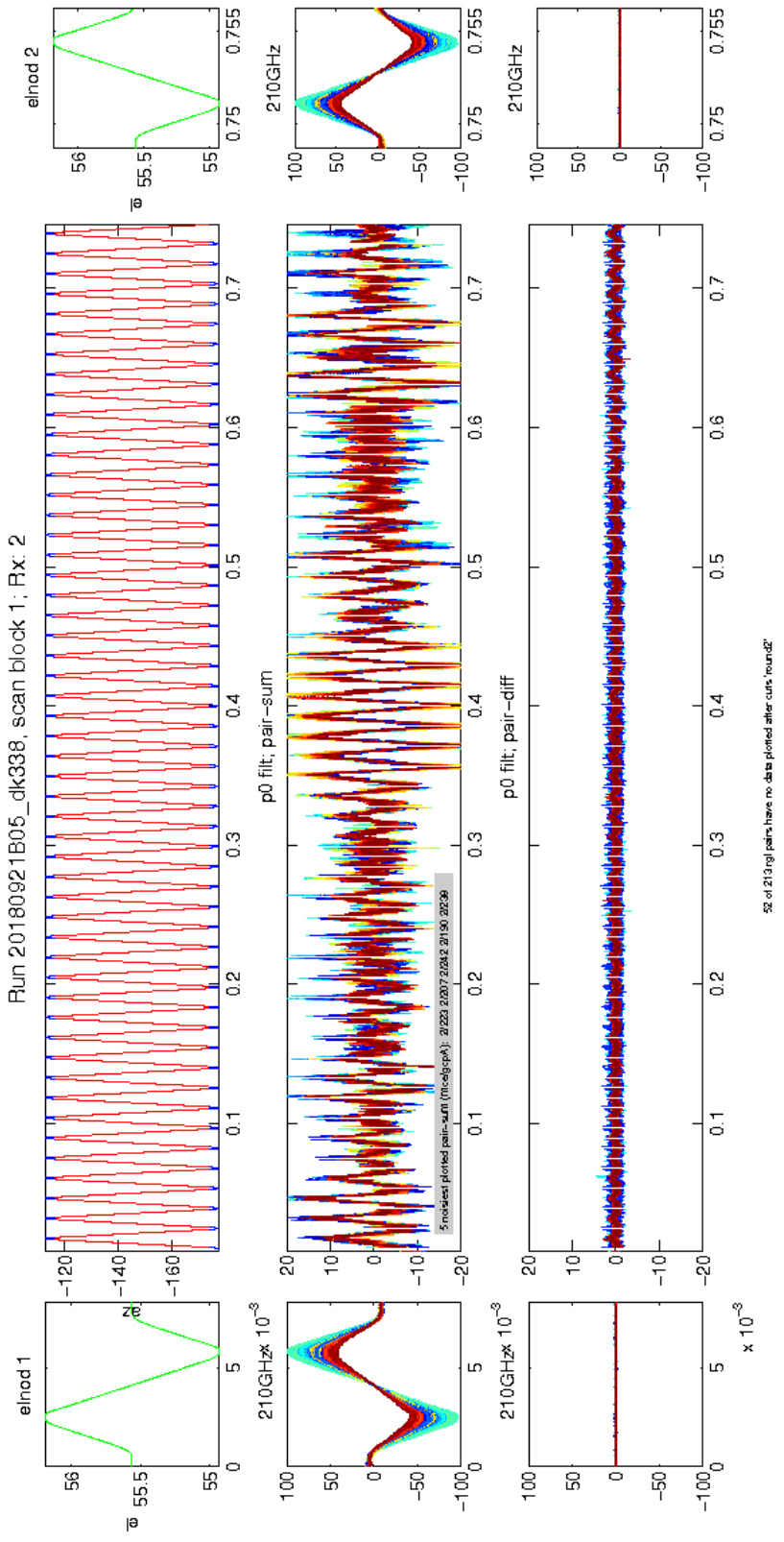


Figure 4.1: Reduc plots show the scanning motion of telescopes and timestream response for detectors. Left and right columns are the leading and trailing elnodes, while the center column shows constant-elevation scans. The pair-sum timestream has scan-synchronous response, while the pair-diff shows very little due to common-mode rejection.

The time-ordered data (TOD) from each detector depends on stokes  $T$ ,  $Q$ ,  $U$  parameters of the incident radiation as well as the gain  $g$ , polarization efficiency  $\gamma$  and polarization orientation  $\psi$ . The detector response is given by:

$$d = g [T + \gamma (Q \cos 2\psi + U \sin 2\psi)], \quad (4.4)$$

where  $d$  is the detector signal,  $T$ ,  $Q$ , and  $U$  are the Stokes parameters,  $\psi$  is the polarization orientation, and  $g$  is the gain.

The pair sum and pair difference are used to estimate the CMB temperature and polarization respectively, with pair difference particularly useful for removing common unpolarized atmospheric noise. The pair difference  $d_{\text{pair}}$  for a pair of orthogonal detectors  $a$  and  $b$  is given by:

$$d_{\text{pair}} = \frac{1}{2} \left( \frac{d_a}{g_a} - \frac{d_b}{g_b} \right) = \frac{1}{2} (\alpha Q + \beta U), \quad (4.5)$$

where the coefficients  $\alpha$  and  $\beta$  are obtained from subtracting orthogonal pairs of detectors, and yields information on the polarization orientation:

$$\begin{aligned} \alpha &= \gamma_a \cos 2\phi_a - \gamma_b \cos 2\phi_b \\ \beta &= \gamma_a \sin 2\phi_a - \gamma_b \sin 2\phi_b \end{aligned} \quad (4.6)$$

This results in a difference signal that contains polarized CMB signal, since the unpolarized common mode atmospheric noise cancels out.

### Data Selection and Cuts

To ensure the accuracy of the final map, we use a set of rules to remove any data that show abnormal behavior during the map-making process. These filters are calculated using bolometer and auxiliary data to provide a complete evaluation of the entire system.

To maintain the quality of the data, a two-stage cutting algorithm is used to identify and eliminate poor-quality data that could be caused by instrument-related issues. The data that is removed is either incompatible with our noise model or corrupted.

Table 4.1: Round 1 Cut Parameters.

Cut Parameter	Description	Threshold
fp_nancount	number of NaNs in timestream data	
fb_std_p0	std. of TODs after p0 filtering	
fb_sd_p0_darks	std. of dark TODs after p0 filtering	
fb_std_p3	std. of TODs after p3 filtering	
fb_std_sd_p0	std. of sum/diff TODs after p0 filtering	
fb_std_sd_p3	std. of sum/diff TODs after p3 filtering	
fb_std_uncal	std. of sum/diff TODs before calibration	
is_fj_row	number of flux jumps in row	
is_fj_col	number of flux jumps in column	
syncsampnum_diff1	check whether data is out of order across time	
syncsampnum_diff2	check whether data is out of order across receivers	
passfrac_col	fraction of channels cut in MUX column	
passfrac_chan	fraction of channels cut in receiver	

It is worth noting that the data cuts do not specifically target time series data that has a higher noise level than average. Instead, they are weighted based on their variance to determine their contribution to map making. As a result, noisy data has a lower contribution to the final map.

The initial set of cuts, known as "round 1 cuts" operate at a time series level before data is binned into pair maps. These rules are capable of discarding data at a per-halfscan level and are designed to remove only the most severely corrupted data using lenient thresholds. Some of the round 1 cuts are set to have an infinite threshold to be used for diagnostic purposes only and not for removing data.

The second stage, also named as round 2 cuts, are applied during coadd stage, and discards data at a per-pair or per-scanset level. These cuts evaluate various data quality metrics and are primarily responsible for removing data, and ensuring good quality in our dataset. Some examples to these cuts include the quality of relative gain calibration, the temperature stability of the focal plane, and statistical noise properties.

In addition to the cuts we implement a set of channel cuts for each year of data, which reject individual channels that display unusual behavior throughout the season. These cuts commonly use external calibration data or statistics derived from full-season data sets with sufficient signal-to-noise ratio to detect subtle effects.

### **Atmospheric Filtering and Ground Subtraction**

Table 4.2: Round 2 Cut Parameters.

Cut Parameter	Description	Threshold
elnod_mean	mean of leading and trailing elnods	
elnod_fracdel	fractional change in elnods	
elnod_ab_ba	ratio of elnods before and after	
elnod_median	median of elnods	
elnod_nancount	number of NaNs in elnods	
elnod_gof Elnod	goodness of fit for elnods	
elnod_chisq_dif	$\chi^2$ of elnod pair difference	
fb_wn_sd_p0	mean PSD in range 1.5 to 2.0 Hz	
fb_1f_sd_p0	mean PSD in range 0.1 to 0.3 Hz	
skewness_dif	skewness of pair difference	
skewness_sum	skewness of pair sum	
satcom	max $\chi^2$ in consecutive fixed azimuth scans	
fp_corr	mean off-diagonal detector pair-diff correlation	
scanset_std	std of scanset	
stationarity_ab	std of per detector fb_std_p3	
stationarity_dif	std of per pair diff fb_std_p3	
tfpu_mean	mean focal plane temperature (K) during scanset	
tfpu_std	std focal plane temperature (K) during scanset	
enc_az_diff	change in az encoders counts	
az_range	range of az angles during scanset	
num_fj	number of flux jumps in scanset	
num_destep	number of jumps removed from scanset	
max_fj_gap	max flux jump	
rtes_frac	fractional TES resistance	
passfrac_halfscan	fraction of halfscans after round 1	
passfrac_scanset	fraction of detectors after round 2	

The signal observed by the BICEP/Keck Array instruments contain  $1/f$  noise from the atmosphere. A third-order polynomial filter is applied to each halfscan, to remove this noise the low-frequency atmospheric fluctuations/

Ground subtraction is another technique used to remove unwanted signals from the data by taking the mean of the timestream signal from all halfscans within a scan. This effectively removes any ground-fixed signals, including signals from the Earth's magnetic field, satellite and radio communications.

### Map Making

Map making is the process of accumulating the pair-sum and pair-difference timestream data over a two dimensional weighted histogram [61]. The sky coordinates right

ascension (RA) and declination (Dec) are used for this binning. The data is binned with 0.25 degrees wide square pixels.

### **Inverse Variance Weighting**

Each detector pair is weighted by the inverse variance of the scanset timestream, after 3rd order polynomial filtering and ground subtraction. Separate weights are used for pair sum and pair difference. Noisy channels and periods of time with bad weather are assigned smaller weights.

$$\sum \omega \begin{pmatrix} d_+ \\ \alpha d_- \\ \beta d_- \end{pmatrix} = \frac{1}{2} \sum \omega \begin{pmatrix} N & 0 & 0 \\ 0 & \alpha^2 & \alpha\beta \\ 0 & \alpha\beta & \beta^2 \end{pmatrix} \begin{pmatrix} T \\ Q \\ U \end{pmatrix}. \quad (4.7)$$

Inverting Equation 4.7 yields the  $Q$  and  $U$  maps. For a single detector orientation, the matrix would be singular. To invert this matrix, many orientations are required. Rotating the deck angles between different schedules solves this problem.

### **Pairmaps**

After filtering and relative calibration, TODs are binned per detector pair, per scanset. Each of these maps are called pairmaps. Per-phase pairmaps are coadded pairmaps that share the same phase. Pairmaps are stored on disk, which allows us to create a variety of map combinations while also allowing us to apply different filters and cuts without having to repeat the low-level reduction.

### **Coadding Maps**

Pairmaps are often coadded over all detectors over the entire season of data. Different combinations of data are created for consistency checks such as jackknives.

### **Pointing**

It is very important to have precise pointing information for the detectors to accurately measure the CMB. The pointing information is obtained through an optical star camera that is installed on the telescope. This camera uses the images of stars to determine the pointing of the telescope. The pointing information is stored for each detector at every timestamp by combining the information with telescope boresight pointing and boresight rotation.

Time series data is grouped into the corresponding right ascension (RA) and declination (Dec) bins once the pointing information is obtained. The Planck 100 GHz temperature map is then used for correcting individual detector points in the receivers.

### Deprojection

Temperature anisotropy will leak into a false polarization signal due to a beam mismatch between the co-located orthogonal A and B detectors, commonly known as T to P leakage. For the BICEP/Keck experiment, a technique for filtering beam mismatch has been developed.

Individual detector beams are modeled using a six-parameter two-dimensional elliptical Gaussian model:

$$B(\vec{x}) = \frac{1}{\Omega} \exp \left[ -(\vec{x} - \vec{\mu})^T \Sigma^{-1} (\vec{x} - \vec{\mu}) / 2 \right], \quad (4.8)$$

where  $1/\Omega$  is the normalization factor,  $\vec{\mu}$  the center of the ellipse and  $\Sigma$  contains information about width and ellipticity.

The covariance matrix for an elliptical Gaussian can be described in terms of major and minor widths  $\sigma_{\text{maj}}$  and  $\sigma_{\text{min}}$ :

$$C = \begin{bmatrix} \sigma_{\text{maj}} & 0 \\ 0 & \sigma_{\text{min}} \end{bmatrix}, \quad (4.9)$$

and a rotation matrix:

$$R = \begin{bmatrix} \cos(\theta) & \sin(\theta) \\ -\sin(\theta) & \cos(\theta) \end{bmatrix}, \quad (4.10)$$

such that :

$$\Sigma = R^{-1} C R, \quad (4.11)$$

yields:

$$\Sigma = \sigma^2 \begin{bmatrix} (1+p) & c \\ -c & (1-p) \end{bmatrix}, \quad (4.12)$$

$$\sigma^2 = \left( \sigma_{\text{maj}}^2 + \sigma_{\text{min}}^2 \right), \quad (4.13)$$

$$p = e \cos(2\theta), \quad (4.14)$$

$$c = e \sin(2\theta), \quad (4.15)$$

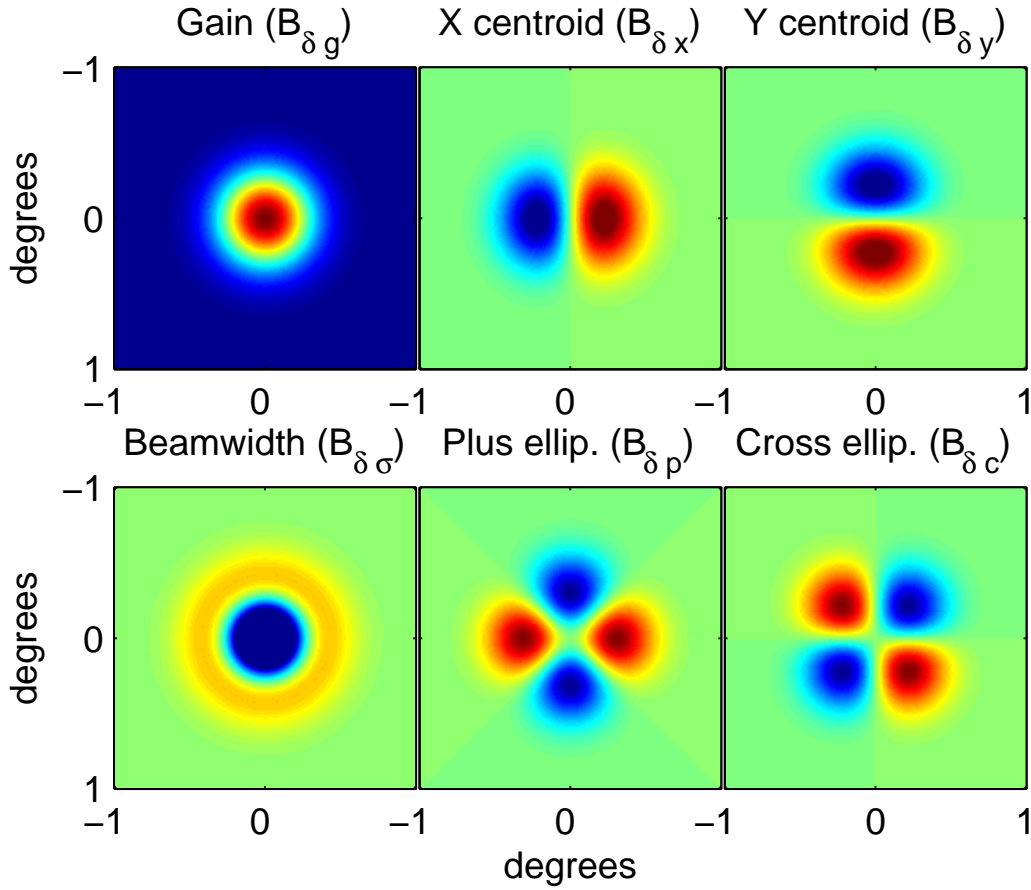


Figure 4.2: Differences of elliptical Gaussian beams, where the total difference beam is the linear combination of these modes. These difference beams couple to different derivatives of the CMB temperature field in the deprojection pipeline. Figure from [34].

where  $p$  and  $c$  are ellipticity parameters corresponding to plus and cross ellipticity determined by the angle of major axis with respect to the x-axis. Total ellipticity is defined as

$$e = \sqrt{p^2 + c^2} = \left( \frac{\sigma_{\text{maj}}^2 - \sigma_{\text{min}}^2}{\sigma_{\text{maj}}^2 + \sigma_{\text{min}}^2} \right). \quad (4.16)$$

The difference in the beams is Taylor expanded up to second order, and expressed in terms of gain  $\delta g$ , differential pointing  $\delta x$ ,  $\delta y$ , beamwidth  $\delta \sigma$ , and ellipticity  $\delta p$ ,  $\delta c$  [34].

**Absolute Gain Calibration (abscal)** The timestream measures the sky in arbitrary Analog to Digital Units (ADU). Temperature maps from Planck are used for converting ADU to  $\mu\text{K}_{\text{CMB}}$ . For each  $\ell$  bin, a scale factor  $g_\ell$  is applied obtained from:

$$g_\ell = \frac{\langle m_{\text{ref}} \times m_{c1} \rangle_\ell}{\langle m_{\text{ref}} \times m_{c2} \rangle_\ell}. \quad (4.17)$$

### Jackknife Tests

Jackknife tests are used to check the internal consistency of our data. For this purpose, we use data from the map-making procedure defined in Section 4.1 to combine and split data into equally weighted pairs. This allows the CMB signal to cancel out when we take the difference of the two maps. Some splits are temporal (such as the first half versus the second half or moon up versus moon down), while others are based on detector pairs (such as the inner and outer detectors on the focal plane).

A well-designed jackknife split would result in the maps being split roughly evenly, allowing the common CMB signal to cancel out and leaving only noise and potential systematic contamination in the resulting difference map, which are referred to as the jackknife maps. For the BK18 data set, we designed 14 different jackknife splits for validation purposes see [93].

We use a distribution of spectra from signal plus noise simulations to compare with the jackknife power spectra. This helps us determine whether a jackknife is passing or failing. Through these jackknives, we test for systematic errors associated with the instrument, ground, and atmosphere. We evaluate whether a jackknife passes by using the Probability to Exceed (PTE) metric, which indicates the probability of having a simulation with the same band power as the real data:

$$\chi^2 = (\mathbf{d} - \langle \mathbf{m} \rangle)^T \mathbf{M}^{-1} (\mathbf{d} - \langle \mathbf{m} \rangle), \quad (4.18)$$

where  $\mathbf{d}$  is the observed bandpower vector,  $\mathbf{m}$  is the mean of the lensed- $\Lambda$ CDM + noise simulations, and are used to obtain  $\mathbf{M}$ , the bandpower covariance matrix [11]. This procedure is also done for all the simulations to evaluate probability to exceed (PTE) of the real data.

The  $\chi^2$  statistic measures the deviation from the expected value, but it does not account for the sign of the deviation. To address this, we use the  $\chi$  statistic:

$$\chi = \sum_i \frac{d_i - \langle m_i \rangle}{\sigma_{m_i}}. \quad (4.19)$$

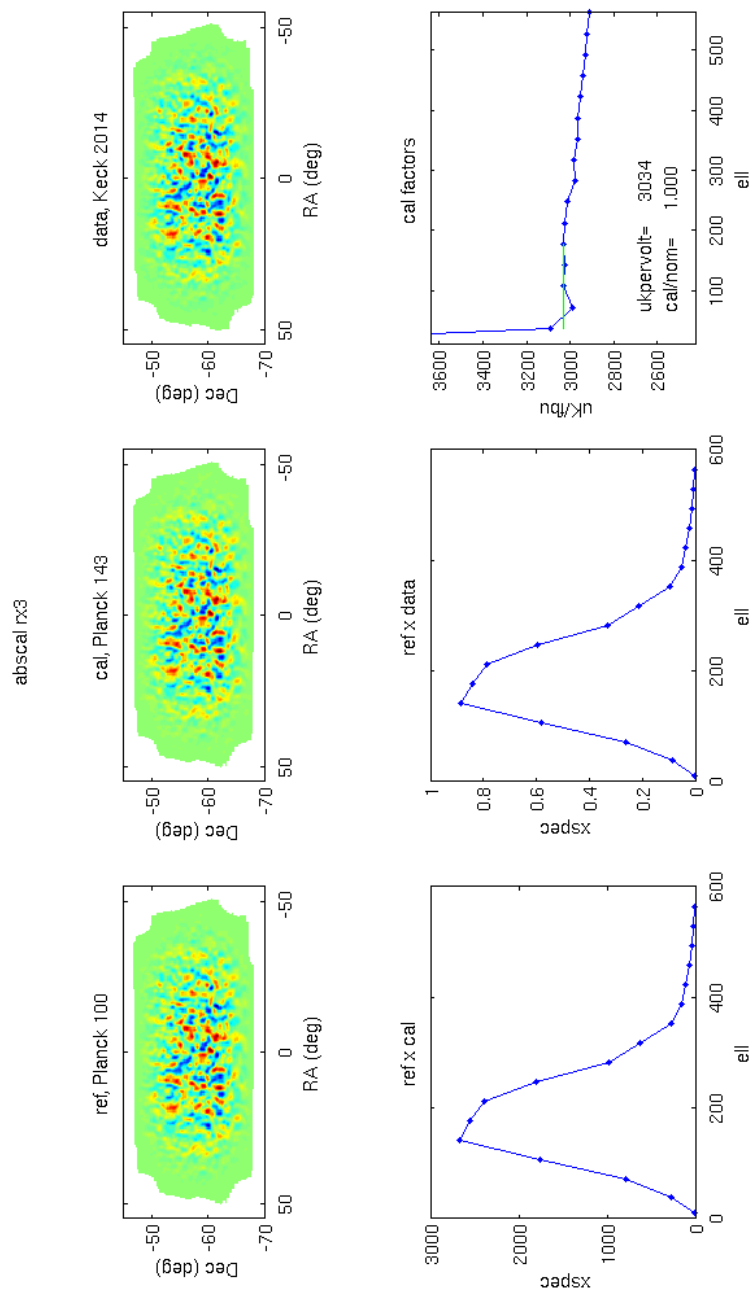


Figure 4.3: Temperature maps from Planck are used for converting ADU to  $\mu\text{K}_{\text{CMB}}$  in the absolute calibration procedure.

## 4.2 Simulations

BICEP/Keck Array experiments observe 1% of the sky and utilize filtering methods that suppress power across spatial modes in its resulting maps. Limited sky coverage, and filtering in the data processing pipeline introduces bias into the map-making process. As a result, maps and power spectrum are bias estimators.

In order to accurately estimate the bias in our observations, we generate 499 Monte Carlo realizations of the microwave sky, simulating the observation conditions of the instruments. Simulations consist of a lensed  $\Lambda$ CDM signal, a noise component, and a dust foreground. To understand the biases, we process these realizations the same way as the real data.

The signal model simulations that we use are as follows:

- Unlensed  $\Lambda$ CDM,
- Lensed  $\Lambda$ CDM,
- Polarized Gaussian Dust,
- Tensor B-modes with a tensor-to-scalar ratio of  $r = 0.1$ .

We also use noise simulations consisting of sign-flip realizations, in addition to the signal simulations.

### Signal Simulations

#### Lensed and Unlensed $\Lambda$ CDM

We calculate the spectra  $C_\ell^{TT}$  for signal-only unlensed  $\Lambda$ CDM simulations using the software CAMB, which is based on the best fit  $\Lambda$ CDM parameters from Planck 2013 [15]. To generate random realizations of CMB maps, we use `synfast` from the HEALPix package, which provides a pixelization subdivision on the surface of a sphere [47].

The non-Gaussian structure of the lensing prohibits the generation of lensed- $\Lambda$ CDM maps using `synfast`. To overcome this limitation, we use `LensPix` package, which can simulate lensed temperature and polarized CMB maps in agreement with  $\Lambda$ CDM by generating lensing deflections and applying them to the unlensed  $\Lambda$ CDM realizations [66].

## Polarized Gaussian Dust

The polarized gaussian dust realizations are also simulated by `synfast` from `HEALPix` package. The input spectrum for dust is:

$$\begin{aligned} C_{\ell,d}^{BB} &= A_d \left( \frac{\ell}{\ell_*} \right)^{\alpha_d} \\ C_{\ell,d}^{EE} &= 2C_{\ell,d}^{BB} \quad , \\ C_{\ell,d}^{TT} &= 0 \end{aligned} \quad (4.20)$$

where  $A_d = 3.75 \mu\text{K}^2$  at 353 GHz,  $\ell_* = 80$ , and  $\alpha_d = -0.4$ .

### Tensor B-modes with $r = 0.1$

Similarly to the unlensed- $\Lambda$ CDM simulations, we calculate the  $C_\ell^{BB}$  spectra using `CAMB` based on the cosmological parameters from Planck 2013 [15]. We generate random realizations using `synfast` from the `HEALPix` package.

We begin with the temperature field of the CMB as the starting point for polarized simulations. The deprojection algorithm for beam systematics requires the temperature field of the CMB as input. To satisfy the linearity requirements of the map-making pipeline by observation and purification matrices, the simulations must have a fixed sky temperature.

*Planck* measured the temperature field of the CMB with high signal to noise. We use temperature map from *Planck* Needlet Internal Linear Combination, [14] as our starting point. Once the temperature is fixed, we allow the polarization fields to vary for these realizations. We use `synfast` to calculate the constrained  $a_{\ell m}$ s. We use an equation derived from the Cholesky decomposition of  $2 \times 2$  covariance matrix of  $C_\ell^{TT}$  and  $C_\ell^{EE}$  [7, 42]:

$$a_{\ell m}^E = \frac{C_\ell^{TE}}{C_\ell^{TT}} a_{\ell m}^T + \sqrt{C_\ell^{EE} - \frac{(C_\ell^{TE})^2}{C_\ell^{TT}}} n_{\ell m}, \quad (4.21)$$

where  $n_{\ell m}$  is a complex Gaussian with unit variance and zero mean. The requirement for real E-mode maps is  $n_{\ell m}^* = (-1)^m n_{\ell m}$ . To generate an E-mode realization of the sky, for a known  $TE$  correlation, we solve the system of equations for the E-mode coefficients  $a_{\ell m}^E$ .

### Noise Simulations

It is practically very difficult to model and simulate various sources of noise in the BICEP/Keck Array instruments. The source of noise include detector photon and phonon noise, readout electronics, cryogenics. When making a noise model it is required to consider detector to detector and temporal correlations. However computing the noise covariance matrix to generate noise realizations would be computationally very expensive.

BICEP1 used the PSD from pair-difference timestreams, binning the spectrum into logarithmic spaced frequency bins, and constructing a covariance matrix for detector-detector correlations [31]. Cholesky decomposition created random realizations, which are transformed back to time domain for the appropriate noise.

As the number of detectors increased with BICEP2, a more computationally feasible approach is used derive the noise realizations from real pairmaps, called the sign-flip noise model. This noise model randomly assigns an equal amount of positive and negative coefficients to the per-phase maps [11, 43]. When the per-phase maps are coadded the signal cancels out and only the noise component remains, including the detector-detector correlations.

For  $N$  per-phase scansets, there are  $\binom{N}{N/2}$  available independent permutations of sign-flip realizations that could be generated. Using Stirling's approximation it can be shown that the binomial coefficient scales with  $\approx 2^N/\sqrt{\pi N}$ . There are about 5000 per-phase scansets per observing season that goes into generating the noise realizations. Since the number of per-phase scansets is very large, there are enough degrees of freedom to generate 499 noise realizations.

### 4.3 Filtering for PSD Estimators

We investigate the power spectral density (PSD) of the pair dif/sum timestreams for analyzing the quality of calibration we have for each pair. A model is fit to estimate  $f_k$ , denoted  $f_k$ , which is the frequency value separating white noise from the atmospheric noise. The exponent alpha, denoted  $\alpha$ , is a good indicator for the atmosphere, especially for the pair sum. the equation is given by:

$$P = w \left[ 1 + \left( \frac{f_k}{f} \right)^\alpha \right]. \quad (4.22)$$

A no-linear fitting procedure is done to estimate parameters  $w$ ,  $f_k$  and  $\alpha$ . Maximum

range of fitting is  $f = 3$  Hz. There is a low pass filter beyond this range so it is not considered in the fit.

#### 4.4 Power Spectra

In the CMB literature it is customary to scale the 1-D power spectrum  $D_\ell$  defined in terms of  $C_\ell$ :

$$D_\ell \equiv \frac{\ell(\ell + 1)C_\ell}{2\pi}. \quad (4.23)$$

#### Apodization Mask

An apodization mask is applied to the maps before estimating the power spectrum. There are two main reasons for applying this mask:

- Pixels towards the center of the map get both more observation time and number of detectors than the pixels at edge of the maps. As a result, the edge of the maps will be noisier than the central regions. We use the apodization mask to provide more weight on the central region, and less weight on the edges.
- A step function in the apodization mask in map space would create ringing in harmonic space. To avoid ringing, the transition to zero is constructed to be smooth in the apodization mask.

The apodization mask in BICEP/Keck Array maps are derived from variance maps.  $Q$  and  $U$  maps share the same inverse variance apodization mask

$$m_{\text{Pvar}} \equiv \frac{1}{2} (m_{\text{Qvar}} + m_{\text{Uvar}}), \quad (4.24)$$

where  $m_{\text{Qvar}}$  and  $m_{\text{Uvar}}$  are smoothed variance for  $Q$  and  $U$  respectively. In the likelihood analysis, we use the geometric mean of apodization masks from different frequencies:

$$\bar{m}_{\text{Pvar}} = \left( \prod_{i=1}^n m_{\text{Pvar}} \right)^{1/n}. \quad (4.25)$$

BICEP3 observes a larger area in the sky. A larger apodization mask is created separately. We have the larger apodization mask for BICEP3 and smaller apodization mask for BICEP2 / Keck Array maps [6].

### Flat Sky Approximation

The MASTER algorithm converts the maps into a power spectra estimate  $\tilde{C}_\ell^{XX}$  of the full sky power spectra  $C_\ell^{XX}$ .

The map making process results in pixelized partial sky maps of  $T$ ,  $Q$ , and  $U$ . The  $T$ ,  $Q$ , and  $U$  maps can be expanded in Fourier basis. A full sky map, such as *Planck*, requires the use of spherical harmonics for the power spectra. However since BICEP/Keck Array observes a small fraction of the sky, we use flat sky approximation for the angular power spectrum:

$$\begin{aligned}\tilde{T}(\vec{\ell}) &= \int d^2\hat{r} T(\hat{r}) \exp(-i\vec{\ell} \cdot \hat{r}) \\ \tilde{Q}(\vec{\ell}) &= \int d^2\hat{r} Q(\hat{r}) \exp(-i\vec{\ell} \cdot \hat{r}) \\ \tilde{U}(\vec{\ell}) &= \int d^2\hat{r} U(\hat{r}) \exp(-i\vec{\ell} \cdot \hat{r}).\end{aligned}\tag{4.26}$$

and the spectra is calculated with the Discrete Fast Fourier Transform (DFFT):

$$\begin{aligned}\tilde{T}(\vec{\ell}) &= \sum_{x,y} W(x,y) T(x,y) \exp[-i(\ell_x x + \ell_y y)] \\ \tilde{Q}(\vec{\ell}) &= \sum_{x,y} W(x,y) Q(x,y) \exp[-i(\ell_x x + \ell_y y)] \\ \tilde{U}(\vec{\ell}) &= \sum_{x,y} W(x,y) U(x,y) \exp[-i(\ell_x x + \ell_y y)],\end{aligned}\tag{4.27}$$

where  $(x, y)$  is the position on the map and  $\vec{\ell}$  is the position on the Fourier plane. The window function  $W(x, y)$  apodizes the full sky map.

$\tilde{E}(\vec{\ell})$  and  $\tilde{B}(\vec{\ell})$  can be written in terms of  $\tilde{Q}(\vec{\ell})$  and  $\tilde{U}(\vec{\ell})$ :

$$\begin{aligned}\tilde{E}(\vec{\ell}) &= \tilde{Q}(\vec{\ell}) \cos 2\phi + \tilde{U}(\vec{\ell}) \sin 2\phi \\ \tilde{B}(\vec{\ell}) &= \tilde{Q}(\vec{\ell}) \sin 2\phi - \tilde{U}(\vec{\ell}) \cos 2\phi,\end{aligned}\tag{4.28}$$

where the angle  $\phi$  is equal to  $\arctan(\ell_x/\ell_y)$ .

The real space  $E$  and  $B$  maps can be obtained by the transformation:

$$\begin{aligned}E(\vec{r}) &= \int \frac{d^2\vec{\ell}}{2\pi} \left[ \tilde{Q}(\vec{\ell}) \cos 2\phi + \tilde{U}(\vec{\ell}) \sin 2\phi \right] \exp(i\vec{\ell} \cdot \vec{r}) \\ B(\vec{r}) &= \int \frac{d^2\vec{\ell}}{2\pi} \left[ \tilde{Q}(\vec{\ell}) \sin 2\phi - \tilde{U}(\vec{\ell}) \cos 2\phi \right] \exp(i\vec{\ell} \cdot \vec{r}),\end{aligned}\tag{4.29}$$

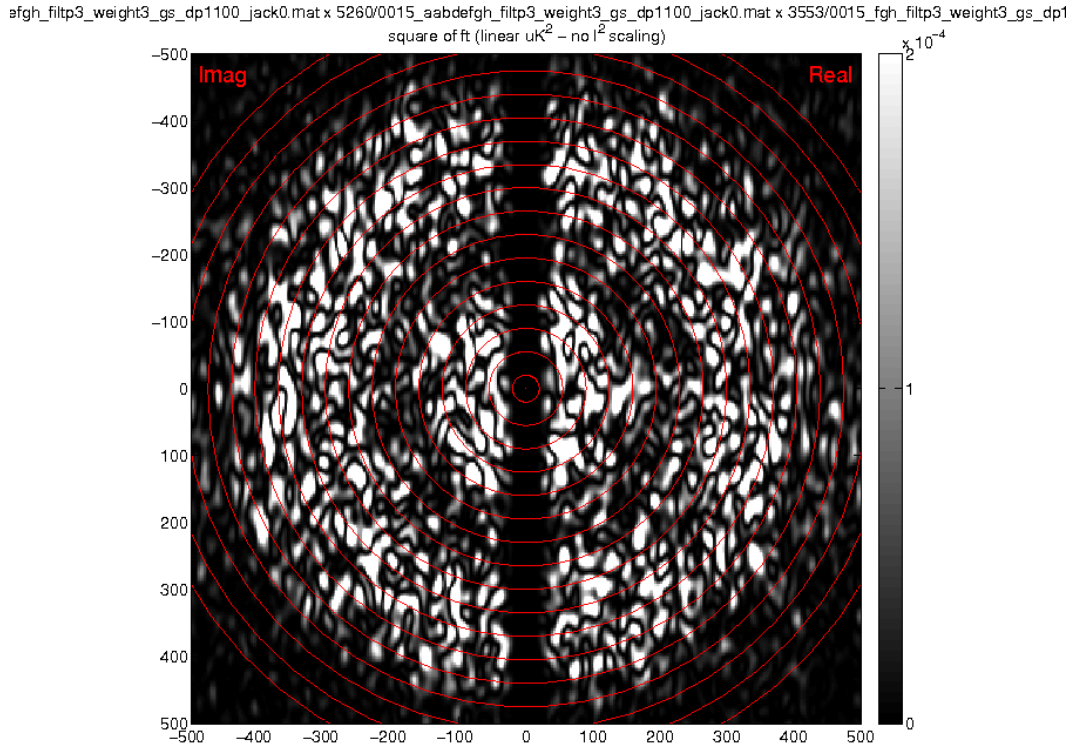


Figure 4.4: E-mode spectrum on two-dimensional Fourier Plane for BICEP3 lensed- $\Lambda$ CDM simulation. These two concentric rings of brighter modes are the first and second acoustic peaks, respectively. At higher values of  $\ell$  response is suppressed with the beam rolling. Modes along  $|l_x| \lesssim 40$  are suppressed as a result of polynomial and scan-synchronous timestream filters due to constant declination scanning strategy. The left side shows the imaginary part of complex Fourier modes, and the right side shows the real part of complex Fourier modes. The faint red circles indicate the bandpower bins, where bins 2 through 10 are used for cosmological results.

The two dimensional angular power spectrum  $(\ell_x, \ell_y)$  can be plotted on a plane. The E-mode spectrum for BICEP3 lensed- $\Lambda$ CDM simulation is shown in Figure 4.4. The left and the right sides shows the imaginary real parts of the complex Fourier modes. The vertical stripe on modes  $|l_x| \lesssim 40$  are suppressed as a result of polynomial and scan-synchronous timestream filters due to constant declination scanning strategy.

The one dimensional spectra  $\ell = \sqrt{\ell_x + \ell_y}$  is formed by binning.

## Bandpowers

The small angle approximation, and the pixelization of the maps makes the adjacent  $(\ell_x, \ell_y)$  modes to be correlated. The  $D_\ell^{EE}$  and  $D_\ell^{BB}$  spectra from lensed- $\Lambda$ CDM or tensor-to-scalar ratio are expected to be smooth over the multipole values. These motivate the binning of the spectrum into bandpowers over multipole ranges defined by:

$$D_\ell = \frac{1}{N_b} \sum_{\ell \in \ell_b} \frac{\ell(\ell+1)}{2\pi} |X_\ell|^2, \quad (4.30)$$

where  $b$  is the bin that covers the multipole range  $\ell_b = \{\ell | \ell_{b,\text{high}} \leq \ell < \ell_{b,\text{high}}\}$ ,  $N_b$  is the number of modes in bin  $b$ , and  $X$  can be chosen to for any auto or cross spectral combination of  $\{T, E, B\}$ . The BICEP/Keck Array has 17 bandpowers starting at  $\ell = 20$ , and uniform width of  $\Delta\ell = 35$ . The bandpowers are shown as faint red circles in 4.4.

## Bandpower Window Functions

In a CMB experiment, the observed spectra  $D_\ell^{\text{obs}}$  typically does not correspond to the theoretical values  $D_\ell$ . There is suppression and mixing of modes due to filtering, observation matrix, limited sky coverage and the apodization mask. For the bandpower bins defined in equation 4.30, the suppression and the mode mixing is captured by the matrix  $M_{\ell\ell'}$  where the entries are the mode to mode couplings of the theoretical and the observed values of the sky:

$$D_\ell^{\text{obs}} = M_{\ell\ell'} D_{\ell'} + \tilde{N}_\ell, \quad (4.31)$$

where  $\tilde{N}_\ell$  is the noise bias obtained from the mean of the signflip simulations defined in Section 4.2.

The observed data contain both signal  $\tilde{S}$  and noise modes  $\tilde{N}$ . The signal and the noise terms are assumed to be uncorrelated and should average out to zero in the products:

$$\langle |\tilde{S} + \tilde{N}|^2 \rangle = \langle |\tilde{S}|^2 \rangle + \langle |\tilde{N}|^2 \rangle, \quad (4.32)$$

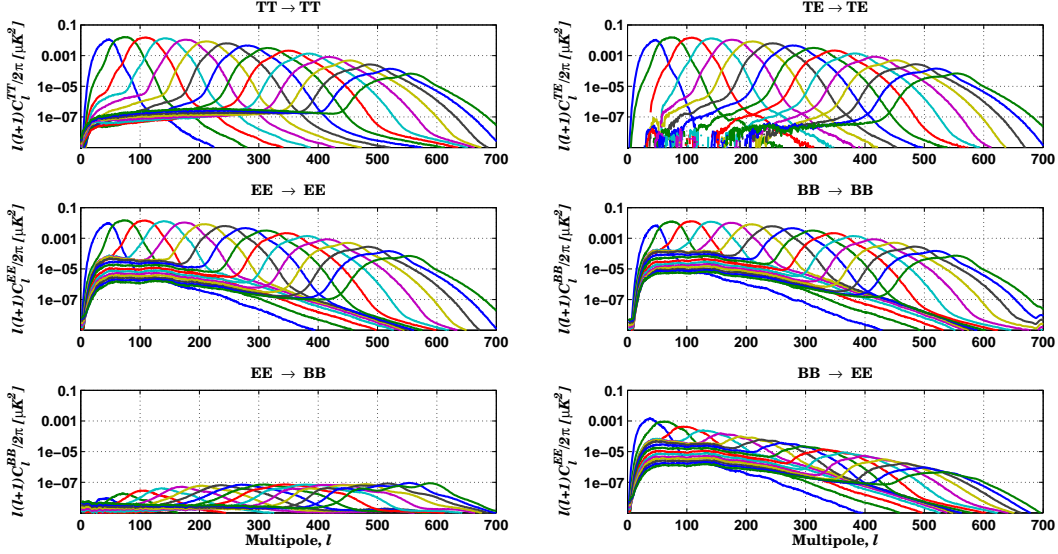


Figure 4.5: Bandpower window functions (BPWFs)  $M_{\ell\ell'}^{XX}$  with coupling of input  $TT$ ,  $EE$ ,  $BB$  to measured spectra. E to B and B to E leakage are labeled as  $EE \rightarrow BB$  and  $BB \rightarrow EE$  respectively. The beam function dominates the suppression factor at high  $\ell$ , filtering dominates at low  $\ell$ . Purification of the  $B$ -modes suppress the BPWFs for  $EE \rightarrow BB$  compared to the symmetric case of  $BB \rightarrow EE$ . Figure from [7].

Since  $\langle |\tilde{N}|^2 \rangle$  is a positive quantity, it adds a positive bias on the observed data. To account for this noise bias we subtract the mean of the signflip simulations from the observed spectra.

In order to determine the response of each bandpower, we simulate 100 realizations with unit power at a given multipole. We then reobserve these realizations and estimate the bandpower window function. The suppression factors are defined as the integral of these bandpower windows functions and account for suppression of the theoretical spectra.

### Matrix Based E/B Separation & Purification

If we consider an  $E$ -mode only input map with no  $B$ -modes, the map the map making process will estimate a non-zero power for  $B$ . Map projection, apodization, third order polynomial filtering on the scansets, scan-synchronous subtraction, de-projection of beam systematics, and observing a finite region of sky with the flat sky approximation will break the orthogonality of the harmonic decomposition in Equation 1.28. The result is a leakage of the modes to each other:  $E \rightarrow B$  and  $B \rightarrow E$ .

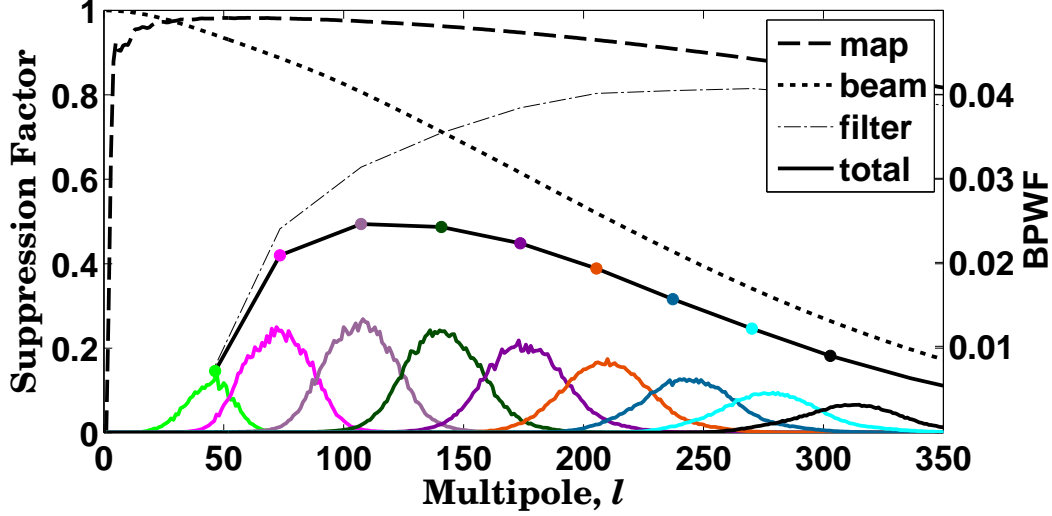


Figure 4.6:  $BB$  suppression factor. The beam function dominates the suppression factor at high  $\ell$ , filtering dominates at low  $\ell$ . The map window function for  $0^\circ.25$  pixels and finite size of the map is shown as dashed lines. Figure from [7].

In this section we focus on the leaked  $B$ -modes from  $E$ -modes since  $\Lambda$ CDM is much stronger than the lensing or tensor  $B$ -mode spectrum and the science results are based on  $B$ -modes only. For foregrounds, such as dust where the ratio of  $E/B$  is of order 2, there is some  $B$  to  $E$  leakage that is not accounted for but it is still relatively small.

Smith method uses pseudo- $C_\ell$  quadratic estimators for an analytical correction for partial sky observation [84]. However the Smith method can only correct for a fraction of the mixing when the pipeline contains many steps of filtering. Instead we use a generalized numerical method adapted for BICEP/Keck Array using eigenvalue decomposition [36].

Here we present a brief overview. For full construction refer to [7, 90] and for improvements refer to [93].

Consider a polarization field  $\mathbf{P}$ :

$$\mathbf{P}(\mathbf{r}) = \begin{bmatrix} Q(\mathbf{r}) \\ U(\mathbf{r}) \end{bmatrix} = - \sum_{\ell=2}^{\infty} \sum_{m=-\ell}^{\ell} a_{\ell m}^E Y_{\ell m}^E(\hat{n}) + a_{\ell m}^B Y_{\ell m}^B(\hat{n}). \quad (4.33)$$

On a manifold  $\Omega$ , the inner product of the polarization fields is defined as

$$\mathbf{P} \cdot \mathbf{P}' \equiv \int_{\Omega} \mathbf{P} \cdot \mathbf{P}' d\Omega. \quad (4.34)$$

On a full sky E and B mode polarization fields are orthogonal from the spherical harmonic relation:

$$\int_{S^2} Y_{\ell m}^E(\mathbf{r}) \cdot Y_{\ell' m'}^B(\mathbf{r}) dS = 0. \quad (4.35)$$

We look at the observed maps that are filtered and cover a portion of the sky. The overlapping subspace between the observed E and B modes is called the ambiguous space. We decompose the vector fields into three components: pure  $E$ -modes, pure  $B$ -modes, and ambiguous modes.

A pure  $B$ -modes is defined as the orthogonal space to observed  $E$ -modes, and therefore has no ambiguous mode contribution:

$$\mathbf{b}^T \cdot \mathbf{Y}_{\ell m}^E = 0, \quad (4.36)$$

where  $\mathbf{b}$  is a vector in the subspace of pure  $B$ -modes. We multiply the above by the conjugate transpose and sum over multipole values:

$$\sum_{\ell m} |a_{\ell m}^E \mathbf{b}^T \mathbf{Y}_{\ell m}^E|^2 = \mathbf{b}^T \left( \sum_{\ell m} a_{\ell m}^E a_{\ell m}^{E*} Y_{\ell m}^E Y_{\ell m}^{E\dagger} \right) \mathbf{b}. \quad (4.37)$$

Using the relation  $C_\ell^{EE} = \langle a_{\ell m}^E a_{\ell m}^{E*} \rangle$  we define the  $E$ -mode covariance matrix  $C_E$ :

$$\begin{aligned} \mathbf{C}_E &\equiv \sum_{\ell m} \langle a_{\ell m}^E a_{\ell m}^{E*} \rangle Y_{\ell m}^E Y_{\ell m}^{E\dagger} \\ &= \sum_{\ell m} C_\ell^{EE} Y_{\ell m}^E Y_{\ell m}^{E\dagger}, \end{aligned} \quad (4.38)$$

Consider the observation matrix  $\mathbf{R}$  that transforms a vector of true sky  $\mathbf{m} = [T, Q, U]$  into a vector of observed map  $\tilde{\mathbf{m}} = [\tilde{T}, \tilde{Q}, \tilde{U}]$ :

$$\begin{bmatrix} \tilde{T} \\ \tilde{Q} \\ \tilde{U} \end{bmatrix} = \mathbf{R} \begin{bmatrix} T \\ Q \\ U \end{bmatrix}, \quad (4.39)$$

where the reobservation matrix  $R$  is a  $3 \times 3$  block of matrices:

$$R = \begin{bmatrix} R_{TT} & 0 & 0 \\ 0 & R_{QQ} & R_{QU} \\ 0 & R_{UQ} & R_{UU} \end{bmatrix}, \quad (4.40)$$

we are only concerned about the subset of  $Q$  and  $U$ :

$$R = \begin{bmatrix} R_{QQ} & R_{QU} \\ R_{UQ} & R_{UU} \end{bmatrix}, \quad (4.41)$$

and:

$$\begin{aligned} \tilde{C}_E &= RC_E R^T \\ \tilde{C}_B &= RC_B R^T, \end{aligned} \quad (4.42)$$

where  $\tilde{C}_E$  and  $\tilde{C}_B$  are the reobserved  $E$  and  $B$  mode signal covariance matrices.

We solve the generalized eigenvalue problem to isolate pure B-modes:

$$\left( \tilde{C}_B + \sigma^2 \mathbf{I} \right) \mathbf{x} = \lambda \left( \tilde{C}_E + \sigma^2 \mathbf{I} \right) \mathbf{x}, \quad (4.43)$$

where  $\lambda$  is the eigenvalue of the eigenvector  $\mathbf{x}$ ,  $\mathbf{I}$  is the identity matrix, and  $\sigma$  is a small constant chosen to be 1/100 times the mean of the diagonal elements of the covariance matrices.

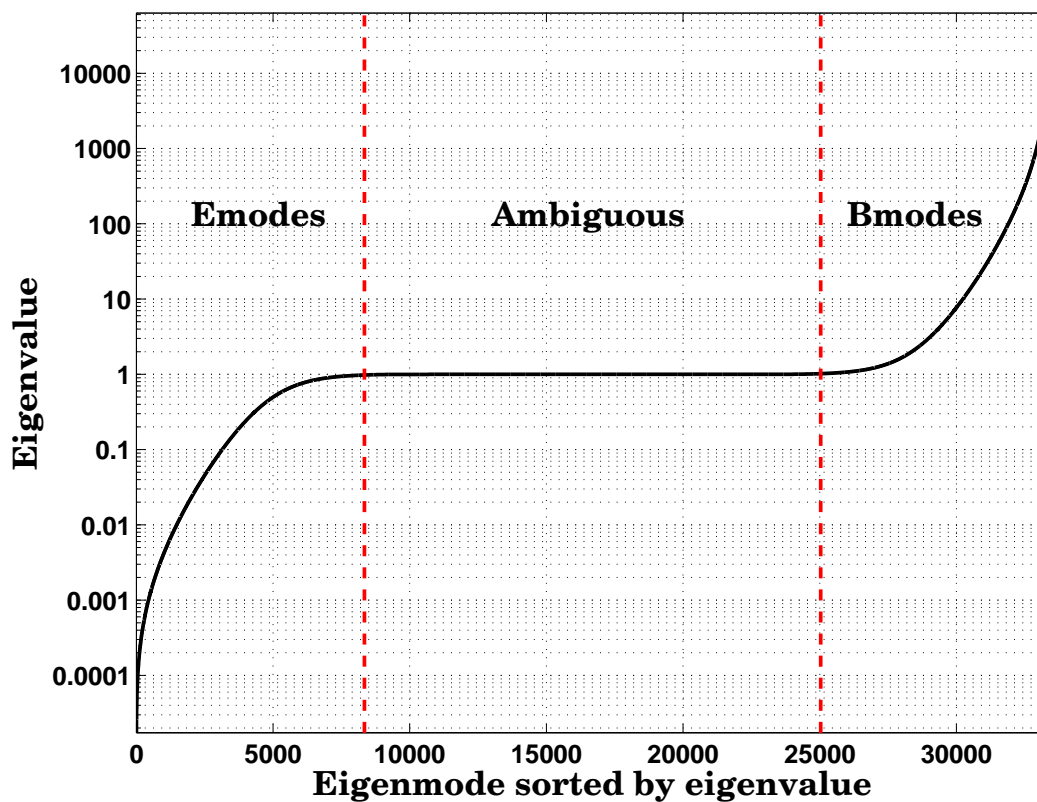


Figure 4.7: The magnitude-ordered generalized eigenvalues for the BICEP2 observed covariance matrix. The largest and the smallest 1/4 of the eigenvalues are used to construct the  $B$  and  $E$  modes that can be observed with BICEP/Keck Array scanning strategy and analysis. Eigenvalues close to 1 correspond to ambiguous modes, the modes that are simultaneously  $E$  and  $B$  in the observed space and are thrown out. Figure from [7].

*Chapter 5*

## MULTI-COMPONENT ANALYSIS

In this chapter we present our multi-component, multi-frequency, spectral-based analysis framework used as our analysis pipeline for extracting cosmological parameters from polarized cosmic microwave background (CMB) data. The primary objective of this analysis framework is to analyze polarized CMB data and isolate any primordial gravitational wave signal from polarized astrophysical foregrounds including B-mode signals from gravitational lensing on small scales, synchrotron radiation emitted by charged particles in our galaxy's magnetic fields at lower frequencies, and polarized dust emission at higher frequencies.

CMB observations are made using ground-based, balloon-borne, and space-based instruments. The number of detectors used by these experiments are rapidly increasing, leading to increasingly placing stronger constraints on cosmological parameters. Our main scientific goal is to improve the sensitivity on the tensor-to-scalar ratio  $r$ . To achieve this, we have developed a likelihood analysis framework that can be used to analyze data from different polarized CMB experiments. In our likelihood analysis, we use data from BICEP/Keck Array, *Planck*, and *WMAP*.

Over the past decade, the BICEP/Keck Array series of telescopes has significantly improved in terms of detector count and frequency coverage. BICEP2 had a single receiver at 150 GHz, while the Keck Array diversified this coverage to include 95 GHz and 220 GHz in the BK15<sup>1</sup> data set. In our latest BK18 analysis, we include data from BICEP3, which is a single receiver dedicated to 95 GHz observation, and Keck Array, which has four receivers deployed at 220 GHz.

---

<sup>1</sup>BK15, BK18: all data taken up to and including the 2015, 2018 observing season respectively

## 5.1 Historical Overview and Motivation

In 2014 BICEP2 detected a B-mode signal at angular scales [11]. However, subsequent analyses, including one that incorporated additional data from the *Planck* satellite [13], revealed that the B-modes detected by BICEP2 had a significant contribution from galactic dust. These analysis relied on a single BICEP/Keck band which consisted of a high signal to noise map at 150 GHz. In a subsequent analysis by BKP, the BICEP/Keck band was cross-correlated with the *Planck*/WMAP maps, which were known to be noisy [13]. This analysis resulted in an upper limit on the tensor-to-scalar ratio  $r$  of  $r < 0.12$  at a confidence level of 95%. However it was necessary to obtain high signal-to-noise ratio maps and multi-frequency coverage to further constrain the value of  $r$ .

The addition of the 95 GHz bands to the Keck Array allowed for an improvement in the upper bound on  $r$  down to  $r < 0.09$  with the BK14 data [12]. Subsequently, data at 95 GHz and 220 GHz at Keck further improved the upper bound, yielding  $r < 0.072$  with BK15 data [9].

An analysis framework was developed to accurately account for a multi-component, multi-frequency, multi-experiment spectral-based likelihood analysis of polarized cosmic microwave background (CMB) data

The BICEP/Keck Array instruments have successfully measured the lensing component in the CMB at angular scales. Other experiments such as ACTPol, Polarbear, and SPTpol have also measured the lensing component at smaller angular scales, as illustrated in Figure 5.2.

## 5.2 Multi-Component Model

A multi-component likelihood framework is used to estimate the cosmological parameters. This framework takes into account various components, including both cosmological and foreground components, and uses their values to estimate bandpower expectation values. The cosmological component is composed of lensing and tensor modes, which are carefully considered in the likelihood analysis.

The values of the multi-component model, which includes cosmological and foreground components, are used to estimate the bandpower expectation values. Lensing and tensor modes contribute to the cosmological component. The cosmological

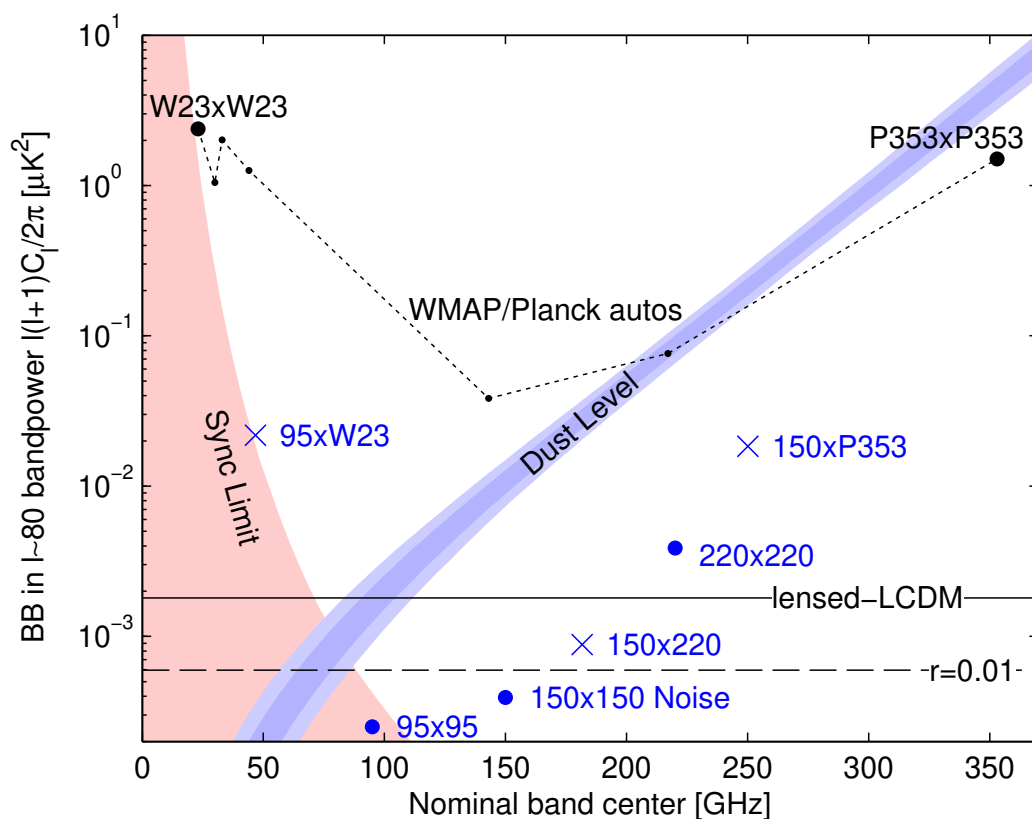


Figure 5.1: BB bandpower expectation values and noise uncertainties in BICEP/Keck Array field. The expected signal power of lensed- $\Lambda$ CDM and tensor-only cosmological models are shown as solid and dashed black lines. The signal levels are flat with frequency since CMB units are used. The blue bands represent the range of dust, while the red shaded region shows the 95% upper limit on synchrotron emissions in the baseline analysis, including the uncertainties in the amplitude and frequency spectral index parameters. The noise uncertainties of the BICEP/Keck Array auto-spectrum are shown as large blue circles, and WMAP/Planck evaluated in the BICEP/Keck Array field are shown in black. The noise uncertainty of selected cross-spectra is represented by blue crosses. Figure taken from [9].

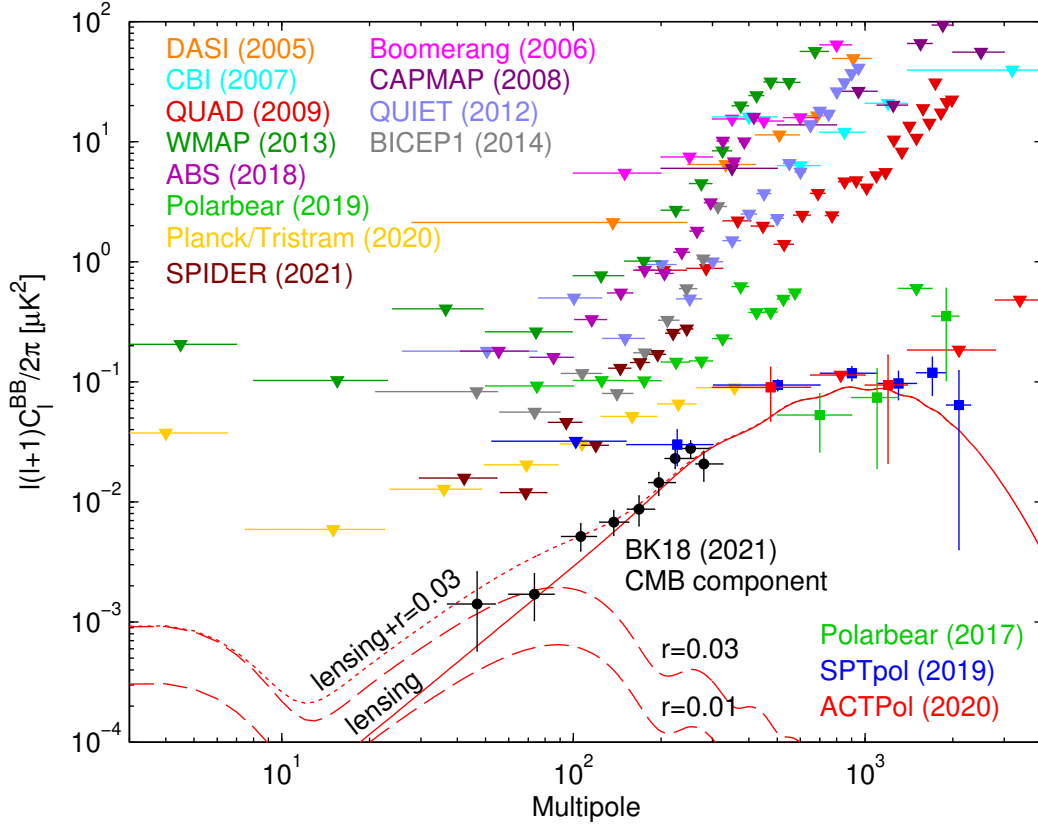


Figure 5.2: A summary of B-mode polarization measurements. The lensing B-modes, which are expected to peak at arcminute scales, are represented by solid red lines, while the tensor modes are shown by dashed red lines. Upper bounds on the tensor-to-scalar ratio are denoted by triangles, while detections are represented by circles. Galactic foregrounds have been removed from the BK18 data shown in this figure. Figure taken from [9].

component of BB for the multi-component model can be expressed as:

$$D_{l, BB, \text{cosmology}}^{v_1 \times v_2} = \left( \frac{r}{0.1} \right) D_{l, BB, \text{tensor}}^{v_1 \times v_2} + A_L D_{l, BB, \text{lensing}}^{v_1 \times v_2}, \quad (5.1)$$

where  $D_{l, BB, \text{tensor}}$  is the tensor signal with  $r = 0.1$ ,  $D_{l, BB, \text{lensing}}$  is the expected lensing spectrum from lensed E-modes. The tensor and lensing contributions are characterized by the parameters  $r$  and  $A_L$  respectively.

To summarize, the multi-component model includes both lensed  $\Lambda$ CDM and tensor components, which can be parameterized by:

- $r$ : Tensor to scalar ratio;

- $A_L$ : Amplitude of lensing potential.

The foreground components of the multi-component model include galactic dust, galactic synchrotron, and a spatially correlated component of dust and synchrotron. Dust and synchrotron components allow for a frequency decorrelation and are carefully considered in the analysis. The foreground component of the multi-component model for the BB bandpower can be expressed as:

$$\begin{aligned}
 D_{l, BB}^{\nu_1 \times \nu_2} &= A_d \Delta'_d f_d^{\nu_1} f_d^{\nu_2} \left( \frac{\ell}{80} \right)^{\alpha_d} \\
 &+ A_s \Delta'_s f_s^{\nu_1} f_s^{\nu_2} \left( \frac{\ell}{80} \right)^{\alpha_s} \\
 &+ \epsilon \sqrt{A_d A_s} \left( f_d^{\nu_1} f_s^{\nu_2} + f_s^{\nu_1} f_d^{\nu_2} \right) \left( \frac{\ell}{80} \right)^{(\alpha_d + \alpha_s)/2},
 \end{aligned} \tag{5.2}$$

where the first term is the dust contribution, the second term is the synchrotron contribution, and the third term corresponds to the correlated dust-synchrotron component. The parameters used in equation 5.2 for the foreground model are:

- $A_d, A_s$ : The amplitude for dust and synchrotron in units of  $\mu\text{K}_{\text{CMB}}^2$ , measured at an angular scale of  $\ell = 80$ . The dust amplitude is defined at a pivot frequency of 353 GHz, and synchrotron amplitude is defined at a pivot frequency of 23 GHz.
- $f_d^\nu, f_s^\nu$ : The frequency scaling coefficients for dust and synchrotron  $f_d^\nu, f_s^\nu$ , for a given bandpass, allow us to scale the spectral energy density to a given frequency response.

The spectral energy density (SED) is a power-law with a blackbody spectrum at temperature  $T_d$  for dust and a power law for synchrotron:

$$\begin{aligned}
 f_d^{\nu_i} &\propto \frac{\int R_i(\nu) \nu^{3+\beta_d} [\exp(h\nu/k_B T_d) - 1]^{-1} d\nu}{\nu_{\text{pivot}}^{3+\beta_d} [\exp(h\nu_{\text{pivot}}/k_B T_d) - 1]^{-1}} \\
 f_s^{\nu_i} &\propto \frac{\int R_i(\nu) \nu^{2+\beta_s} d\nu}{\nu_{\text{pivot}}^{2+\beta_s}},
 \end{aligned} \tag{5.3}$$

where  $k_B$  is the Boltzmann constant,  $h$  is the Planck constant,  $T_d$  is the dust temperature as measured by *Planck* at intermediate Galactic latitudes to be 19.6 K [17],  $R_i(\nu)$  is the bandpass of corresponding to the band  $i$ , measured in  $\mu\text{K}_{\text{CMB}}$  as a function of frequency  $\nu$ .

We convert Rayleigh-Jeans temperature to CMB temperature through the proportionality factor  $f^{\nu_i}$ :

$$f^{\nu} = \frac{\nu_{\text{pivot}}^4 \exp(h\nu_{\text{pivot}}/k_B T_{\text{CMB}}) [\exp(h\nu_{\text{pivot}}/k_B T_{\text{CMB}}) - 1]^{-2}}{\int R_i(\nu) \nu^4 \exp(h\nu/k_B T_{\text{CMB}}) [\exp(h\nu/k_B T_{\text{CMB}}) - 1]^{-2} d\nu}. \quad (5.4)$$

In the likelihood analysis we report values for the spectral indices  $\beta_d, \beta_s$ .

- $\alpha_d, \alpha_s$ : Power law scaling parameters of dust and synchrotron with multipole  $\ell$ .
- $\epsilon$ : Spatial correlation between the dust and synchrotron components. We assume the scaling is constant with respect to multipole  $\ell$ .
- $\Delta_d, \Delta_s$ : Decorrelation of dust and synchrotron, defined to be in range  $[0, 1]$ . The case  $\Delta = 1$  corresponds to no decorrelation, whereas  $\Delta = 0$  would correspond to complete loss due to decorrelation.

### 5.3 Data Selection

Multi-component likelihood analysis uses polarized data from BICEP2, Keck, BICEP3, WMAP, and Planck. BICEP2, Keck, BICEP3 are combined to generate three bands: 95, 150, and 220 GHz. Due to its bigger aperture, BICEP3 provides data deeper than Keck any band, with greater angular resolution than Keck 95 and 150 GHz and bigger region of observation. Planck maps are full mission maps from Planck science release. 23 GHz (K-band) and 33 GHz (Ka-band) are used from WMAP 9 year mission results.

The BICEP/Keck Array bands that go into BK18 likelihood analysis consist of BICEP2 data at 150 GHz, Keck data at 95, 150, and 220 GHz, and BICEP3 data at 95 GHz. The total Keck receiver-year equivalent of the data is 28, 18, and 14 receiver years at 95, 150, and 220 GHz respectively [18].

Table 5.1: A summary of Multicomponent Model Parameters

Variable	Parameter
$r$	Tensor to scalar ratio
$A_L$	Lensing amplitude
$A_d$	Dust amplitude in $\mu\text{K}_{\text{CMB}}^2$ at 353 GHz and $\ell = 80$
$\beta_d$	Dust spectral index
$T_d$	Dust temperature
$\alpha_d$	Dust spatial spectral index
$\Delta_d$	Dust frequency decorrelation
$EB_d$	EE to BB ratio for dust
$A_s$	Sync amplitude in $\mu\text{K}_{\text{CMB}}^2$ at 23 GHz and $\ell = 80$
$\beta_s$	Sync spectral index
$\alpha_s$	Sync spatial spectral index
$\Delta_s$	Sync frequency decorrelation
$EB_s$	EE to BB ratio for synchrotron
$\epsilon$	Synchrotron - dust spatial correlation

BICEP/Keck Array are filtered due to polynomial filtering, ground subtraction. Planck maps are filtered by their effective instrumental beams. In the analysis the difference in the filtering strategy have been accounted by the reobservation framework.

During the reobservation, WMAP and Planck maps are deconvolved with their respective instrumental beams and then convolved with the BICEP/Keck beam profile using HEALPix framework. A coordinate rotation for T, Q, U maps is performed from Galactic to celestial coordinates with HEALPix function ALTERALM. Polynomial filtering, ground subtraction, and deprojection is performed in an identical way to BICEP/Keck data processing pipeline. The reobserved maps are generated, after applying deprojection to the filtered data.

The power spectra of the reobserved maps are estimated using the matrix purification method to avoid E to B mode leakage. Purification matrices are generated for all BICEP/Keck bands. For small field external WMAP and Planck maps the purification matrix for 150 GHz are used, whereas for the large field external WMAP and Planck maps, the purification matrix for Bicep3 95 GHz are used. We consider all possible auto and cross spectra between all the available bands.

The set of real bandpowers consists that is used for the likelihood analysis consist of all the possible auto and cross spectra for all the bands involved.

## 5.4 Likelihood Analysis

The BICEP/Keck Array series of telescopes observe a small fraction of the sky, limiting the number of degrees of freedom. This leads to non-Gaussianity of the likelihood, especially low values of  $\ell$ .

We use Hamimeche-Lewis likelihood (HL likelihood) approximation [49], which uses a quadratic estimator for a quick computation after transforming the bandpowers and the bandpower covariances.

The HL likelihood function  $\mathcal{L}$  is given by:

$$-2 \log \mathcal{L} (\{D_b\}|\{\hat{D}_b\}) = \mathbf{X}^T \mathbf{M}_f^{-1} \mathbf{X}, \quad (5.5)$$

where  $\{\mathbf{D}_b\}$  are expected bandpowers of the model,  $\{\hat{\mathbf{D}}_b\}$  are the bandpowers from real data,  $\mathbf{M}_f$  is the bandpower covariance matrix (BPCM) for a given fiducial model calculated from 499 realizations of signal and noise simulations. The vector  $\mathbf{X}$  is a vector of bandpowers transformed with:

$$\mathbf{X}_b \equiv \text{vecp} \left[ \left( \mathbf{D}_b^f \right)^{1/2} g \left( \mathbf{D}_b^{-1/2} \hat{\mathbf{D}}_b \mathbf{D}_b^{-1/2} \right) \left( \mathbf{D}_b^f \right)^{1/2} \right], \quad (5.6)$$

where  $\mathbf{D}_b^f$  are the theoretical bandpower matrix for a fiducial model. The  $\text{vecp}(\mathbf{A})$  function returns a column vector consisting of the upper triangular elements of the symmetric matrix  $\mathbf{A}$ . The function  $g(x)$  is given by the the function:

$$g(x) = \text{sign}(x - 1) \sqrt{2(x - \ln x - 1)}. \quad (5.7)$$

The matrix notation for  $\mathbf{D}$  indicates that this is a symmetric matrix containing auto-spectra on the diagonal and cross-spectra off diagonal.

We use 499 realizations of signal and noise simulations to calculate the BPCM. The signal simulations use  $\Lambda$ CDM as its basis. We include signal  $\times$  signal, signal  $\times$  noise, and noise  $\times$  noise terms evaluated independently in the BPCM. This approach of including signal and noise terms separately allows us to rescale signal and noise for different fiducial models under consideration or making future forecasts.

In order to reduce uncertainty from Monte Carlo sampling, some terms with zero expectation are manually set to zero. All off-diagonal terms between  $\ell$  bandpower bins separated by more than one  $\ell$ -bin are set to zero [37].

The posterior probability distribution is sampled with CosmoMC [67] Markov Chain Monte Carlo (MCMC) engine.

## 5.5 BK18 Likelihood

The BK18 data [18] includes all data up to and including the 2018 observing season. With the addition of BICEP3 and additional *Keck* Array data, the BK18 data set is equivalent to 28/18/14 *Keck* Array receiver years at 95/150/220 GHz. The  $Q/U$  maps reach depths of 2.8, 2.8, and 8.8  $\mu\text{K}_{\text{CMB}}$  – arcmin at 95, 150, and 220 GHz respectively, over an area of  $\approx 400$  square degrees at 150 and 220 GHz, and  $\approx 600$  square degrees at 95 GHz.

In the BK18 likelihood analysis, we take the 66 BB auto and cross spectra between the BICEP/*Keck* Array and publicly available *Planck* and WMAP polarized maps from 23 to 353. We use nine bandpowers per spectrum in the range  $20 < \ell < 330$ . The  $\Lambda\text{CDM} + r + \text{dust} + \text{synchrotron} + \text{noise}$  multi-component model consists of eight free parameters allowed to vary in the baseline likelihood analysis.

We start with a fiducial model to evaluate BPCM:  $r = 0$ ,  $A_d = 3.75 \mu\text{K}^2$ ,  $A_s = 0 \mu\text{K}^2$ ,  $\beta_d = 1.59$ ,  $\beta_s = -3.0$ ,  $\alpha_d = -0.42$ ,  $\alpha_s = -0.6$  and  $\epsilon = 0$ . The lensing amplitude is held fixed at  $A_L = 1$  as shown by *Planck* 2018 cosmological parameters [22].

In BK15 we used a Gaussian prior on the dust frequency spectral index  $\beta_d$  based on other regions of sky from *Planck* data. With BK18, the signal to noise of 220 GHz maps exceed that of *Planck* at 353 GHz, so a prior on the dust frequency spectral index is no longer used. We continue to use a Gaussian prior for the synchrotron frequency spectral index  $\beta_s = -3.1 \pm 0.3$  obtained from WMAP 23 and 33 GHz maps [46]. We use uniform priors on the multipole power law scaling parameters  $\alpha_d$  and  $\alpha_s$  in the range  $-1$  to  $0$ , and the spatial correlation between the dust and synchrotron component  $\epsilon$  in the range  $-1$  to  $1$ .

The likelihood analysis is performed on 499 realizations of  $\Lambda\text{CDM} + r + \text{dust} + \text{synchrotron} + \text{noise}$  simulations. We use the mean value of these simulations to check for biases, and the standard deviation as the  $1\sigma$  uncertainty in parameter

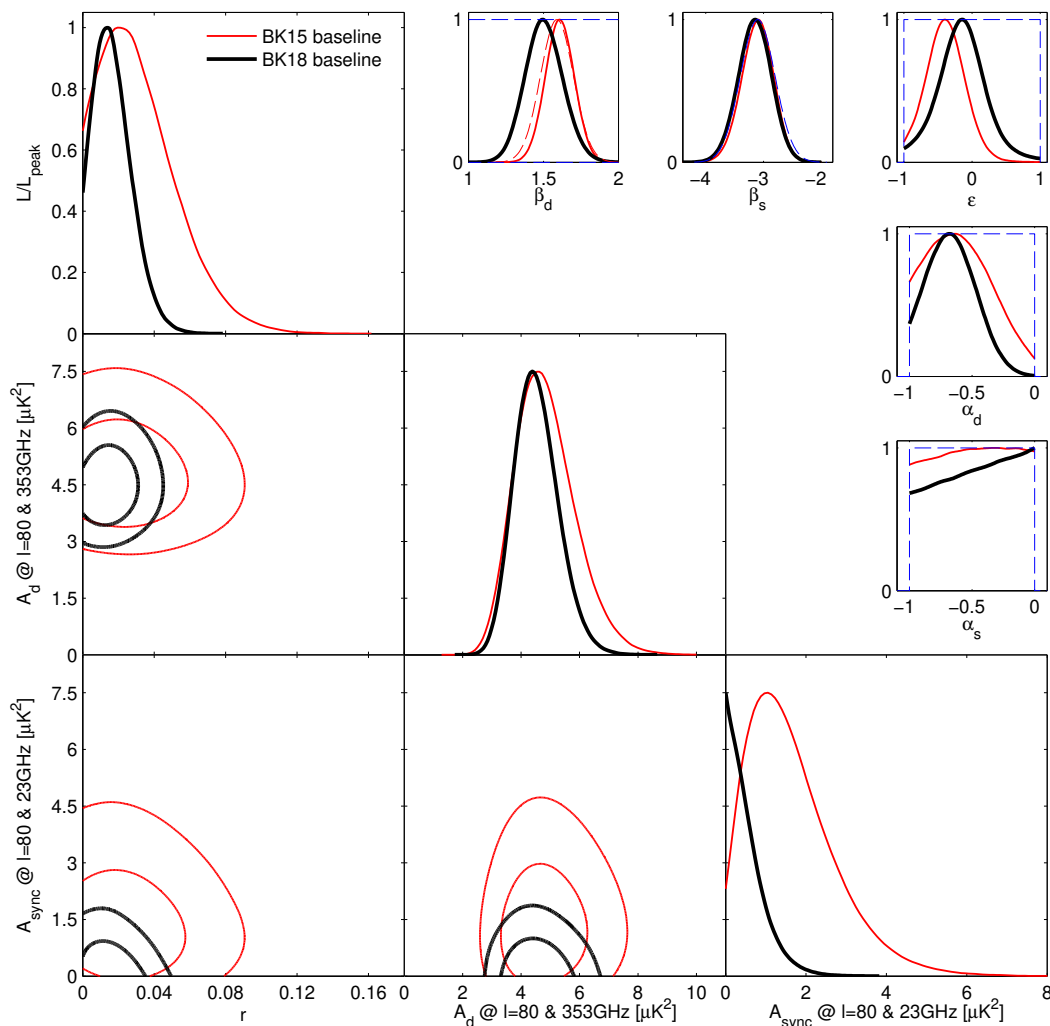


Figure 5.3: Multicomponent multi-spectral likelihood analysis of BICEP/Keck Array data. The red curves correspond to the results obtained in the BK15 results, whereas the black curves represent the baseline BK18 results. These results include a significant amount of additional data at 95 and 220 GHz, observed by Keck Array and BICEP3 during the 2016-2018 observing seasons. The upper limit on the tensor-to-scalar ratio is further constrained to  $r < 0.036$  at a 95% confidence level. The parameters  $A_d$  and  $A_s$  denote the amplitudes of the dust and synchrotron B-mode power spectra, respectively, and  $\beta$  and  $\alpha$  represent their corresponding frequency and spatial spectral indices. We also include a spatial correlation coefficient  $\epsilon$  between dust and synchrotron. The dashed lines here correspond to priors that were placed on these parameters. Gaussian prior on  $\beta_d$  has been removed going from BK15 to BK18 as the additional data 220 GHz has enough constraining power. Figure from [18].

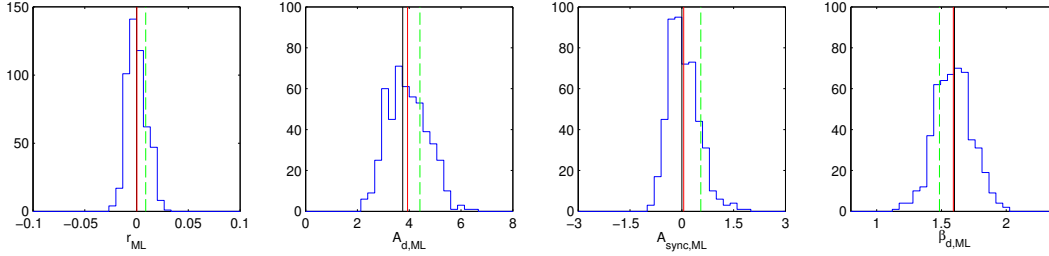


Figure 5.4: Maximum likelihood results from 499 realizations of  $\Lambda$ CDM +  $r$  + dust + synchrotron + noise simulations ( $r = 0$ ,  $A_d = 3.75 \mu\text{K}^2$ ,  $A_s = 0 \mu\text{K}^2$ ,  $\beta_d = 1.6$ ,  $\alpha_d = -0.42$ ). The input values are shown in vertical black lines. The recovered likelihoods of the 499 realizations are shown in blue histogram and the red vertical lines are their mean values. The vertical dashed green lines are the likelihood results from real BK18 data. Figure from [18].

estimation. The biases are very small for BK18 as seen in Figure 5.4.

The peak value of the BK18 likelihood corresponds to  $r_{0.05} = 0.014^{+0.010}_{-0.011}$ , which has tightened significantly and slightly shifted down compared to BK15 results ( $r_{0.05} = 0.020^{+0.021}_{-0.018}$ ) [9]. BK18 detects dust with amplitude  $A_d = 4.4^{+0.8}_{-0.7} \mu\text{K}^2$ . There is a down shift on  $\beta_d$ , resulting from the removal of the Gaussian prior, however the widths remain consistent. The additional *Keck* Array receivers at 220 GHz provide comparable constraining power with the previous Gaussian prior used in BK15 (Gaussian prior:  $\beta_d = 1.59 \pm 0.11$ ).

BK15 showed weak evidence for synchrotron  $A_s = 1.0^{+1.2}_{-0.8} \mu\text{K}^2$  ( $A_s < 3.7 \mu\text{K}^2$  at 95% confidence). With the subsequent BK18 data, this weak evidence is no longer present as the curve for the synchrotron amplitude  $A_s$  peaks at zero ( $A_s < 1.4 \mu\text{K}^2$  at 95% confidence).

With BK18, the upper bound constraint on  $r$  becomes  $r < 0.36$  at 95% confidence, with  $\sigma(r) = 0.009$ .

## 5.6 Fisher Forecasting

Fisher information matrix is used to calculate expected uncertainties in an experiment. We use the Fisher matrix formalism to forecast the space of cosmological parameter sensitivities for future CMB polarization experiments. We use our current performance of the BICEP / Keck receivers for the forecasting.

Fisher analysis assumes the likelihoods to follow a Gaussian distribution, which might not always be the case [94]. The Fisher approximation is computationally

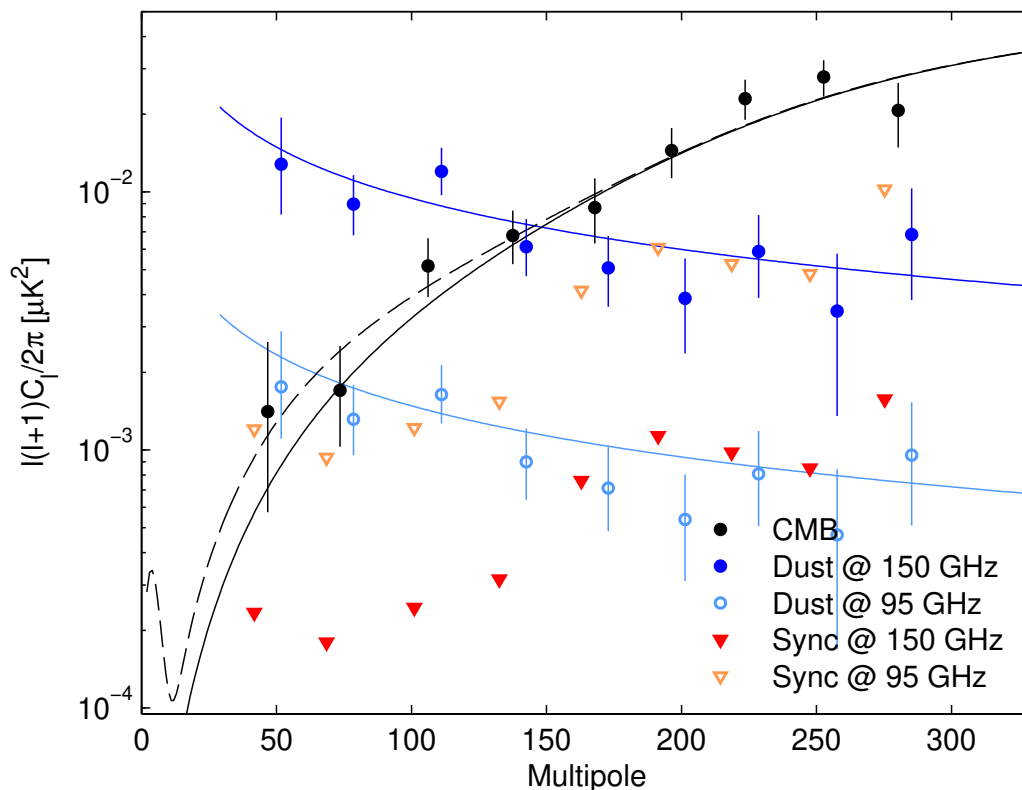


Figure 5.5: BB spectral decomposition into synchrotron (red), CMB (black), and dust (blue) components at 95 GHz (filled) or 150 GHz (open). The decomposition is calculated independently in each bandpower, and marginalized over  $\beta_d$ ,  $\beta_s$ , and  $\epsilon$ . Error bars correspond to 68% intervals, with the point marking the most probable value. For synchrotron, which is not detected, the downward triangles correspond to 95% upper limits. Figure from [18].

very efficient [95] and useful for quickly determining constraints. A more accurate but computationally more expensive way to forecast is to generate  $\Lambda$ CDM +  $r$  + dust + synchrotron + noise simulations. Instead of generating each component from scratch, we scale noise simulations to get an estimate of adding more receiver years. This method is discussed in Section 5.7. We use this method to validate the Fisher predictions with maximum likelihood estimations. The predictions are accurate when all parameters have flat priors. However, when we include Gaussian priors the results disagree.

The input for the Fisher information matrix is the signal-only, noise-only and signal  $\times$  noise bandpower covariance terms and signal and noise bandpowers obtained from 95, 150, and 220 GHz maps from BICEP/Keck Array. The noise terms include

contributions from detector performance, weather, and detector yield. When we make forecasting we assume a survey weight that scales appropriately with the number of detectors, and the detector noise is uncorrelated.

Forecasts are computed using B-mode noise spectra and map derived covariance matrices. The spectral-based Fisher formalism (developed by [37]).

Given data bandpowers  $d$ , the likelihood function  $\mathcal{L}$  as a function of theory parameters  $\theta$ , expectation values  $\mu(\theta)$ , and bandpower covariance matrix  $\Sigma(\theta)$  is assumed to be of the form:

$$\mathcal{L}(\theta|d) \propto \frac{1}{\sqrt{|\Sigma(\theta)|}} \exp \left[ -\frac{1}{2} (d - \mu(\theta))^T \Sigma(\theta)^{-1} (d - \mu(\theta)) \right]. \quad (5.8)$$

The terms in the Fisher matrix, evaluated at a fiducial model  $\theta_f$  are:

$$F_{ij} = - \left\langle \frac{\partial^2 \log \mathcal{L}}{\partial \theta_i \partial \theta_j} \bigg|_{\theta=\theta_f} \right\rangle, \quad (5.9)$$

after doing some algebra and collecting the terms, the Fisher terms are:

$$F_{ij} = \frac{\partial \mu^T}{\partial \theta_i} \Sigma^{-1} \frac{\partial \mu}{\partial \theta_j} + \frac{1}{2} \text{Tr} \left( \Sigma^{-1} \frac{\partial \Sigma}{\partial \theta_i} \Sigma^{-1} \frac{\partial \Sigma}{\partial \theta_j} \right). \quad (5.10)$$

The sensitivity of parameter  $\theta_i$  are on the diagonal of the inverse Fisher matrix:

$$\sigma_{ii} \equiv \sigma(\theta_i) = \sqrt{(F^{-1})_{ii}}. \quad (5.11)$$

If there is a prior with width  $\sigma_i$ , we add the term  $P$  where  $P$  is 0 except for the term  $P_{ii} = 1/\sigma_i^2$  to the Fisher matrix:

$$\sigma_{ii} \equiv \sigma(\theta_i) = \sqrt{((F + P)^{-1})_{ii}}. \quad (5.12)$$

## 5.7 Forecasting with Maximum Likelihood

In addition to the Fisher forecasting described in Section 5.6, we also use ML search to forecast how BK/BA may constrain complex dust models. Parameter sensitivities  $\sigma$  are estimated by 499 realizations of  $\Lambda$ CDM +  $r$  + dust + synchrotron + noise simulations. For forecasting, we scale noise sims with the appropriate number of receiver years.

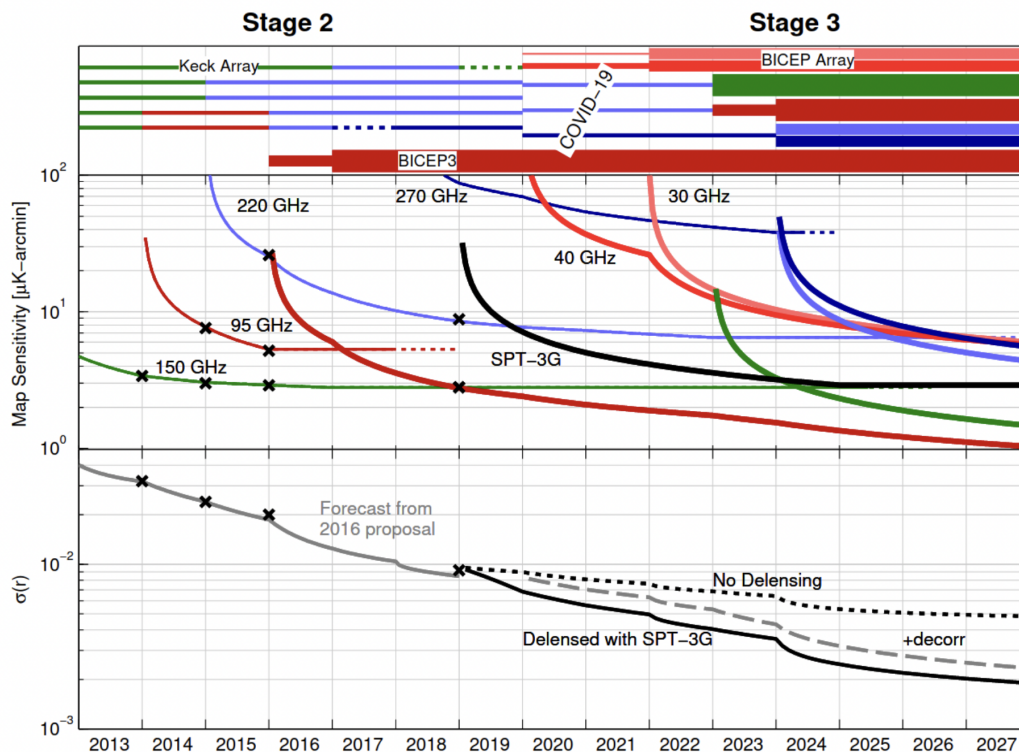


Figure 5.6: Projection of the sensitivity of the ongoing and future *BICEP/Keck* Array program. The projections involve direct scaling from published end-to-end analyses and include real-world inefficiencies and removal of dust and synchrotron foregrounds. The top panel provides a representation of the program, showing the frequency bands covered by the various receivers through each observing season. The middle panel shows the map depth for each frequency, and the bottom panel displays the sensitivity to the tensor-to-scalar ratio, after marginalizing over all foreground parameters, as well as the raw sensitivity, which is the sensitivity achieved if there were no no-foregrounds. The solid line shows the gain in sensitivity with delensing effort that we can achieve by working with SPT-3G. Figure from [76].

## 5.8 Priors in Fisher and ML Search

The maximum likelihood search has been used for estimating biases and uncertainties associated with various model and data choices. We use priors on parameters, such as  $\beta_d$  and  $\beta_s$  to the likelihood function to obtain the maximum of the posterior probability distribution function. This approach enables a computationally efficient search for the peak location of the posterior compared to evaluating the full posterior for each realization. However, for parameters dominated by the prior, the width of the distribution becomes very small, rather than returning the width of the prior.

Consider a simplified problem involving two parameters  $\alpha$  and  $\beta$ , with values equal

to zero. Our estimates are subject to Gaussian measurement uncertainty that can be written as a covariance matrix  $\mathbf{C}$ :

$$\mathbf{C} = \begin{bmatrix} \sigma_\alpha^2 & \epsilon\sigma_\alpha\sigma_\beta \\ \epsilon\sigma_\alpha\sigma_\beta & \sigma_\beta^2 \end{bmatrix}. \quad (5.13)$$

We make realizations using this covariance matrix. We solve for parameters  $x$  that minimize  $\chi^2$  in the maximum likelihood search for each realization:

$$\chi^2 = -2 \log \mathcal{L} = (x - \hat{x})^\dagger \mathbf{C}^{-1} (x - \hat{x}), \quad (5.14)$$

For this particular case, the standard deviations of parameters obtained from maximum likelihood agree with parameter uncertainties derived from a Fisher matrix. Fisher matrix  $\mathbf{F}$  is just  $\mathbf{C}^{-1}$  for this case.

The standard deviations of parameters obtained from maximum likelihood are:

$$\sigma_{\alpha,\text{ML}}^2 = (1, 0) \mathbf{C} \begin{pmatrix} 1 \\ 0 \end{pmatrix} = \sigma_\alpha^2 \quad (5.15)$$

$$\sigma_{\beta,\text{ML}}^2 = \sigma_\beta^2, \quad (5.16)$$

the standard deviations of parameters obtained from inverse Fisher matrix are:

$$\sigma_{\alpha,\text{F}}^2 = (\mathbf{F}^{-1})_{00} = \sigma_\alpha^2 \quad (5.17)$$

$$\sigma_{\beta,\text{F}}^2 = (\mathbf{F}^{-1})_{11} = \sigma_\beta^2. \quad (5.18)$$

Moving forward, we shall incorporate a Gaussian prior into parameter  $\beta$ , with mean zero, representing the real value, and width  $w_\beta$ . The maximum likelihood search now includes a multiplicative prior term. The  $\chi^2$  statistic can be expressed as:

$$\chi^2 = -2 \log \mathcal{L} = (x - \hat{x})^\dagger \mathbf{C}^{-1} (x - \hat{x}) + \frac{\beta^2}{w_\beta^2}. \quad (5.19)$$

We solve this system of equations by taking derivatives with respect to  $\alpha$  and  $\beta$  and equating them to zero. For the maximum likelihood solution we obtain the following parameter standard deviations:

$$\sigma_{\alpha, \text{ML}}^2 = \sigma_{\alpha}^2 \left( 1 - \frac{2\epsilon^2 \sigma_{\beta}^2}{w_{\beta}^2 + \sigma_{\beta}^2} + \frac{\epsilon^2 \sigma_{\beta}^4}{(w_{\beta}^2 + \sigma_{\beta}^2)^2} \right) \quad (5.20)$$

$$\sigma_{\beta, \text{ML}}^2 = \sigma_{\beta}^2 \left( \frac{w_{\beta}^2}{w_{\beta}^2 + \sigma_{\beta}^2} \right)^2. \quad (5.21)$$

We use with Fisher information matrix  $\mathbf{F}$  and the prior covariance matrix  $\mathbf{P}$ , denoted as  $\mathbf{F} + \mathbf{P}$ , where  $\mathbf{P}$  represents the prior covariance matrix:

$$\mathbf{P} = \begin{bmatrix} 0 & 0 \\ 0 & \frac{1}{w_{\beta}^2} \end{bmatrix}. \quad (5.22)$$

Inverting the sum of the Fisher information matrix  $\mathbf{F}$  and the prior covariance matrix  $\mathbf{P}$  yields the uncertainties associated with parameters  $\alpha$  and  $\beta$ :

$$\sigma_{\alpha, \text{F}}^2 = \sigma_{\alpha}^2 \left( \frac{w_{\beta}^2}{w_{\beta}^2 + \sigma_{\beta}^2} \right) \left[ 1 + (1 - \epsilon^2) \frac{\sigma_{\beta}^2}{w_{\beta}^2} \right] \quad (5.23)$$

$$\sigma_{\beta, \text{F}}^2 = \sigma_{\beta}^2 \left( \frac{w_{\beta}^2}{w_{\beta}^2 + \sigma_{\beta}^2} \right). \quad (5.24)$$

It is worth noting that  $\sigma_{\beta, \text{ML}}^2$  contains an additional factor of  $w_{\beta}^2/(w_{\beta}^2 + \sigma_{\beta}^2)$  that leads to an underestimation of  $\sigma_{\beta}^2$  when there is a strong prior ( $w_{\beta}^2 \ll \sigma_{\beta}^2$ ). On the other hand, even though the expression for  $\sigma_{\alpha, \text{ML}}$  is very different from the Fisher expression, they have identical outcomes when there is zero correlation ( $\epsilon = 0$ ), a weak prior ( $w_{\beta}^2 \gg \sigma_{\beta}^2$ ), or a strong prior ( $w_{\beta}^2 \ll \sigma_{\beta}^2$ ).

*Chapter 6*

## DUST POLARIZATION ANALYSIS

An accurate characterization of the polarized emission from interstellar dust is very important for improving our understanding of astrophysical phenomena in the interstellar medium and for studying the polarization of the cosmic microwave background.

Dust emission is linearly polarized due to the preferential alignment of the short axes of non-spherical rotating dust grains with the local magnetic field. At high enough frequencies and large enough scales, polarized dust emission is the brightest polarized foreground in CMB measurements.

To detect any primordial B-mode signals, it is necessary to accurately model and remove the contribution from polarized dust emission in CMB measurements. By doing so, we can place better constraints on the tensor to scalar ratio  $r$ .

In the absence of any preferred direction in a polarized map, the power from E and B modes is expected to be equal. However indicate that the power in the B mode is only half of that in the E mode. This apparent asymmetry may be attributed to the preferred alignment of dust grains with the local magnetic field, which introduces a preferred orientation in the polarization map as discussed in Section 1.5.

Dust decorrelation can arise due to spatial variations in unpolarized dust temperature  $T_d$  and spectral index  $\beta_d$  and would result in a decrease in the power in the cross-spectrum between high and low-frequency maps. This can cause residuals to remain in low-frequency maps that are cleaned using templates from higher-frequency maps. Failure to account for this can lead to an underestimation of the contribution of dust and an upward bias in the measurement of the tensor-to-scalar ratio  $r$ . Therefore it is important to characterize the level of variations across the sky. Furthermore, it is important to also consider whether the assumption that the dust parameters are constant across the sky may introduce bias in  $r$  or change the sensitivities of the parameters in the analysis.

## 6.1 Dust Decorrelation

Dust decorrelation is defined as the ratio of cross-spectra to the geometric mean of the corresponding auto-spectra.

$$\Delta_d \equiv \frac{D_{80,BB}^{353 \times 217}}{\sqrt{D_{80,BB}^{217 \times 217} D_{80,BB}^{353 \times 353}}}. \quad (6.1)$$

It is expected that there will be a certain degree of decorrelation due to variations in the polarization angle and temperature of dust clouds along the line of sight. This observation is consistent with a physical model that describes the generation of dust polarization through the interaction of dust grains with the magnetic field of the galaxy.

This can be generalized to scale to any pair of frequencies  $\nu_1$  and  $\nu_2$ , for any spatial scale  $\ell$ . A factor of  $f(\nu_1, \nu_2)$  is applied to scale the frequencies:

$$f(\nu_1, \nu_2) = \frac{(\log(\nu_1/\nu_2))^2}{(\log(217/353))^2}, \quad (6.2)$$

and a factor of  $g(\ell)$  is applied to scale the spatial scales:

$$g(\ell) = \begin{cases} 1 & \text{flat scaling} \\ (\ell/80) & \text{linear scaling} \end{cases} \quad (6.3)$$

The scaling above can produce non physical results. In order to avoid this a remapping function is applied to limit the values of correlation  $\Delta'_d$  to be between 0 and 1 [91].

$$\Delta'_d(\nu_1, \nu_2, \ell) = \exp[\log(\Delta_d) f(\nu_1, \nu_2) g(\ell)]. \quad (6.4)$$

We detected no decorrelation when it is included as a free parameter in the maximum likelihood search shown in Figure 6.1.

## 6.2 High Frequency Band Forecasting

The goal of this study is to forecast the potential constraints on polarized dust emission through an upgrade to the *BICEP/Keck* Array instrument, achieved by

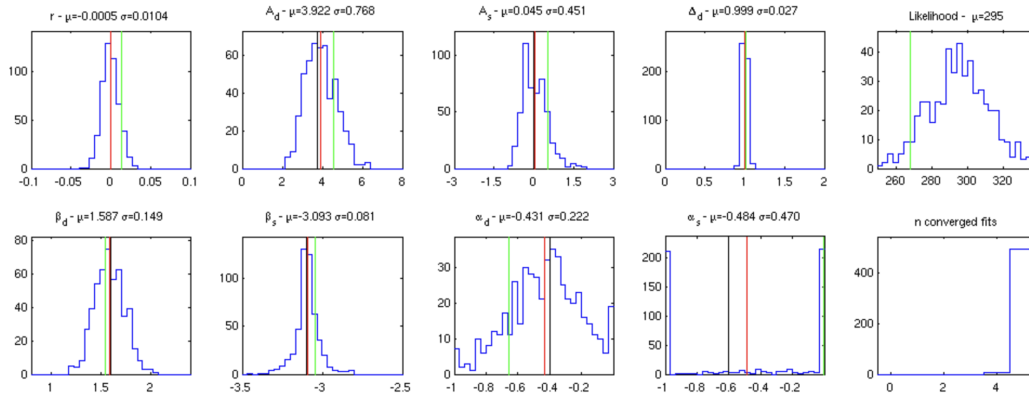


Figure 6.1: Likelihood results when dust decorrelation is added as a free parameter. The results are consistent with no loss of correlation in dust in the *BICEP/Keck* Array field.

including a PILOT-like balloon experiment operating at a frequency of 1.2 THz. In this analysis, we vary the expected signal-to-noise level for *BB* at  $\ell = 72.5$  using the Fisher pipeline discussed in Section 5.6. By doing so, we obtain a range of possible outcomes and understand how the proposed performance is affected by different scenarios.

The Polarized Instrument for Long-wavelength Observation of the Tenuous Interstellar Medium (PILOT) is a balloon-borne experiment designed to measure the polarized emission of thermal dust at a wavelength of 1.2 THz [74, 70]. A high signal-to-noise experiment at this frequency would significantly increase our sensitivity to the parameters of dust emission.

Signal-to-noise is derived from survey weight:

$$S/N = \frac{\text{survey weight}}{9.30 \times 10^{-11} \mu\text{K}^{-2}}. \quad (6.5)$$

To investigate the effect of the external 1.2 THz auto spectrum on our Fisher estimates, we considered two cases. In the first case, we kept the cross spectrum between the 1.2 THz experiment and the BK15/18 bands while removing the external 1.2 THz auto spectrum from the bandpower covariance matrix. In the second scenario, we kept all the spectra and did not remove the external 1.2 THz auto spectrum from the bandpower covariance matrix. To remove the 1.2 THz auto-spectrum on the bandpower covariance matrix, we drop the rows and columns that correspond to

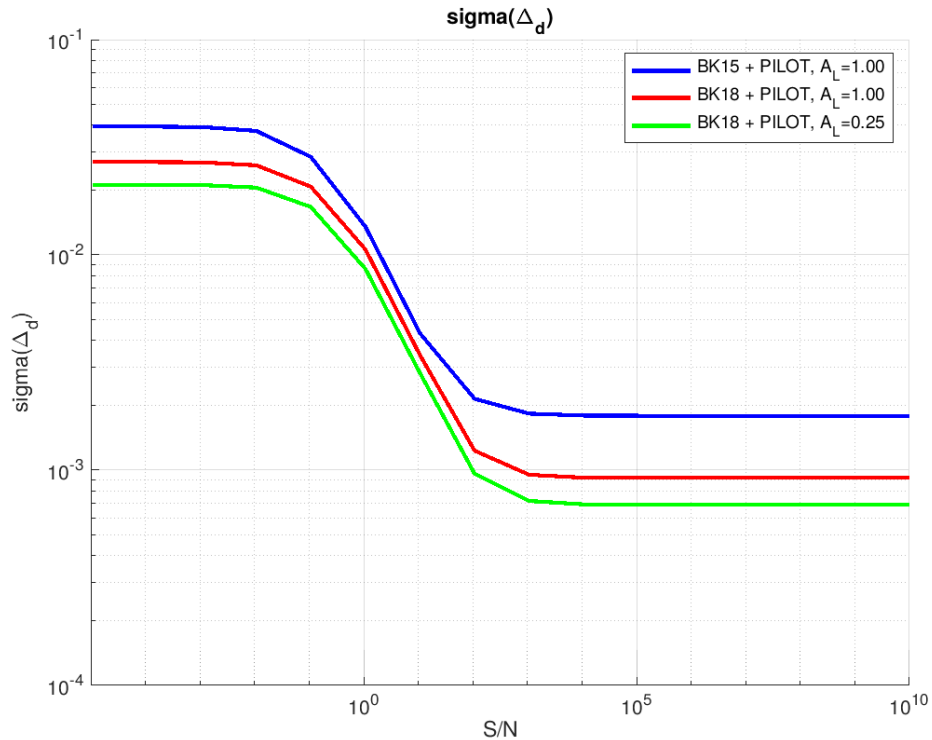


Figure 6.2: Fisher forecasting for BK15 and BK18 data when adding an experiment at 1.2 THz at various levels of signal-to-noise.

the 1.2 THz auto spectrum for all multipole moments. This effectively removes the contribution of the external band to the BPCM.

To assess the performance of the PILOT-like experiment, we generated 499 Gaussian noise simulations at a frequency of 1.2 THz. These maps were generated such that they use signal-to-noise ratio for  $BB$  at  $\ell = 72.5$  as an input. We reobserved these noise realizations through the standard pipeline and generated angular power spectra for  $BB$  for all the BK15 and 1.2 THz frequency bands.

In our forecasting analysis, the bandpass for the external 1.2 THz frequency band is modeled as a Dirac-delta function centered at 1.2 THz. The beam is scaled to  $3.75'$  using a scaling relation with respect to the 150 GHz beam. We use angular power spectra for multipole moments ranging from 37.5 to 317.5, corresponding to bins 2-10 in our analysis.

From Table 6.1 and Figure 6.2, we observe that the main advantage of having a high signal-to-noise band at 1.2 THz is a significant reduction in  $\sigma(\beta_d)$  and  $\sigma(\Delta_d)$ .

Table 6.1: Maximum Likelihood Results for Forecasting an Experiment at 1.2 THz

Experiment	Decorr	auto	$\sigma(r)$	$\sigma(A_d)$	$\sigma(\beta_d)$	$\sigma(\alpha_d)$	$\sigma(\Delta_d)$
BK15	on	-	0.024	1.143	0.214	0.354	0.0395
BK15	off	-	0.021	1.128	0.213	0.350	-
BK18	on	-	0.011	0.823	0.155	0.263	0.0270
BK18	off	-	0.010	0.804	0.144	0.262	-
BK15 + S/N=1.0	on	on	0.020	0.950	0.148	0.344	0.0140
BK15 + S/N=1.0	off	on	0.019	0.880	0.137	0.340	-
BK15 + S/N=1.0	on	off	0.020	0.971	0.154	0.344	0.0147
BK15 + S/N=1.0	off	off	0.019	0.884	0.139	0.340	-
BK18 + S/N=1.0	on	on	0.010	0.732	0.110	0.260	0.0109
BK18 + S/N=1.0	off	on	0.010	0.722	0.106	0.259	-
BK18 + S/N=1.0	on	off	0.010	0.735	0.112	0.260	0.0112
BK18 + S/N=1.0	off	off	0.010	0.722	0.107	0.259	-
BK15 + S/N=4.0	on	on	0.018	0.778	0.088	0.321	0.0072
BK15 + S/N=4.0	off	on	0.018	0.747	0.085	0.316	-
BK15 + S/N=4.0	on	off	0.018	0.825	0.106	0.327	0.0091
BK15 + S/N=4.0	off	off	0.018	0.751	0.092	0.318	-
BK18 + S/N=4.0	on	on	0.009	0.667	0.076	0.251	0.0060
BK18 + S/N=4.0	off	on	0.009	0.658	0.070	0.250	-
BK18 + S/N=4.0	on	off	0.009	0.679	0.085	0.253	0.0071
BK18 + S/N=4.0	off	off	0.009	0.659	0.072	0.250	-
BK15 + S/N=20.0	on	on	0.016	0.679	0.048	0.251	0.0033
BK15 + S/N=20.0	off	on	0.014	0.664	0.047	0.248	-
BK15 + S/N=20.0	on	off	0.016	0.713	0.066	0.282	0.0056
BK15 + S/N=20.0	off	off	0.015	0.670	0.059	0.264	-
BK18 + S/N=20.0	on	on	0.009	0.609	0.039	0.220	0.0024
BK18 + S/N=20.0	off	on	0.009	0.608	0.039	0.218	-
BK18 + S/N=20.0	on	off	0.009	0.620	0.054	0.230	0.0043
BK18 + S/N=20.0	off	off	0.009	0.611	0.043	0.223	-

Based on our analysis, we can conclude that the addition of a 1.2 in the *BICEP/Keck* Array instrument with a PILOT-like experiment does not lead to a significant improvement in the sensitivity of the tensor-to-scalar ratio, irrespective of the signal-to-noise ratio. This is reflected in the value of  $\sigma(r)$  which remains unchanged.

Table 6.1 suggest that adding a band at 1.2 THz would lead to a significant reduction in the values of  $\sigma(\beta_d)$  and  $\sigma(\Delta_d)$ . Even though the addition of the high-frequency band does not have a significant impact on  $\sigma(r)$  this analysis only takes into account statistical errors. The inclusion of the new band enables us to study  $\sigma(C_d)$ , which can be used to estimate the expected bias on  $r$ .

Furthermore, we find that the B-mode signal-to-noise ratio of the PILOT experiment at the  $\ell = 70$  band in the BK field is only  $2 \times 10^{-3}$ , and hence it does not provide any substantial improvements over the current dust parameter sensitivities achieved by the BICEP/Keck Array instrument. Based on our analysis, we find that in order to see improvements on dust parameters from adding a 1.2 THz band, a signal-to-noise level of approximately 1 is required. On the other hand, to be limited by lensing, a signal-to-noise level of approximately 100 is needed.

### 6.3 Spatial Variations in $\beta_d$

In our analysis, the value of dust spectral index  $\beta_d$  is assumed to be constant across the region of observational. In this section we explore whether this assumption adds any significant bias to the maximum likelihood search parameters or change their sensitivities.

#### Planck Commander Map

Planck Commander Maps use Bayesian parametric component separation, where each component is modelled with an amplitude and spectral index for each pixel. MCMC Gibbs sampling is used to fit these parameters to data.

We use  $\beta_d$  values from T since they are better constrained. Planck Commander component map is obtained from Planck Legacy Archive. This map has NSIDE = 256, FWHM = 60.0 arcmin.

Thermal dust emission map from COMMANDER has two estimations for  $\beta_d$ . The means posterior average estimation  $\beta_{d,\text{mean}}$  is noisy, and very likely to be driven by Monte Carlo uncertainties since only a limited number of samples were used to derive the mean and large number of dimensions in posterior distributions. The maximum likelihood estimation  $\beta_{d,\text{ML}}$  corresponds to non-linear optimizations of the posterior distribution and very likely to converge faster to the peak.

In the BICEP / Keck field, we estimate the mean value of the maximum likelihood estimator to be  $\langle \beta_{d,\text{ML}} = 1.5605 \rangle$  and root mean square of the variations in the map  $\langle \beta_{d,\text{err}} = 0.0777 \rangle$ .

#### Planck GNILC Map

We obtain CIB-removed dust spectral index map produced by the GNILC method [78] from Planck Legacy Archive. This map has NSIDE = 2048. The data used by

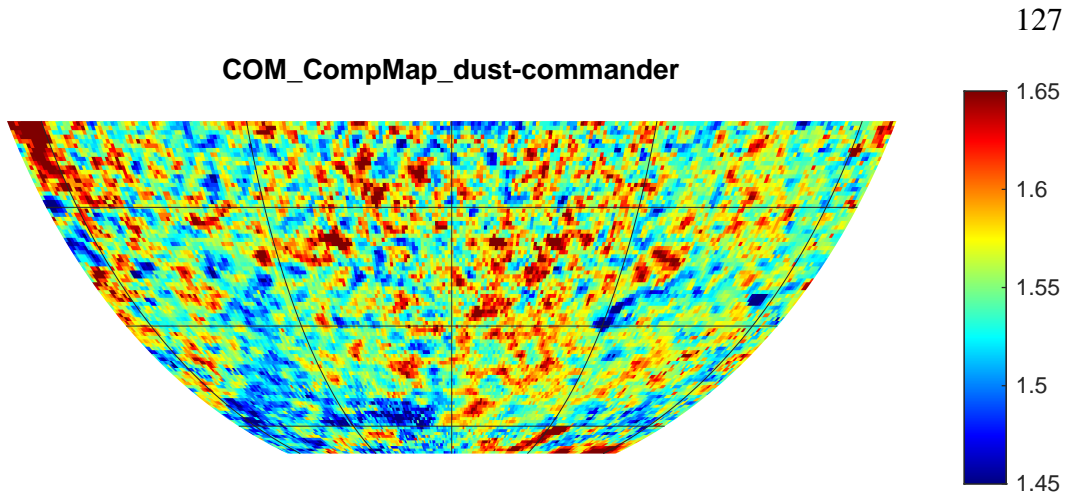


Figure 6.3: Commander dust spectral index plotted in the BICEP3 field. Planck Commander Maps use Bayesian parametric component separation, where each component is modelled with an amplitude and spectral index for each pixel. MCMC Gibbs sampling is used to fit these parameters to data.

GNILC for the analysis are the Planck data release 2 (PR2) frequency maps from 30 to 857 GHz, and a 100 micron hybrid map combined from the SFD map at large angular scales ( $> 30'$ ) and the IRIS map at small angular scales ( $< 30'$ ). Spectral index for dust was found by fitting MBB to the dust component maps of GNILC at 353, 545, 857 HFI bands, and 100  $\mu\text{m}$  [25]. There is no prior assumption about the galactic signal, but the CIB and CMB power spectrum are used as priors. The CIB power spectrum comes from Planck XXX [20].

In the BICEP / Keck field, we estimate the mean value of the maximum likelihood estimator to be  $\langle \beta_{d,\text{GNILC}} \rangle = 1.8092$  and root mean square of the error  $\langle \beta_{d,\text{err}} \rangle = 0.0708$ .

### $\chi^2$ Estimation

Before we run the full maximum likelihood search machinery to the component map, we need to verify whether the spatial variations in the  $\beta_d$  map obtained from Planck data are statistically significant. To test this, we smooth  $\beta_d$  map with different beam sizes, aiming to look for a scale where variations in  $\beta_d$  are significant, while keeping the values from being too smoothed out. We assume  $\beta_d$  is a linear parameter for the purpose of smoothing, even though it is actually a nonlinear parameter. We assume that pixels in the original Commander results are independent, since *Planck* does not provide the covariance matrix.

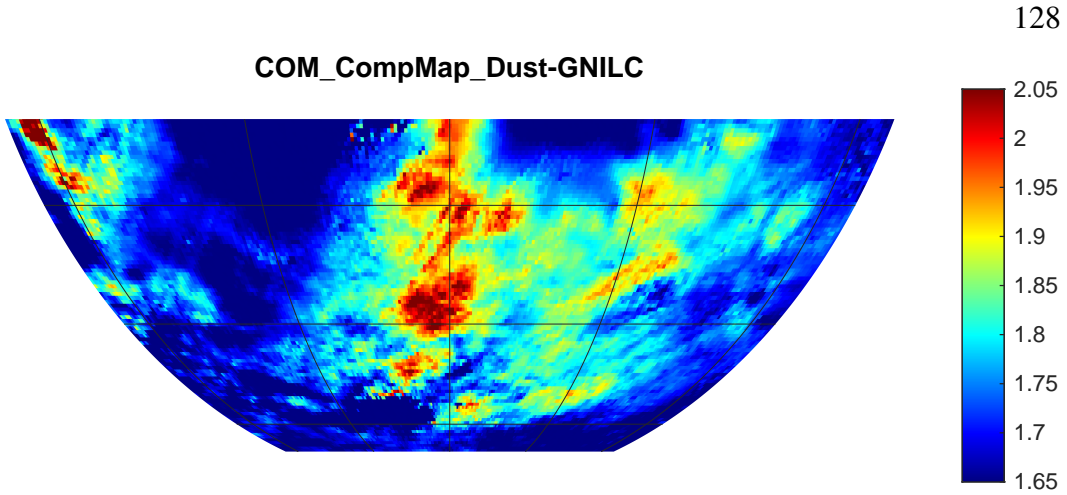


Figure 6.4: GNILC dust spectral index plotted in the BICEP3 field. These maps are CIB-removed dust spectral index map produced by the GNILC method, using Planck data release 2 (PR2) frequency maps from 30 to 857 GHz, and a 100 micron hybrid map combined from the SFD map at large angular scales ( $> 30'$ ) and the IRIS map at small angular scales ( $< 30'$ ). Spectral index for dust was found by fitting MBB to the dust component maps of GNILC at 353, 545, 857 HFI bands, and 100  $\mu\text{m}$ .

Error per beam element  $\tilde{\beta}_{err}$  is defined as:

$$\tilde{\beta}_{err} = \frac{\sqrt{\langle \beta_{err}^2 \rangle}}{\sqrt{\pi/4} \times 0.7 \times \text{FWHM}/\text{pix\_side}}, \quad (6.6)$$

where  $\sqrt{\langle \beta_{err}^2 \rangle}$  is the average root mean square (RMS) in the map, and the factors of  $\sqrt{\pi/4}$  and 0.7 are the conservative estimates to take care of circular beam, and the core region of the gaussian respectively.

Pixel size for the component map is given by:

$$\text{pix\_side} \approx \frac{3600}{\text{NSIDE}}, \quad (6.7)$$

where  $\text{pix\_side} \approx 14.0625$  for  $\text{NSIDE} = 256$ , and scale the FWHM with quadrature sum:

$$\text{FWHM}_F^2 = \text{FWHM}_0^2 + \text{smoothing}^2, \quad (6.8)$$

where  $\text{FWHM}_0 = 60.0$  arcmin.

The estimated error as a function of FWHM is:

$$\tilde{\beta}_{err}(FWHM_F) = \tilde{\beta}_{err}(FWHM_0) \times \frac{FWHM_0}{\sqrt{FWHM_0^2 + \text{smoothing}^2}} \quad (6.9)$$

$$= \tilde{\beta}_{err}(FWHM_0) \times \frac{1}{\sqrt{(1 + (\text{smoothing}/FWHM_0)^2)}}. \quad (6.10)$$

and finally we can use this to get  $\chi$  values to estimate statistical significance:

$$\chi_\beta = \frac{\beta - \langle \beta \rangle}{\tilde{\beta}_{err}}. \quad (6.11)$$

We expect that, as smoothing is increased, the difference smooths out however errors per pixel gets smaller due to averaging. The above method assumes a single error value  $\tilde{\beta}_{err}$  for the entire map. As an alternative approach we can use the HEALPIX function `ud_grade` to reduce NSIDE to obtain  $\tilde{\beta}_{err}$  per pixel. However, in this case we don't smooth the maps with a Gaussian beam, but simply degrade the  $\beta_d$  map by using bigger pixels whose value is the average of the  $\beta_d$  values of all the smaller pixels that fall in the big pixel:

$$\tilde{\beta}_{err,ud}(\text{pix}) = \frac{\sqrt{\langle \beta_{err}^2 \rangle_{\text{pix}}}}{(\text{NSIDE\_IN}/\text{NSIDE\_OUT})}, \quad (6.12)$$

where the average is taken over the pixels, and define  $\chi_\beta(\text{pix})$ :

$$\chi_\beta(\text{pix}) = \frac{\beta_{ud}(\text{pix}) - \langle \beta_{ud} \rangle}{\tilde{\beta}_{err,ud}(\text{pix})}. \quad (6.13)$$

As the smoothing is increased, we observe smaller gradient in mean subtracted maps, however errors average out and lead to greater values of  $\chi$ . At  $FWHM = 5.73^\circ$  there is about  $4\sigma$  statistical significance in the BICEP/Keck Array field for spatial variations in  $\beta_d$  as can be seen in Table 6.3.

### Dust Realizations and Maximum Likelihood

Gaussian dust realizations are generated with  $A_d = 3.75 \mu\text{K}^2$ ,  $\alpha_d = -0.4$ ,  $T_d = 19.6 \text{ K}$ , and  $EE/BB$  ratio of 2.

We have generated two types of signal maps: one with a constant value of  $\beta_d$ , using the mean values of Commander and GNILC in the BK field, and another with

Table 6.2: As the smoothing is increased, we observe smaller gradient in mean subtracted maps, however errors average out and lead to greater values of  $\chi$ .

FWHM ( $^{\circ}$ )	$\tilde{\beta}_{err}$ (big field)	$\tilde{\beta}_{err}$ (bk field)
2.86	0.0088	0.0094
5.72	0.0046	0.0049
11.46	0.0023	0.0025
22.92	0.0012	0.0012
28.65	0.0009	0.0010
57.30	0.0005	0.0005
114.50	0.0002	0.0002

spatially varying  $\beta_d$  that is not smoothed. Each realization has  $\beta_d$  drawn from a Gaussian distribution with a mean equal to the mean value of the parameter in the BICEP/Keck Array field, and a standard deviation equal to the RMS =  $\sqrt{\langle \beta_d^2 \rangle}$  of the parameter in the BICEP/Keck Array field. We reobserve the dust realizations using BK18 sensitivities and run maximum likelihood search to estimate parameter biases and sensitivities.

Table 6.3: We present maximum likelihood (ML) search results for the tensor-to-scalar ratio ( $r$ ) using the Commander spectral index for the BK field and the GNILC spectral index for the same field. The values of  $r$  obtained from these two methods are denoted as  $r_{COMM}$  and  $r_{GNILC}$  respectively. The difference between these values is represented by  $\Delta r$ , and the sensitivity of the results is quantified by  $\sigma(r_{COMM})$ . To estimate the statistical significance of our results, we calculate the ratio  $\sigma_r \equiv \sqrt{499}\Delta r/\sigma(r)$ .

$\beta_d$	prior	$r_{COMM}$	$r_{GNILC}$	$\Delta r$	$\sigma(r)$	$\sigma_r$
COMM const	on	7.07e-04	7.49e-04	4.22e-05	9.18e-03	0.103
GNILC const	on	7.75e-04	8.15e-04	3.98e-05	8.43e-03	0.106
COMM const	off	4.52e-04	3.27e-04	1.25e-04	9.30e-03	0.301
GNILC const	off	4.96e-04	5.25e-04	2.85e-05	8.57e-03	0.0743

According to our analysis and results shown in Table 6.3 and 6.3, there is no significant bias or change in parameter sensitivities observed in any of the model parameters when considering dust-only simulations, even though spatial variations in  $\beta_d$  across the BICEP/Keck Array field are not included in our analysis pipeline. In other words, the parameter sensitivities and biases would remain consistent with BK18 even if the assumed spatial variations were actually real.

Table 6.4: We report the parameter sensitivities obtained from our maximum likelihood (ML) search. Our results indicate that there is no statistically significant difference between the constant and spatially varying  $\beta_d$  realizations.

$\beta_d$	$\beta_d$ prior	$A_d$	$\sigma(A_d)$	$\beta_d$	$\sigma(\beta_d)$	$\alpha_d$	$\sigma(\alpha_d)$
COMM const	on	4.56	0.673	1.56	0.0522	-0.433	0.207
COMM gaus	on	4.57	0.708	1.55	0.0668	-0.435	0.199
GNILC const	on	4.59	0.671	1.80	0.0552	-0.445	0.220
GNILC gaus	on	4.56	0.710	1.80	0.0624	-0.435	0.226
COMM const	off	4.55	0.775	1.55	0.115	-0.432	0.207
COMM gaus	off	4.55	0.815	1.55	0.147	-0.433	0.199
GNILC const	off	4.58	0.833	1.80	0.146	-0.442	0.220
GNILC gaus	off	4.55	0.852	1.80	0.165	-0.433	0.226

#### 6.4 EE to BB Ratio For Dust

The *BICEP/Keck* Array papers do not use the EE spectra to derive the dust model, but the spectra are found to be consistent with the asymmetry in power between the dust E-mode and B-modes as measured by Planck at 353 GHz, where  $EE/BB = 2$  for dust [3, 29]. While Planck has measured this ratio for the entire sky, it is not clear whether this holds true for the *BICEP/Keck* Array field.

##### Likelihood Analysis with free $EB_d$

We performed a maximum likelihood analysis, setting the ratio of EE to BB spectra for dust ( $EB_d$ ) as a free parameter with a range of  $[0, 4]$ . The analysis included both EE and BB spectra. We compared the likelihood results obtained for a fixed  $EB_d$  with that of a varying  $EB_d$ . In the varying case,  $EB_d$  was free in the range 0 to 4, with an initial starting point drawn from a Gaussian distribution with mean  $\mu = 2$  and standard deviation  $\sigma = 0.1$ . To check for consistency, we repeated the analysis with a Gaussian distribution of mean  $\mu = 1.5$ , which was found to agree well with the results obtained for  $\mu = 2$ .

From Figure 6.6, it can be seen that including E-modes into the baseline likelihood analysis introduces an upward bias on  $r$  and  $A_d$ , while  $\sigma(r)$  remains unchanged. Furthermore, the inclusion of E-modes leads to a reduction in  $\sigma(A_d)$  and  $\sigma(\beta_d)$ . This upward bias is may be due to unidentified systematic from the much brighter  $\Lambda$ CDM E-modes as compared to the dust foreground. To investigate this hypothesis, we explore two methods: spectral difference and map-based difference of the *BICEP/Keck* Array bands.

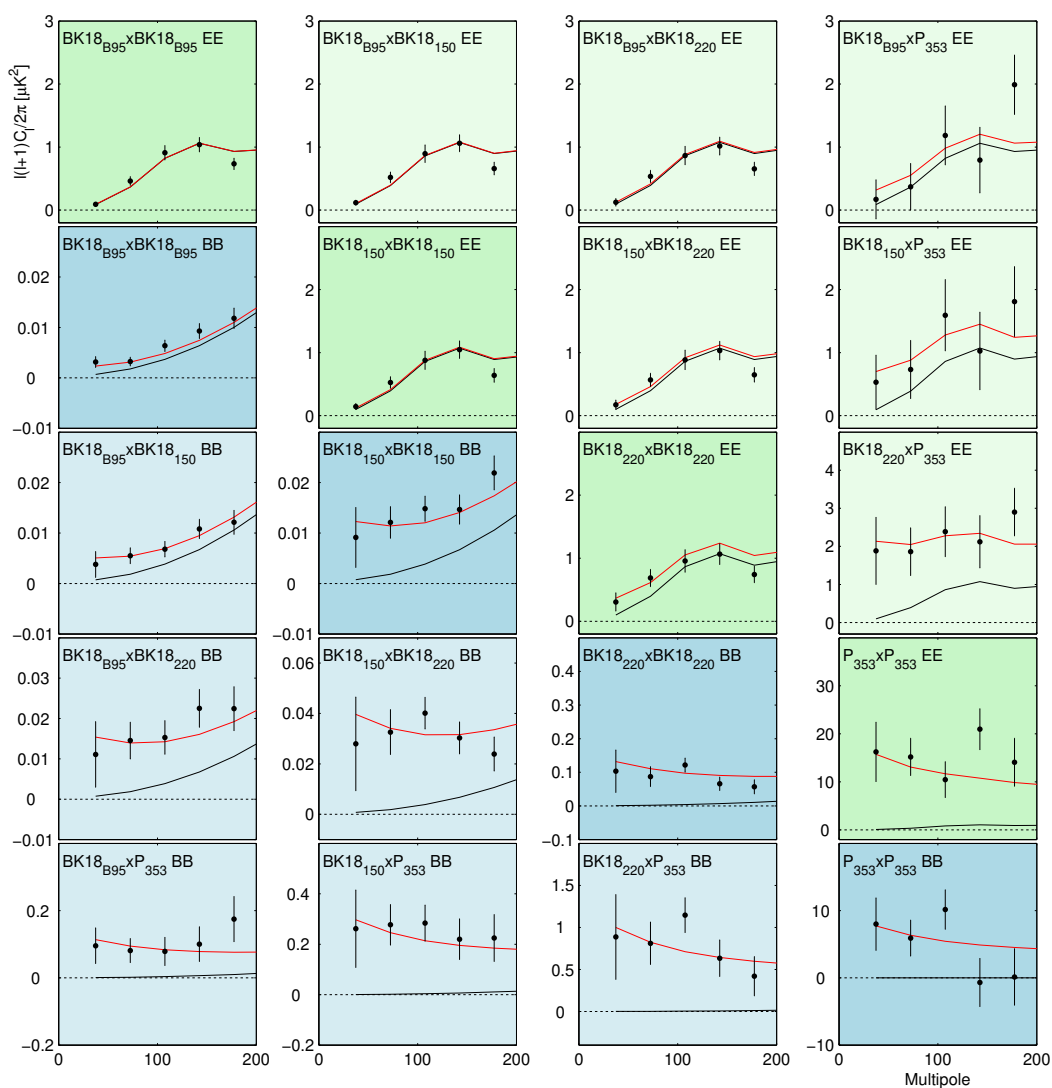


Figure 6.5: EE (shown in green background) and BB (shown in blue background) auto (dark colors) and cross spectra (light colors) using BICEP3 95 GHz, Bicep2 / Keck 150 GHz, 220 GHz, and Planck 353 GHz bands. BK bands use data taken up to and including 2018 season (BK18).  $\Lambda$ CDM model expectations are plotted in black.  $\Lambda$ CDM + dust model expectations are plotted in red. The model shown has  $r = 0$ ,  $A_d = 4.75 \mu K$ ,  $\beta_d = 1.6$ ,  $\alpha_d = -0.4$ . The model in this Figure is fit using only BB and excluding the newly added BICEP 95 GHz. However the agreement with EE and the newly added 95 GHz is a good validation. Figure taken from [18].

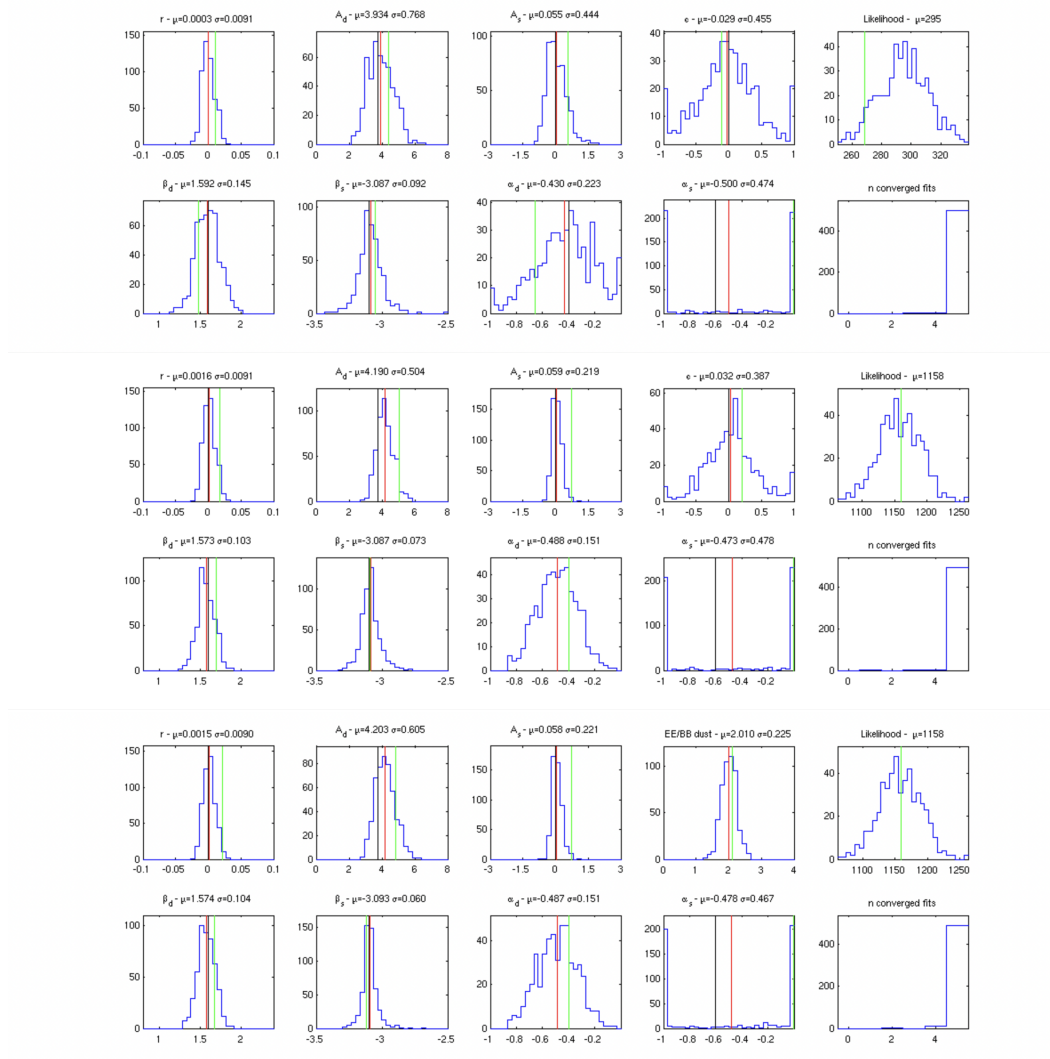


Figure 6.6: The figure shows the results of the maximum likelihood search for BB only (top two), EE only (middle two), and BB+EE (bottom two). Real data is presented as green, black is model input, and red is the mean of the realizations. When fitting for EE+BB, the ratio of dust EE to BB is set as a free parameter. We observe that real values of data have  $r$  and  $\beta_d$  showing a significant increase. However when switching from BB to EE,  $\sigma(A_d)$ ,  $\sigma(A_s)$ , and  $\sigma(\beta_s)$  all decrease, while  $\sigma(\beta_d)$  slightly increases. The EE-only case lacks constraining power on  $r$ , as expected.

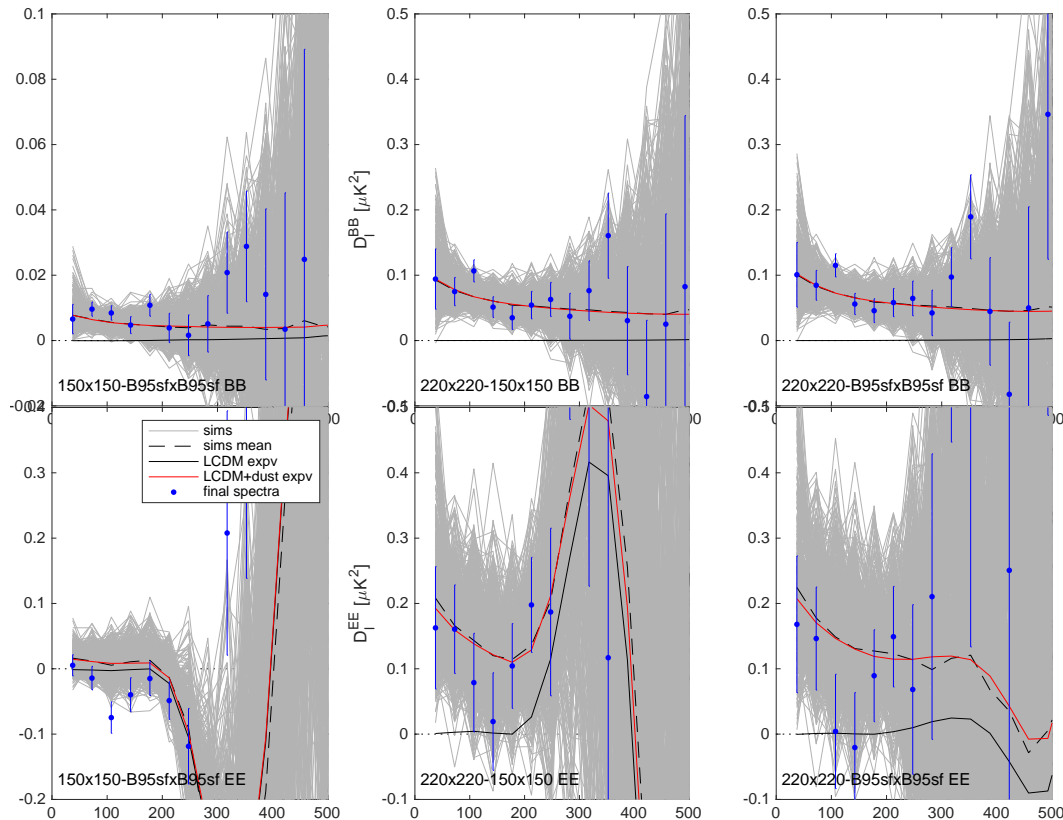


Figure 6.7: The spectral-based approach, where the final spectra that have already been corrected for all the suppression factors due to filtering and beam effects, have been subtracted from each other for all *Keck* Array and BICEP3 spectra in the smaller field of observation. This spectral-based approach is expected to cancel common signals, leaving spectra that are free of lensed E-modes and  $\Lambda$ CDM in our region. However EE spectrum of  $150 \times 150 - \text{B95sf} \times \text{B95sf}$  does not match the expected difference based on simulations that include lensed  $\Lambda$ CDM, noise, and dust. Furthermore, the subtracted spectra obtained from the maps are not consistent with zero for lensed  $\Lambda$ CDM only simulations, especially at high  $\ell$ . This is because at high  $\ell$ , the bandpower window functions become more non-ideal, leading to leakage of the lensed- $\Lambda$ CDM E-modes and B-modes into the subtracted spectra.

### Spectral Difference

The final spectra obtained from BK18, shown in Figure 6.5, have been corrected for all the suppression factors due to filtering and beam effects, making it an ideal estimator for the dust signal in our field after removing the  $\Lambda$ CDM contribution. In order to perform this removal, we take the difference of each *Keck* Array and BICEP3 spectra, all of which were observed within the smaller *Keck* field. This spectral-based approach is expected to cancel common signals, leaving spectra that are free of lensed E-modes and  $\Lambda$ CDM in our region.

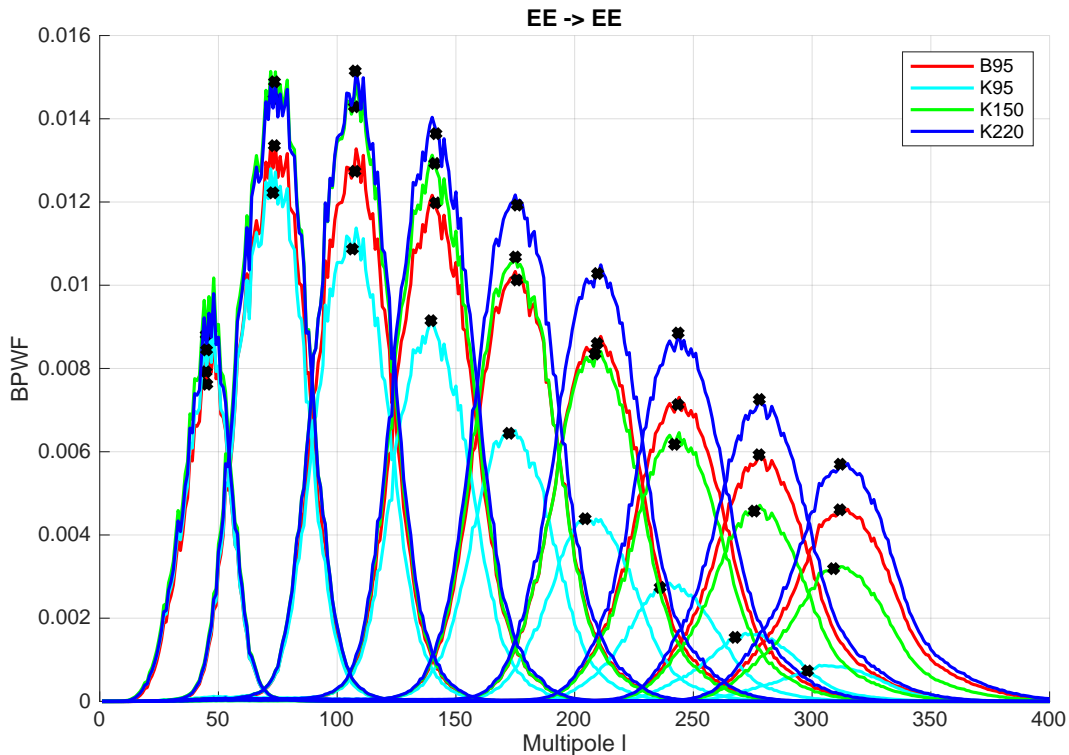


Figure 6.8: Bandpower window functions (BPWFs)  $M_{\ell\ell'}^{XX}$  obtained from BK18 data with E to E leakage are labeled as  $EE \rightarrow EE$ . At high  $\ell$  the BPWF shapes become increasingly non-ideal. Points that sit on the theory line are plotted estimated by the at the center-of-gravity of the BPWF, shown as the black crosses in the figure, and are not at the peak locations for higher  $\ell$  values.

In Figure 6.7, we observe some issues when we take the difference of these bands. First, the subtracted spectra obtained from the maps are not consistent with zero for lensed  $\Lambda$ CDM only simulations, especially at high  $\ell$ . This is because at high  $\ell$ , the bandpower window functions become more non-ideal as seen in Figure 6.8, leading to leakage of the lensed- $\Lambda$ CDM E-modes and B-modes into the subtracted spectra. At high  $\ell$  the BPWF shapes become increasingly non-ideal. Points that sit on the theory line are plotted estimated by the at the center-of-gravity of the BPWF, shown as the black crosses in the figure, and are not at the peak locations for higher  $\ell$  values. Second, we observe that the EE spectrum of  $150 \times 150 - \text{B95sf} \times \text{B95sf}$  at the third science bin ( $\ell \sim 100$ ) does not match the expected difference based on simulations that include lensed  $\Lambda$ CDM + dust + noise.

The constrained simulations used in the analysis are based on the Planck temperature map, which is fixed across the whole sky. The  $TE$  correlation in Equation 4.21

between the temperature and E-mode polarization patterns means that the E-mode pattern is semi-fixed across the sky, containing some of the T-pattern at any given angular scale as the  $TE$  spectrum swings positive/negative. As a result, the average of the constrained simulations in each bandpower in a given patch is pushed away from the  $\Lambda$ CDM expectation value by an amount that depends on whether the Planck T sky has more/less structure than the  $\Lambda$ CDM expectation in that patch and whether the  $TE$  is positive/zero/negative in that ell range. This push is patch dependent and will differ slightly between small and large field patches for *Keck* Array and BICEP3 . However, the majority of the difference is likely due to the difference in the shapes of the bandpower window functions for the two masks. For large field patches, the RA/Dec projection used in the analysis produces scale mixing and it is not recommended to use  $\ell > 330$  for science at this point. If we were using spherical coordinates (e.g. HEALPIX), some of this effect would go away.

The absolute calibration factor, as discussed in Section 4.1, is a plausible contributing factor for the observed discrepancy between the real data and simulations. Our proposed approach to correct for abscale involves combining all years of observation for each band. In addition, since the BICEP3 map was calculated for a large field, we also repeated the analysis by restricting the map to the smaller field. This resulted in a correction factor of 0.9923 for BICEP3 . We also obtained a coadded correction factor for all 150 GHz receivers over the observing seasons of 2013-2018, which is 1.0124 at  $\ell = 80$ , as shown in Figure 6.9. These correction factors, though small, are significant due to the strong  $\Lambda$ CDM signal, and correcting for them results in between agreement between the real data and simulations for the E-modes, as shown in Figure 6.10. The B-mode spectra remains mostly unchanged.

In addition to investigating the absolute calibration factor, we also explored the possibility of BB to EE leakage as a potential explanation for the discrepancy. In our input lensed  $\Lambda$ CDM realizations, the B to E leakage is small since there are no B modes signal in the input. However, this may not be the case for our dust simulations, as the dust model includes both E and B mode polarization, which is constructed to have an  $EE/BB$  ratio of 2. To estimate the B to E leakage from dust, we take the mean of the dust-only EE simulation spectrum in each frequency and compare it to the model. The difference between the mean of sims and the model provides an estimate of the B to E leakage from dust. We then subtract the mean of the simulation data point from the model, which should correspond to just the

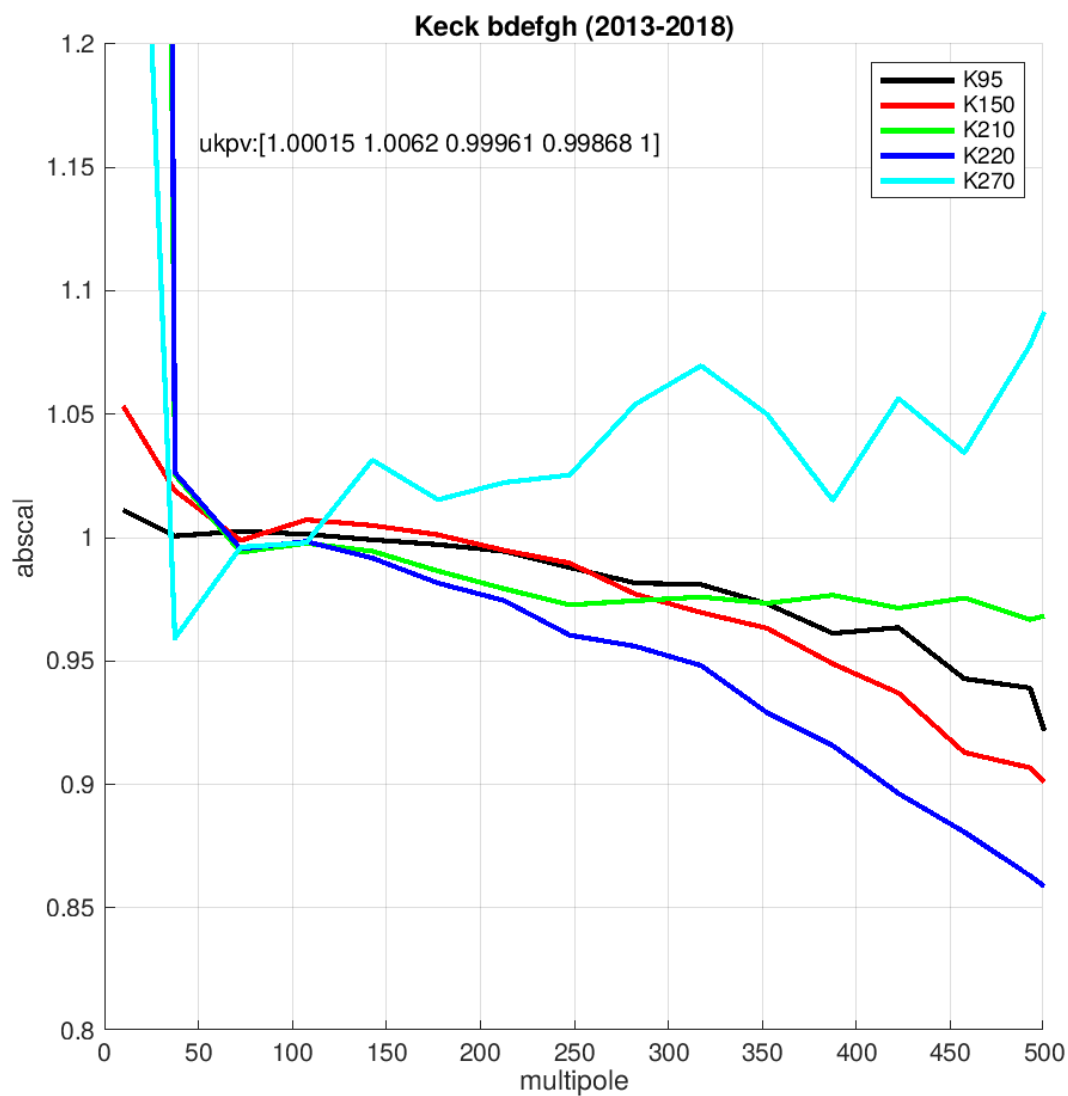


Figure 6.9: Our proposed approach to correct for abscal is to combine all years of observation for each band. In addition, since the BICEP3 map was calculated for a large field, we also repeated the analysis by restricting the map to the smaller field. This resulted in a correction factor of 0.9923 for BICEP3. We also obtained a coadded correction factor for all 150 GHz receivers over the observing seasons of 2013-2018, which is 1.0124 at  $\ell = 80$ . Plotted in this figure are the corrections obtained for *Keck* Array receivers.

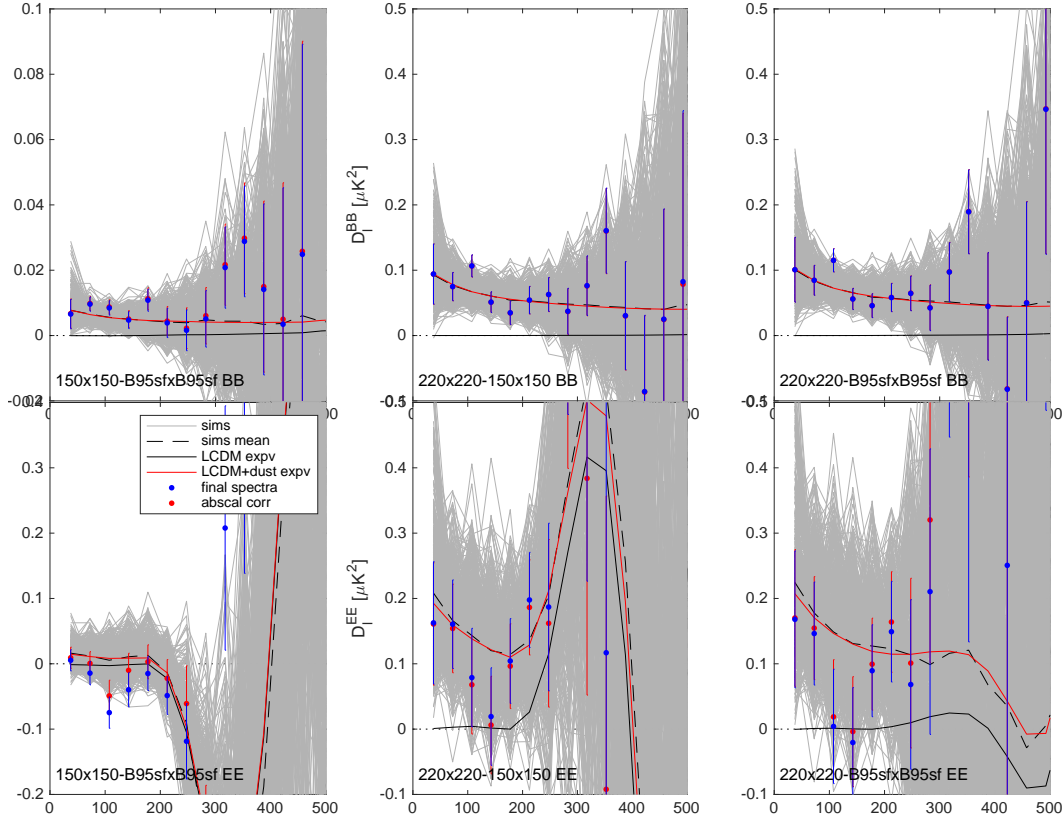


Figure 6.10: Spectral Difference of Bands after abscal corrections. Abscal is a plausible contributing factor for the observed discrepancy between the real data and simulations. The corrected spectra (shown in red) are in better agreement with the realizations.

leakage from B to E in the dust input model. No significant E to B leakage has been observed.

We also examined the leakage between bandpowers by generating realizations for T, Q, U using synfast with an input  $C_\ell$  spectrum. The idea is to investigate whether the non-ideal bandpower window function causes leakage of the E-mode spectrum peaks in Figure 6.11 into lower multipoles. The input spectra were set as follows:

$$C_\ell = \frac{1}{\ell(\ell+1)} \quad (\text{flat in } D_\ell), \quad (6.14)$$

$$C_\ell = \frac{\delta(\ell - \ell_0)}{\ell(\ell+1)} \quad \text{for } \ell_0 \in 37, 72, 107. \quad (6.15)$$

The reobservation pipeline was used to obtain the final spectra of these dust-only realizations. We anticipate some level of leakage in the adjacent bins due to overlapping bandpower window functions (BPWF). The expected amount of power to leak

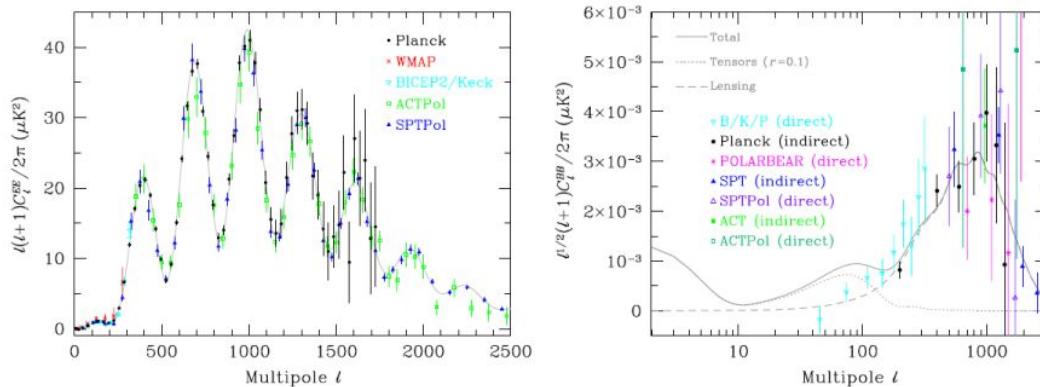


Figure 6.11: The left panel displays the EE power spectra for various experiments, while the right panel shows the BB power spectra. Figure taken from <https://ned.ipac.caltech.edu>.

at  $\ell = 107$  from the EE peak at  $\ell = 400$  is  $4.00 \times 10^{-4}, \mu\text{K}^2$ ,  $0.92 \times 10^{-4}, \mu\text{K}^2$ , and  $4.90 \times 10^{-4}, \mu\text{K}^2$  for B95sf, 150, and 220, respectively. A more accurate method of generating synfast realizations would be to use a normalization  $A_{\text{bp}}$  which is the sum of the corresponding BPWF bin for  $\ell_0$ , defined as:

$$C_\ell = A_{\text{bp}}\delta(\ell - \ell_0) \quad \text{for } \ell_0 \in 37, 72, 107. \quad (6.16)$$

This thesis does not investigate the possibility of leakage between multipoles, as it is evident that this cannot account for the observed discrepancy.

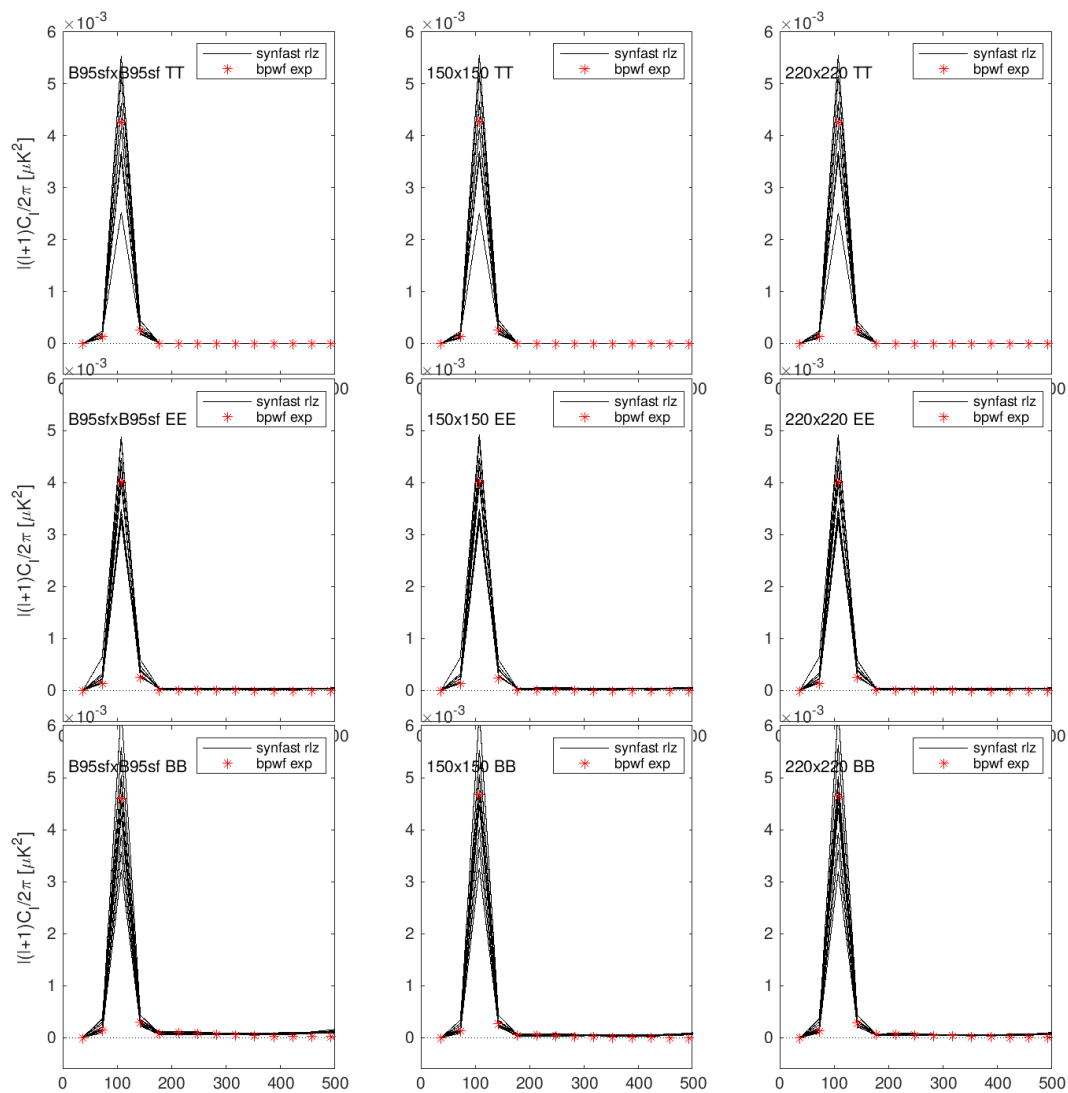


Figure 6.12: Expected normalized EE leakage for  $D_\ell = \delta(\ell - 107)$ , drops down very quickly. The red points are the expected leakage due to difference in the bandpower window functions.

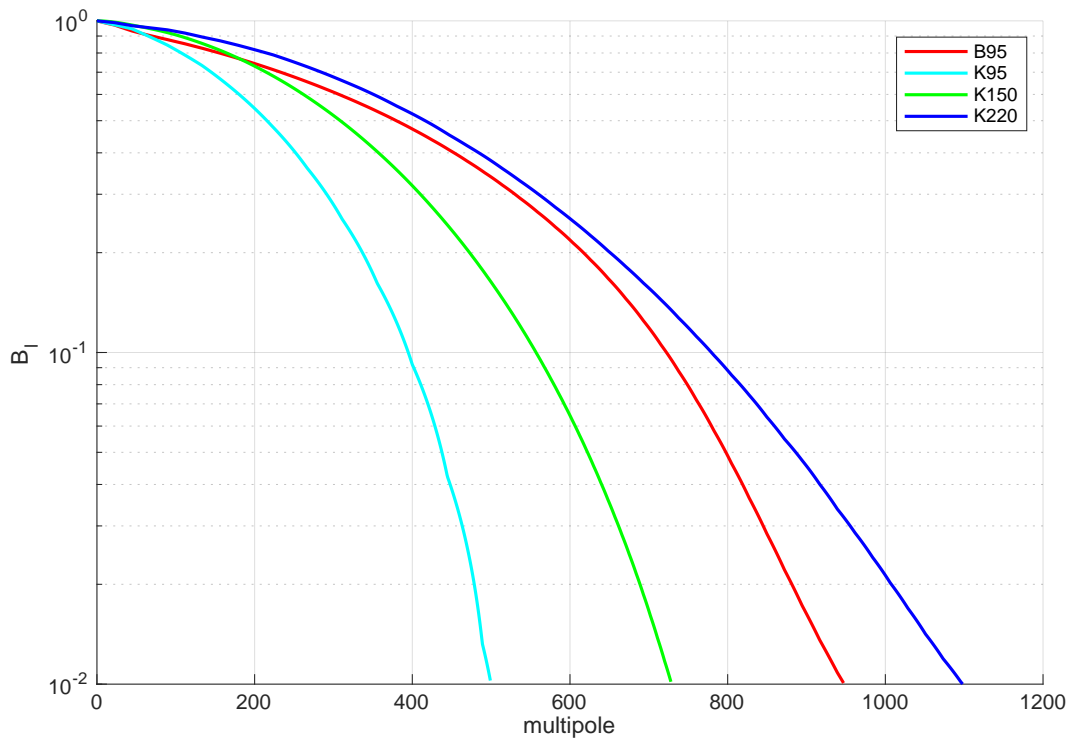


Figure 6.13: Beam window functions  $B_\ell$  for the BICEP/Keck Array bands obtained by a Fourier transform of the beams after they are averaged in azimuth.

### Map Based Difference

In the previous section, we encountered that the spectral-based difference method lacks consistency between the data and simulations. To overcome this limitation, we propose a new approach in this section based on difference in map space. More specifically we correct the maps using the beam window functions  $B_\ell$  (shown in Figure 6.13) to perform the subtraction in map space. This approach is expected to eliminate common signals in the difference maps, leading to maps that are free of lensed E-modes and  $\Lambda$ CDM in our region of interest.

In the convolution / deconvolution procedure, a filter is created by taking the product of the inverse of the beam function  $B_l$ , (where  $B_l$  is set to 0 for values less than  $1 \times 10^{-2}$ ), a Wiener filter  $s/(s+n)$  where  $s$  and  $n$  are the mean power spectra of the lensed- $\Lambda$ CDM and noise realizations, and an additional low pass filter which rolls off with  $\cos^2$ . The standard apodization mask is then applied to the maps and the Fourier-modes are multiplied by the filter before transforming back. The procedure is plotted in Figure 6.14.

To extract the relevant signal from our data, we subtract all BK maps from each other

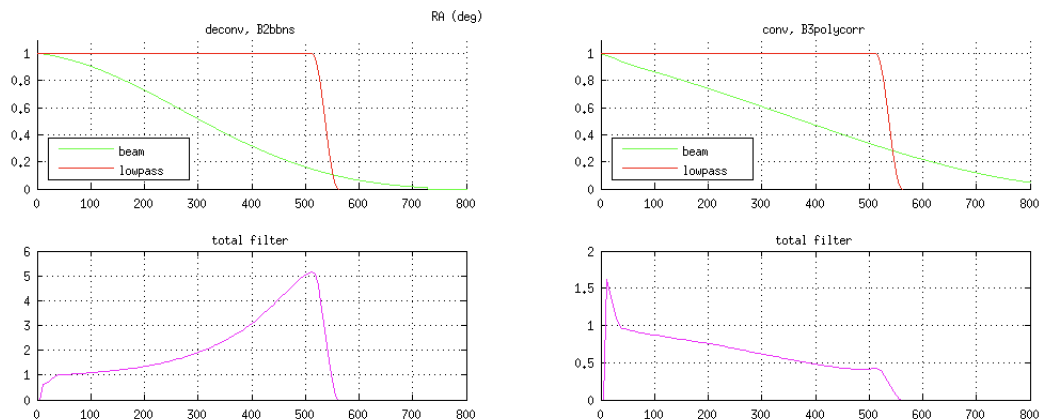


Figure 6.14: Convolution / deconvolution procedure, where the 150 GHz maps band is deconvolved with the 150 GHz beam and convolved with the 220 GHz beam. This plot shows the beams that have been deconvolved and convolved, along with the total filter. The beam that is being deconvolved is plotted on the left, while the beam that is being convolved is plotted on the right. The total filter is shown in magenta.

while correcting for the beam profile. Specifically, we applied the deconvolution procedure to the map with the finer beam using its own beam profile, followed by convolution with the beam of the other map. After visual examination, we noticed that the Keck 220 - Keck 150 (220-150), Keck 220 - Bicep3 95 (220-B95), and Keck 150 - Bicep3 95 (150-B95) maps show similar patterns in terms of EE and BB modes, separately. This can be seen in Figure 6.16 and Figure 6.17.

According to the propagation of uncertainties, we anticipate that the 220-B95 and 220-150 maps will be mainly affected by the 220 GHz noise. Nevertheless, due to the comparable levels of B95 and 150 GHz noise, we expect an increase in the overall noise levels of approximately 40%. To illustrate this, we have plotted the noise levels in Figure 6.18.

Since 220-B95 and 220-150 maps are dominated by the dust and noise levels of 220 maps, we reuse the bandpower window function for 220 maps, and expect little to no E-mode  $\Lambda$ CDM leakage for  $\ell < 200$ . This is not the case for 150-B95, and since the dust level is low in this band we omit it in the map based difference.

The spectra of map based difference, shown in Figure 6.19 contains some leaked  $\Lambda$ CDM due to differences in the bandpower window function. However the dust model (cyan) agrees well with mean of sims (dashed black).

Due to the mismatch in the bandpower window function, there is a leakage in

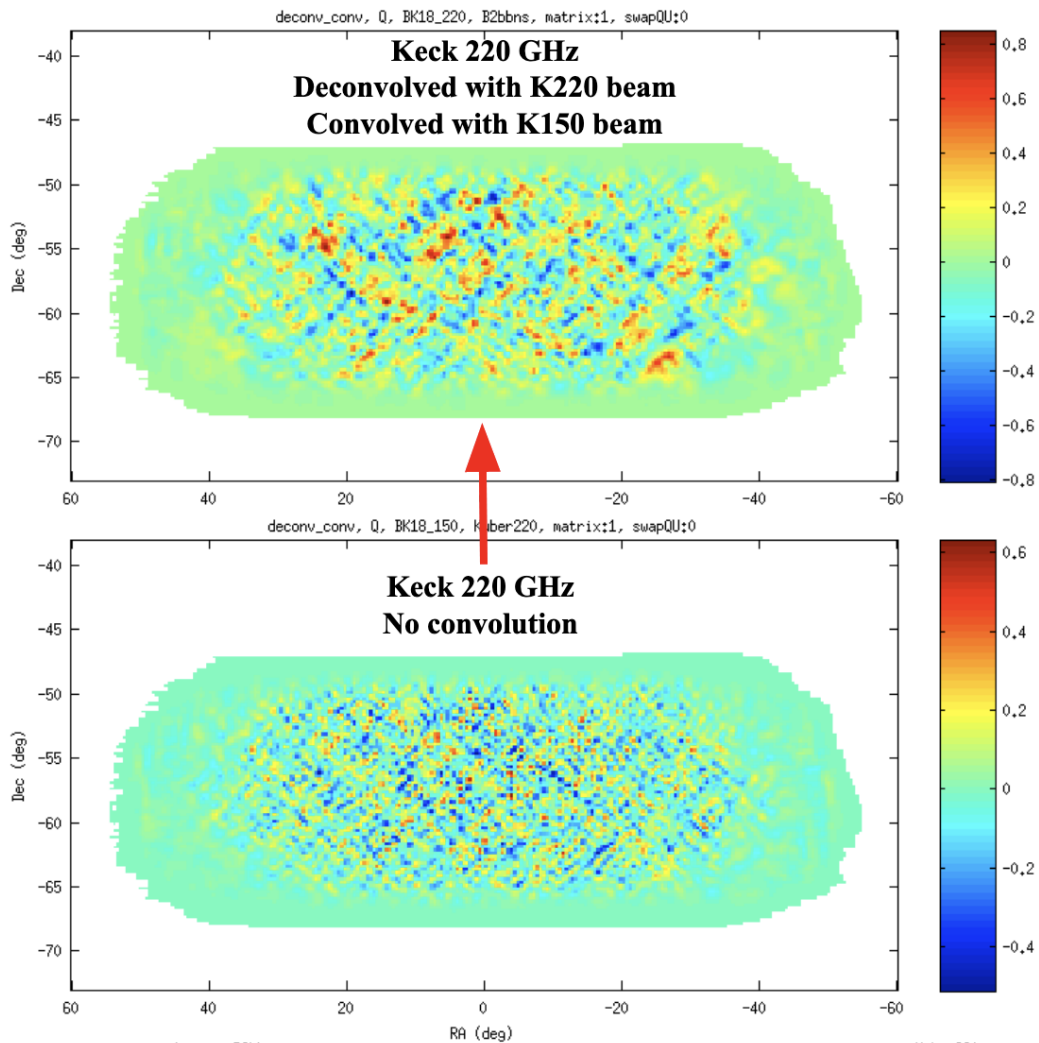


Figure 6.15: We used a Keck 220 GHz map, which we first applied the deconvolution using the K220 beam profile. Next, we convolved the resulting map with the K150 beam profile. As a result, the finer details in the original map got smoothed out. To visualize this, we show the original Keck 220 Q polarization map in the lower panel, and the processed map in the upper panel.

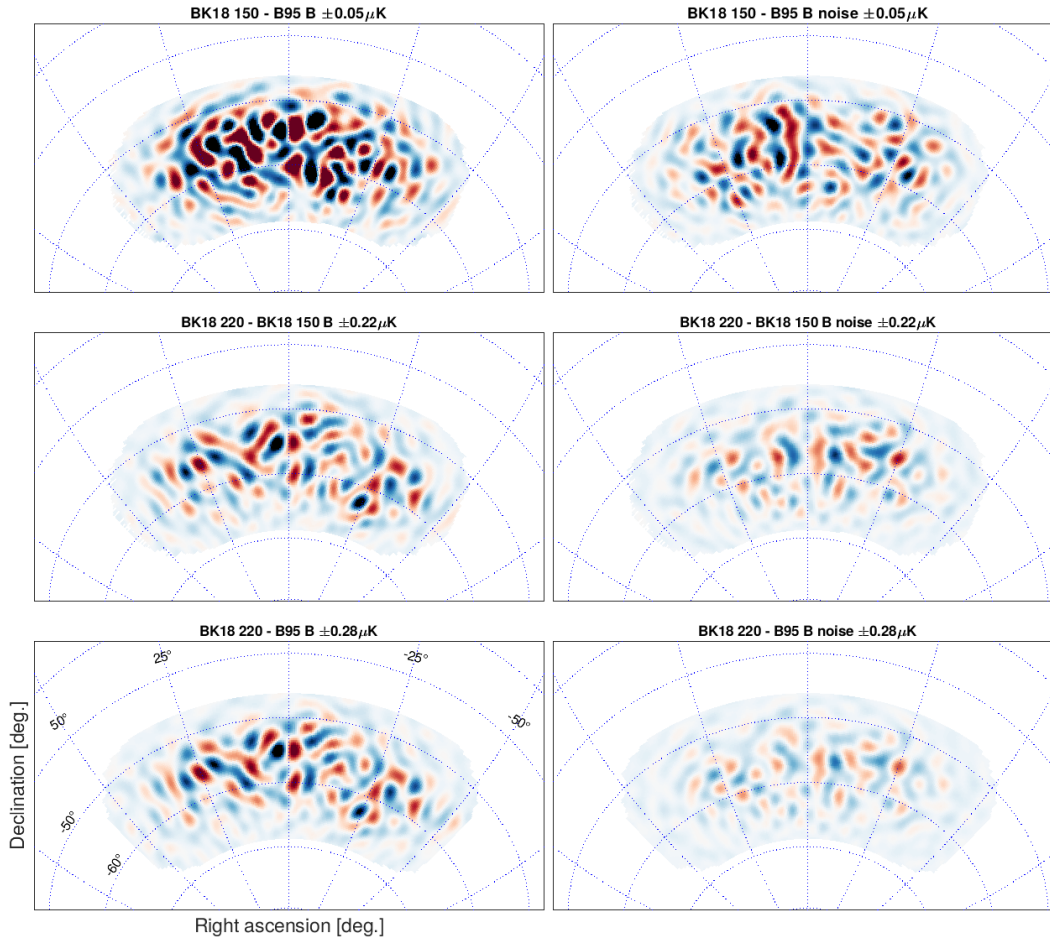


Figure 6.16: The B-mode maps from map based difference (left column) and expected noise from signflip realizations (right column) maps for the difference maps of 150-B95, 220-150, and 220-B95 GHz in CMB units. These maps have been filtered to degree angular scales. This approach is expected to eliminate common signals in the difference maps, leading to maps that are free of lensed E-modes in our region of interest.

the spectra. This is evident in the 150-B95, the realizations get very strong at higher values of  $\ell$ . To resolve this effect, we removed the mean of the  $\Lambda$ CDM-only realizations. The resulting spectra, with the bias removed, is shown in Figure 6.20.

Direct measurement of  $EE/BB$  as ratio of the spectra result in  $EE/BB = 1.69 \pm 0.58$  for  $\ell < 212$ , and  $EE/BB = 1.77 \pm 0.47$  for  $\ell < 352$ . These results are within  $1\sigma$  from 2, which was measured by Planck.

We run maximum likelihood search on the 220-95 and 220-150 maps for EE and BB spectra with  $\ell < 212$ . The ML model assumed zero  $\Lambda$ CDM and lensing, but there was an issue with the EE cross spectra between the BK18 bands and difference

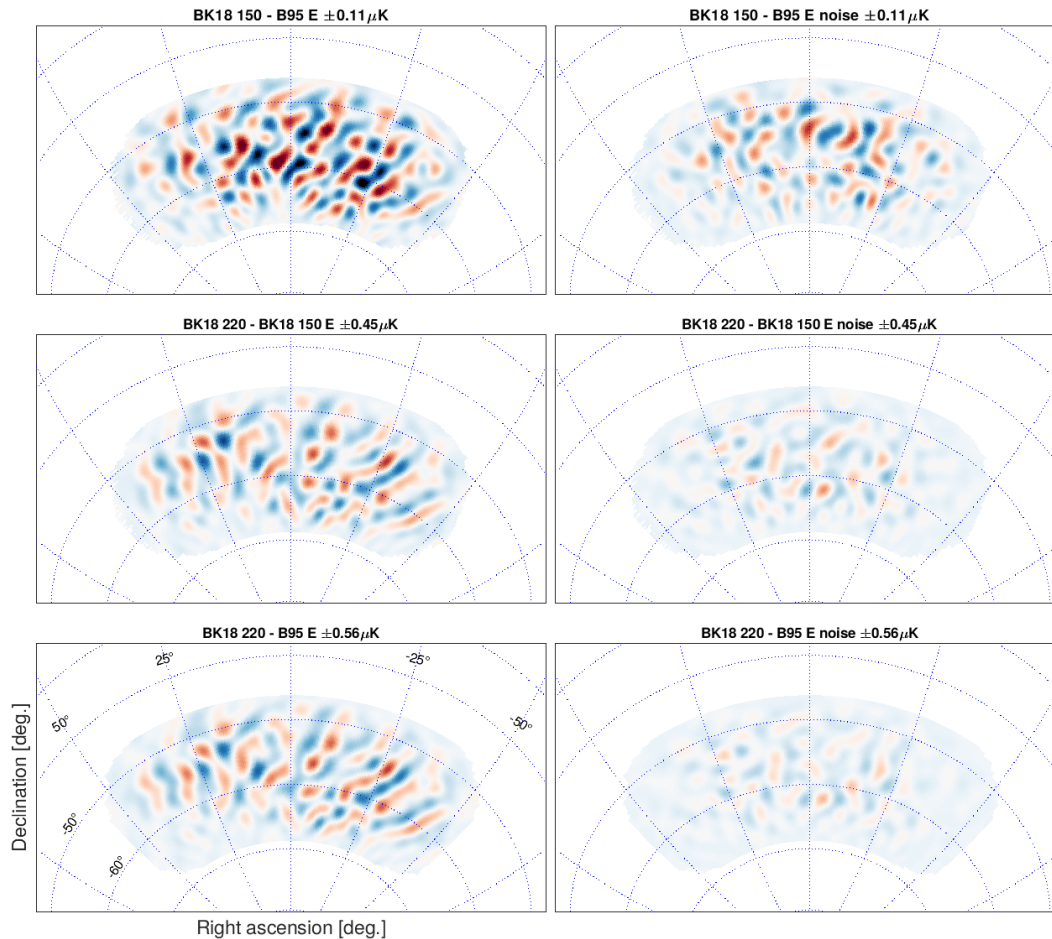


Figure 6.17: The E-mode maps from map based difference (left column) and expected noise from signflip realizations (right column) maps for the difference maps of 150-B95, 220-150, and 220-B95 GHz in CMB units. These maps have been filtered to degree angular scales. This approach is expected to eliminate common signals in the difference maps, leading to maps that are free of  $\Lambda$ CDM in our region of interest.

maps. The value of  $\beta_d$  was fixed at 1.6 to avoid degeneracy with  $A_d$  for only two bands, and the initial value of  $EE/BB$  was set to 1.5. There is a slightly negative and small bias on  $A_d$ .

A likelihood analysis with 17 bands of B-modes (BK18 baseline) + E-modes from (220-B95) and (220-150) for  $\Lambda$ CDM-free dust E-mode maps is the natural next step for this analysis, but this was not included in the thesis. The analysis is expected to bring down the bias on  $r$  and dust amplitude if the bias was due to  $\Lambda$ CDM E-modes and improve dust parameter sensitivities.

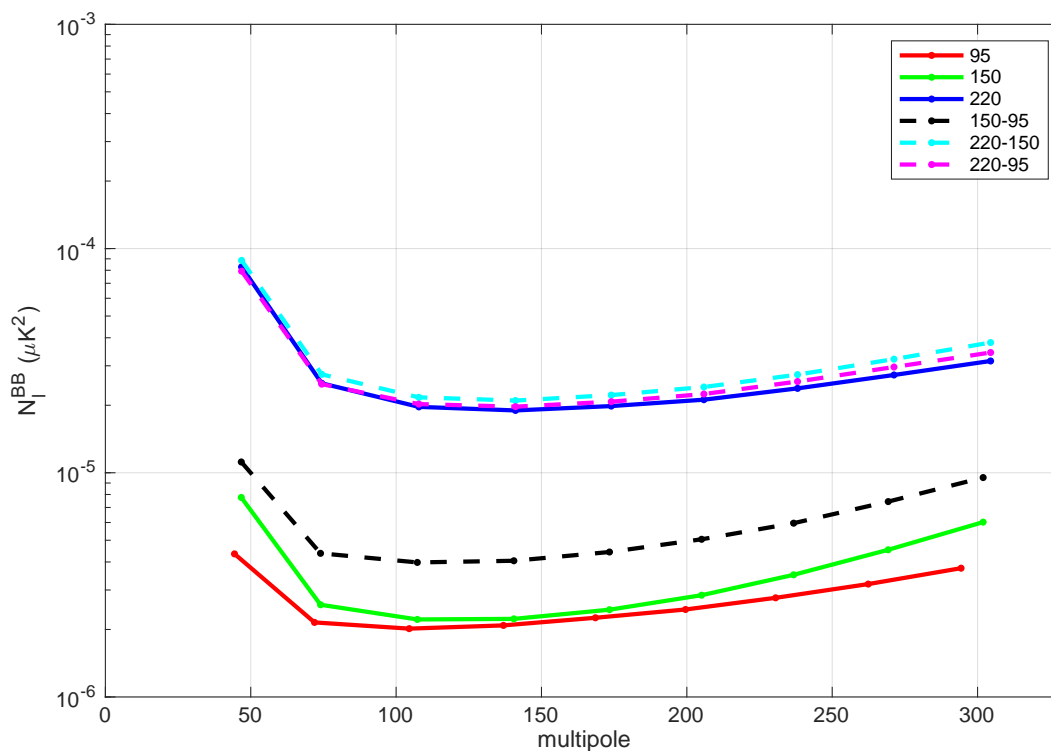


Figure 6.18: the noise spectra of the BK18 maps, represented by solid lines, alongside the anticipated noise levels of the difference spectra denoted by dashed lines. The noise levels for the BICEP3 95 GHz map are depicted in red, the BICEP2/Keck 150 GHz map in green, and the Keck 220 GHz map in blue. Additionally, the difference spectra are indicated by dashed lines: the 150-B95 difference in black, the 220-150 difference in cyan, and the 220-B95 difference in magenta. The filtering effects due to beam roll-off, timestream filtering, and B-mode purification have been corrected in the spectra. We did not apply any  $\ell^2$  scaling. 220-B95 and 220-150 maps are dominated by the dust and noise levels of 220 maps. Due to the comparable levels of B95 and 150 GHz noise, we expect an increase in the overall noise levels of approximately 40% for 150-95.

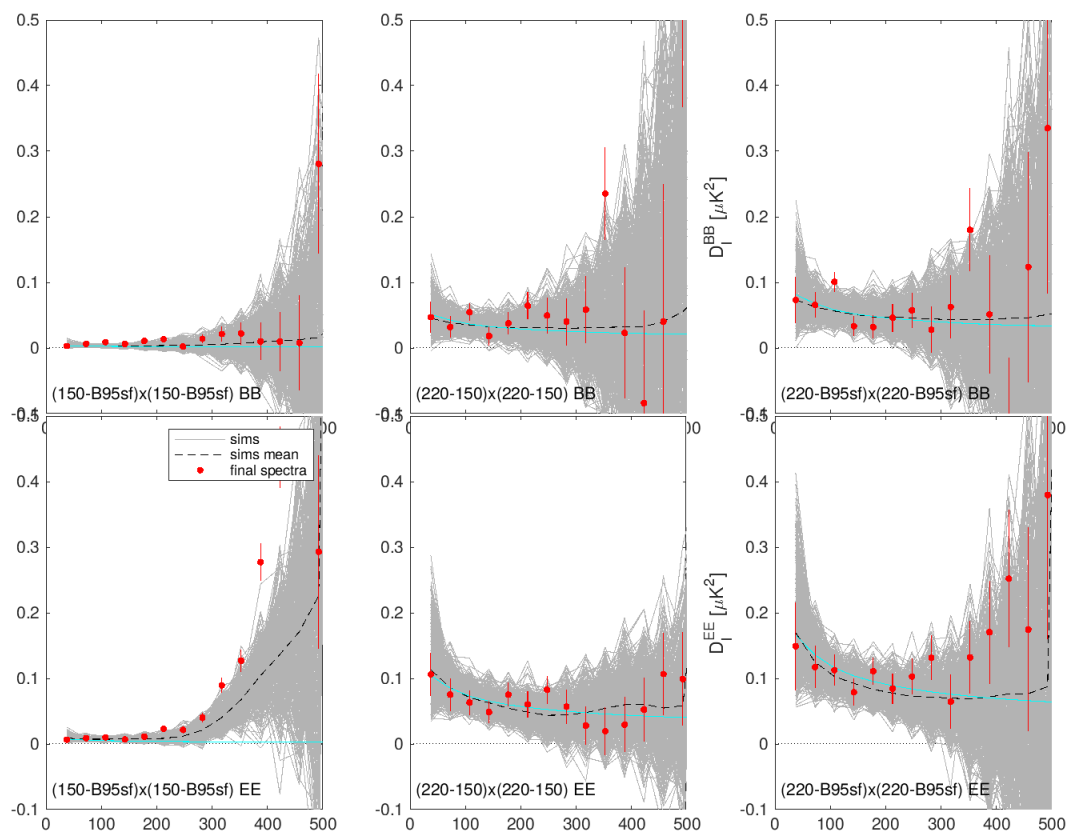


Figure 6.19: Dust model (cyan) agrees well with the mean of simulations (gray). The dust model is obtained by the difference of dust and temperature scaling, but does not use the bandpass information. We can estimate the EE/BB from the spectra directly, or feed it into the likelihood analysis to obtain all the parameters.

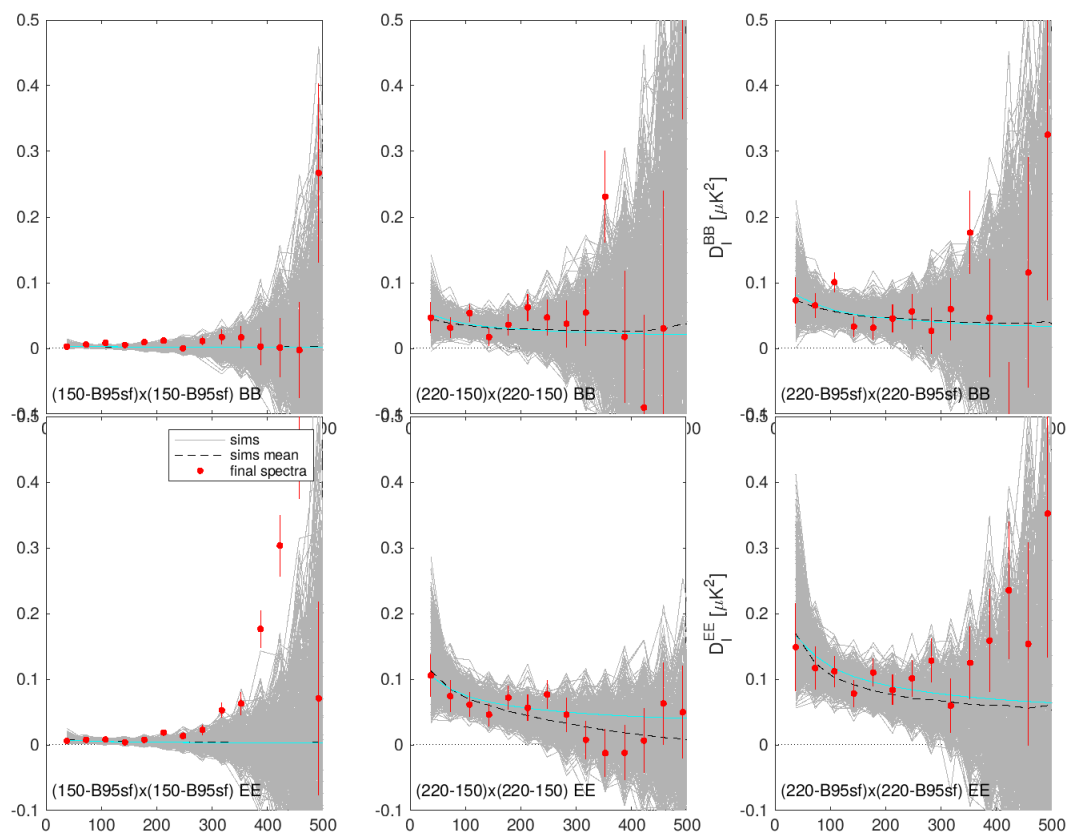


Figure 6.20: This figure is similar to Figure 6.19, but with the addition of noise debiasing to remove the leakage resulting from mismatch in the bandpower window function. The bias is estimated as the mean value of the  $\Lambda$ CDM-only realizations.

*Chapter 7*

## CONCLUSION

BICEP/Keck Array series of experiments have provided some of the most precise measurements of CMB polarization. Using these measurements, we have attempted to constrain primordial gravitational waves. We used a maximum likelihood approach and a multi-component model to extract the estimate the amplitude of the primordial gravitational waves and foreground parameters.

Measuring foregrounds is very critical for accurately estimating the primordial B-mode polarization signal. To achieve this, the BICEP/Keck Array series of telescopes measure the polarization signal at multiple frequencies, spanning from 95 GHz to 270 GHz. This wide frequency coverage allows for accurate modeling and subtraction of polarized foregrounds.

We use a joint likelihood analysis approach that simultaneously fits for the cosmological parameters and the astrophysical foreground models. We model the foregrounds using physically motivated templates and account for their spectral properties. We apply this analysis framework to the data from the BICEP/Keck Array experiments. Our results show that foregrounds are no longer the limiting factor, and we present constraints on the cosmological parameters, including the tensor-to-scalar ratio,  $r$ . Our results are consistent with the  $\Lambda$ CDM model and improve the previous constraints on  $r$ .

We also discuss the challenges and limitations of our analysis framework, including the need for accurate modeling of the astrophysical foregrounds, the impact of instrumental and observational effects, and the potential biases that may arise from assumptions made in the analysis. Overall, our analysis framework provides a robust and reliable method for extracting cosmological parameters from polarized CMB data and can be applied to future experiments with improved sensitivity and resolution.

Accurately modeling and removing the contribution from polarized dust emission is critical for detecting any primordial B-mode signals and placing better constraints on the tensor-to-scalar ratio  $r$ . The polarized dust emission is due to the alignment of

non-spherical dust grains with the local magnetic field. We explored that the spatial variations in unpolarized dust temperature and spectral index can cause residuals do not cause any significant bias in the multi-component model foreground parameters. We have also explored a new analysis technique, subtracting bands from each other in spectral and map space to remove common signals and used this to estimate polarized foreground dust parameters.

## BIBLIOGRAPHY

- [1] K.N. Abazajian et al. “Inflation physics from the cosmic microwave background and large scale structure”. In: *Astroparticle Physics* 63 (Mar. 2015), pp. 55–65. ISSN: 0927-6505. DOI: [10.1016/j.astropartphys.2014.05.013](https://doi.org/10.1016/j.astropartphys.2014.05.013). URL: <http://dx.doi.org/10.1016/j.astropartphys.2014.05.013>.
- [2] R. Adam et al. “Planck2015 results”. In: *Astronomy & Astrophysics* 594 (Sept. 2016), A10. ISSN: 1432-0746. DOI: [10.1051/0004-6361/201525967](https://doi.org/10.1051/0004-6361/201525967). URL: <http://dx.doi.org/10.1051/0004-6361/201525967>.
- [3] R. Adam et al. “Planckintermediate results”. In: *Astronomy & Astrophysics* 586 (Feb. 2016), A133. ISSN: 1432-0746. DOI: [10.1051/0004-6361/201425034](https://doi.org/10.1051/0004-6361/201425034). URL: <http://dx.doi.org/10.1051/0004-6361/201425034>.
- [4] Fred C. Adams et al. “Natural inflation: Particle physics models, power-law spectra for large-scale structure, and constraints from the Cosmic Background Explorer”. In: *Physical Review D* 47.2 (1993), pp. 426–455. DOI: [10.1103/physrevd.47.426](https://doi.org/10.1103/physrevd.47.426). URL: <https://doi.org/10.1103/physrevd.47.426>.
- [5] P. A. R. Ade et al. “BICEP2/Keck Array IV: Optical Characterization and Performance of the BICEP2 and Keck Array Experiments”. In: *Astrophys. J.* 806.2 (2015), p. 206. DOI: [10.1088/0004-637X/806/2/206](https://doi.org/10.1088/0004-637X/806/2/206). arXiv: [1502.00596](https://arxiv.org/abs/1502.00596) [astro-ph.IM].
- [6] P. A. R. Ade et al. “Bicep/KeckXV: The Bicep3 Cosmic Microwave Background Polarimeter and the First Three-year Data Set”. In: *Astrophys. J.* 927.1 (2022), p. 77. DOI: [10.3847/1538-4357/ac4886](https://doi.org/10.3847/1538-4357/ac4886). arXiv: [2110.00482](https://arxiv.org/abs/2110.00482) [astro-ph.IM].
- [7] P. A. R. Ade et al. “BICEP2 / Keck Array VII: Matrix based E/B Separation applied to BICEP2 and the Keck Array”. In: *Astrophys. J.* 825.1 (2016), p. 66. DOI: [10.3847/0004-637X/825/1/66](https://doi.org/10.3847/0004-637X/825/1/66). arXiv: [1603.05976](https://arxiv.org/abs/1603.05976) [astro-ph.IM].
- [8] P. A. R. Ade et al. “BICEP2 / Keck Array VIII: Measurement of gravitational lensing from large-scale B-mode polarization”. In: *Astrophys. J.* 833.2 (2016), p. 228. DOI: [10.3847/1538-4357/833/2/228](https://doi.org/10.3847/1538-4357/833/2/228). arXiv: [1606.01968](https://arxiv.org/abs/1606.01968) [astro-ph.CO].
- [9] P. A. R. Ade et al. “BICEP2 / Keck Array x: Constraints on Primordial Gravitational Waves using Planck, WMAP, and New BICEP2/Keck Observations through the 2015 Season”. In: *Phys. Rev. Lett.* 121 (2018), p. 221301. DOI: [10.1103/PhysRevLett.121.221301](https://doi.org/10.1103/PhysRevLett.121.221301). arXiv: [1810.05216](https://arxiv.org/abs/1810.05216) [astro-ph.CO].

- [10] P. A. R. Ade et al. “BICEP2 II: Experiment and Three-Year Data Set”. In: *Astrophys. J.* 792.1 (2014), p. 62. DOI: [10.1088/0004-637X/792/1/62](https://doi.org/10.1088/0004-637X/792/1/62). arXiv: [1403.4302](https://arxiv.org/abs/1403.4302) [[astro-ph.CO](#)].
- [11] P. A. R. Ade et al. “Detection of *B*-Mode Polarization at Degree Angular Scales by BICEP2”. In: *Phys. Rev. Lett.* 112.24 (2014), p. 241101. DOI: [10.1103/PhysRevLett.112.241101](https://doi.org/10.1103/PhysRevLett.112.241101). arXiv: [1403.3985](https://arxiv.org/abs/1403.3985) [[astro-ph.CO](#)].
- [12] P. A. R. Ade et al. “Improved Constraints on Cosmology and Foregrounds from BICEP2 and Keck Array Cosmic Microwave Background Data with Inclusion of 95 GHz Band”. In: *Phys. Rev. Lett.* 116 (2016), p. 031302. DOI: [10.1103/PhysRevLett.116.031302](https://doi.org/10.1103/PhysRevLett.116.031302). arXiv: [1510.09217](https://arxiv.org/abs/1510.09217) [[astro-ph.CO](#)].
- [13] P. A. R. Ade et al. “Joint Analysis of BICEP2/KeckArray and Planck Data”. In: *Phys. Rev. Lett.* 114 (2015), p. 101301. DOI: [10.1103/PhysRevLett.114.101301](https://doi.org/10.1103/PhysRevLett.114.101301). arXiv: [1502.00612](https://arxiv.org/abs/1502.00612) [[astro-ph.CO](#)].
- [14] P. A. R. Ade et al. “Planck 2013 results. XII. Diffuse component separation”. In: *Astron. Astrophys.* 571 (2014), A12. DOI: [10.1051/0004-6361/201321580](https://doi.org/10.1051/0004-6361/201321580). arXiv: [1303.5072](https://arxiv.org/abs/1303.5072) [[astro-ph.CO](#)].
- [15] P. A. R. Ade et al. “Planck 2013 results. XVI. Cosmological parameters”. In: *Astron. Astrophys.* 571 (2014), A16. DOI: [10.1051/0004-6361/201321591](https://doi.org/10.1051/0004-6361/201321591). arXiv: [1303.5076](https://arxiv.org/abs/1303.5076) [[astro-ph.CO](#)].
- [16] P. A. R. Ade et al. “Planck 2015 results. XIII. Cosmological parameters”. In: *Astron. Astrophys.* 594 (2016), A13. DOI: [10.1051/0004-6361/201525830](https://doi.org/10.1051/0004-6361/201525830). arXiv: [1502.01589](https://arxiv.org/abs/1502.01589) [[astro-ph.CO](#)].
- [17] P. A. R. Ade et al. “Planck intermediate results. XXII. Frequency dependence of thermal emission from Galactic dust in intensity and polarization”. In: *Astron. Astrophys.* 576 (2015), A107. DOI: [10.1051/0004-6361/201424088](https://doi.org/10.1051/0004-6361/201424088). arXiv: [1405.0874](https://arxiv.org/abs/1405.0874) [[astro-ph.GA](#)].
- [18] P. A. R. Ade et al. “Improved Constraints on Primordial Gravitational Waves using Planck , WMAP, and BICEP/ Keck Observations through the 2018 Observing Season”. In: *Physical Review Letters* 127.15 (Oct. 2021). ISSN: 1079-7114. DOI: [10.1103/physrevlett.127.151301](https://doi.org/10.1103/physrevlett.127.151301). URL: <http://dx.doi.org/10.1103/PhysRevLett.127.151301>.
- [19] P. A. R. Ade et al. “Planck2013 results. XVI. Cosmological parameters”. In: *Astronomy & Astrophysics* 571 (Oct. 2014), A16. ISSN: 1432-0746. DOI: [10.1051/0004-6361/201321591](https://doi.org/10.1051/0004-6361/201321591). URL: <http://dx.doi.org/10.1051/0004-6361/201321591>.
- [20] P. A. R. Ade et al. “Planck2013 results. XXX. Cosmic infrared background measurements and implications for star formation”. In: *Astronomy & Astrophysics* 571 (Oct. 2014), A30. ISSN: 1432-0746. DOI: [10.1051/0004-6361/201322093](https://doi.org/10.1051/0004-6361/201322093). URL: <http://dx.doi.org/10.1051/0004-6361/201322093>.

- [21] Peter AR Ade et al. “Planck 2013 results. XII. Diffuse component separation”. In: *Astronomy & Astrophysics* 571 (2014), A12.
- [22] N. Aghanim et al. “Planck 2018 results. VI. Cosmological parameters”. In: *Astron. Astrophys.* 641 (2020). [Erratum: *Astron. Astrophys.* 652, C4 (2021)], A6. DOI: [10.1051/0004-6361/201833910](https://doi.org/10.1051/0004-6361/201833910). arXiv: [1807.06209](https://arxiv.org/abs/1807.06209) [[astro-ph.CO](https://arxiv.org/abs/1807.06209)].
- [23] N. Aghanim et al. “Planck intermediate results - L. Evidence of spatial variation of the polarized thermal dust spectral energy distribution and implications for CMB B-mode analysis”. In: *Astron. Astrophys.* 599 (2017), A51. DOI: [10.1051/0004-6361/201629164](https://doi.org/10.1051/0004-6361/201629164). arXiv: [1606.07335](https://arxiv.org/abs/1606.07335) [[astro-ph.CO](https://arxiv.org/abs/1606.07335)].
- [24] N. Aghanim et al. “Planck 2018 results: I. Overview and the cosmological legacy of Planck”. In: *Astronomy and Astrophysics* 641 (2020). ISSN: 14320746. DOI: [10.1051/0004-6361/201833880](https://doi.org/10.1051/0004-6361/201833880).
- [25] N. Aghanim et al. “Planckintermediate results”. In: *Astronomy & Astrophysics* 596 (Dec. 2016), A109. ISSN: 1432-0746. DOI: [10.1051/0004-6361/201629022](https://doi.org/10.1051/0004-6361/201629022). URL: <http://dx.doi.org/10.1051/0004-6361/201629022>.
- [26] M. Aguilar Faúndez et al. “Cross-correlation of POLARBEAR CMB Polarization Lensing with High- $z$  Sub-mm Herschel-ATLAS galaxies”. In: *Astrophys. J.* 886.1 (2019), p. 38. DOI: [10.3847/1538-4357/ab4a78](https://doi.org/10.3847/1538-4357/ab4a78). arXiv: [1903.07046](https://arxiv.org/abs/1903.07046) [[astro-ph.CO](https://arxiv.org/abs/1903.07046)].
- [27] Y. Akrami et al. “Planck 2018 results. IV. Diffuse component separation”. In: *Astron. Astrophys.* 641 (2020), A4. DOI: [10.1051/0004-6361/201833881](https://doi.org/10.1051/0004-6361/201833881). arXiv: [1807.06208](https://arxiv.org/abs/1807.06208) [[astro-ph.CO](https://arxiv.org/abs/1807.06208)].
- [28] Y. Akrami et al. “Planck 2018 results. XI. Polarized dust foregrounds”. In: *Astron. Astrophys.* 641 (2020), A11. DOI: [10.1051/0004-6361/201832618](https://doi.org/10.1051/0004-6361/201832618). arXiv: [1801.04945](https://arxiv.org/abs/1801.04945) [[astro-ph.GA](https://arxiv.org/abs/1801.04945)].
- [29] Y. Akrami et al. “Planck 2018 results”. In: *Astronomy & Astrophysics* 641 (Sept. 2020), A11. ISSN: 1432-0746. DOI: [10.1051/0004-6361/201832618](https://doi.org/10.1051/0004-6361/201832618). URL: <http://dx.doi.org/10.1051/0004-6361/201832618>.
- [30] Andreas Albrecht and Paul J. Steinhardt. “Cosmology for Grand Unified Theories with Radiatively Induced Symmetry Breaking”. In: *Phys. Rev. Lett.* 48 (17 1982), pp. 1220–1223. DOI: [10.1103/PhysRevLett.48.1220](https://doi.org/10.1103/PhysRevLett.48.1220). URL: <https://link.aps.org/doi/10.1103/PhysRevLett.48.1220>.
- [31] D. Barkats et al. “Degree-Scale CMB Polarization Measurements from Three Years of BICEP1 Data”. In: *Astrophys. J.* 783 (2014), p. 67. DOI: [10.1088/0004-637X/783/2/67](https://doi.org/10.1088/0004-637X/783/2/67). arXiv: [1310.1422](https://arxiv.org/abs/1310.1422) [[astro-ph.CO](https://arxiv.org/abs/1310.1422)].

- [32] Daniel Baumann. *TASI Lectures on Inflation*. 2012. arXiv: [0907.5424](https://arxiv.org/abs/0907.5424) [[hep-th](#)].
- [33] Fedor Bezrukov and Mikhail Shaposhnikov. “The Standard Model Higgs boson as the inflaton”. In: *Physics Letters B* 659.3 (2008), pp. 703–706. DOI: [10.1016/j.physletb.2007.11.072](https://doi.org/10.1016/j.physletb.2007.11.072). URL: <https://doi.org/10.10162Fj.physletb.2007.11.072>.
- [34] Bicep2 Collaboration et al. “Bicep2 III: Instrumental Systematics”. In: *Astrophys. J.* 814.2, 110 (Dec. 2015), p. 110. DOI: [10.1088/0004-637X/814/2/110](https://doi.org/10.1088/0004-637X/814/2/110). arXiv: [1502.00608](https://arxiv.org/abs/1502.00608) [[astro-ph.IM](#)].
- [35] Lotfi Boubekur and David H Lyth. “Hilltop inflation”. In: *Journal of Cosmology and Astroparticle Physics* 2005.07 (2005), pp. 010–010. DOI: [10.1088/1475-7516/2005/07/010](https://doi.org/10.1088/1475-7516/2005/07/010). URL: <https://doi.org/10.1088%2F1475-7516%2F2005%2F07%2F010>.
- [36] Emory F. Bunn et al. “E/B decomposition of finite pixelized CMB maps”. In: *Phys. Rev. D* 67 (2003), p. 023501. DOI: [10.1103/PhysRevD.67.023501](https://doi.org/10.1103/PhysRevD.67.023501). arXiv: [astro-ph/0207338](https://arxiv.org/abs/astro-ph/0207338).
- [37] Victor Buza. “Constraining Primordial Gravitational Waves Using Present and Future CMB Experiments”. PhD thesis. Harvard U. (main), 2019.
- [38] M. Cicoli, C. P. Burgess, and F. Quevedo. “Fibre Inflation: Observable Gravity Waves from IIB String Compactifications”. In: *JCAP* 03 (2009), p. 013. DOI: [10.1088/1475-7516/2009/03/013](https://doi.org/10.1088/1475-7516/2009/03/013). arXiv: [0808.0691](https://arxiv.org/abs/0808.0691) [[hep-th](#)].
- [39] S. E. Clark, J. E.G. Peek, and M. E. Putman. “Magnetically aligned H i fibers and the rolling hough transform”. In: *Astrophysical Journal* 789 (1 2014). ISSN: 15384357. DOI: [10.1088/0004-637X/789/1/82](https://doi.org/10.1088/0004-637X/789/1/82).
- [40] S. E. Clark et al. “Neutral hydrogen structures trace dust polarization angle: Implications for cosmic microwave background foregrounds”. In: *Phys. Rev. Lett.* 115.24 (2015), p. 241302. DOI: [10.1103/PhysRevLett.115.241302](https://doi.org/10.1103/PhysRevLett.115.241302). arXiv: [1508.07005](https://arxiv.org/abs/1508.07005) [[astro-ph.CO](#)].
- [41] J. Dunkley et al. “Prospects for polarized foreground removal”. In: *AIP Conference Proceedings* (2009). DOI: [10.1063/1.3160888](https://doi.org/10.1063/1.3160888). URL: <http://dx.doi.org/10.1063/1.3160888>.
- [42] Cora Dvorkin, Hiranya V. Peiris, and Wayne Hu. “Testable polarization predictions for models of CMB isotropy anomalies”. In: *Phys. Rev. D* 77 (2008), p. 063008. DOI: [10.1103/PhysRevD.77.063008](https://doi.org/10.1103/PhysRevD.77.063008). arXiv: [0711.2321](https://arxiv.org/abs/0711.2321) [[astro-ph](#)].
- [43] A. Van Engelen et al. “A measurement of gravitational lensing of the microwave background using south pole telescope data”. In: *Astrophysical Journal* 756 (2 2012). ISSN: 15384357. DOI: [10.1088/0004-637X/756/2/142](https://doi.org/10.1088/0004-637X/756/2/142).

- [44] D. P. Finkbeiner, M. Davis, and D. J. Schlegel. “Extrapolation of Galactic Dust Emission at 100 Microns to Cosmic Microwave Background Radiation Frequencies Using FIRAS”. In: *The Astrophysical Journal* 524 (Oct. 1999), pp. 867–886.
- [45] Katherine Freese, Joshua A. Frieman, and Angela V. Olinto. “Natural inflation with pseudo - Nambu-Goldstone bosons”. In: *Phys. Rev. Lett.* 65 (1990), pp. 3233–3236. DOI: [10.1103/PhysRevLett.65.3233](https://doi.org/10.1103/PhysRevLett.65.3233).
- [46] U. Fuskeland et al. “Spatial variations in the spectral index of polarized synchrotron emission in the 9-yr WMAP sky maps”. In: *Astrophys. J.* 790 (2014), p. 104. DOI: [10.1088/0004-637X/790/2/104](https://doi.org/10.1088/0004-637X/790/2/104). arXiv: [1404.5323](https://arxiv.org/abs/1404.5323) [[astro-ph.CO](https://arxiv.org/abs/1404.5323)].
- [47] K. M. Górski et al. “HEALPix - A Framework for high resolution discretization, and fast analysis of data distributed on the sphere”. In: *Astrophys. J.* 622 (2005), pp. 759–771. DOI: [10.1086/427976](https://doi.org/10.1086/427976). arXiv: [astro-ph/0409513](https://arxiv.org/abs/astro-ph/0409513).
- [48] Alan H. Guth. “Inflationary universe: A possible solution to the horizon and flatness problems”. In: *Phys. Rev. D* 23 (2 1981), pp. 347–356. DOI: [10.1103/PhysRevD.23.347](https://doi.org/10.1103/PhysRevD.23.347). URL: <https://link.aps.org/doi/10.1103/PhysRevD.23.347>.
- [49] Samira Hamimeche and Antony Lewis. “Likelihood Analysis of CMB Temperature and Polarization Power Spectra”. In: *Phys. Rev. D* 77 (2008), p. 103013. DOI: [10.1103/PhysRevD.77.103013](https://doi.org/10.1103/PhysRevD.77.103013). arXiv: [0801.0554](https://arxiv.org/abs/0801.0554) [[astro-ph](https://arxiv.org/abs/0801.0554)].
- [50] D. Hanson et al. “Detection of B-Mode Polarization in the Cosmic Microwave Background with Data from the South Pole Telescope”. In: *Physical Review Letters* 111.14 (Sept. 2013). ISSN: 1079-7114. DOI: [10.1103/PhysRevLett.111.141301](https://doi.org/10.1103/PhysRevLett.111.141301). URL: <http://dx.doi.org/10.1103/PhysRevLett.111.141301>.
- [51] James B. Hartle and Jennie Traschen. “Gravity: An introduction to Einstein’s general relativity”. In: *Physics Today* 58 (1 2005). ISSN: 00319228. DOI: [10.1063/1.1881902](https://doi.org/10.1063/1.1881902).
- [52] Patrick Hennebelle. “On the origin of non self-gravitating filaments in the ISM”. In: *Astron. Astrophys.* 556 (2013), A153. DOI: [10.1051/0004-6361/201321292](https://doi.org/10.1051/0004-6361/201321292). arXiv: [1306.5452](https://arxiv.org/abs/1306.5452) [[astro-ph.GA](https://arxiv.org/abs/1306.5452)].
- [53] Brandon S. Hensley and Philip Bull. “Mitigating Complex Dust Foregrounds in Future Cosmic Microwave Background Polarization Experiments”. In: *The Astrophysical Journal* 853.2 (Jan. 2018), p. 127. ISSN: 1538-4357. DOI: [10.3847/1538-4357/aaa489](https://doi.org/10.3847/1538-4357/aaa489). URL: <http://dx.doi.org/10.3847/1538-4357/aaa489>.

- [54] Eric Hivon et al. “MASTER of the Cosmic Microwave Background Anisotropy Power Spectrum: A Fast Method for Statistical Analysis of Large and Complex Cosmic Microwave Background Data Sets”. In: *The Astrophysical Journal* 567.1 (Mar. 2002), pp. 2–17. DOI: [10.1086/338126](https://doi.org/10.1086/338126). URL: <https://doi.org/10.1086%2F338126>.
- [55] Wayne Hu and Takemi Okamoto. “Mass reconstruction with cmb polarization”. In: *Astrophys. J.* 574 (2002), pp. 566–574. DOI: [10.1086/341110](https://doi.org/10.1086/341110). arXiv: [astro-ph/0111606](https://arxiv.org/abs/astro-ph/0111606).
- [56] Wayne Hu and Martin J. White. “A CMB polarization primer”. In: *New Astron.* 2 (1997), p. 323. DOI: [10.1016/S1384-1076\(97\)00022-5](https://doi.org/10.1016/S1384-1076(97)00022-5). arXiv: [astro-ph/9706147](https://arxiv.org/abs/astro-ph/9706147).
- [57] Wayne Hu and Martin J. White. “Acoustic signatures in the cosmic microwave background”. In: *Astrophys. J.* 471 (1996), pp. 30–51. DOI: [10.1086/177951](https://doi.org/10.1086/177951). arXiv: [astro-ph/9602019](https://arxiv.org/abs/astro-ph/9602019).
- [58] Howard Hui et al. “BICEP Array: a multi-frequency degree-scale CMB polarimeter”. In: *Proc. SPIE Int. Soc. Opt. Eng.* 10708 (2018). Ed. by George Z. Angeli and Philippe Dierickx, p. 1070807. DOI: [10.1117/12.2311725](https://doi.org/10.1117/12.2311725). arXiv: [1808.00568](https://arxiv.org/abs/1808.00568) [[astro-ph.IM](https://arxiv.org/abs/astro-ph.IM)].
- [59] Kiyotomo Ichiki. “CMB foreground: A concise review”. In: *Progress of Theoretical and Experimental Physics* 2014.6 (June 2014). 06B109. ISSN: 2050-3911. DOI: [10.1093/ptep/ptu065](https://doi.org/10.1093/ptep/ptu065). eprint: <https://academic.oup.com/ptep/article-pdf/2014/6/06B109/4447714/ptu065.pdf>. URL: <https://doi.org/10.1093/ptep/ptu065>.
- [60] K.D. Irwin and G.C. Hilton. “Transition-Edge Sensors”. In: *Cryogenic Particle Detection*. Ed. by Christian Enss. Berlin, Heidelberg: Springer, 2005, pp. 63–150.
- [61] William C. Jones et al. “Instrumental and Analytic Methods for Bolometric Polarimetry”. In: *Astron. Astrophys.* 470 (2007), p. 771. DOI: [10.1051/0004-6361:20065911](https://doi.org/10.1051/0004-6361:20065911). arXiv: [astro-ph/0606606](https://arxiv.org/abs/astro-ph/0606606).
- [62] Renata Kallosh and Andrei Linde. “BICEP/Keck and cosmological attractors”. In: *JCAP* 12.12 (2021), p. 008. DOI: [10.1088/1475-7516/2021/12/008](https://doi.org/10.1088/1475-7516/2021/12/008). arXiv: [2110.10902](https://arxiv.org/abs/2110.10902) [[astro-ph.CO](https://arxiv.org/abs/astro-ph.CO)].
- [63] Marc Kamionkowski, Arthur Kosowsky, and Albert Stebbins. “A probe of primordial gravity waves and vorticity”. In: *Physical Review Letters* 78 (11 1997). ISSN: 10797114. DOI: [10.1103/PhysRevLett.78.2058](https://doi.org/10.1103/PhysRevLett.78.2058).
- [64] Sarah Kernasovskiy. “Measuring the polarization of the cosmic microwave background with the Keck Array and Bicep2”. PhD thesis. Stanford U., 2014.

- [65] A. Kogut et al. “Three-Year Wilkinson Microwave Anisotropy Probe (WMAP) Observations: Foreground Polarization”. In: *The Astrophysical Journal* 665.1 (Aug. 2007), pp. 355–362. ISSN: 1538-4357. DOI: [10.1086/519754](https://doi.org/10.1086/519754). URL: <http://dx.doi.org/10.1086/519754>.
- [66] Antony Lewis. “Lensed CMB simulation and parameter estimation”. In: *Phys. Rev. D* 71 (2005), p. 083008. DOI: [10.1103/PhysRevD.71.083008](https://doi.org/10.1103/PhysRevD.71.083008). arXiv: [astro-ph/0502469](https://arxiv.org/abs/astro-ph/0502469).
- [67] Antony Lewis and Sarah Bridle. “Cosmological parameters from CMB and other data: A Monte Carlo approach”. In: *Phys. Rev. D* 66 (2002), p. 103511. DOI: [10.1103/PhysRevD.66.103511](https://doi.org/10.1103/PhysRevD.66.103511). arXiv: [astro-ph/0205436](https://arxiv.org/abs/astro-ph/0205436).
- [68] Antony Lewis and Anthony Challinor. “Weak gravitational lensing of the CMB”. In: *Phys. Rept.* 429 (2006), pp. 1–65. DOI: [10.1016/j.physrep.2006.03.002](https://doi.org/10.1016/j.physrep.2006.03.002). arXiv: [astro-ph/0601594](https://arxiv.org/abs/astro-ph/0601594).
- [69] Andrei D. Linde. “A New Inflationary Universe Scenario: A Possible Solution of the Horizon, Flatness, Homogeneity, Isotropy and Primordial Monopole Problems”. In: *Phys. Lett. B* 108 (1982). Ed. by Li-Zhi Fang and R. Ruffini, pp. 389–393. DOI: [10.1016/0370-2693\(82\)91219-9](https://doi.org/10.1016/0370-2693(82)91219-9).
- [70] A. Mangilli et al. *PILOT balloon-borne experiment in-flight performance*. 2019. arXiv: [1804.05645](https://arxiv.org/abs/1804.05645) [[astro-ph.IM](https://arxiv.org/abs/1804.05645)].
- [71] D. H. Martin and E. Puplett. “Polarised interferometric spectrometry for the millimeter and submillimeter spectrum.” In: *Infrared Physics* 10 (Jan. 1970), pp. 105–109. DOI: [10.1016/0020-0891\(70\)90006-0](https://doi.org/10.1016/0020-0891(70)90006-0).
- [72] Liam McAllister, Eva Silverstein, and Alexander Westphal. In: 82.4 (2010). DOI: [10.1103/physrevd.82.046003](https://doi.org/10.1103/physrevd.82.046003). URL: <https://doi.org/10.1103/PhysRevD.82.046003>.
- [73] A. Men’shchikov et al. “Filamentary structures and compact objects in the Aquila and Polaris clouds observed by Herschel”. In: *Astronomy and Astrophysics* 518 (8 2010). ISSN: 14320746. DOI: [10.1051/0004-6361/201014668](https://doi.org/10.1051/0004-6361/201014668).
- [74] R. Misawa et al. “PILOT: a balloon-borne experiment to measure the polarized FIR emission of dust grains in the interstellar medium”. In: *SPIE Proceedings*. Ed. by Wayne S. Holland and Jonas Zmuidzinas. SPIE, 2014. DOI: [10.1117/12.2055506](https://doi.org/10.1117/12.2055506). URL: <https://doi.org/10.1117/12.2055506>.
- [75] Charles W. Misner, K. S. Thorne, and J. A. Wheeler. *Gravitation*. San Francisco: W. H. Freeman, 1973.
- [76] L. Moncelsi et al. “Receiver development for BICEP Array, a next-generation CMB polarimeter at the South Pole”. In: *Proc. SPIE Int. Soc. Opt. Eng.* 11453 (2020), p. 1145314. DOI: [10.1117/12.2561995](https://doi.org/10.1117/12.2561995). arXiv: [2012.04047](https://arxiv.org/abs/2012.04047) [[astro-ph.IM](https://arxiv.org/abs/2012.04047)].

- [77] R. W. Ogburn et al. “The BICEP2 CMB polarization experiment”. In: vol. 7741. 2010. DOI: [10.1117/12.857864](https://doi.org/10.1117/12.857864).
- [78] Mathieu Remazeilles, Jacques Delabrouille, and Jean-François Cardoso. “Foreground component separation with generalized Internal Linear Combination”. In: *Monthly Notices of the Royal Astronomical Society* 418.1 (Sept. 2011), pp. 467–476. ISSN: 0035-8711. DOI: [10.1111/j.1365-2966.2011.19497.x](https://doi.org/10.1111/j.1365-2966.2011.19497.x). URL: <http://dx.doi.org/10.1111/j.1365-2966.2011.19497.x>.
- [79] George B. Rybicki and Alan P. Lightman. *Radiative Processes in Astrophysics*. 1986.
- [80] Uroš Seljak and Matias Zaldarriaga. “Signature of gravity waves in the polarization of the microwave background”. In: *Physical Review Letters* 78 (11 1997). ISSN: 10797114. DOI: [10.1103/PhysRevLett.78.2054](https://doi.org/10.1103/PhysRevLett.78.2054).
- [81] C. D. Sheehy et al. “The Keck Array: a pulse tube cooled CMB polarimeter”. In: vol. 7741. 2010. DOI: [10.1117/12.857871](https://doi.org/10.1117/12.857871).
- [82] Christopher Sheehy and Anže Slosar. “No evidence for dust B-mode decorrelation in Planck data”. In: *Phys. Rev. D* 97.4 (2018), p. 043522. DOI: [10.1103/PhysRevD.97.043522](https://doi.org/10.1103/PhysRevD.97.043522). arXiv: [1709.09729](https://arxiv.org/abs/1709.09729) [[astro-ph.CO](https://arxiv.org/abs/1709.09729)].
- [83] Eva Silverstein and Alexander Westphal. “Monodromy in the CMB: Gravity waves and string inflation”. In: *Physical Review D* 78.10 (2008). DOI: [10.1103/physrevd.78.106003](https://doi.org/10.1103/physrevd.78.106003). URL: <https://doi.org/10.1103/PhysRevD.78.106003>.
- [84] Kendrick M. Smith. “Pseudo- $C_\ell$  estimators which do not mix E and B modes”. In: *Phys. Rev. D* 74 (2006), p. 083002. DOI: [10.1103/PhysRevD.74.083002](https://doi.org/10.1103/PhysRevD.74.083002). arXiv: [astro-ph/0511629](https://arxiv.org/abs/astro-ph/0511629).
- [85] Juan Diego Soler et al. “An Imprint of Molecular Cloud Magnetization in the Morphology of the Dust Polarized Emission”. In: *Astrophys. J.* 774 (2013), p. 128. DOI: [10.1088/0004-637X/774/2/128](https://doi.org/10.1088/0004-637X/774/2/128). arXiv: [1303.1830](https://arxiv.org/abs/1303.1830) [[astro-ph.GA](https://arxiv.org/abs/1303.1830)].
- [86] Alexei A. Starobinsky. “A New Type of Isotropic Cosmological Models Without Singularity”. In: *Phys. Lett. B* 91 (1980). Ed. by I. M. Khalatnikov and V. P. Mineev, pp. 99–102. DOI: [10.1016/0370-2693\(80\)90670-X](https://doi.org/10.1016/0370-2693(80)90670-X).
- [87] Y. D. Takahashi et al. “Characterization of the bicep telescope for high-precision cosmic microwave background polarimetry”. In: *Astrophysical Journal* 711 (2 2010). ISSN: 15384357. DOI: [10.1088/0004-637X/711/2/1141](https://doi.org/10.1088/0004-637X/711/2/1141).
- [88] Max Tegmark. “How to measure CMB power spectra without losing information”. In: *Phys. Rev. D* 55 (10 May 1997), pp. 5895–5907. DOI: [10.1103/PhysRevD.55.5895](https://doi.org/10.1103/PhysRevD.55.5895). URL: <https://link.aps.org/doi/10.1103/PhysRevD.55.5895>.

- [89] Grant Teply. “Measurement of the Polarization of the Cosmic Microwave Background with the BICEP2 and Keck Array Telescopes”. California Institute of Technology, 2015.
- [90] Jamie Tolan. “Testing inflationary cosmology with BICEP2 and the Keck Array”. PhD thesis. Stanford U., 2014.
- [91] F. Vansyngel et al. “Statistical simulations of the dust foreground to cosmic microwave background polarization (Corrigendum)”. In: *Astronomy & Astrophysics* 618 (Oct. 2018), p. C4. ISSN: 1432-0746. DOI: [10.1051/0004-6361/201629992e](https://doi.org/10.1051/0004-6361/201629992e). URL: <http://dx.doi.org/10.1051/0004-6361/201629992e>.
- [92] Steven Weinberg and R. H. Dicke. “Gravitation and Cosmology: Principles and Applications of the General Theory of Relativity”. In: *American Journal of Physics* 41 (4 1973). ISSN: 0002-9505. DOI: [10.1119/1.1987308](https://doi.org/10.1119/1.1987308).
- [93] Justin Willmert. “Constraining Inflationary B-modes with the BICEP/Keck Array telescopes”. PhD thesis. University of Minnesota, Twin Cities, Jan. 2019.
- [94] Laura Wolz et al. “On the validity of cosmological Fisher matrix forecasts”. In: *Journal of Cosmology and Astroparticle Physics* 2012.09 (2012), p. 009.
- [95] W. L. K. Wu et al. “A Guide to Designing Future Ground-based Cosmic Microwave Background Experiments”. In: *Astrophys. J.* 788 (2014), p. 138. DOI: [10.1088/0004-637X/788/2/138](https://doi.org/10.1088/0004-637X/788/2/138). arXiv: [1402.4108 \[astro-ph.CO\]](https://arxiv.org/abs/1402.4108).
- [96] Hung-I. Yang. “Constraining primordial gravitational waves and characterizing B-modes with the Keck array and BICEP3 CMB experiments”. PhD thesis. Stanford U., 2021.
- [97] Ki Won Yoon et al. “The Robinson Gravitational Wave Background Telescope (BICEP): A bolometric large angular scale CMB polarimeter”. In: *Proc. SPIE Int. Soc. Opt. Eng.* 6275 (2006). Ed. by John C. Mather, Howard A. MacEwen, and Mattheus W. M. de Graauw, 62751K. DOI: [10.1117/12.672652](https://doi.org/10.1117/12.672652). arXiv: [astro-ph/0606278](https://arxiv.org/abs/astro-ph/0606278).
- [98] Matias Zaldarriaga. “Nature of the E B decomposition of CMB polarization”. In: *Phys. Rev. D* 64 (2001), p. 103001. DOI: [10.1103/PhysRevD.64.103001](https://doi.org/10.1103/PhysRevD.64.103001). arXiv: [astro-ph/0106174](https://arxiv.org/abs/astro-ph/0106174).
- [99] Matias Zaldarriaga and Uroš Seljak. “All-sky analysis of polarization in the microwave background”. In: *Physical Review D - Particles, Fields, Gravitation and Cosmology* 55 (4 1997). ISSN: 15502368. DOI: [10.1103/PhysRevD.55.1830](https://doi.org/10.1103/PhysRevD.55.1830).
- [100] Matias Zaldarriaga and Uroš Seljak. “Gravitational lensing effect on cosmic microwave background polarization”. In: *Physical Review D - Particles, Fields, Gravitation and Cosmology* 58 (2 1998). ISSN: 15502368. DOI: [10.1103/PhysRevD.58.023003](https://doi.org/10.1103/PhysRevD.58.023003).